Low Mass WIMP Detection with CCDs

Dissertation*

zur

Erlangung der naturwissenschaftlichen Doktorwürde
(Dr. sc. nat.)

vorgelegt der

Mathematisch-naturwissenschaftlichen Fakultät

der

Universität Zürich

von

Junhui Liao

aus

V.R.China

Promotionskommission

Prof. Dr. Ben Kilminster(Vorsitz)

Laura Baudis

Juan Estrada

Marc Schumann

Zürich, 2016

Acknowledgements

There are many people I should acknowledge who have helped me greatly in finishing my Ph.D. thesis. However, I can not list everyone here whom I should acknowledge.

First of all, I should thank Prof. Ben Kilminster who offered me a position of PhD student in the Department of Physics, University of Zurich where some of the greatest physicists such as Albert Einstein and Erwin Schrödinger have studied and/or worked. This position enabled me to research low-mass dark matter direct detection techniques, giving me a great opportunity to search for particles that have been observed at the galactic scale but never directly detected on earth.
Prof. Kilminster is a very nice person : he picked me up from Zurich airport when I had arrived in the first time with a couple of big luggages which was a very warm reception for me. He also helped me to rent a room before I came to Zurich.
Prof. Kilminster impressed me by his broad and deep understanding in physics, data analysis and detector physics. His passion for physics is infectious, he is always open to discuss any physical topics. He helped me to speed up my research progress. For instance, when I was stuck in data analysis, he provided good suggestions on how to go forward and helped me to get support from internal collaborators; when I was confused in comparing the event rate of EFT O_1 and the standard S.I. analytically, he helped me to get support from a theorist which are very useful.
He is a very good speaker and has shared his experiences of presentation to me. He has helped me improve my *CV* and *cover letter*, and spent a quite some time improving the quality of this thesis.

Secondly, I should thank Dr. Juan Estrada who has been my local supervisor at Fermilab. We worked together for around 2 years. Juan is the spokesperson of DAMIC and an expert on CCDs. He has a very wide knowledge of cosmology, astrophysics, particle physics, data analysis and detector physics etc, while he is very humble. He taught me how to take the images of CCDs. Also, I benefited a lot from the discussions with him on quite a few topics, especially the CTI(Charge Transfer Inefficiency) and CCD detection efficiency. We discussed quite some details about the quenching factor experiment.
Besides physics research, there are many other good memories with him: we watched

the 2014 word cup both in his house and lab[1]. We played soccer quite a few times together. Although he is not very fast, he is unstoppable when he has accelerated to his top speed, ⌣̈. We talked a lot about Maradona, Messi, the Argentinian national team and FC Barca. He is also an expert on Argentinian toast.

Dr. Gaston Gutierrez is a respectable senior physicist at Fermilab who has a very deep understanding and broad experience in physics. I learned a lot from him. One of the most impressive things for me is that he is always open to discuss any physics problems(no matter what kind of question it is) and share his physics knowledge without any reservation. We have cooperated for the Antonella experiment. The cooperation with him(and Marco Reyes) is one of the best research memories I've ever experienced : we exchanged ideas and shared skills and understanding in an open-mind and effective way. The discussions were always productive, the progress of the research was very fast and fruitful.
We had been to the "Montri Thai" restaurant near the east gate of Fermilab so many times for lunch that the waitress even knew we are friends. There are many topics during our lunch discussion : physics, the Antonella experiment, soccer and even finance. He compared Maradona and Messi in a very comprehensive way : Maradona is a fighter while Messi is not. So, Maradona can inspire his team mates to win championships like the World Cup, but Messi can't do same thing ...

Javier Tiffenberg is a postdoc of Fermilab. He helped me on CCD data taking and the charge transfer inefficiency(CTI) analysis. The CTI analysis script I developed is based on his scripts. He is an expert on CCDs. I have asked him lots of questions on CCDs and he always explains to me very clearly. Besides, I appreciate that he helped me to settle down during the first days of my arrival in Fermilab.

Alvaro Chavarria is a post-doc of the University of Chicago who helped me in CCD charge analysis, DAMIC background understanding and shared the limit plotting tools. The EFT analysis scripts I developed are based on the script he used for the limit setting of the standard S.I. for DAMIC.

Marco Reyes is a professor in Mexico. As mentioned above, I enjoyed cooperating with him. Also, it's a good experience for me to cooperate with Dante Amidei, Gustavo Cancelo, Federico Izraelevitch and Alexander Kavne on the quenching factor experiment.

Anthony Diffranzo is a theorist from University of California, Irvine. I should thank him for help understanding the EFT and the mathematica script "dmformfactor.m" at the first stage of my analysis.
Paddy Fox is a theorist at Fermilab who I thank for his comments on how to do the EFT analysis with DAMIC data, and whose answers to my technical questions regarding

[1]Fermilab encouraged people to watch the games on site when U.S. had a game. There was a huge screen on the ground floor of Wilson Hall building playing the games

EFT have improved my understanding.
I also thank Dr. Nikhil Anand and Prof. Wick Haxton who helped me to understand their papers by Emails. I also thank Prof. Gino Isidori and Dr. Thomas Jacques for theoretical discussions.

Prof. Dan Hooper and Dr. Alex Drlica-Wagner thankfully organized "*Munch*"(Monday lunch) in Fermilab which is a casual seminar at lunch time on every Monday bringing brand new papers for discussion from the arXiv in astro-particle physics, cosmology and particle physics. I like munch and many other good academic events, seminars, colloquiums and conferences at Fermilab.

There are many people I would like to thank at the University of Zurich. Prof. Laura Baudis invited me to join in her weekly group meeting several times as an orientation into the dark matter community. I have discussed dark matter a few times with her during my stay at U. Zurich. She recommended me a review about the local dark matter density which has been used in my thesis.
I should thank Dr. Roland Bernet for providing very efficient and effective computer-related solutions, no matter where I have stayed : Fermilab or Zurich.
I should thank all of the secretaries of the Department of Physics, Carmelina Genovese, Ruth Halter, Monika Röllin and especially Regina Schmid since she has dealt with lots of my paperwork.
I also thank to my Chinese friends in the Department of Physics at UZH, HuanYao Cun, Shangxiong Huangfu, Qiang Wang, Yuehuan Wei, Yong Yang and Xiaofu Zhang. I enjoyed to have lunch with them in the "Mensa", and do other activities like hiking and barbecues.

Last but most important, I should thank my family for their selfless support.

Abstract

Astronomical evidence from all length scales for the existence of DM (Dark Matter) is consistent and robust. However, so far there is no solid evidences of the direct detection of DM.

DAMIC (DArk Matter In CCDs) utilizes scientific CCDs (Charge Couple Devices) with a thickness of $\sim 700\mu m$, and a very low and stable noise of $\sim 2e^-$ (RMS) to search for low-mass WIMPs (Weakly Interacting Massive Particles).

The material of DAMIC CCDs is silicon. DAMIC has launched an experiment Antonella at Notre Dame, IN, U.S. to measure the quenching factor of recoil energy down to $\sim$ 1.0 keV. We first calibrated the detectors to be used in the experiment, then calibrated the neutron beam in situ. Based on the data taken in two weeks, the results of our analysis showed that the measurement of the quenching factor is in agreement with the Lindhard model and other experiments for nuclear recoil energies above 5.0 keV, while there exists a discrepancy below 5.0 keV.

The CTI (Charge Transfer Inefficiency) performance of a CCD is important, and its measurement for DAMIC CCDs is presented here, demonstrating that the CCDs have excellent performance.

The standard S.I. (Spin Independent) and S.D. (Spin Dependent) models provide the "tree-level" interaction of WIMP-nucleon elastic scattering. By considering the many types of possible interactions between an incident WIMP and the internal nucleons of a detector nucleus, EFT $\mathcal{O}$s are capable of presenting leading order, next-to-leading order and next-to-next-leading order elastic scattering[2].

In this thesis, the event rate of the EFT $\mathcal{O}_1$ and the standard S.I. have been analyzed and compared. With DAMIC 2015 data, $\sim 0.4\ Kg * day$, upper limits with 90% confidence level have been set for all of the 14 EFT $\mathcal{O}$s.

[2]Here, the order refers to the transferred momentum or WIMP velocity

Table of Contents

1

Introduction

1.1 The evidence of the existence of Dark Matter from astrophysics and cosmology

The universe is comprised of only 4.9% atoms. A much greater fraction, 25.9% of the universe, is a different kind of matter that interacts gravitationally but does not emit or absorb light, "dark matter(DM)". The biggest fraction of the current composition of the universe, 69.2%, is a source of unknown energy("dark energy") that is driving the acceleration of the expansion of the universe. Figure 1.1 shows the constituents of the universe today as determined by Planch data [Planck 2015, XIII].

Scientists infer the existence of dark matter mainly based on three types of astronomical evidence. First, the gravitational pull it exerts on the luminous material we can see, including galaxy cluster and galaxy rotation, and gravitational lensing. Second, the observation that the total amount of mass in the universe exceeds the inventory of atoms we think were made in the Big Bang. Third, galactic simulations showing that the evolution of the large-scale structure in the universe requires a significant dark matter density in order to see the formation of tendrils and filaments of galaxies that are observed.

However, there is no solid evidence for DM interactions other than gravitational, despite attempts to search for them with earth-based direct searches and particle accelerators, as well as space-based telescopes. These three methods of DM hunting are shown in figure 1.2. The "direct detection" method aims to observe the possible signals of DM scattering on a detector which is made of SM particles. To reduce the possible neutron backgrounds which are distinguishable from DM scattering, the detector usually is placed deep underground to shield it from the cosmic rays which can produce neutrons by scattering the materials of a detector system or rock. Using "collider experiments", we hope to see the possible production of DM matter particles during a collision of SM particles(in an accelerator). In this method, the DM particles are identified as missing momentum. The "indirect detection" method aims to find possible signals, for instance, X-rays, produced by DM annihilation in dense regions such as the center of a galaxy.

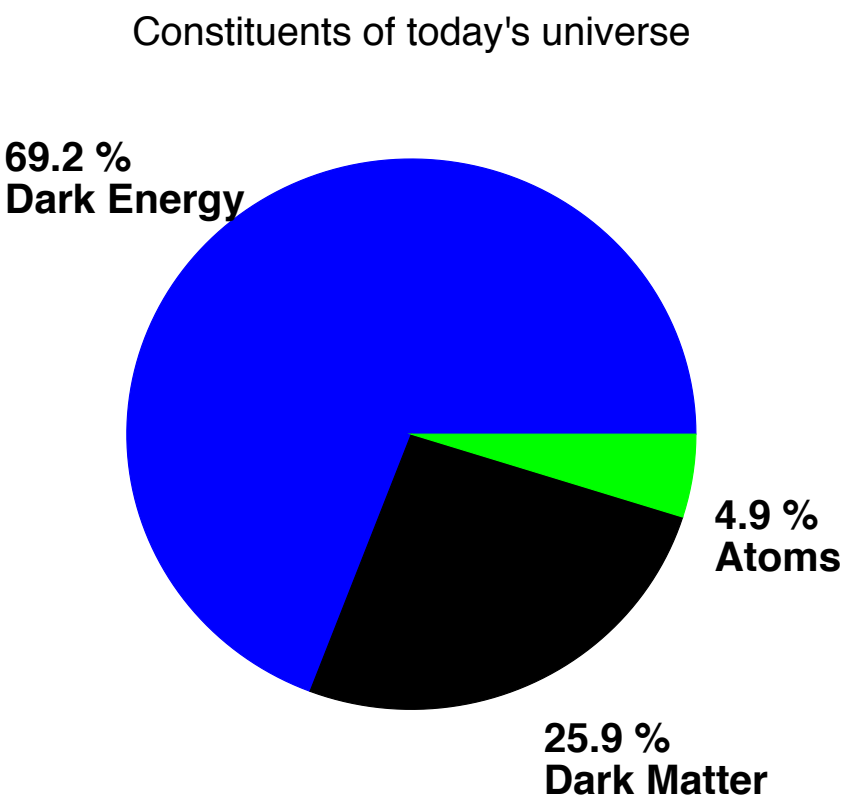

Figure 1.1: Constituents of the universe, the results of Planck data [Planck 2015, XIII]

Determining the nature and distribution of DM is one of the most pressing and interesting open questions in modern science - it resides at the interface of particle physics, nuclear physics, astrophysics and gravity.

1.1.1 Evidence from gravitational pull

A Swiss astronomer, Fritz Zwicky working at the CalTech, first pointed out the existence of DM while studying how galaxies move within the Coma cluster in the 1930s [Zwicky]. By measuring the velocities of the galaxies of the Coma cluster as shown in figure 1.3, Fritz Zwicky realized that there is more mass inside the Coma cluster than the observed luminous matter. Galaxies toward the edge of the cluster were moving far too fast, if their motions were to be explained by the gravitational influence of the other galaxies in the cluster. Zwicky took this as evidence that the cluster must contain a great deal of matter that he couldn't see with his telescope. Although his original paper proposed incorrectly that the mass of dark matter might be ~ 400 times that of visible matter [Zwicky], his paper has been widely accepted as the first publication pointing out the existence of

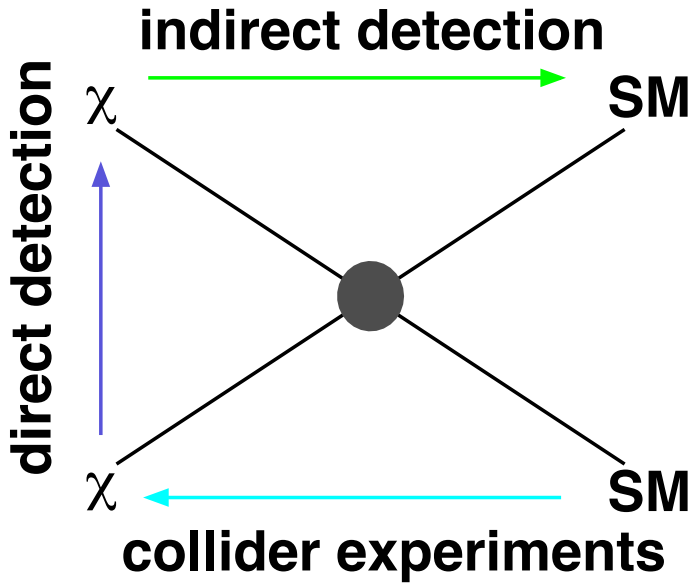

Figure 1.2: The main methods of DM searches. "χ " represents the DM particles and "SM" is the standard model. The "direct detection" method refers to observing the possible signals of DM scattering on a detector composed of SM particles. "collider experiments" refers to the search for production of DM by colliding SM particles, and "indirect detection" indicates the search for the SM produced in the annihilation of DM particles.

dark matter explicitly.

From the 1970s, Vera Cooper Rubin and her collaborator Kent Ford measured the velocity of hydrogen gas clouds in and near the Andromeda(Another notation is $M33$) galaxy [Rubin 1970]. Figure 1.4 shows that the observed velocities of objects orbiting in the M33 galaxy as a function of their distance from the galactic center do not agree with the expected velocities of the objects as determined by the luminous matter observed in the galaxy. The rotational velocity of objects outside the galaxy is far greater than the prediction. If, however, there were a large amount of non-luminous matter in the galaxy, objects far from the galactic center would move much faster. The solid green line is the velocity predicted for the orbiting objects if there is dark matter in M33 [Rubin 1970]. Later, Rubin and her collaborators observed similar phenomena for 21 galaxies which covers a large range of luminosities and radii of galaxies [Rubin 1980]. These rotation curves provide strong indirect evidence for the existence of dark matter.

Alternative explanations of the Andromeda observations soon emerged. The theory of Modified Newtonian Dynamics(MOND) [Milgrom 1983] tried to explain the findings by modifying the gravitational interaction over galactic and larger distance scales. At very low accelerations, which correspond to galactic distances, the theory posits that the

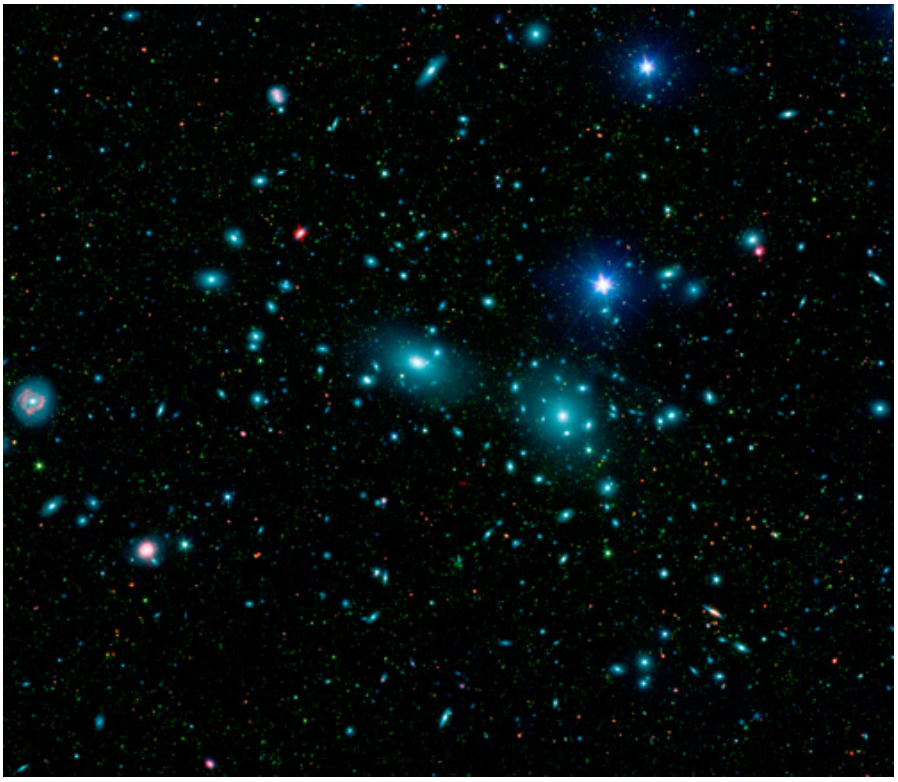

Figure 1.3: The Coma cluster. By measuring the velocities of these galaxies, Fritz Zwicky realized that there is more to the Coma cluster than observed luminous matter

gravitational force varies inversely with the distance alone rather than the square of the distance.
However, MOND would overturn Einstein's theory : General Relativity is based on the simple idea of the *equivalence principle* which states that there is no difference between gravitational mass(the mass that causes the gravitational force) and inertial mass(the mass that resists acceleration). There is no fundamental reason to expect these two masses to be the same, nor is there any reason to expect them to be different. But their equivalence forms the cornerstone of Einstein's general theory. MOND theories break that equivalence because they modify either gravity or inertia. If MOND were correct, a fundamental assumption underlying all of modern physics would be false. Experiments have verified that the *equivalence principle* holds to a part in 10^{13} [S. Schlamminger et al., 2008].

Recent observations of the Bullet Cluster [D. Clowe et al., 2006] using gravitational lensing have provided a stringent test for both standard dark matter and MOND theories. Gravitational lensing is a consequence of general relativity and can be understood from figure 1.4. On the left, a massive body, in this case a galaxy, has the effect of bending

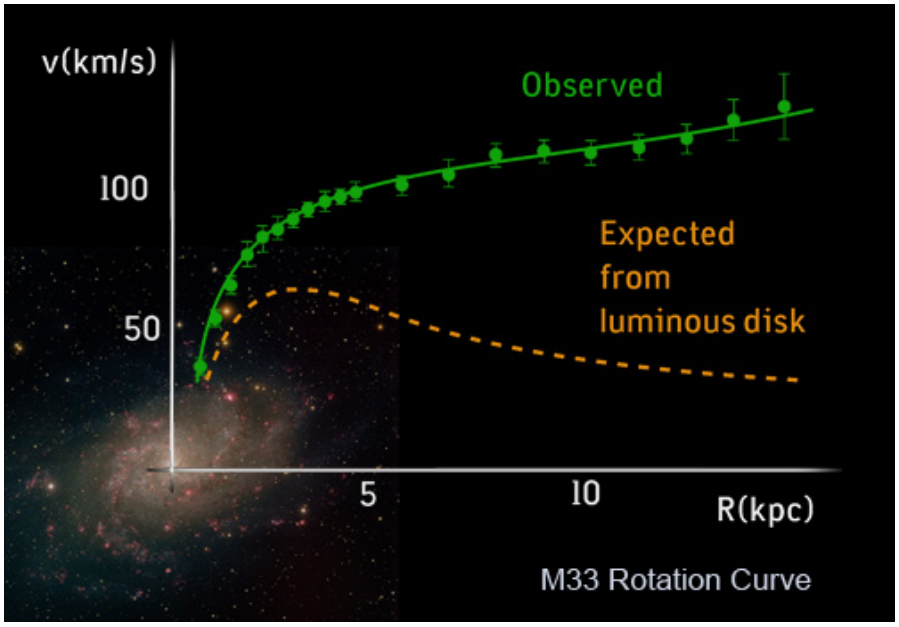

Figure 1.4: The Andromeda(M33) galaxy. Rubin and Ford observed the velocity as green points shown, while the expected velocity is shown as dashed yellow curve if there is no dark matter inside of the M33 galaxy.

the path of light from a distant quasar as it travels toward earth. Quasars are extremely bright objects that can be resolved from great distances across the visible universe. Since many quasars are visible behind galaxies, their light must pass through those intervening galaxies on the way to us. We know from general relativity that the matter in any galaxy - both normal and dark matter - bends space time. That bending distorts the image of any quasar whose light passes through a galaxy. The image of a gravitationally lensed object can be distorted, or even appear as multiple images, as shown on the right of figure 1.5. This Hubble Space Telescope image of the gravitational lens *G2237 + 0305* is sometimes referred to as the "Einstein Cross". The four distinct, bright spots are actually all images of the same quasar. The diffuse central spot is a foreground galaxy that has acted as a gravitational lens, bending light from the quasar so that it appears to be in four places at once. Careful measurements of lensed quasars can reveal information about the distribution of dark matter in the galaxy(or galaxy cluster) that acts as a lens [E.L. Turner, 1988].

Observing colliding galaxy clusters provides a useful way of understanding the nature of dark matter. When two clusters collide, dark matter in one would pass through the other unaffected since dark matter interacts very weakly with itself and normal matter. However, the normal matter in one cluster will interact with the normal matter in the other cluster. During a collision of clusters, the normal matter therefore is dragged back by the normal matter of the other cluster. The net effect of the collision is therefore to

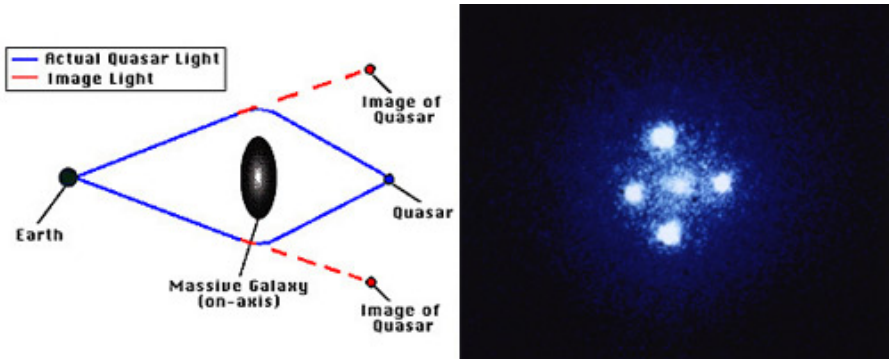

Figure 1.5: Quasars and gravitational lenses

cause the normal matter in each cluster to separate and fall behind the dark matter in the same cluster.

In 2004, NASA's orbiting Chandra x-ray observatory captured an X-ray image of the Bullet Cluster that gives the locations of the normal matter in the two sub-clusters. Meanwhile, astronomers could determine the average position of dark matter in each of the sub-clusters by gravitational lensing measurements since the galaxy clusters contain a few times as much dark matter as normal matter.
Therefore the measurements are capable of testing whether there exists dark matter in the Bullet Cluster or not : in the absence of dark matter, the gravitational potential will trace the dominant visible matter component, which is the X-ray image. If, on the other hand, the mass is indeed dominated by dark matter, the potential will trace the distribution of that component, which is expected to be spatially coincident with the visible galaxies.

Figure 1.6 demonstrates the merger in the Bullet Cluster. The white contours on both sub-figures show the positions of centers of the total mass using gravitational lensing observation which only relies on the mass of the cluster, whereas the temperature map on the right indicates the distribution of luminous matter with the blue crosses on the left figure indicating the centers of the passing sub-clusters. Clearly, the centers of normal matter and total matter are separated, thereby strongly proving that the dominant mass component of the sub clusters is a weakly interacting dark matter component [D. Clowe et al., 2006].

These findings have dealt a severe blow to the MOND theory, which is unable to provide a consistent explanation of the data .

Research on the Bullet Cluster is still ongoing to determine the maximum-allowed self-interactions of DM allowed by such mergers [A. Robertson et al., 16].

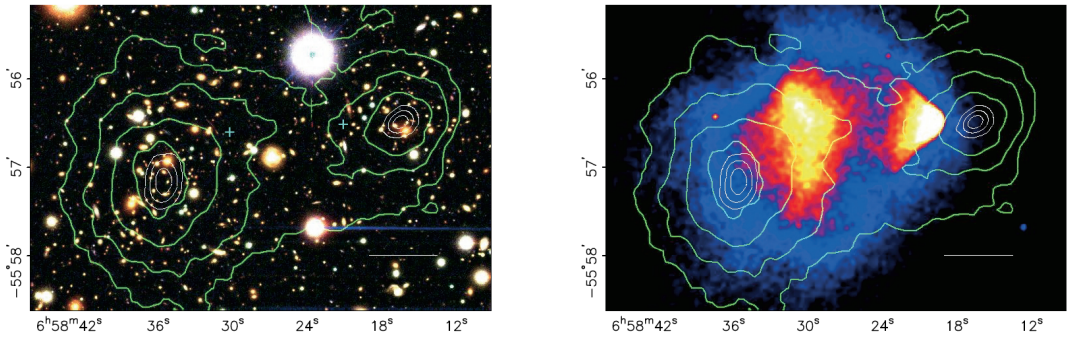

Figure 1.6: Green contours in both panels are the total mass of the two sub-clusters measured by gravitational lensing, the white contours show the errors on the central positions corresponding to 1,2 and 3 σ. The blue crosses show the location of the centers determined from the mass of the normal matter [D. Clowe et al., 2006].

1.1.2 Evidence from the Cosmic Microwave Background

Physicists predicted in late 1940s the existence of the Cosmic Microwave Background(CMB) as an afterglow of the Big Bang. Around twenty years later, two Bell labs scientists, Arno Penzias and Robert Wilson detected it. Since the 1990s, a few spacecrafts have been launched to detect small anisotropies of the CMB : COBE(Cosmic Background Explorer), WMAP(Wilkinson Microwave Anisotropy Probe) and Planck.

About one second after the Big Bang, astrophysicists believe, a very dense mixture of protons, neutrons, photons, electrons and other subatomic particles filled the universe[1]. The temperature was so high that the electrons and protons could not bind together to form atoms. Instead, all the particles scattered off of each other at high rates. The photons also scattered off of the protons and electrons such that they could not "escape". At roughly 380,000 years after the Big Bang, the temperature of the universe dropped to about 3000 Kelvin. By that point, all the electrons and protons had bound to form electrically neutral hydrogen atoms, and all the other charged particles had decayed. After that, the universe became transparent to photons and they have been traveling throughout it for the entire 13.7 billion years since then. The relic photons from the early universe now have a microwave wavelength, and are known as the cosmic microwave background, or CMB .

Before neutral hydrogen formed, matter was distributed uniformly in space with small variations in the density of both normal and dark matter due to quantum mechanical fluctuations in the early moments of the Big Bang. Gravity pulled the normal and dark matter in toward the center of each fluctuation. While the dark matter continued to

[1]The dark matter is expected to have thermally froze out long before this, roughly $\sim 10\ ns$ after the Big Bang [Feng review 10]

move inward, the normal matter fell in only until the pressure of photons pushed it back, causing it to flow outward until the gravitational pressure overcame the photon pressure and the matter began to fall in once more. Each fluctuation "rang" in this way with a frequency that depended on its size. The damped "yo-yoing effect" influenced the temperature of the normal matter. It heated up when it fell in and cooled off when it flowed out. The dark matter, which doesn't interact with photons, remained unaffected by this ringing effect .

When the neutral hydrogen formed, areas into which the matter had fallen were hotter than the surroundings. Areas from which matter had streamed were cooler. The temperature of the matter in different regions of the sky reflects the distribution of dark matter due to initial density fluctuations and the ringing normal matter. This pattern of temperature variations was frozen into the cosmic microwave background. So, a map of the temperature variations in the CMB traces out the location and amount of different types of matter $380,000$ years after the Big Bang .

Figure 1.7 shows the CMB with Planck 2015 publication [Planck 2015 results. IX.]. By analyzing the detailed pattern in this map, Planck scientists infer that around 5 percent of the universe is ordinary matter, and 26 percent is dark matter.

1.1.3 Evidence from galactic simulation

The cold dark matter (ΛCDM) model is the leading theoretical picture for the formation of structure in the universe. Figure 1.8 shows the distribution of dark matter in the universe according to simulations with this model. In this figure, the zoomed-out panel at the bottom of the figure reveals a tight network of cold dark matter clusters and filaments of characteristic size $\sim 100h^{-1}\ Mpc$(h is Hubble's constant, Mpc is mega-parsec, 1 parsec $\approxeq$ 3.25 light-years.). On larger scales, there is little discernible structure and the distribution appears homogeneous and isotropic. The top image reveals several hundred dark matter substructures, resolved as independent, gravitationally bound objects orbiting within a cluster halo. These substructures are the remnants of dark matter halos that fell into the cluster at earlier times of the universe [V. Springel, 2005].

The independent observations from Planck [Planck 2015, XIII] and WMAP [WMAP, 2013] strongly support the ΛCDM model. The parameters obtained from both collaborations are consistent and fit well within the prediction of the model.

1.2 Local dark matter density

The values of the density and velocity of dark matter in the vicinity of the earth are important parameters for experiments searching for interactions of dark matter with

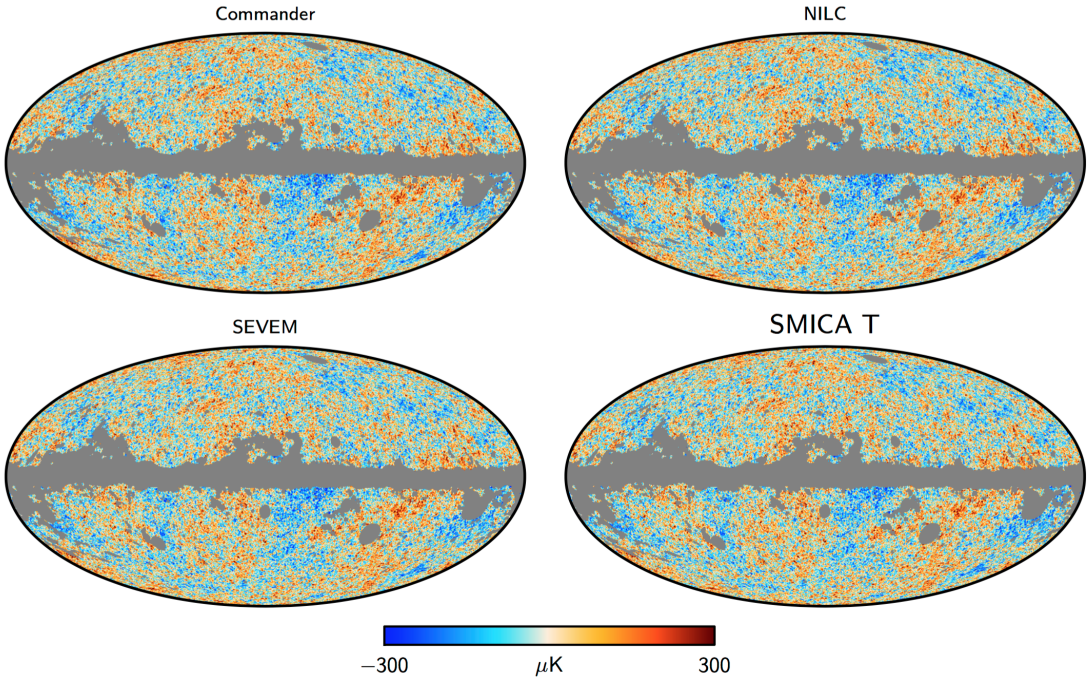

Figure 1.7: CMB temperature maps [Planck 2015 results. IX.]. The datasets of the four sub-figures are the same but the analysis algorithms that have been applied are different : "Commander", "NILC", "SEVEN" and "SMICA T" [Planck 2015 results. IX.].

earth-based detectors. The local dark matter density (ρ_{dm}) [Local DM density] is an average over a "small" volume, typically a few hundred parsecs cubed around the Sun. Efforts to measure the local dark matter density has been ongoing since the 1920s, as shown in figure 1.9. The gray band on the figure covers the most likely measured density. For DM direct detection, physicists often take $\sim (0.3 - 0.4) GeV/cm^3$ as the local dark matter mass density[2].

As opposed to the simulation and fit of 10 million galaxies as performed by "Millennium Run" [V. Springel, 2005], the Aquarius project aims to simulate the structure within galaxies the size of our Milky Way in order to understand the detailed structures such as the "cuspy" dark matter and other sub-halo level features, [V. Springel, 2005].
Figure 1.10 shows the expected local dark matter velocity from simulation
[M. Vogelsberger et al., 2009]. For direct detection experiments, physicists often take $\sim 220 km/s$ as the local dark matter velocity.

The measurement of the local dark matter density is an area of active research. The Gaia satellite, launched in 2013, will, among other research in its 9 year mission lifetime,

[2]In this thesis, $h = c = 1$.

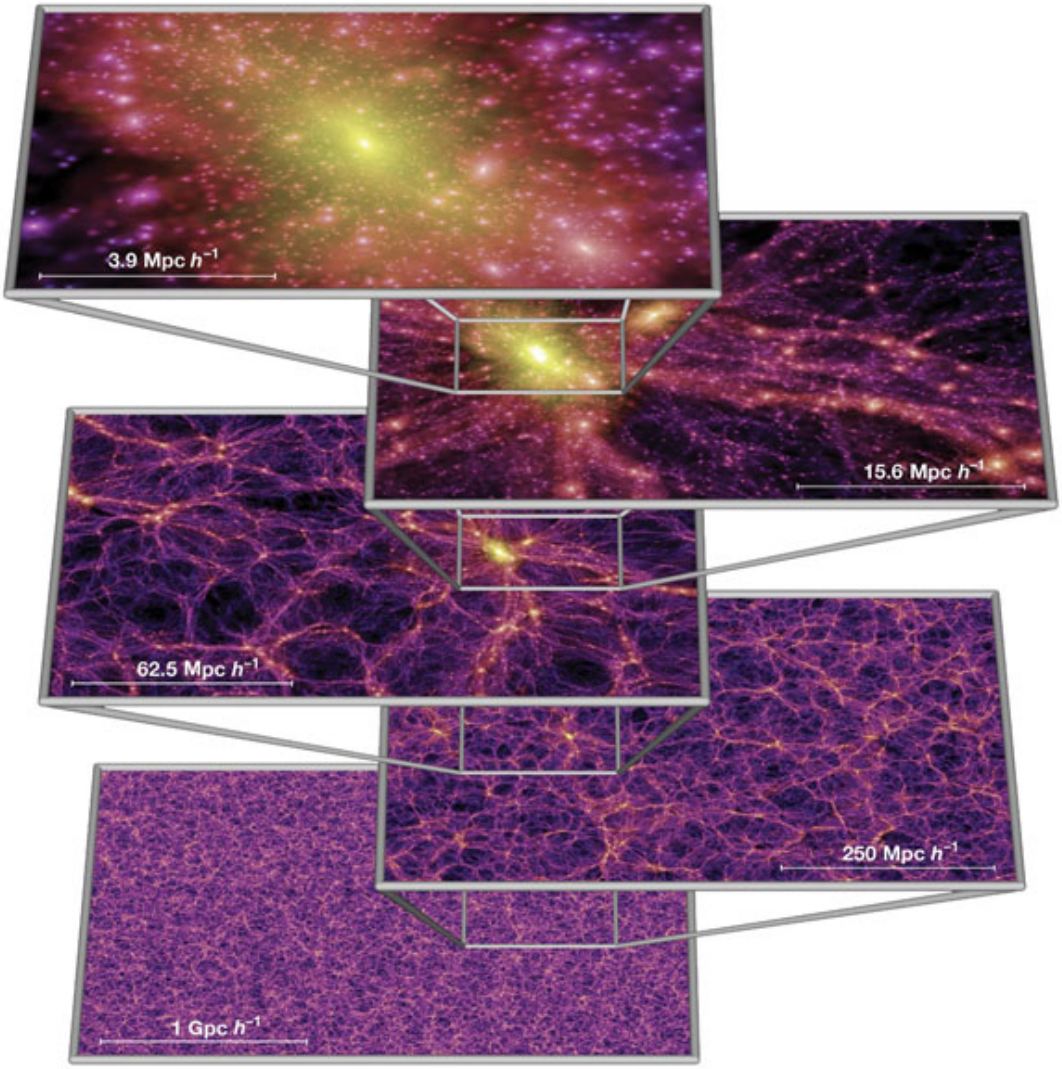

Figure 1.8: The dark matter density field on various scales according to simulation. Each individual image shows the projected dark matter density field in a slab of thickness $15h^{-1}$ Mpc(h is Hubble's constant, Mpc is mega-parsec, 1 prasec $\approxeq$ 3.25 light-years), color-coded by density and local dark matter velocity dispersion. The zoom sequence displays consecutive enlargements by factors of four, centered on one of the many galaxy cluster haloes present in the simulation [V. Springel, 2005]

measure the large scale motion of stars in the Milky Way in order to more precisely probe ρ_{dm} [Gaia].

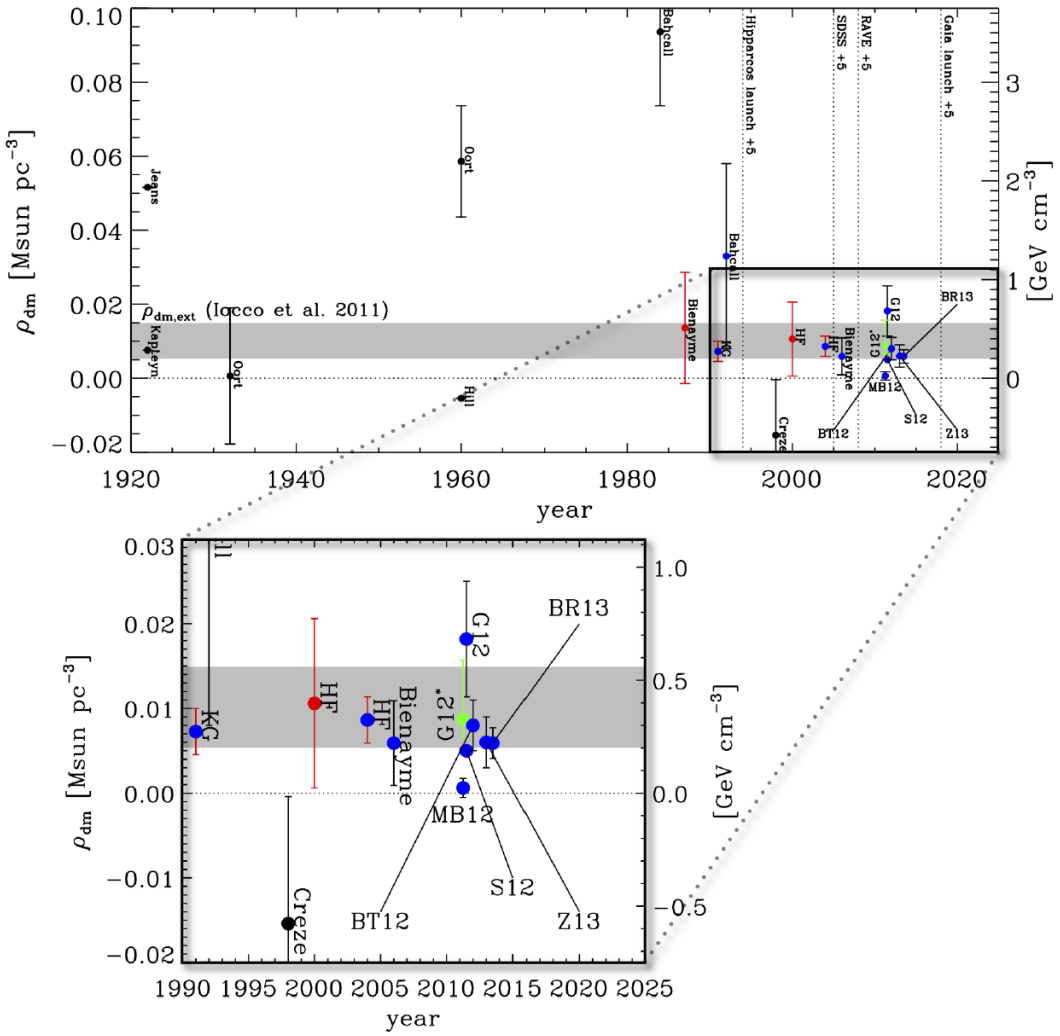

Figure 1.9: A century of measurements of ρ_{dm}. All error bars represent either 1σ uncertainties or 68% confidence intervals [Local DM density].

1.3 Theoretical review on Dark Matter candidates

Most models of DM treat it as non-baryonic matter. The model of MACHOs (Massive Astrophysical Compact Halo Objects) is an exception which proposes non-luminous baryonic matter as the DM candidate. Such a model can be tested using the microlensing effect [B. Paczynski]. The MACHO collaboration observed a signal with a DM candidate mass of 0.4 solar masses and put an upper limit that it can can explain up to 40% [C. Alcock] of DM. In such a case, a contribution from non-baryonic DM would still be required.

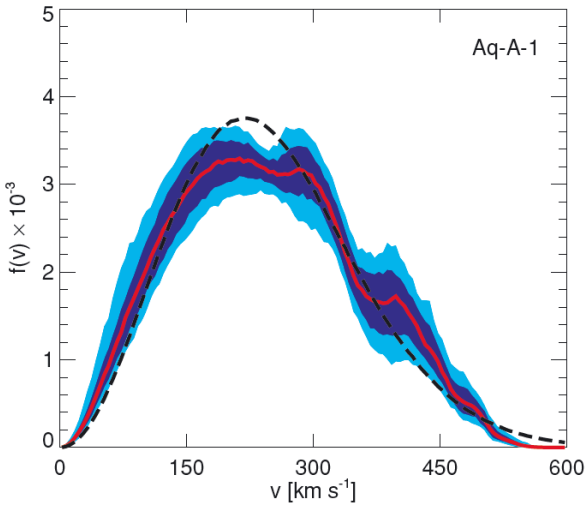

Figure 1.10: Local dark matter velocity. A thick red line gives the median of the measured distributions, a dashed black line gives the the median of the fitted multivariate Gaussians. The dark and light blue contours enclose 68 and 95 percent of the measured distributions at each velocity, [M. Vogelsberger et al., 2009].

The successful ΛCDM model indicates that most DM should be "cold", *i.e.*, should be non-relativistic when galaxies formed. Candidates for non-baryonic DM must satisfy several conditions:
1. They must be stable on the time scale of the life of the universe otherwise they could not be observed by current telescopes. This requirement excludes most of the standard model quarks, leptons and bosons.
2. They must interact very weakly with electromagnetic radiation otherwise they would have been observed already. This requirement rejects electrons and photons as the DM candidate.
3. They must have the right relic density otherwise the mass density of DM in the current universe could not be 5 times greater than matter. This makes the SM neutrino not eligible to be the candidate of DM[3].
Therefore, none of the standard model particles provide viable candidates for DM.

The connection between dark matter and gravity bears special mention because it is the one thing about dark matter of which physicists are certain. Everything we know about dark matter so far comes from astronomy. The astronomical measurements deal exclusively with the way in which dark mater interacts gravitationally . However, these

[3]The sterile neutrino could be a possible candidate of DM which interacts with matter via gravity. So it is different from the known SM neutral hadrons which are charged under the weak interaction. However, the sterile neutrino is a theoretical construct, and would need to be discovered in data to confirm its existence.

measurements actually leave the nature of DM and its interactions with either itself or normal matter completely unknown. Physicists hope to find other kinds of interactions between DM and normal matter besides gravitational. Attempts to understand DM more directly by looking for signals of its interaction with SM particles are taking place on a variety of experimental frontiers. Direct detection of DM with earth-based detectors in underground facilities would provide a vital demonstration of the interaction of the DM in our galaxy with SM particles.
Being motivated by different physics goals, the most currently discussed dark matter candidates are : WIMPs (Weakly Interacting Massive Particles), which are motivated by theories that solve the gauge hierarchy problem, [Scherrer & Turner 86]; Axions, which are motivated to solve the strong CP problem [Peccei & Quinn 77]; ADM (Asymmetric Dark Matter), which is motivated by the ratio of DM density to that of matter [Nussinov 85]; and "WIMPless" DM which is one of the only interpretations based solely on the thermal relic density [Feng & Kumar 08]. There are many possible DM candidates with mass ranging from $keV - TeV$.

1.3.1 WIMP : Gauge hierarchy problem

The WIMP is the most studied DM candidate. If a WIMP exists and is stable, it is naturally produced with the relic abundance consistent with that required of dark matter. This often is called "the WIMP miracle", implies that particles are motivated by the gauge hierarchy problem, a purely microphysical puzzle, turns out to be an excellent dark matter candidates, a cosmological components.

A hierarchy problem occurs when the fundamental value of some physical parameter, such as a coupling constant or a mass, in some Lagrangian is vastly different from its effective value, which is the value that gets measured in an experiment. This happens because the effective value is related to the fundamental value by a prescription known as renormalization, which imposes corrections on it. Typically the renormalized value of parameters are close to their fundamental values, but in some cases, it appears that there has been a delicate cancellation between the fundamental quantity and the quantum corrections. Hierarchy problems are related to fine-tuning problems and problems of naturalness [Peskin & Schroeder 95].

In particle physics, the gauge hierarchy problem is the question of why the physical Higgs boson mass m_h is so small, $m_h \sim 100GeV \lll M_{Pl}$, where $M_{Pl} = 1.2 \times 10^{19}\ GeV$ is the Planck mass. $M_{Pl} = \sqrt{hc/G_N}$, where h, c and G_N are Planck constant, the speed of light and Newton's gravitational constant, respectively. We therefore expect the natural value of m_h should be either 0, if enforced by a symmetry, or the order of M_{Pl} if the symmetry is broken. In the SM(Standard Model), the electroweak symmetry is broken, and the Higgs boson mass is non-zero, but $m_h \lll M_{Pl}$. The problem is exacerbated by SM quantum corrections. The physical mass of the SM Higgs boson is $m_h^2 = m_{h0}^2 + \Delta m_h^2$,

where m_{h0}^2 is the tree-level mass of the Higgs, and Δm_h^2, as shown in(1.1),

$$\Delta m_h^2 \sim \frac{\lambda^2}{16\pi^2}\int^{\Lambda}\frac{d^4p}{p^2} \sim \frac{\lambda^2}{16\pi^2}\Lambda^2, \tag{1.1}$$

where the integral is over the momenta of particles in the loops. The λ is an $\mathcal{O}1$ dimensionless coupling, and Λ is the energy scale at which the SM is no longer a valid description of nature. In the SM, $\Lambda \sim M_{Pl} \Rightarrow \Delta m_h^2 \sim 10^{34}$ according to Eq. (1.1) and $\lambda^2 \sim 10^{-2}$, $1/(16\pi^2) \sim 10^{-2}$ and $\Lambda^2 \sim 10^{38}\ GeV$. This implies that to get the correct Higgs mass, $m_h \sim 100GeV$, m_{h0}^2 and Δm_h^2 must cancel to 1 part in 10^{34}. This and other similar interpretations hardly seam natural [4].
The gauge hierarchy problem may be eliminated if $\Lambda \lesssim 1\ TeV$, implying new physics at the weak scale $\sim 10\ GeV - TeV$. Alternatively, the Higgs boson may not be a fundamental scalar, but in this case, too, its structure requires new physics at the weak scale. So far, every attempt to ameliorate the gauge hierarchy problem has implied new particles with mass around the weak scale. The gauge hierarchy problem is the arguable leading motivation for WIMP dark matter candidates [Feng review 10].

1.3.2 WIMP mirarcle

If a WIMP exists and is stable, it is naturally produced with a relic density consistent with that required of dark matter. This observations is sometimes referred to as "the WIMP miracle".
Most cosmological models describe the early universe initially as dense and hot with all particles in thermal equilibrium. The universe then cools to temperatures below the dark matter particle's mass, $T < m_\chi$, and the number of dark matter particles becomes Boltzmann suppressed, dropping exponentially as $e^{-m_\chi/T}$. The number of dark matter particles would drop to zero except that the universe is also expanding. As a result, the universe becomes large enough that the dark matter particles become too dilute to annihilate into normal matter particles. The dark matter then "freezes out", with the number density asymptotically approaching a constant, which is known as their thermal relic density.
This process is described quantitatively by the Boltzmann equation,

$$\frac{dn}{dt} = -3Hn - <\sigma_A v>(n^2 - n_{eq}^2) \tag{1.2}$$

where n is the number density of the dark matter particle χ, H is the Hubble parameter of the expansion of the universe, $<\sigma_A v>$ is the thermally averaged annihilation cross

[4] Note 1 : in reference of [Feng review 10], it says the cancellation is 1 part in 10^{36} which might be because the reference did not use the additional factor of $1/(16\pi^2) \sim 10^{-2}$.
Note 2 : This [Feng review 10] is not the only interpretation of the gauge hierarchy problem. An alternative one is described in reference [Peskin & Schroeder 95] in which the cancellation is 1 part in 10^{28} because it is expected to be $10^{16}\ GeV$ in the context of GUT(Grand Unification Theory) rather than $1.2 \times 10^{19}\ GeV$ as the energy of Λ because the β functions corresponding to a supersymmetric multiplet of particles are of order at $\sim 10^{16}\ GeV$.

section, and n_{eq} is the dark matter number density in thermal equilibrium. On the RHS (Right Hand Side) of (1.2), $-3Hn$ accounts for the dilution from expansion; the n^2 arises from the processes $\chi\chi \to SM\ SM$ in which χ particles annihilate to produce SM particles, where SM denotes SM particles; and the n_{eq}^2 comes from the reverse process of $SM\ SM \to \chi\chi$, which creates χ particles.
The thermal relic density is determined by solving the Boltzmann equation numerically. A rough approximation is also instructive [Feng review 10], as in

$$n_f \sim (m_\chi T_f)^{3/2} e^{-m_\chi/T_f} \sim \frac{T_f^2}{M_{Pl} < \sigma_A v >} \tag{1.3}$$

where the subscripts f denote quantities at freeze out, and m_χ is the mass of dark matter . The ratio $x_f \equiv m_\chi/T_f$ appears in the exponential and is therefore highly insensitive to the dark matter's properties and may be considered as a constant, $x_f \sim 20$.
The thermal relic density is,

$$\Omega_\chi = \frac{m_\chi n_0}{\rho_c} = \frac{m_\chi T_0^3}{\rho_c}\frac{n_0}{T_0^3} \sim \frac{m_\chi T_0^3}{\rho_c}\frac{n_f}{T_f^3} \sim \frac{x_f T_0^3}{\rho_c M_{Pl}} < \sigma_A v >^{-1} \tag{1.4}$$

where Ω_χ is the relic density of dark matter, ρ_c is the critical density, and the subscripts 0 denote present-day quantities. The thermal relic density is insensitive to the dark matter mass m_χ and inversely proportional to the annihilation cross section $< \sigma_A v >$.

Assuming $m_\chi = 100\ GeV$, the evolution of a thermal relic's number density is shown in figure 1.11.
Although m_χ does not enter Ω_χ directly, in many models the mass determines the annihilation cross section. On dimensional grounds, the cross section can be written as

$$\sigma_A v = k\frac{g_{weak}^4}{16\pi^2 m_\chi^2}(1\ or\ v^2) \tag{1.5}$$

where the factor v^2 is absent or present for $S-$ or $P-$wave annihilation, respectively, and terms of higher-order in v have been neglected. The constant $g_{weak} \approxeq 0.65$ is the weak interaction gauge coupling, and k parameterizes deviations from this estimate.
With this parameterization, given a choice of k, the relic density is determined as a function of m_χ. The results are shown in figure 1.12. The width of the band comes from considering both $S-$ or $P-$wave annihilation, and from letting k vary from 1/2 to 2. A particle that makes up all of dark matter is predicted to have a mass in the range of $m_\chi \sim 100\ GeV - 1\ TeV$; a particle that makes up 10% of dark matter would have a mass of $m_\chi \sim 30\ GeV - 300\ GeV$, [Feng review 10].
This is "the WIMP miracle" : weak-scale particles make excellent dark matter candidates. It is at present the strongest reason to expect that central problems in particle physics and astrophysics may in fact be related [Feng review 10].

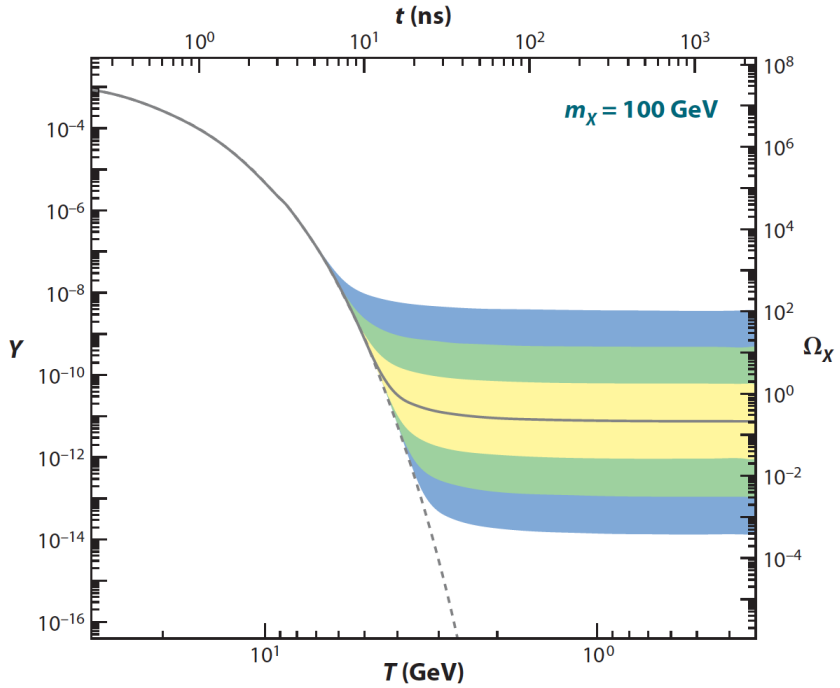

Figure 1.11: The comoving number density Y(left) and resulting thermal relic density(right) of a 100 GeV, P-wave annihilating dark matter particle as a function of temperature T(bottom) and time t(top). The solid gray contour is for an annihilation cross section that yields the correct relic density, and the shaded regions are for cross sections that differ by $10, 10^2$ and 10^3 from this value. The dashed gray contour is the number density of a particle that remains in thermal equilibrium [Feng review 10].

1.3.3 WIMPs : Current upper limits and future sensitivity

Although WIMPs have been considered as a miracle, the limits combined from direct detection and the LHC(Large Hadron Collider) both set the limit of the cross-section of WIMP-nucleon interaction much more lower than expected from the the weak interaction, $\sim 10^{-40} cm^2$, for ~ 100 GeV WIMPs. Figure 1.13 shows results from recent direct detection searches and 1.14 shows a comparison with results from LHC experiments for specific interactions with some assumptions on parameter choices.

One needs to be aware that the cross-section limits on both direct detection and the LHC experiments are for a WIMP interacting with a nucleon(proton or neutron), rather than with quarks via the exchange of W, Z and H bosons. This is done by summing up over the collective scattering of the individual particles. A detailed description is shown in the classic reference [G. Jungman et al, 96]. This topic will be addressed further in chapter 5.

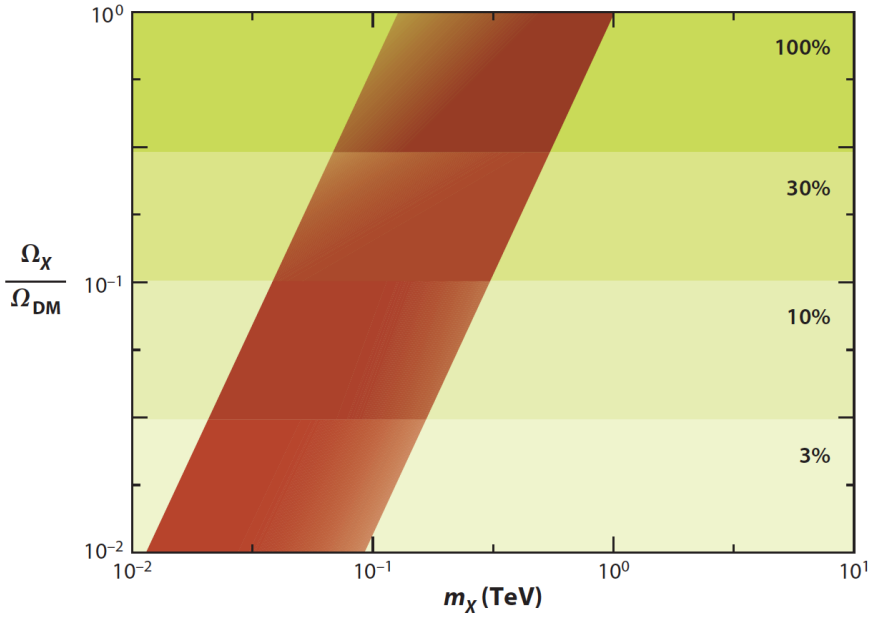

Figure 1.12: A band of natural values in the $(m_\chi, \Omega_\chi/\Omega_{DM})$ plane for a weakly interacting thermal relic dark matter, where Ω_{DM} is the required total dark matter density [Feng review 10].

Facing the absence of the expected WIMP signals, new efforts have been exerted both from experimental and theoretical communities. Experimentally, there are two "directions" for the next step of WIMPs searches. One is building bigger detectors to reach lower and lower cross-sections until the neutrino floor. G2(Generation 2) detectors like LUX, SuperCDMS Snolab are these kinds of efforts. G2 detectors typically have tons of target material. Higher mass G3 (Generation 3) detectors, such as DARWIN [Darwin collaboration] and Argo [DarkSide-20k experiment] with the goal of reaching the so-called neutrino-floor, where neutrino backgrounds become visible, are in the R&D phase.
Another direction of research is the pursuit of lower-mass $\sim keV$ (warm)dark matter. Some new concepts of detectors have been suggested, using superconducting technologies [Hochberg et al, 15], and superfluid Helium [Schutz & Zurek, 16].

Theoretically, the absence of signals at the LHC for physics beyond the SM, as well as the discovery of the SM-like Higgs boson with mass near 125 GeV, constrains many well-motivated WIMP models [PDG 15]. There are many interesting models arising, for instance, the "WIMPless miracle" which demonstrates that other combinations of the dark matter particle's mass m_χ and coupling constants g_χ may satisfy the correct thermal relic density without weak-scale mass or interactions that would result in detection at

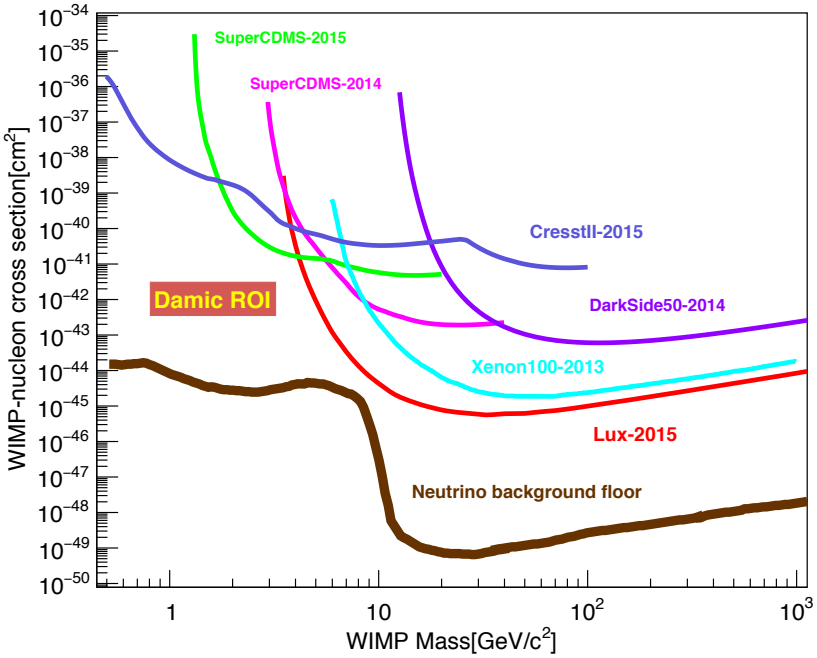

Figure 1.13: The latest limits from direct detection experiments have also shown here. The limit of "SuperCDMS-2015" cited from reference [SuperCDMS 15]. The limit of "SuperCDMS-2014" cited from reference [SuperCDMS 14]. "CresstII-2015" from reference [Cresst 15]. "DarkSide50-2014" from reference [DarkSide 14]. "Xenon100-2013" from reference [XENON100 13]. "Lux-2015" from reference [LUX 15]. "Neutrino background floor" from reference [Billard 13]. Also shown is the DAMIC region of interest, the subject of this thesis.

the LHC, such that

$$\Omega_\chi \sim < \sigma_A v >^{-1} \sim \frac{m_\chi^2}{g_\chi^4} \tag{1.6}$$

where Ω_χ is the dark matter density, m_χ is the dark matter mass, g_χ is the coupling constant of dark matter to normal matter. Apparently, there are many other combinations of m_χ and g_χ that could give the correct Ω_χ. Essentially, these are models for "dark matter that naturally has the correct relic density, but does not necessarily have a weak-scale mass or weak interactions", as mentioned in [Feng & Kumar 08, Feng review 10]. On the reference of [Feng et al, 08], a complete model has been built which generalizes the WIMP paradigm to the largest range possible for viable thermal relics and provides a framework for exploring dark matter signals across nine orders of magnitude in dark matter mass, $keV \lesssim m_\chi \lesssim TeV$.
This theory expands the horizon of DM direct detection experiments. Since thermal

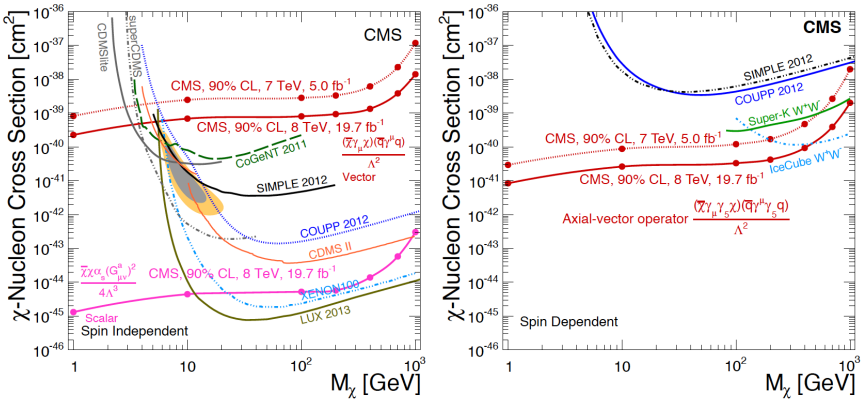

Figure 1.14: Upper limits on the DM-nucleon cross section, at 90% CL, plotted against DM particle mass and compared with previously published results. Left plot : limits for vector and scalar operators . Right plot : limits from a axial-vector [CMS-8TeV DM 14].

relic density is the only solid measurement of DM besides its gravitational interaction, this theory aids direct dark matter experiments in interpreting and cross-section of interaction with matter.

1.3.4 Axion

The Axion is another DM candidate [Peccei & Quinn 77]. The SM Lagrangian includes the term : $g_3^2\theta_3/(32\pi^2)\epsilon^{\mu\nu\rho\sigma}G^{\alpha}_{\mu\nu}G^{\alpha}_{\rho\sigma}$, where g_3 is the coupling of the strong interactions, θ_3 is an angle parameter, $\epsilon^{\mu\nu\rho\sigma}$ is the totally antisymmetric 4-index tensor, and $G_{\mu\nu}$ is the gluon field strength. This term contributes to CP-violating, flavor-conserving observables, such as the electric dipole moment(EDM) of the neutron d_e. For $\theta_3 \sim 1$, one expects $d_e \sim 10^{-16} e \cdot cm$. The EDM hasn't been observed yet, but current limits already imply $d_e < 3.0 \times 10^{-26} e \cdot cm (90\% CL)$ [J. Pendlebury et al, 15]. This is therefore a fine-tuning problem of 1 part in 10^{10}, and it motivates axions as dark matter candidates [Feng review 10].

The axion solution solution follows from introducing a new pseudo scalar field "a" with coupling

$$\mathcal{L}_a = -\frac{g_3^2}{32\pi^2}\frac{a}{f_a}\epsilon^{\mu\nu\rho\sigma}G^{\alpha}_{\mu\nu}G^{\alpha}_{\rho\sigma} \tag{1.7}$$

where f_a is a new mass scale, the axion decay constant. This term $\frac{a}{f_a}$ makes the coefficient of $\epsilon^{\mu\nu\rho\sigma}G^{\alpha}_{\mu\nu}G^{\alpha}_{\rho\sigma}$ dynamical.

The axion's mass and interactions are determined by f_a up to a model-dependent constant.

$$m_a \approxeq 6\mu eV(\frac{10^{12}GeV}{f_a}) \tag{1.8}$$

However, in contrast to WIMPs, axions do not naturally have the correct density. Under the assumption that inflation occurs after the Peccei-Quinn(PQ) transition [Peccei & Quinn 77], the allowed mass of the axion is $6\mu eV\theta_i^2 \lesssim m_a \lesssim 6\ meV$, but there is no prior to determine the value within this available mass window.

Axions interact with photons through the coupling

$$\mathcal{L}_{a\gamma\gamma} = -g_\gamma \frac{\alpha}{\pi}\frac{a}{f_a}\overrightarrow{E}\cdot\overrightarrow{B} \equiv -g_{a\gamma\gamma}a\overrightarrow{E}\cdot\overrightarrow{B} \tag{1.9}$$

where α is the fine-structure constant and g_γ is a model-dependent parameter.

The Axion Dark Matter Experiment(ADMX) searches for cosmological axions by looking for the resonantly enhanced conversion of dark matter axions to photons through scattering off a background magnetic field, $a\gamma^* \to \gamma$. This experiment scans over different frequencies(f_a). The latest exclusion limits on Axion couplings vs. mass are shown in figure 1.15 [ADMX 14].

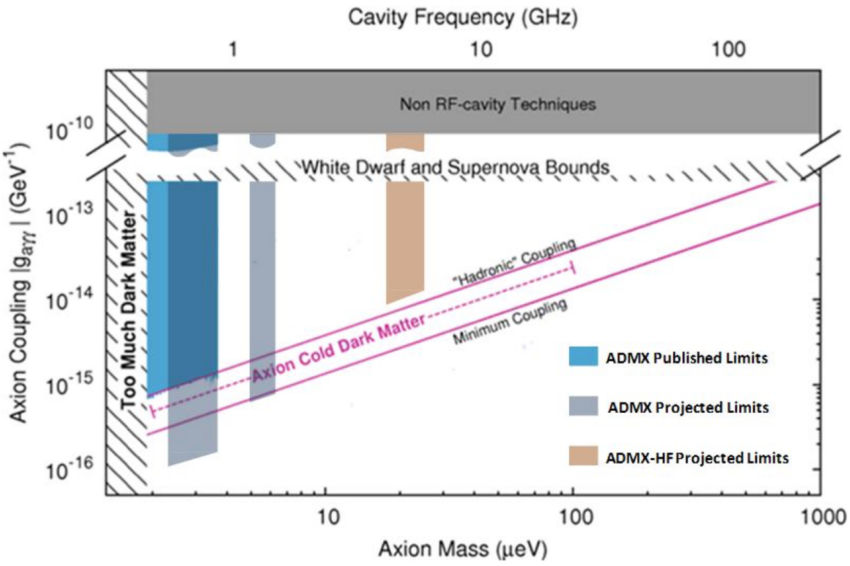

Figure 1.15: Axion exclusion from ADMX. The typical name of KSVZ is labeled as "Hadronic's Coupling" on the plot and the DFSZ limit is labeled as "Minimum Coupling" [ADMX 14].

1.3.5 ADM : Asymmetric Dark Matter

The mass density of DM and baryon abundances are very close to each other according to the observation of WMAP and Planck, $\rho_{DM}/\rho_B \cong 5$, [Planck 2015, XIII, WMAP, 2013], where ρ_{DM} and ρ_B are the mass density of DM and baryons, respectively. However, in the paradigm of Weakly Interacting Massive Particles(WIMPs), the mass densities are not a priori related to each other [K. Zurek, 13]. The DM density in the WIMP freeze-out paradigm is fixed when the annihilation rate drops below the expansion rate,

$$n(T_{fo})\langle\sigma_{ann}v\rangle < H(T_{fo})$$

where T_{fo} is the temperature when DM annihilation freezes-out, $n(T_{fo})$ is the DM number density, and $\langle\sigma_{ann}v\rangle$ is a thermal annihilation cross-section. So the DM number density today is related to the annihilation cross-section. On the other hand in baryogenesis, the baryon density is set by CP-violating parameters and out-of-equilibrium dynamics associated with baryon number violating processes [A.G. Cohen et al, 93]. Since the baryon density and the DM density result from different physical mechanisms, it seems surprising that the observed two densities are so close to each other. It is possible that this is an accident, or this is an indication of a new scenario, ADM, for instance.
The connection between the densities of DM and baryons arises naturally when the DM has an asymmetry in the number density of matter over anti-matter similar to baryons.

$$n_\chi - n_{\bar{\chi}} \sim n_b - n_{\bar{b}} \tag{1.10}$$

where $n_\chi, n_{\bar{\chi}}$ are the DM and anti-DM number densities, and $n_b, n_{\bar{b}}$ are the baryon and anti-baryon densities.
The DM density then is set by an asymmetry, which can be directly connected to the baryon asymmetry, rather than by its annihilation cross-section. Since $\rho_{DM}/\rho_B \sim 5$, Eq.(1.10) suggests $m_\chi \sim 5\ m_p \cong 5\ GeV$, where m_p is the mass of a proton.

The idea that the DM and baryon asymmetries might be related to each other dates almost from the time of the WIMP paradigm. The initial motivation for a DM asymmetry was to solve the solar neutrino problem, by accumulating DM that affects heat transport in the Sun [Nussinov 85].

A strong motivation for the DAMIC direct detection experiment is provided by ADM.

1.4 Experimental review on DM detection: Basics, technologies and current limits

1.4.1 Basics of WIMP direct detection

Since the earth moves through the galactic halo of DM, if the DM particles interact weakly, they can be directly detected through their nuclear recoils with matter. Such

interaction rates are characterized by galactic velocities of order 10^{-3} c, where c is the speed of light, and typical nuclear recoil energies of $1 - 100$ keV. The recoil energy can be obtained by the following equation [Lewin and Smith, 1996],

$$E_R = \frac{4m_\chi m_T}{(m_\chi + m_T)^2} E_0, \tag{1.11}$$

where E_R is the recoil energy, m_χ and m_T are the masses of the WIMP and target detector nuclei, E_0 is the kinematic energy of incident WIMPs.
The shape of the nuclear recoil spectrum results from the convolution of the WIMP velocity distribution, usually taken as a Maxwell distribution in the galactic rest frame, shifted into the Earth rest frame, with the angular scattering distribution, which is isotropic to first approximation but forward-peaked for high nuclear mass(typically higher than the mass of Ge) due to the nuclear form factor. Overall, this results in a roughly exponential spectrum [PDG 15].

Assuming a S.I.(Spin Independent) interaction, the event rates of a WIMP interacting with a target detector is shown in Eq.(1.12) [A. Kurylov & M. KamionKowski 03],

$$\frac{dR}{dE_R} = \frac{\rho_\chi}{2m_\chi m_{red}^2(m_{nuc})} \times \sigma_{0\chi N}^{SI} \times F_{SI}^2(E) \times \int_{V_{min}}^{\infty} \frac{f_1(v)}{v} dv, \tag{1.12}$$

where ρ_χ is the mass density of dark matter at the earth, m_χ is the mass of the dark matter particle itself, $m_{red}(m_{nuc})$ is the reduced mass of the dark matter and the target nucleus, $\sigma_{0\chi N}^{SI}$ is the S.I. cross-section of WIMP and the target nucleus, $F_{SI}^2(E)$ is the form factor, v_{min} is the minimum velocity for which the WIMP could deposit detectable energy, and $f_1(v)$ is the WIMP speed distribution.
The typical mass density of dark matter in the region of our solar system is $\sim 0.39\, GeV/cm^3$ [PDG 15]. The form factor arises when the momentum transfer $q = \sqrt{2m_T E_R}$, where m_T and E_R are the mass of the target nucleus and recoil energy separately, is such that the wavelength h/q is no longer large compared to the nuclear radius, where h is Planck's constant. Under this context, the effective cross-section begins to fall with increasing q. It is convenient to represent this by a form factor, which is a function of the dimensionless quantity $qr_n/\hbar$ where r_n is an effective nuclear radius [Lewin and Smith, 1996][5].
The integration of speed depends on the relative velocities between the WIMPs and the Earth. The quantity v_{min} is the dark matter velocity corresponding to E_{min} which is the smallest particle energy that can give a recoil energy of E_R, will be discussed further in chapter 5.

As an example of a distribution of event rate, dR/dE, figure 1.16 shows the expectation for both 5 and 35 GeV WIMPs, assuming a silicon detector target, with a S.I. model, a cross-section of $\sigma = 1.0 \times 10^{-4}$ pb, and an exposure of 0.3 $Kg \cdot day$. While a 1 KeV

[5]However, once momentum transfers reach the point where $\bar{q}\bar{x}(i)$, where $\bar{x}(i)$ the nucleon coordinate within the nucleus, is no longer small, not only form factors, but new operators arise [EFT PRC 14]. Chapter 5 will discuss further on this topic.

threshold for a 35 GeV WIMP would be sufficient for the 5 GeV WIMP, the energy threshold of the detector should be well below 1 KeV, with good energy resolution. The search for low-mass (∼5 GeV dark matter) is one of the primary motivations of the experiment explained in this thesis.

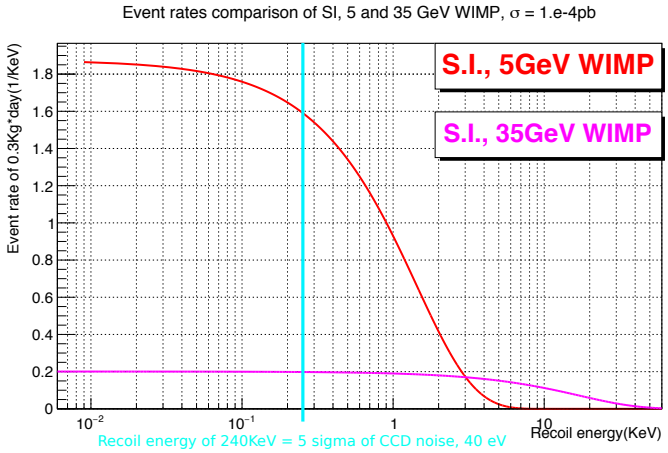

Figure 1.16: Event rate of a silicon detector for 5 and 35 GeV WIMP, assuming the cross-section is 1.0×10^{-4} pb and the exposure is 0.3 $Kg \cdot day$.

1.4.2 WIMP direct detection technologies

The technologies used to search for WIMPs via direct detection depend on the mass of the dark matter candidate. All experiments focus on improving signal to noise ratios, reducing and understanding background levels, and using widely accepted models to characterize possible signals. The focus of detecting low mass dark matter (1 MeV ... 20 GeV) is typically on reducing energy threshold, while the focus on high mass dark matter (20 GeV ... 1000 GeV) is on engineering a larger mass detector.

1). Low mass($1MeV \lesssim m_\chi \lesssim 20GeV$) WIMP detection
There are several projects with a main emphasis on low mass dark matter, including CRESST, PICO, SIMPLE, CDMS, and the experiment explained in this thesis called DAMIC. To detect a possible signal from incident low-mass WIMPs, one of the key features of the detector is its noise level. As is shown in figure 1.16, the lower the noise level, the more signal events can be recorded, and therefore the more sensitive the detector will be to lower cross-sections of interactions. CDMS Lite has achieved a 170 eV ionization energy threshold which is roughly equivalent to a 800 eV nuclear recoil threshold [CDMS Si 13], CRESST has reached 307 eV [Cresst 15], PICO has achieved 3.2 keV [Pico 15], and SIMPLE, 8 KeV [SIMPLE 11]. The DAMIC experiment explained in this thesis aims to get down to below 40 eV(5 σ noise) ionization energy, for a nuclear recoil threshold of 240 eV, which would be the lowest threshold of any of these detectors.

These detectors usually work at low temperatures to reach low noise and stable performance. One of the main backgrounds is from electron recoils which are electromagnetic interactions with the electrons of the atoms, without a nuclear recoil. These electron recoils can be distinguished from nuclear recoils by using multiple methods for measuring the signal. The nuclear recoil of dark matter with detector nuclei would produce ionization energy, phonons, and scintillation light. SuperCDMS uses phonons and ionization to reject electron recoils, while CRESST uses phonons and scintillation light [Cresst 15]. To get to WIMP mass scales of KeV, with recoil energies of meV, would require new technologies such as superconducting detectors [Hochberg et al, 15], and superfluid Helium detectors [Schutz & Zurek, 16].
The large-scale dark matter experiments focusing on discovering high mass WIMPs have also pushed down to low energy thresholds in order to probe low-mass dark matter candidates. For instance, LUX [LUX 15] was able to achieve a nuclear recoil energy threshold of 1.1 keV, and set limits at 4 GeV around $1.2 \times 10^{-42} cm^2$ with 90%CL . Xenon 100 reached 0.7 keV, allowing an exclusion of WIMPs with mass of 6 GeV above $1.2 \times 10^{-41} cm^2$ with 90%CL [Xenon low mass, 16].

2). High mass (20 $GeV \lesssim m_\chi \lesssim 1000\ GeV$) WIMP detection
Most experiments are focused on high mass WIMP detection, including DarkSide, DEAP, LUX (future is LZ), PandaX, and Xenon 100 (future is Xenon 1T). These experiments use higher energy thresholds above a few keV, and rely on large fiducial masses to reach very low cross-sections. Currently, these experiments are upgrading from the 100 kg scale to the tonne scale in mass. In the future, 100-tonne scale experiments will probe down to levels which reach the level of neutrino backgrounds. Liquid Xenon (LXe) and liquid Argon (LAr) have proven to be the best materials for high mass detection. LXe can be highly purified and is chemically inert and radio-pure. The detectors are typically TPCs (Time Projection Chambers), that are dual-phase in order to produce a prompt scintillation signal (S1) and a delayed one (S2), the ratio of which can be used to distinguish electron recoils from nuclear ones. LAr experiments employ a very similar design as LXe, with the advantage that the pulse shape discrimination is better in LAr, while the disadvantages are that the threshold for recoils is higher and there is a ^{39}Ar intrinsic radioactive background. R&D to reduce the cosmogenic-activated ^{39}Ar using underground Ar sources is promising. The three best limits from LUX, Xenon 100, and PandaX all use two-phase liquid Xenon TPCs.

1.4.3 Annual modulation and directional detection

If an excess over expected background is detected by a direct detection experiment, the excess can be measured as a function of time in order to see if it is consistent with the change in the earth's velocity with respect to the average speed of the WIMP halo. Since the earth changes its relative velocity with respect to the sun by 30 km/s throughout the course of the year, the event rate which is dependent on the velocity also changes. This so-called "annual modulation" has been reported with 9.3 Sigma by the DAMA/LIBRA

collaboration [DAMA 13]. However, if the signal is interpreted as evidence of WIMP dark matter, it is in strong tension with results from many other experiments, which have excluded this signal, including LUX, Xenon 100, PandaX, and CDMS. To date, the signal has not been confirmed by any other experiment, and there is no explanation for the modulating excess that has achieved consensus in the community [Snowmass CF1 13]. To eliminate other annual systematic effects, it is useful to have experiments in both the northern and southern hemisphere, such that the phase of the modulation would be shifted by 6 months. DM-Ice will attempt to reproduce the signal seen in DAMA by placing a similar detector in the southern hemisphere. The main challenge is the radio purity of the NaI crystal used as the detector. Utilizing 60.8 kg*yr of data, DM-Ice's latest results are still more than an order of magnitude away in sensitivity from the cross-sections of the DAMA signal [DMIce 16].

The motion of the earth through the galaxy creates a "WIMP wind" emanating from the direction of the constellation Cygnus. Since backgrounds other than those from neutrino-induced events are expected to be isotropic, detection of a signal with a preferred direction could provide a powerful additional discriminant against backgrounds. Directional detectors attempt to reconstruct the direction of the nuclear recoil track in order to correlate with the expected average direction from the WIMP wind [Mayet 16]. The DRIFT [Drift 11], NEWAGE [Newage 10], MIMAC [Mimac 16], and DMTPC [Dmtpc 13] experiments have achieved results in directional detection using gas TPCs. For instance, DRIFT has achieved limits of WIMP-proton S.D. (Spin Dependent) interactions of 1 pb for an 80 GeV WIMP mass [Drift 11].

1.4.4 Current constraints on DM

As shown in figure 1.2, there are three main ways to detect its weak interactions. The first is "indirect" detection of dark matter, in which matter particles produced from dark matter annihilation are detected, "collider" searches, where collisions of matter produce dark matter particles that can be inferred from the event kinematics, and "direct" detection, in which dark matter interacts with matter producing a signal.

1). Limits from indirect detection
There are three main categories of indirect detection experiments aiming to detect the byproducts of dark matter annihilation.

a). Neutrinos from dark matter annihilations in the core of the Sun.
As the sun travels on its spiral of the Milky Way, WIMPs from the DM halo could occasionally be acquired inside it after losing energy by scattering off nuclei in the sun. These WIMPs could then annihilate in the solar core. The decays of the annihilated products might generate neutrinos which could propagate through the sun and reach the earth and be detected by an underground neutrino detector like Super-Kamiokande. The energy of the neutrinos generated by this mechanism are expected to be much greater than those

from solar-fusion which are typically $\sim 10\ MeV$. The Super K collaboration has set limits for S.I. interactions of roughly $\sim 10^{-42} cm^2$ and S.D. of $\sim 10^{-40} cm^2$ for WIMPs of masses $4 - 200\ GeV$ [SuperK 15]. Using 329 live-days of data taking by the inner most 86-string detectors, the IceCube collaboration hasn't found any neutrino excess for the various final states of : $\chi\chi \to b\bar{b}$, $\chi\chi \to \tau^+\tau^-$, $\chi\chi \to \mu^+\mu^-$ and $\chi\chi \to \nu\bar{\nu}$. For dark matter masses between 200 GeV and 10 TeV, the limit of the cross-section of $\sigma_A v$ for the channels of $\chi\chi \to \tau^+\tau^-$ reaches $10^{-23} cm^3 s^{-1}$, where $\sigma_A v$ is the velocity-averaged WIMP self-annihilation cross section [IceCube 16].

b). Dark matter annihilation would occur mostly in the dense areas in the center of galaxies, producing an excess of anti-matter over expected background sources. Several experiments have identified excesses in e+, such as AMS-01(02), PAMELA, Fermi-LAT [AMS 02, FermiLAT 15, FermiLAT 15]. These excesses may be due to dark matter annihilations or from pulsars, and the current best data from AMS-02 cannot currently distinguish between these possibilities [AMS 14].
If the excess of e^+ comes from pulsars, the positron spectrum above 200 GeV is expected to decrease slowly and a dipole anisotropy should be observed due to the Earth's annual motion relative to the Sun. If, on the other hand, it comes from dark matter collisions, the positron spectrum above 200 GeV will decrease rapidly with energy due to the finite and specific mass of the dark matter particle(s), and no dipole anisotropy will be observed. Over its life time until ~ 2030, AMS will reach a dipole anisotropy sensitivity of $\delta \cong 0.01$ at the 95% C.L.

c). Dark matter annihilations to photons. Dark matter annihilations that occur in the center of our Milky Way galaxy and other nearby galaxies would also produce an excess of photons. Using data from Fermi PASS-8, the Fermi-LAT collaboration set limits on DM with mass less than 100 GeV coming from dwarf spheroidal satellite galaxies [FermiLAT 15]. An analysis of this data and photons originating from the center of the Milky Way has claimed evidence of the existence of dark matter $m_\chi \cong 20 - 50$ GeV with a significance of 4.2 Sigma (3.6 Sigma after trials factor) [Hooper 15].

2). DM detection at the LHC
Particle colliders, such as the LHC, could produce dark matter particles which escape the detector, but are discovered as an excess of events with "missing energy". Both ATLAS and CMS collaborations have been conducting a broad scan for DM, considering both supersymmetry and general models with effective field theories using 8 TeV and 13 TeV proton-proton collisions [ATLAS & CMS DM searches 15]. The current limits of ATLAS and CMS are both model and channel dependent. Not surprisingly, their limits are quite similar : for the mono-jet channel, the S.I. limits for both collaborations are $\sim 10^{-45} cm^2$(scalar) and $\sim 10^{-40} cm^2$(vector) ; the S.D. limits are both $\sim 10^{-41} cm^2$(Axial-vector), [ATLAS-8TeV DM 15, CMS-8TeV DM 14].
Because the LHC is such a high energy collider, if dark matter is produced, it will be boosted to very high momenta. The missing energy of dark matter particles with masses below $\sim 50\ GeV$ would be dominated by the momentum of the particle rather than the

mass, and therefore, the missing energy signal measured in the CMS and ATLAS detectors would be indistinguishable for dark matter below about 50 GeV. This gives CMS and ATLAS the advantage that they would have equal sensitivity to all dark matter masses below about 50 GeV, all the way down to almost 0 GeV.

3). Direct detection

WIMPs can be directly detected by their elastic scattering with nuclei. Axions can be detected through their interactions with photons in a magnetic field.

The typical shape of a limit in direct detection has the shape similar to a "V" : at low WIMP mass, the sensitivity drops because of the detector energy threshold, whereas at high masses, the sensitivity also decreases because, for a fixed mass density, the WIMP flux decreases $\propto 1/m_\chi$ where m_χ is the mass of a WIMP [PDG 15].

For WIMP detection, WIMP-nucleon couplings are classified as S.D. when the sign of the scattering amplitude depends on the relative orientation of particle spins, or S.I. when spin orientations do not affect the amplitude. For S.D., the WIMP effectively couples to the net nuclear spin. For S.I., the total nuclear cross section is enhanced by the square of the atomic mass due to the coherent summations over all the scattering centers in the nucleus. This increases event rates on heavy target nuclei relative to lighter nuclei significantly due to the "A^2" scaling [PDG 15].

The basic methodology for direct detection experiments is to search for rare events that might be the signature of WIMP interactions, namely the elastic scattering of a WIMP from a target nucleus. DM direct detection experiments must be located in deep underground laboratories to avoid cosmic ray backgrounds which produce neutrons that could be mistaken for WIMPs signals. The experiment must also shield the detectors from the decay products of radioactivity in the environment and in the materials of the detector itself.

In summary, according to the published papers, the lowest limit for $m_\chi \lesssim 10GeV$ is $\sim 10^{-41}cm^2$ set by CRESST-II [Cresst 15]; for $m_\chi \gtrsim 10GeV$, it is $\sim 10^{-46}cm^2$ at $\sim 33GeV$ set by LUX [LUX 15].

The sensitivity of the next generation of dark matter detectors will be close to the level of solar and atmospheric neutrino backgrounds. For dark matter below 10 GeV, the recoil energy spectrum from Coherent Neutrino Scattering(CNS) on a dark matter experiment due to solar neutrinos from the ^8B reaction is almost indistinguishable from the spectrum of 6 GeV WIMP-nucleon interactions with cross-section of $5 \times 10^{-45}cm^2$. Above 20 GeV, atmospheric neutrinos become the limiting background, with recoil spectra very similar to WIMPs with a mass of 100 GeV and a WIMP-nucleon cross section of $2 \times 10^{-49}cm^2$, as shown in figure 1.13.

2

DAMIC experiment and CCDs

DAMIC(DArk Matter In CCDs) is a direct-detection dark matter search motivated by models predicting low-mass WIMPs (1 GeV $<$ Mass$_{WIMP}$ $<$ 20 GeV). The nuclear recoil energy of such low-mass dark matter candidates is ideally suited for measurement by the low noise of the CCDs used in DAMIC.
DAMIC is an international collaboration hosted by Fermilab. The institutions of DAMIC(by Sep, 2015) are Centro Atomico Bariloche, Argentina; Fermi National Accelerator Laboratory, U.S.A.; SNOLAB, Canada; Universidad Federal Rio Janerio, Brazil; Universidad Nacional de Asuncion, Paraguay; Universidad Nacional Autonoma de Mexico; University of Chicago, U.S.A.; University of Michigan, U.S.A.; University of Zurich, Switzerland.

2.1 An introduction to DAMIC CCDs

2.1.1 CCD introduction

The CCD stands for Charge-Coupled Device and was invented in 1969 at AT&T Bell labs by Willard Boyle and George E. Smith who were awarded the *Nobel prize for physics* in 2009. Its original name was "Charge 'bubble' Devices", [Janesick, 2001].
The CCD was designed to transfer charge along the surface of a semiconductor from one storage unit to the next. The storage unit is a MOS(Metal-Oxide-Semiconductor) capacitor. Figure 2.1 shows the charge stored in an electrical potential well of a CCD with 3x3 pixels, moving from right to left. The states P1, P2, and P3 are relative voltage levels that are used to control the potential wells in the horizontal direction, similarly H1, H2, and H3 move the charge vertically.
Because charge moves from a high to low voltage, one can move the charge from one pixel to its neighbor by controlling the relative voltage between them. This procedure is shown in the right column of the figure 2.1. On state 1, the voltage of P_2 is lower than P_1 and P_3, so the charge indicated by red circles stays in the capacitor of P_2. On state 2, the voltage of P_1 and P_2 are same, so the charge stays on both capacitors of P_1 and P_2. On state 3, where the voltage of P_1 is low, while both P_2 and P_3 are high, the charge then moves to the P_1 capacitor. After such a cycle, the charge has been moved horizontally from the capacitor of P_2 to P_1. The movement will continue until the charge reaches the last horizontal capacitor. The charge then moves vertically step

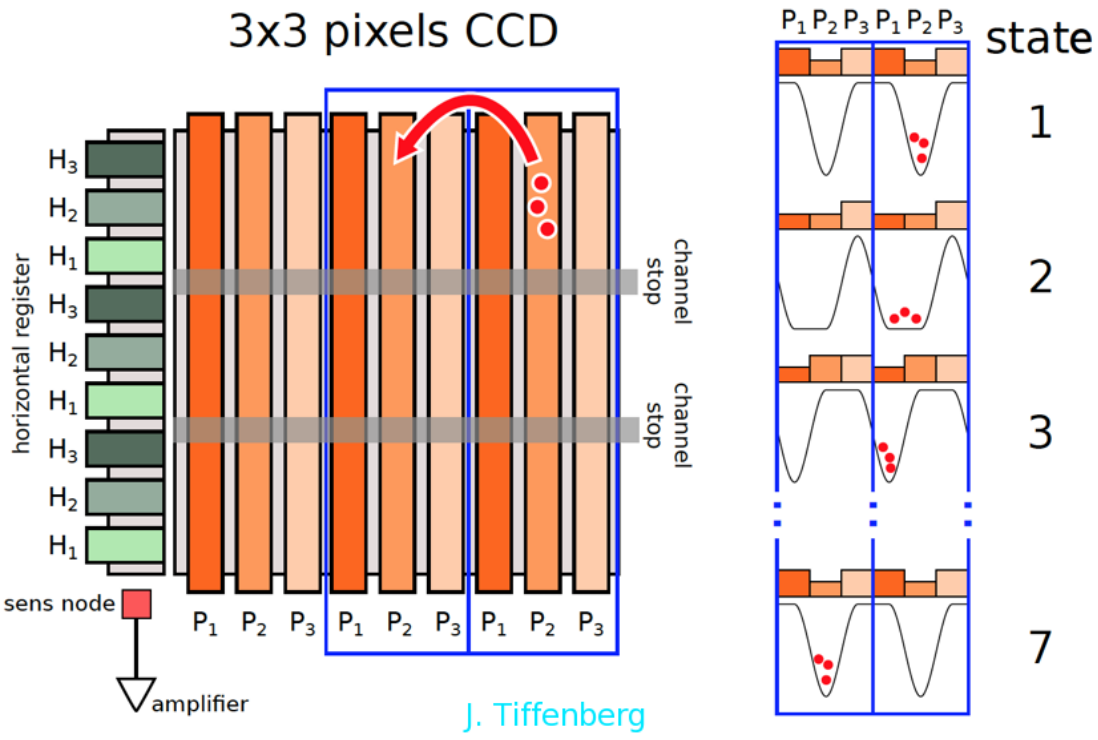

Figure 2.1: Introduction to CCDs.

by step until it reaches the edge of a CCD where the charge could be read out by an amplifier and the downstream data acquisition chain.
There are two types of MOS semi-conductor : p-type and n-type. P-type is boron-doped and contains a large concentration of holes; n-type is phosphorus-doped and contains a large concentration of mobile electrons. Both types of CCD are best operated at low temperature since the ionizing energy of phosphorus in silicon from the conduction edge and boron from the valence edge are both ~ 0.05eV, is close to the thermal excitation at room temperature 20°C(293K) of $kT \approxeq 0.025$ eV, where k is the Boltzmann constant and T is the absolute temperature.

2.1.2 DAMIC CCDs

In order to increase the near-IR photon detection efficiency of CCDs, the Lawrence Berkeley National Laboratory MicroSystems Lab has developed and fabricated CCDs on high-resistivity, N-type silicon. Figure 2.2[Holland et al., 2003] shows a diagram of a cross-section of this kind of CCD. The thickness of CCDs is typically 200-675 μm[1]; the

[1]The thickness of a general CCD is only 10s of μm, while the newest DAMIC CCDs are fabricated at 675 μm.

resistivity is $\sim$ 100k-120kΩ·cm, corresponding to a donor density of $3.6-4.3\times10^{11}cm^{-3}$. To reach fully depleted operation, the bias voltage is $\sim +20V$. By the virtue of their high quantum efficiencies(60%+ for wavelength of 400 - 1000nm), these CCDs were selected for the Dark Energy Camera(DECam)[DES, 2005]. The DAMIC experiment originally used 200μm-thick DECam CCDs to search for low-mass WIMPs between 2008-2011 [Barreto et al., 2012], but have since used specially fabricated, thicker CCDs.

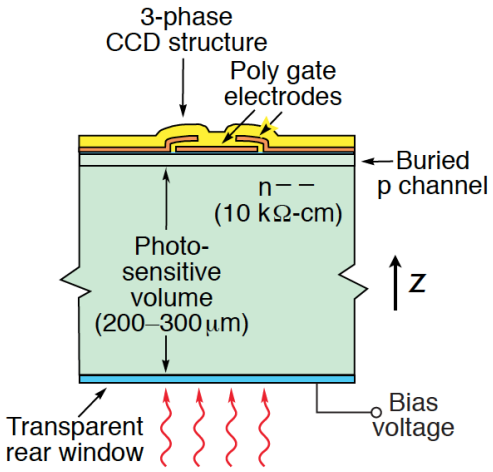

Figure 2.2: Cross-sectional diagram of DECam CCDs[Holland et al., 2003]. The concept of DAMIC CCD is the same as the DECam CCDs.

DAMIC-100 is an experiment comprised of 18 individual CCDs each with an active detector mass of 5.6 grams, for a total active detector mass of about 100 grams. The CCDs are 675 μm thick, and have a pixel size of $15\mu m \times 15\mu m$.

The response of the CCD to a WIMP interaction would be independent of the CCD thickness, although an increased mass would increase the probability of an interaction. As figure 2.3 shows [Chavarria et al., 2014], an incident Dark Matter particle is assumed to be scattered elastically off a silicon nuclei. The scattering will impart a recoil energy to the silicon nuclei which was hit. Because the WIMP is assumed to be neutral charge , it won't couple electromagnetically to the electrons surrounding the nucleus[2]. Part of the recoil energy will be converted to phonons(heat) or electron-hole pairs(ionization). DAMIC CCDs are not capable of detecting phonons but can detect ionization down to tens of eV by virtue of their very low and stable noise, which will be discussed in later sections.

[2]There are warm dark models assuming $\mathcal{O}$(KeV) dark matter particles elastically scattering with electrons, for instance in the reference [Y. Hochbert et al., 2015]. But the produced energy would be $\mathcal{O}$(meV) which is far lower than a DAMIC CCD could reach. The authors of the paper propose to use superconductors for warm dark matter direct detection.

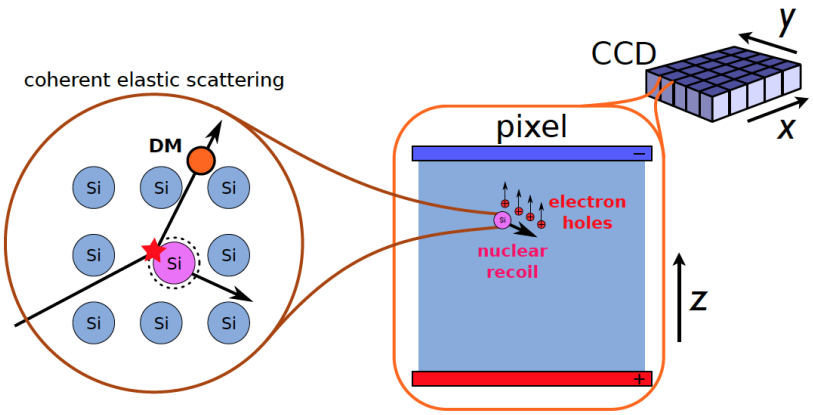

Figure 2.3: A DAMIC CCD responds to a Dark Matter(WIMP) hit, [Chavarria et al., 2014].

Figure 2.4 shows the effect of lateral charge diffusion within a CCD. In the left sub-plot, a small red star in the middle the CCD bulk marks the location where a nuclear recoil has occurred, liberating electron-holes. The middle sub-plot shows the electron holes being drifted to the surface of the CCD due to the existence of bias voltage. During the drift, the charge is diffused laterally until reaching the surface of the CCD; the right sub-plot shows the diffusion expressed as an RMS size σ, as shown from above.

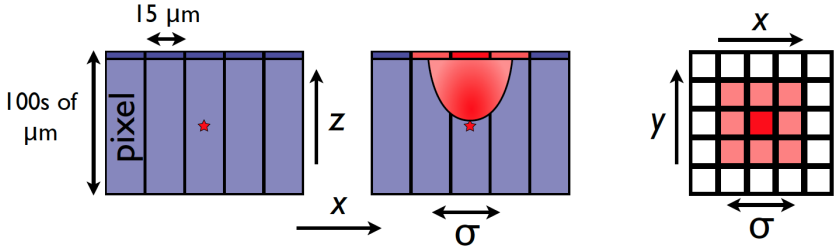

Figure 2.4: A depiction of lateral diffusion within a DAMIC CCD, [Chavarria et al., 2014].

DAMIC CCDs discriminate between different kinds of incident particles by reconstructing the tracks. Figure 2.5c shows typical recorded shapes correspond to different incident particles. In this plot, high energy electron events are "worm-like" because because the masses of the electrons are small compared to the nuclei, and so scattering changes their direction. In general, the electrons mainly come from radiation decays and/or Compton scattering therefore the energy of this kind of electron event is $\leq\sim$MeV.
Diffusion-limited tracks are point-like with a typical track length of much less than the pixel size of 15 μm. Such events are produced either by nuclear recoils from WIMPs,

neutrons, or neutrinos, or from low-energy X-rays or electrons.
Muon tracks are very straight due to the large muon mass, and the energy deposit dE/dx is fairly constant since their energies of around 3 GeV changes very little in 100s of μm of silicon.
Figure 2.5a shows a few muon tracks that have been measured at the earth's surface. There is an obvious width difference between the two ends of the tracks. The thicker end corresponds to the region of the track in the back of the CCD with maximum diffusion due to longer diffusion length of the electron holes. The thinner end corresponds to the front of the CCD. On this plot, the smaller circular hits are diffusion-limited hits.
Radiogenic αs deposit all of their energy in a CCD, producing a high density "cloud" of electron-hole pairs which has been called a "plasma" [J. Estrada et al., 2011]. A typical α event in the back of a CCD is shown in figure 2.5b.

2.1.3 Noise performance of DAMIC CCDs

The detection of nuclear recoil signals from possible, incident WIMPs strongly depends on the noise level of the detector. Because a smaller WIMP mass has less kinematic energy, its event rate spectrum will be shifted towards lower energies. This is shown intuitively in figure 1.16. In this figure, the two curves represent the event rates of 5 and 35 GeV WIMP respectively. The exposure is 0.3Kg*day and the material of the detector is silicon. It is clear that DAMIC has a potential to detect a much wider range of event rates than other silicon detectors in which the selected events are usually $\sim$ KeV, [CDMS Si 13].

The very low noise of sigma = 1.8 e- of the DAMIC CCDs has been demonstrated in situ in the experimental setup at SNOLAB, as in Figure 2.6a. Figure 2.6b shows the noise of the three other CCDs measured in Snolab with the exposure time of 1 month. This figure demonstrates the noise of DAMIC CCDs is quite stable on the time scale of a month. In silicon, a single electron-ion pair can be produced with 3.6 eV energy, therefore each electron or hole measured corresponds to 3.6 eV.

The noise sources of a CCD can be divided into on-chip and off-chip noise, as mentioned in [Janesick, 2001]. On-chip noise sources are caused by the CCD itself; off-chip noise sources are introduced by affiliated readout electronics.
Dark current is one of the on-chip noise sources. It is intrinsic to semiconductors and naturally occurs through the thermal generation of minority carriers. The dark current of a DECam CCD is shown in figure 2.7. For a DAMIC CCD operating at 140K, we determine its dark current to be 0.1e/pixel/day [3].
A very detailed technical summary on noise sources and noise reduction for CCDs has

[3]Strictly speaking, the dark current of a DAMIC CCD should not be exactly the same as a DECam CCD since the thickness of a DAMIC CCD is $500-700\mu m$ while it is is $250\mu m$ for a DECam CCD. However, according to [Janesick, 2001], the dominant contribution to dark current is from the surface of the CCD, so different thickness-CCDs have approximately the same dark current.

2.5a. Muons tracks .

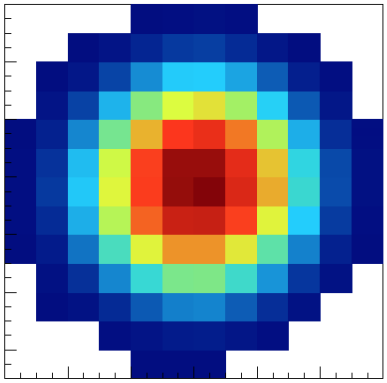

2.5b. A typical α event originating from the back of a CCD.

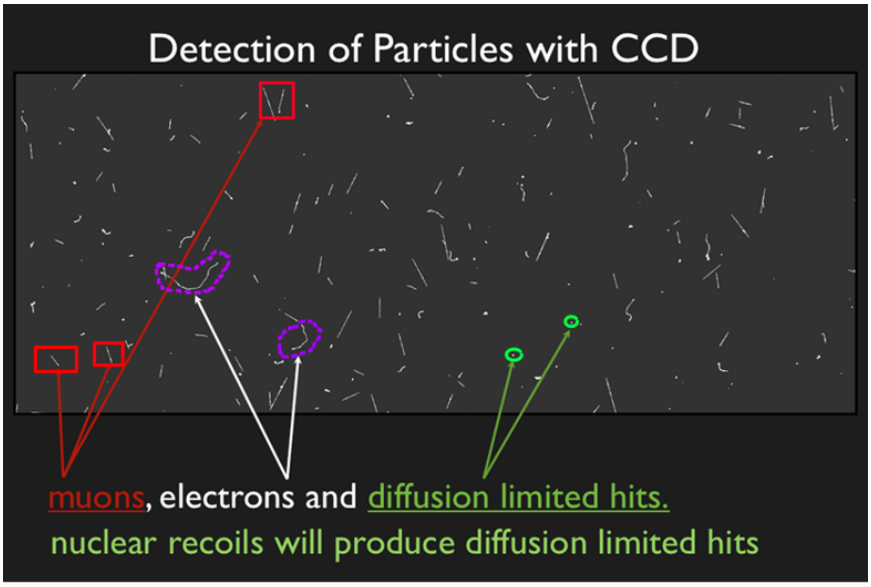

2.5c. Track shapes arising from various particle interactions

Figure 2.5: Events recorded in DAMIC CCDs [Barreto et al., 2012]

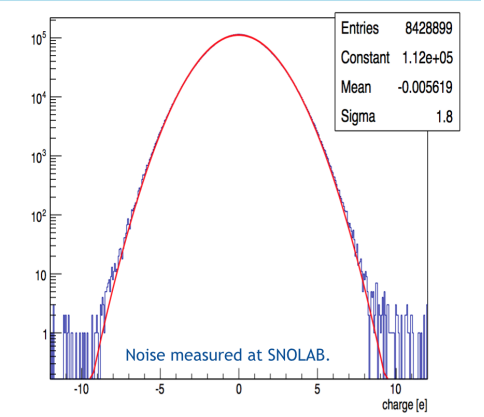

2.6a. $\sigma_{noise} = 1.8e^{-}$.

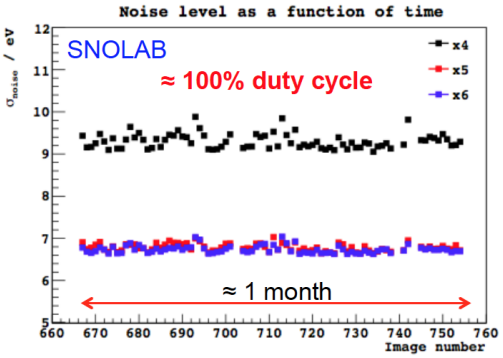

2.6b. measured noise of one month

Figure 2.6: Noise performance of DAMIC CCDs

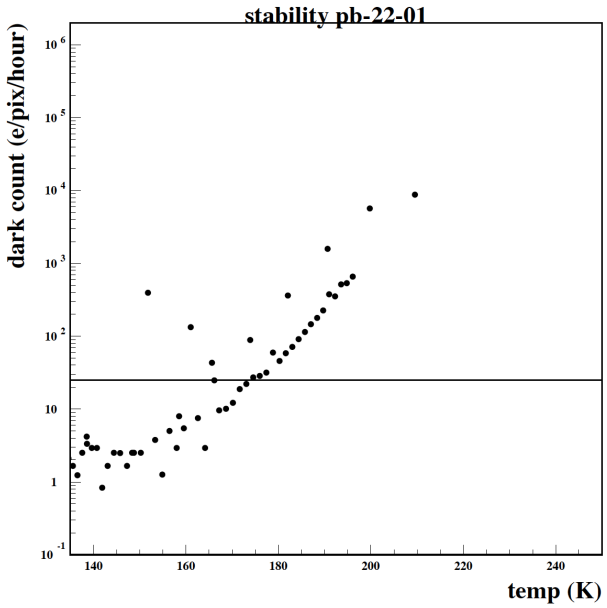

Figure 2.7: Dark current of DECam CCD. [T. Abbott et al., 2014]

been introduced in chapter 7 of [Janesick, 2001].

2.1.4 Energy resolution of DAMIC CCDs

The energy resolution for a WIMP detector is very important. When the energy resolution of a detector is close to the recoil energy threshold to be set, a significant fraction

of the expected spectrum below the effective threshold is smeared above threshold, increasing the sensitivity artificially.
DAMIC CCDs only measure the ionization produced by signals (phonons cannot be detected in CCDs).
Figure 2.8 shows results from energy calibrations of DAMIC CCDs. Figure 2.8a demonstrates the linearity of charge collection, rangeing from 0.3 up to 60 KeV. Figure 2.8b is the spectrum measured with a Fe^{55} source. Figure 2.8c shows further the measured energy resolution of a DAMIC CCD, $\sim 21\ eV$ at $\sim 500\ eV$ deposited (electron equivalent)energy.

Assuming the energy resolution of a CCD only has contribution from the Gaussian fluctuation of produced electron-hole pairs (ignoring the noise of a CCD at the moment), we would expect the same energy resolution for lower energy, where energy resolution $\equiv FWHM/E_0$, where $FWHM$ is Full Width at Half Maximum, E_0 is the energy corresponding to the FWHM value [G. F. Knoll, 2000]. Ideally, we therefore estimate the energy resolution at 40 eV to be : $\sim 1.6\ eV$.

$$\begin{aligned}
\frac{FWHM_{521\ eV}}{E_{521\ eV}} &= \frac{FWHM_{40\ eV}}{E_{40\ eV}} \\
\Rightarrow \frac{\sigma_{521\ eV}}{E_{521\ eV}} &= \frac{\sigma_{40\ eV}}{E_{40\ eV}} \qquad (\text{FWHM} = 2.36\sigma) \\
\Rightarrow \sigma_{40\ eV} &= \frac{\sigma_{521\ eV}}{E_{521\ eV}} E_{40\ eV} \\
&= \frac{21\ eV}{521\ eV} 40\ eV \\
&\approxeq 1.6eV \qquad (2.1)
\end{aligned}$$

where $FWHM_{521\ eV}$, $\sigma_{521\ eV}$, $E_{521\ eV}$ represent the full width at half maximum magnitude, σ and energy of 521 eV which is measured from figure 2.8c.
However, as will be mentioned in section 2.1.3, the noise of a CCD is $2e^-$ which is equivalent to 7.2 eV. So, for the measured energy of 40 eV, the energy resolution σ would be not only 1.6 eV but slightly bigger than 7.2 eV due to noise of CCDs, as figure 2.6a shows. As shown above in figure 1.16, we have set a threshold of 5σ noise = 40 eV of ionization energy. Therefore the energy resolution of CCDs will not significantly affect our sensitivity to low energy recoils.

2.1.5 The spatial resolution of DAMIC CCD

As mentioned, the pixel size of a DAMIC CCD is $15 \times 15\mu m^2$. By measuring the relative charge distribution of a cluster of charge among multiple pixels, the resolution is determined to 7 μm. One important application of this resolution is to measure radioactive contamination of the materials of the CCD by measuring the decay sequence of radioactive isotopes. By searching for energy deposits originating in the same pixels,

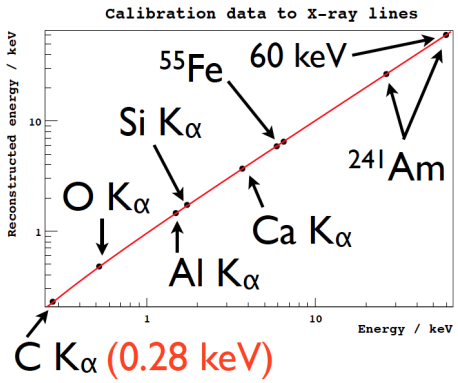

2.8a. Charge linearity.

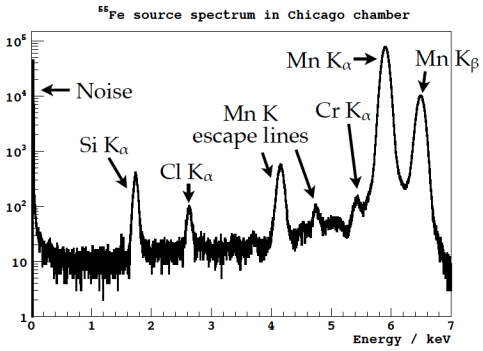

2.8b. Energy spectrum measured with Fe^{55}

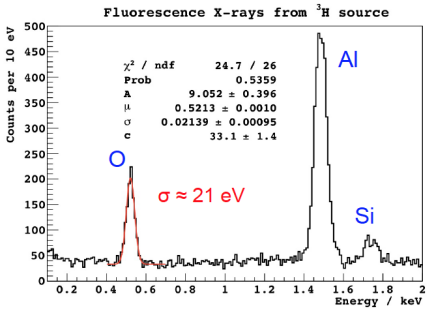

2.8c. Energy spectrum measured with H^3

Figure 2.8: Charge linearity and energy resolution of DAMIC CCDs.

Analysis method	Isotope(s)	Tracer for	Bulk rate $kg^{-1}\,d^{-1}$	Surface rate $cm^{-2}\,d^{-1}$
α spectroscopy	^{210}Po	^{210}Pb	<37	0.011±0.004, 0.078±0.010
	^{234}U + ^{230}Th + ^{226}Ra	^{238}U	<5 (4 ppt)	–
	^{224}Ra–^{220}Ra–^{216}Po	^{232}Th	<15 (43 ppt)	–
β spatial coincidence	^{32}Si–^{32}P	^{32}Si	80^{+110}_{-65}	–
	^{210}Pb–^{210}Bi	^{210}Pb	<33	–

Figure 2.9: Radioactive contamination of DAMIC CCDs. All values are 95% CL upper limits or intervals, except for the ^{210}Po surface rate. [A. Aguilar-Arevalo et al., 2015]

but separated by hours or days, the energies and times of the deposits can be used to determine the type of radioactive decay sequence, and therefore, a measurement or limit can be placed on their abundance in the detector. Table 2.9 shows the constraints placed on various contaminants within the DAMIC detectors[A. Aguilar-Arevalo et al., 2015].

2.2 DAMIC setup in Snolab

Figure 2.10 a) shows a CCD with thickness of 500 μm and 8 Mpix(= 2k × 4k). The CCD is held by a high-purity silicon support. The Kapton signal cable has been glued to the silicon support which conveys CCD clocks and read signals out to the electronics downstream. The copper bar shown in both figure 2.10 a) and b) is the handle of a packaged CCD by which the CCD could be pushed in and pulled out of the copper box. The whole box has been inserted into a copper vacuum vessel where the temperature is roughly 140K and the pressure is $\sim 10^{-6}$ mbar. Inside of the vessel, between the CCDs and the electronics boards, VIB(Vacuum Interface Board), there exists an 18 cm-thick lead block hanging on the upper part of the vessel to shield the detector from the readout electronics boards, as shown in figure 2.10 c). This figure also shows Kapton flex cables connected the CCDs and the VIB has been adhered to the surface of a lead block. The whole vacuum vessel has been surrounded by lead bricks which have 21+ cm thickness in 4π cubic angles , as shown in figure 2.10 d) and figure 2.11. Among the bricks, the innermost inch of lead comes from an ancient Spanish galleon with negligible ^{210}Pb and can suppress the bremsstrahlung γs produced by isotopic decay. It is labeled as "Ancient Lead" in figure 2.11. Outside of the lead bricks is a 42 cm-thick polyethylene shielding which can moderate and absorb neutrons.

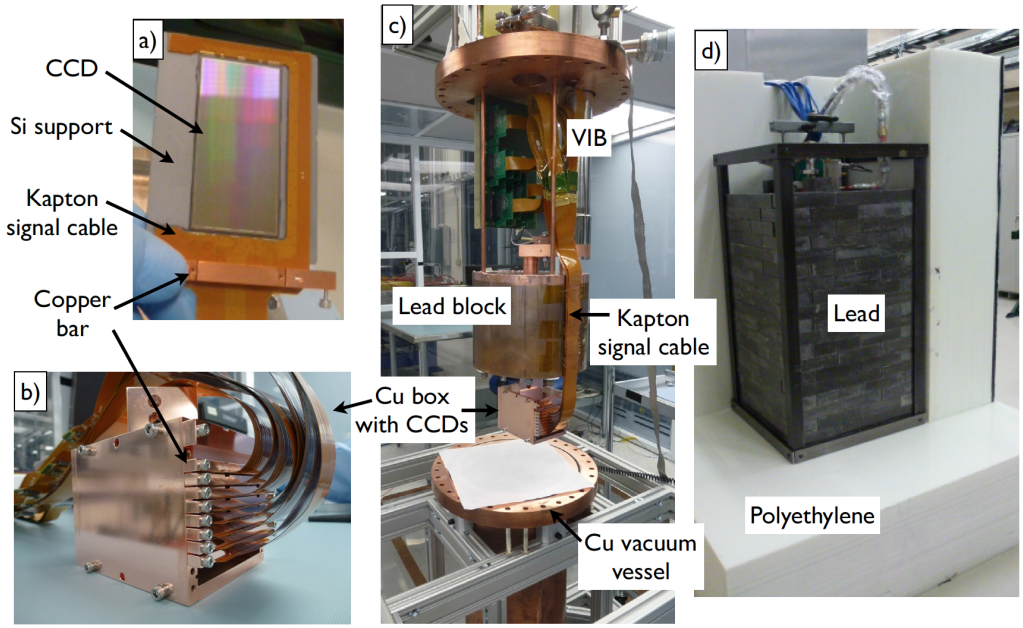

Figure 2.10: DAMIC setup in Snolab. [A. Aguilar-Arevalo et al., 2015]

Figure 2.11: DAMIC lead bricks in Snolab. The vacuum vessel(see figure 2.10 c).) is placed inside.

2.3 Backgrounds study

Lots of effort has been taken to decrease the level of backgrounds. First, we have improved the CCD support by replacing the AlN(Aluminium Nitride) with Silicon, as

shown in figure 2.12. This effort removed 330 ppb[4] of ^{238}U.
Secondly, we replaced the innermost-layer lead bricks with ancient lead that only has $< 0.02Bq/kg$ of ^{210}Pb to block $< 50Bq/kg$ of ^{210}Pb from outer layer lead bricks, as shown in figure 2.11.

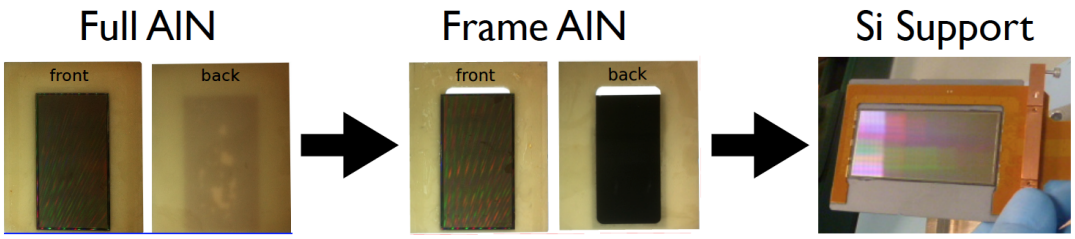

Figure 2.12: Improvement of CCD support in Snolab.

Thirdly, we tried different combinations of shielding to get the lowest possible background, as figure 2.13 shown [Tiffenberg talk @UCLA2016].

After all of these efforts have been applied, the background of the DAMIC experiment has now reached 5 dru[5], as figure 2.14 shows [Tiffenberg talk @UCLA2016].

[4]ppb is parts per billion. 1 microgram / kilogram(μg / kg) = 1ppb.
[5]dru is the abbreviation of *differential rate unit*, 1 dru = 1 events $KeV^{-1}Kg^{-1}day^{-1}$.

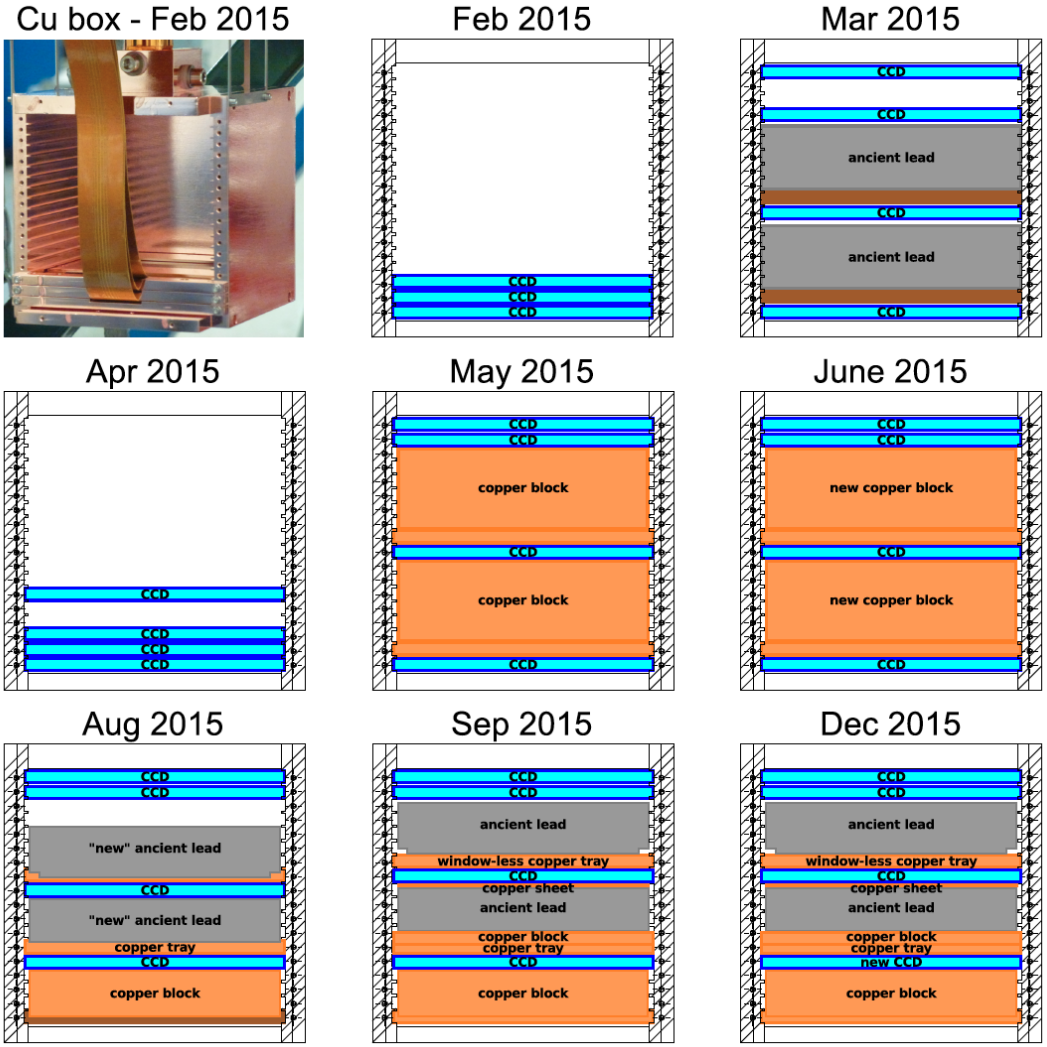

Figure 2.13: Different combinations of shielding for the CCDs.

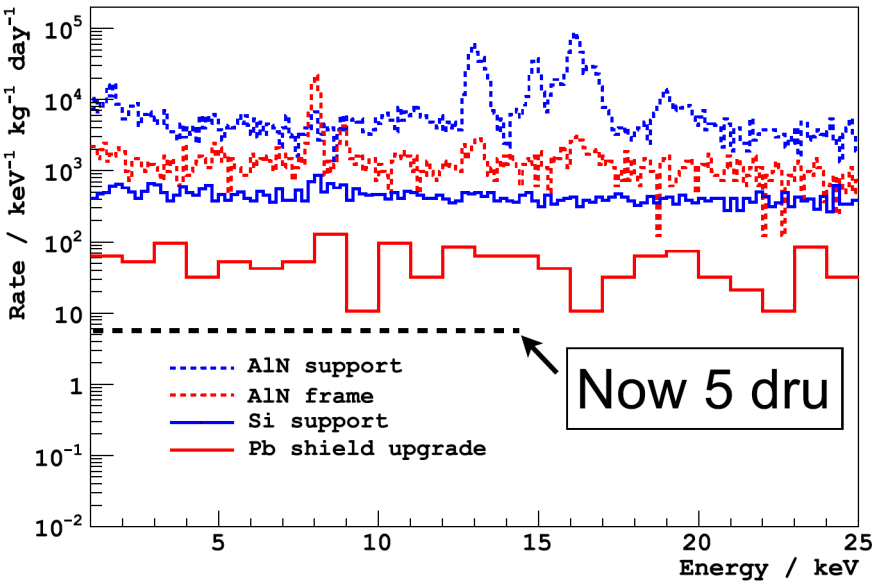

Figure 2.14: Comparison of various phases of the DAMIC experimental setup at Snolab. Colored dashed lines are from simulation, while colored solid lines are measured. The black dashed line is from recent measurements.

3

Charge Transfer Inefficiency

3.1 An introduction to CTE and CTI

CTI is the abbreviation for Charge Transfer Inefficiency. It is complementary to CTE which stands for Charge Transfer Efficiency, as the following equation shows [Janesick, 2001].

$$CTI = 1 - CTE \tag{3.1}$$

The existence of CTI is due to the charge lost during the movement of charge between pixels. On a CCD, charge is moved horizontally (X-axis) or vertically (Y-axis) using phased voltage levels as described in the previous chapter. Charge is typically lost between neighboring pixels in the X-direction due to the physical barrier in this direction, rather than in the Y-direction which has no physical barriers.

The CTE and CTI can be measured by a standard method called X-ray transfer. As figure 3.1 shows [Janesick, 2001], the technique of X-ray transfer is stacking a lot of images of ^{55}Fe to get a plot which contains a track-like pattern(inside of the blue box of figure 3.1). In this plot, the X-axis is the number of pixels, the Y-axis is the amplitude of signals representing the deposited charge in the pixels. Usually, under the exposure of a ^{55}Fe source, one image of a CCD does not contain many ^{55}Fe events, roughly 1000s. These 1000s events in 2000 pixels (like the CCD we used for this test) correspond to a few events per pixel which is not enough to observe explicitly the CTI effect since the measured charge would decrease proportionally with the number of pixels it has traversed. To characterize the CTI quantitively, we therefore need to stack many images to get an explicit enough track-like pattern as shown in figure 3.1.

After obtaining a plot like figure 3.1, one can calculate the CTE with the following formula.

$$CTE = 1 - \frac{S_D(e^-)}{X(e^-) \times N_p} \tag{3.2}$$

where $S_D(e^-)$ is the average deferred charge after N_p pixel transfers(e^-) which corresponds to the "CHARGE LOSS" in figure 3.2. $X(e^-)$ is the x-ray signal level corresponding to the "$Fe^{55} = 1620e^-$, IDEAL SINGLE-PIXEL-EVENT LINE" in the same figure.

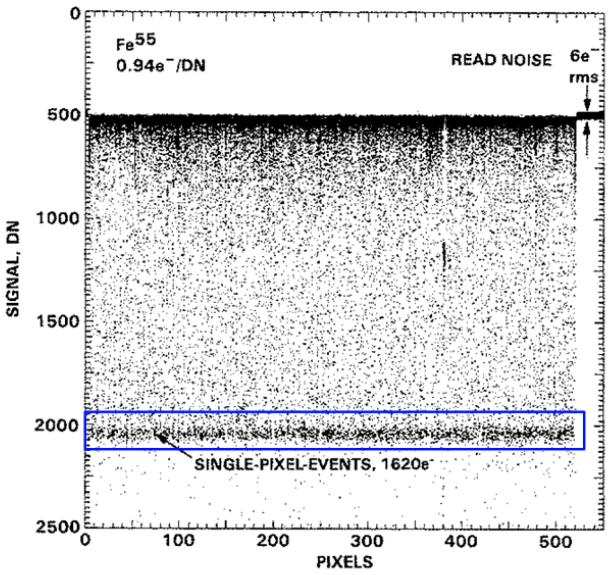

Figure 3.1: The concept of X-ray transfer

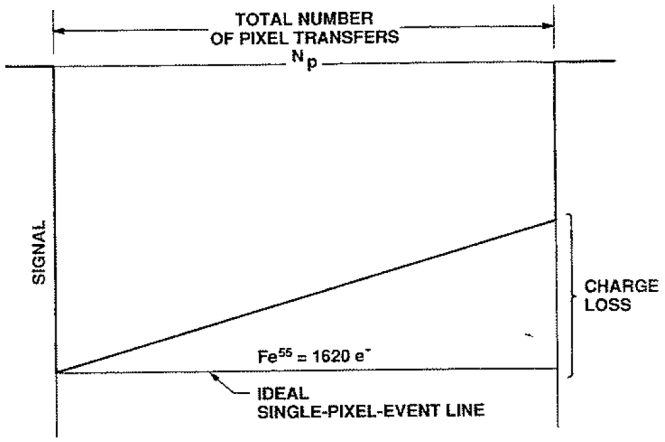

Figure 3.2: The schematic drawing for CTE calculation

3.2 Data taking for the CTI measurement

The methods we utilized for the CTI measurement and data analysis are slightly different from those that the book[Janesick, 2001] introduced. We illuminated the CCD from the front side by a ^{55}Fe source with an exposure time of $\sim$ 800 seconds, then we selected the ^{55}Fe events among all kinds of hits in the image. Figure 3.3 describes the

idea of our analysis : only the events comprising the ^{55}Fe peak are chosen for the CTI analysis[1].

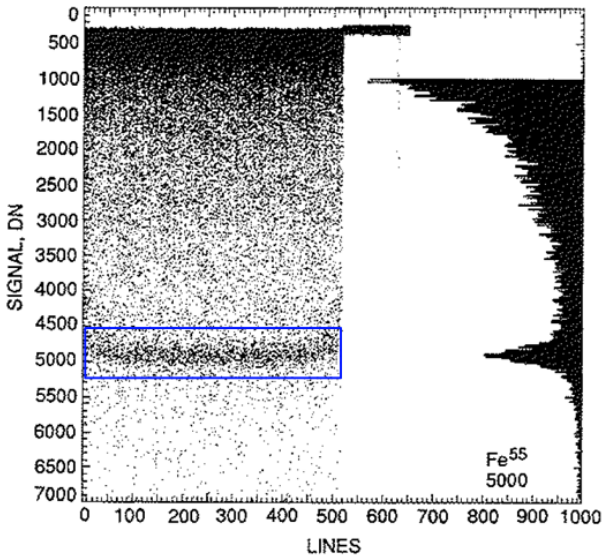

Figure 3.3: A track and its corresponding ^{55}Fe peak

Figure 3.4 shows a typical image used for our CTI analysis. The left side of the CCD contains data, while the right side of the CCD is empty. This feature is due to a fairly standard feature that CCDs often have two readout amplifiers, so that half of each image is read out simultaneously on the left and right side. For the case of DAMIC, instead of using the additional amplifier to speed up readout in this way, we read out all of the data on one amplifier, and then use readout of the other amplifier in order to determine correlated noise. In figure 3.4, the right side is an image only of readout noise. For the CTI analysis, only the left side of the image provides meaningful data.

In figure 3.4, a pink rectangle marks the region of overscan. An overscan is a bulk offset of a CCD, the mean charge level of all pixels in the image which varies from image to image unpredictably with the CCD temperature and time. It is purely an offset, and does not have an associated Poisson noise. All raw CCD images, whether zero-duration or otherwise, always have an overscan. The digital number(DN) of the overscan should be subtracted during a CCD analysis. The green rectangle contains many kinds of hits(muon, electron and ^{55}Fe etc). The hit inside of the red circle is an energy cluster from a ^{55}Fe X-ray, with a column number of 3870 to indicate the number of the column

[1]This figure is just to show a ^{55}Fe peak and its corresponding track(the track correspond approximately to the events in the blue box of figure 3.3.). The shape of the track is not good enough for a CTI analysis

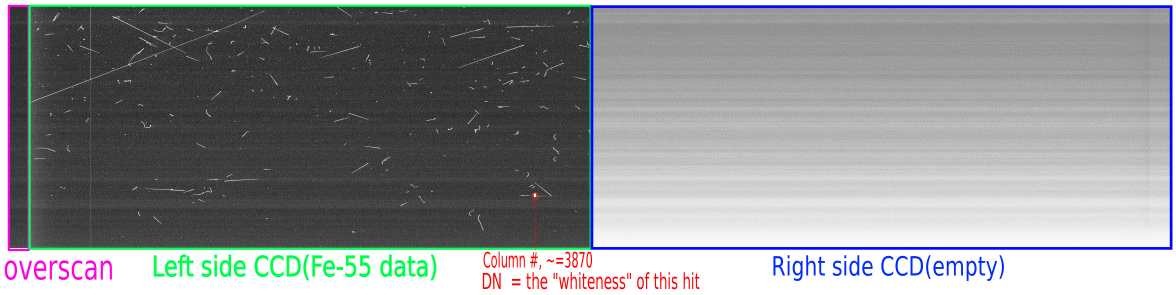

Figure 3.4: A CCD image for CTI analysis

of the hit and a DN indicating its charge. We then fill this event into a histogram with a bin number of 3870 and a bin content as the DN value.
As mentioned above, the CTI in the vertical direction is negligible, so we determine the CTI as a function of the column in the x-direction, by storing the charge deposition as a function of its column number.

3.3 CTI data analysis

The procedure for our CTI analysis is :
Step 1: take a series of images of a CCD irradiated by a ^{55}Fe source on the front side of the CCD. Hits on the front side of the CCD are more likely to be contained within a single pixel since the electron holes do not laterally diffuse along their pathway to the potential well. Exposures are kept short in order to avoid cases where multiple X-rays hit single pixels.

Step 2 : Subtract the overscan image from the data image. Figure 3.5a represents a histogram of the charge distribution measured in a typical raw image. Figure 3.5b is the overscan, and Figure 3.5c is the corrected image after overscan subtraction.

Step 3: Select energy clusters consistent with minimally diffused hits from X-rays impinging on the front of the CCD. In order to isolate X-rays consistent with the 5.9 keV ^{55}Fe decay, we fit the data with a Gaussian distribution, as shown in figure 3.6. A detailed description of the statistical method can be found in the Appendix A.1 and A.2.

Step 4 : Tabulate column and charge, and analyze the results to determine CTI. Whereas individual exposures contain 1k events, the analysis requires greater statistics. Figure 3.7 shows a plot of 24k accumulated events.

In total, 24k events were selected for analysis as shown in figure 3.7. A fit to the slope of the DN value verses column number allows the determination of the CTI to be

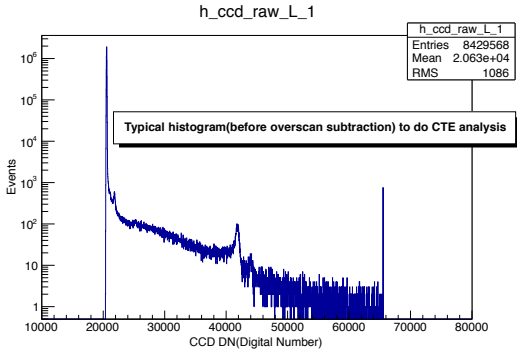

3.5a. histogram represents raw CCD data

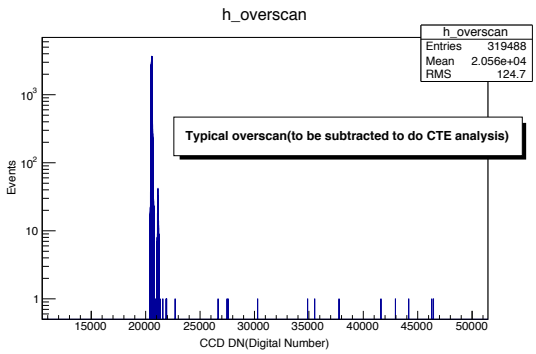

3.5b. histogram of overscan

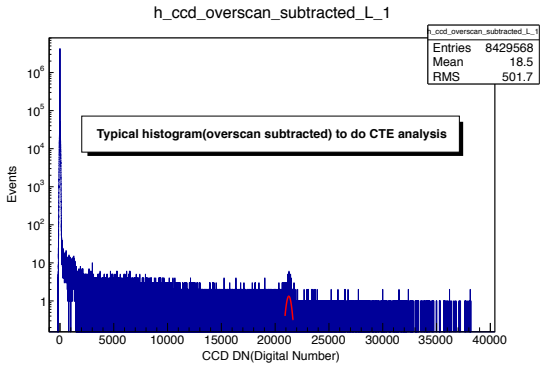

3.5c. The histogram of fig 3.5a has been subtracted its overscan of figure 3.5b.

Figure 3.5: The comparison of before and after overscan subtraction

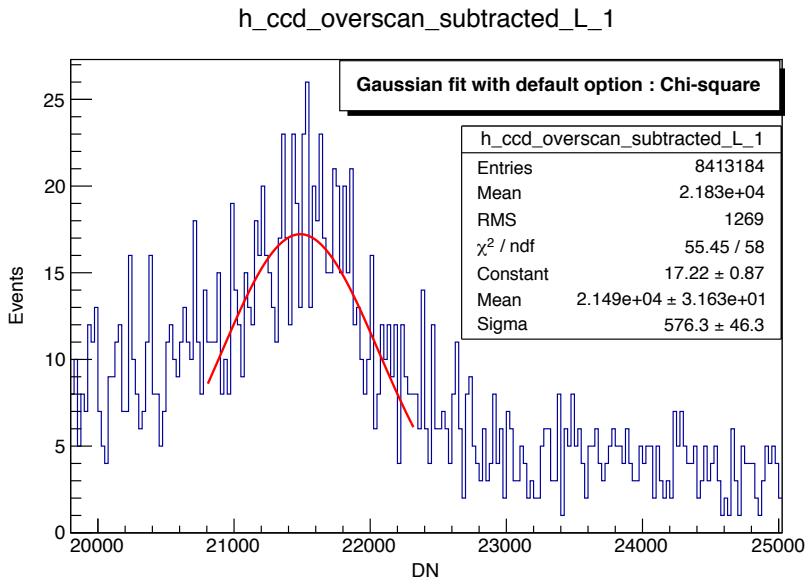

Figure 3.6: Distribution of DN values correlated to 5.9 keV X-ray energy from ^{55}Fe irradiation. Also shown is the fit to determine usable values for measuring CTI.

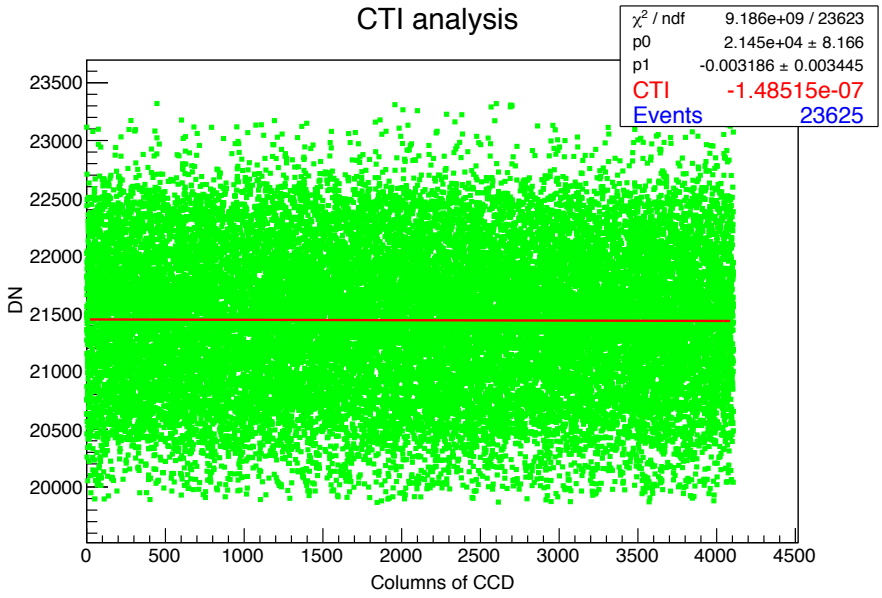

Figure 3.7: A CTI result with ∼24k events

1.5 $E-7 \pm 1.6$ $E-7$. We went on to evaluate the CTI as a function of the number of events recorded in the exposure figure 3.8 . The inefficiency is poorly measured when statistics are low, but as the number of events increases, the inefficiency levels off at an

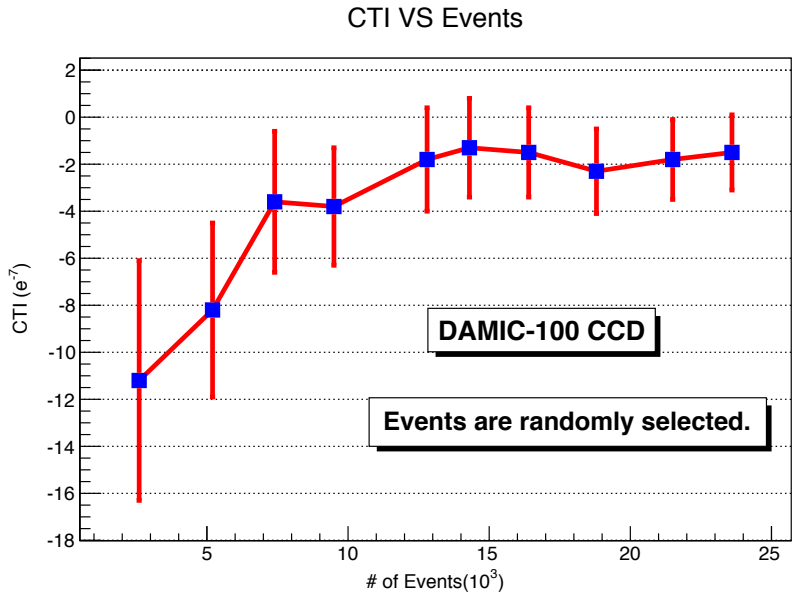

Figure 3.8: CTI values and errors change with the number of events

average of $\sim 2.0\ E-7$, averaging over the last 6 values. This value is comparable to the 10^{-6} reported here [Janesick, 2001], but perhaps slightly better due to more modern fabrication techniques.
The measured value of the CTI, $\sim 2.0\ E-7$ demonstrates that DAMIC CCDs have a negligible loss of charge when readout, such that we do not consider this effect in our data analysis.

Figure 3.9 shows the details of the number of events and the value of CTI which correspond to the points in figure 3.8. The CTI value is negative because the smaller the pixel number on the X-axis, the less number of pixels the charge has floated through, the less charge will be lost, the bigger signal measured, therefore the DN number is bigger. As a result, the CTI value which is represented by the slope of a linear fit is negative.

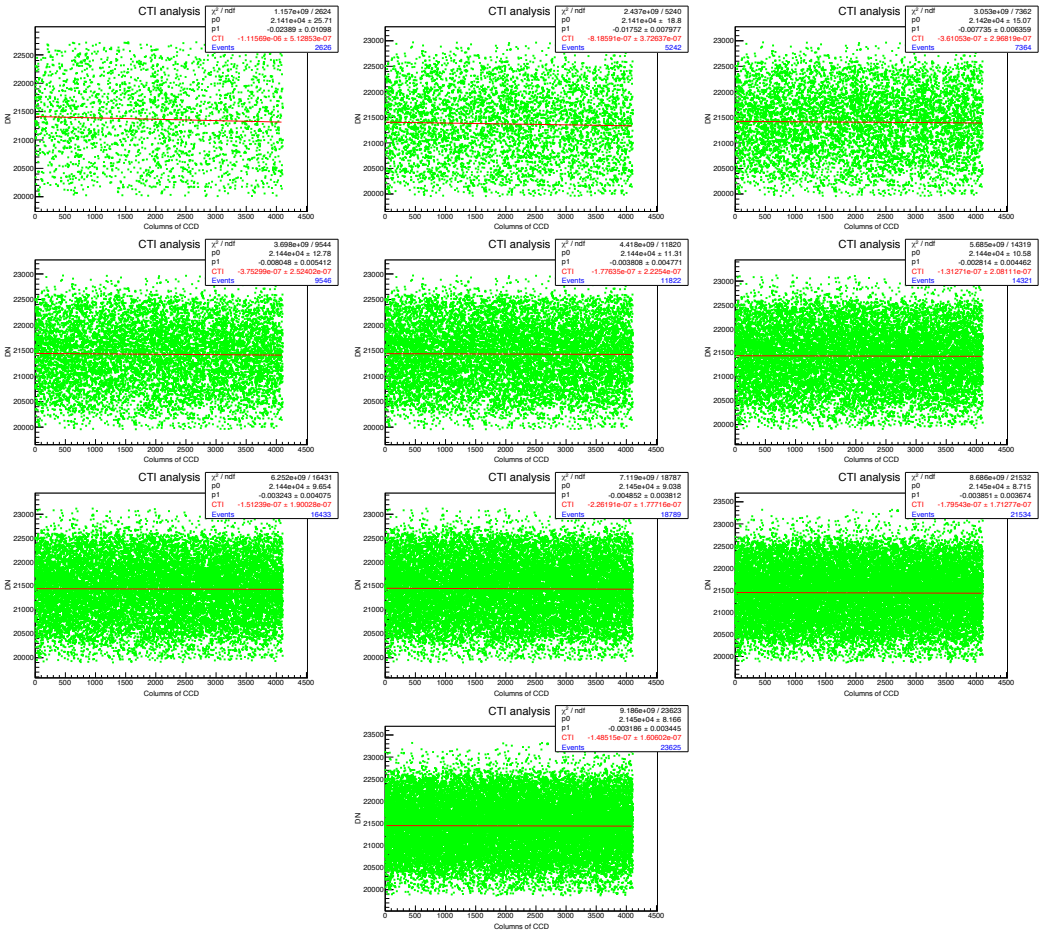

Figure 3.9: Measurement of CTI for each number of events in figure 3.8

4

Quenching Factor experiment

As mentioned in chapter 1, WIMPs are perhaps the most highly motivated dark matter candidate. Since WIMPs are neutral particles, they are not capable of ionizing the detector directly. However, by interacting with detector nuclei very weakly(here, the "weakly" doesn't have the meaning of weak interaction), they would impart recoil energy to the nuclei, leading to an ionization signal that can be detected. In this way, WIMPs would produce a similar signal as neutrons, for which we detect via nuclear recoils. Although nuclear recoils can produce scintillation light and phonons as well, this thesis focuses on ionization energy produced from nuclear recoil.

4.1 Quenching Factor measurement in DM experiments

For ionization detectors, the measurable energy is only a fraction of the total recoil energy produced by a WIMP collision with a detector nuclei. The ratio of the ionized energy to the total recoil energy is known as the quenching factor (QF)[1]. Using the quenching factor, we can convert from measured ionization energy in the detector to recoil energy of the nucleus which allows us to compare to the kinematics of the incoming dark matter particle.

In order to determine the QF of a WIMP, physicists typically calibrate using the neutron, which is neutral and which scatters elastically on the detector producing measurable ionization energy. However, the coupling strength of the candidate particle to the detector nuclei need not be identical to that of the neutron. The interesting energy range of the neutrons for DAMIC is between 100s of eV up to 10s of MeV, and such neutrons are produced in fission, fusion, accelerators, or via nuclear resonances.

4.2 Theoretical review of QF

When the nucleus of a target detector has been scattered elastically by a neutral particle such as a neutron or a WIMP, the nucleus obtains a recoil energy E_R and becomes a pen-

[1] also known as the ionization efficiency

etrating charged particle, which then loses its energy as it moves through the target material via collisions with electrons and other nuclei. Energy loss occurs through two main mechanisms, which are described as electronic and nuclear stopping power. The travel length and the recoil energy of the nucleus, R and E_R can be rescaled to non-dimensional variables ρ and ϵ, respectively. Then, the nuclear energy loss $(\frac{d\epsilon}{d\rho})_n$ can be defined as a universal function $f(\epsilon)$ that can be calculated numerically[H. Chagani et al., 2008].
If the penetrating particle and the atoms of the medium are the same, ϵ could be defined as

$$\epsilon = \frac{11.5}{Z^{\frac{7}{3}}} E_R, \tag{4.1}$$

where Z is the proton number of the medium(detector), and E_R is the recoil energy of the target nucleus with the unit of KeV.

The electronic energy loss is defined as $(\frac{d\epsilon}{d\rho})_e = \kappa\sqrt{\epsilon}$, where, if the penetrating particle is identical to the atoms of the medium, κ can be defined as,

$$\kappa = \frac{0.133 Z^{\frac{2}{3}}}{\sqrt{A}}, \tag{4.2}$$

The Lindhard theory[J. Lindhard et al., 1963] attempts to quantify the fractions of ϵ to be either electronic or nuclear collisions with the the first order of approximation,

$$\epsilon = \bar{\eta} + \bar{\nu}, \tag{4.3}$$

where $\bar{\eta}$ is the energy given to electrons and $\bar{\nu}$ is the energy distributed to other nuclei. Among the total of five approximations used, the key one is that electronic and nuclear collisions can be separated.

The nuclear energy loss can be expressed as [Lewin and Smith, 1996]

$$\bar{\nu} = \frac{\epsilon}{1 + \kappa g(\epsilon)}, \tag{4.4}$$

where κ defined above, and $g(\epsilon)$ is defined as

$$g(\epsilon) = 3\epsilon^{0.15} + 0.7\epsilon^{0.6} + \epsilon. \tag{4.5}$$

So, the quenching factor can be expressed as

$$\frac{\bar{\eta}}{\epsilon} = \frac{\epsilon - \bar{\nu}}{\epsilon} = \frac{\kappa g(\epsilon)}{1 + \kappa g(\epsilon)}. \tag{4.6}$$

4.3 Experimental review on QF measurements

As mentioned above in section 4.2, the materials of the detector and the recoil energies both effect the value of QF. So, many dark matter experiments have to measure their

own quenching factors due to their unique detector material and / or interested recoil energy intervals. QF measurements have been published using the detector material of NaI(Tl) for the nuclear recoil energy range of 50 to 336 KeV [E. Simon et al., 2003], and with the same facilities using a Germanium bolometer for the range 76 to 123 KeV. The paper [G. Gerbier et al., 1990] published a silicon QF measurement for an energy range of 4 to 20 KeV. In order to reach a lower energy range of nuclear recoil, closer to the energy threshold of the DAMIC detectors, collaborators from DAMIC launched a fast neutron beam calibration experiment called "Antonella" to explore the 2 - 20 KeV neutron recoil range.

Although the detailed facilities for QF tests are not quite the same, the setup of this experiment is quite similar to that of figure 4.1 from [Th. Jagemann et al., 2005]. Neutrons are emitted from a source, travel a certain distance, hit the detector causing a recoil which can be measured, and scatter into the detector array.

To determine the QF of the detector (shown in blue in figure 4.1), one needs a measurement of both the recoil energy E_R of the neutron and the the ionization energy E_{ee}(electron equivalent energy), such that $QF = E_{ee}/E_R$. The value of E_R cannot be measured directly, instead it is calculated using the time of flight (ToF) between the scattering detector and the detector array.

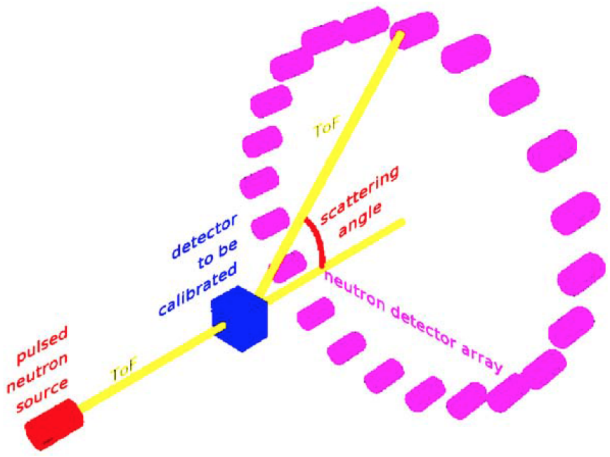

Figure 4.1: The conceptual design of a QF test.

The Antonella experiment did two separate runs aiming at measuring the QF in the range of 2 - 20 KeV, using a ∼500 KeV neutron beam at the University of Notre Dame in Indiana, U.S.A.. In 2013, we did a prototype experiment with two scintillator bars to detect the scattered neutrons. After the successful demonstration run, we performed a second run with a large scintillator array of 21 bars.

A schematic drawing of the prototype experiment is shown in Figure 4.2. A 2.3 MeV proton beam hits a ^7Li target, producing ∼100s-of-KeV energy neutrons via the $^7Li(p,n)^7Be$ reaction. Neutrons are collimated through a central hole of aperture $\phi = 1.0$ cm before hitting a Silicon Drift Detector (SDD), which causes a nuclear recoil and a scatter into a plastic scintillator bar. A SDD is used instead of a CCD since precise timing between the first and second measurement of the neutron is needed, whereas the CCD requires order of minutes to readout. The SDD provides a measurement of E_{ee} and the start of the ToF measurement. The time difference between the SDD and the scintillator bar is used to reconstruct the recoil energy, based on the angle of recoil.

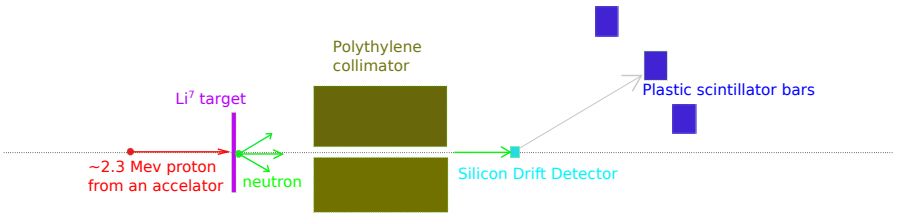

Figure 4.2: Schematic drawing of DAMIC QF prototype experiment.

Figure 4.3a shows the 10MeV Tandem Van de Graaff at Notre Dame which produces the $\sim 2.3MeV$ proton beam. Figure 4.3b shows the energy distribution of the neutron beam, as a comparison between data and GEANT4 simulation, as will be discussed subsequently in section 4.7.

Figure 4.4 shows a diagram of the setup and the calculation used to determine the recoil energy and neutron energy from the angle θ and time of flight ΔT. A detailed derivation of the expressions of E_{NR} and E_R can be found in Appendix A.4. Once the detectors have been fixed into the experimental setup, the variables l, r, and θ are all fixed (m is the neutron mass), so to determine E_R and E_{NR}, we only need to measure the ToF, ΔT. Note that ΔT is the time interval from the moment the neutron is produced in the lithium target until it is measured in the scintillating bar. Appendix A.4 explains the relations of these distances and times.

The measurement of ΔT is challenging for several reasons. Neutrons of ∼500s KeV have a cross-section of a few barn on silicon as shown in figure 4.9c, and this elastic interaction changes the energy and direction of the neutron. Therefore, unlike charged particle beams (such as of ∼100s GeV pions), where one can track particles with thin layers of material to measure ionization energy that without altering the course, such a technique does not work with neutrons. Another problem is that the neutron energy spectrum is not mono-energetic (see figure 4.3b); it must be determined from simulation and data, and the energy of each neutron is different in each event. Another problem is that the yield of usable signal events is low. According to our GEANT4 simulation, from 10 M incoming neutrons, we would expect only 2.4×10^4 events to interact with

4.3a. 10MeV Tandem Van de Graaff at University of Notre Dame, IN, U.S.

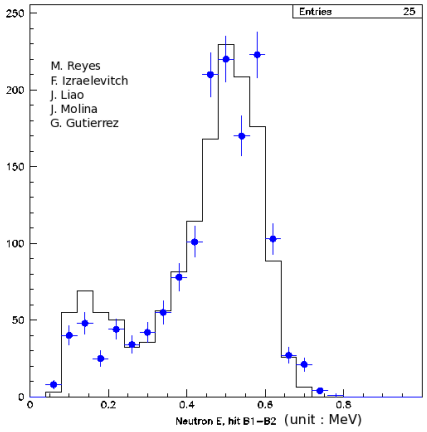

4.3b. Measured and simulated incident neutron spectrum

Figure 4.3: The accelerator DAMIC used for QF beam tests and the neutron spectrum

both the SDD and the scintillator, for an efficiency of 2.4×10^{-3}. This rate is low for several reasons : (1), the SDD is small, with a cylindrical shape of 2.82 mm diameter and 0.5 mm length, and according to simulation only 3% of neutrons passing through it will interact in the silicon; (2), the plastic scintillator bars need to record the coincident interaction, and they do not cover the full 4π solid angle.

The beam test data has even more challenges due to the existence of prompt gammas from the proton collisions. Most of the recorded data was triggered in the SDD by prompt gammas, whereas only 2% of the events come from neutrons. We also need to reject events triggered by detector noise by requiring a timing coincidence of two PMTs (photo multiplier tubes) for each scintillator bar hit and within the expected timing window of the drift between the scintillator and the SDD. Finally, with 10 days of 24 hours of beam tests, we recorded only 5,000 candidate events.

4.4 Simulation of Antonella experiment

In order to understand energy distributions, timing distributions, rates, efficiencies, rates, and backgrounds, as well as the optimization of the detector, a full simulation of the experiment is needed. For this purpose, we have used the GEANT4 toolkit, which is standard software in high energy, nuclear, accelerator, medical, and space particle physics [Geant4].

The version we have used for QF tests is : 4.0.00.p02. We used the GPS(General Particle Source) package to describe the incident neutron beam. The materials and geometries

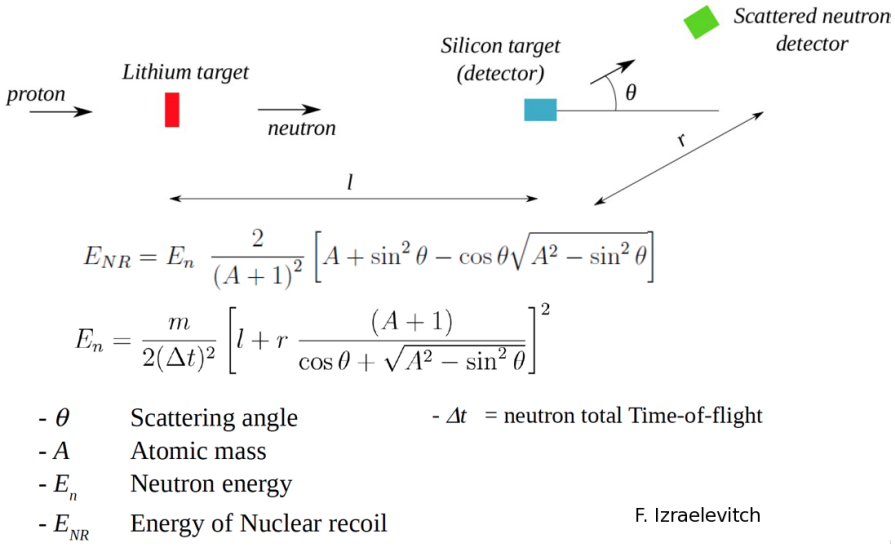

Figure 4.4: Kinematics of recoil energy of our QF tests

of the collimator, silicon detector and scintillator bars, etc., have been simulated in a very detailed way. One of the examples is the tip of the SDD, which is shown with the cover on, and with the cover off to reveal the fine detail as in figure 4.5.

In addition to the default physics packages of GEANT4, our simulation makes use of a specific package for low energy neutron "ENDF/B-VI"[ENDF webpage] covering the energy range from thermal neutrons up to 20 MeV, as well as the high-precision neutron interactions (NeutronHP) package which implements more precise cross-section predictions than the default packages, and also the "Underground Dark Matter Detector Advanced Example" package.

We performed two QF experiments at Notre Dame, in January 2013 with 2 scintillator bars to detect scattered neutrons, and in February 2015, with 21 scintillator bars. Accordingly, we have written two simulations, one corresponding to each experimental setup. The 2013 simulation was written after the 2013 run, and proved crucial for understanding the data and analyzing its features. The 2015 simulation was written prior to the 2015 data taking and was used also to optimize the design of the 2015 experiment in order to provide improved measurements.

During the 2013 prototype running, we took two runs. The first run is referred to as "2 bars only", where only scintillator bars were installed : one bar was used to measure the incident neutron, and one was used to measure the scattered neutron. The first bar was placed at the same location as would be the silicon detector, and the second bar was placed 21.0 cm away. This setup was dedicated to calibrating the neutron beam flux (discussed later), and was similar to that of figure 4.2, with a plastic scintillator bar

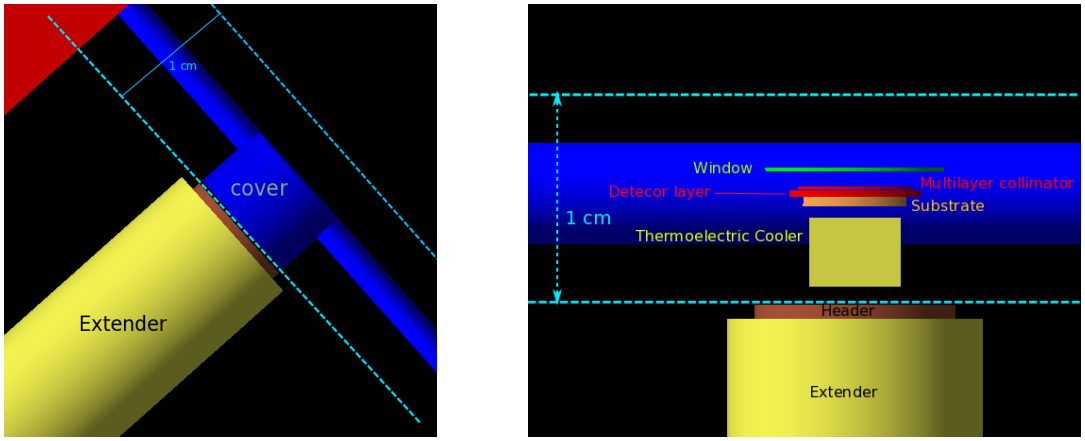

4.5a. with the cover

4.5b. the cover has been removed

Figure 4.5: Detailed view of the SDD(Silicon Drift Detector) in beam test

instead of "Silicon Drift Detector". The second run is referred to as "silicon detector + 2 bars", using the same setup as figure 4.2 with two scintillator bars. For details, refer to section 4.7.

For the 2015 beam test, the two bars were replaced by an array consisting of 21 scintillator bars. We produced a full simulation on this new setup, providing iterative versions in order to optimize the geometrical design and complete the data analysis. For details, refer to section 4.8.

The GEANT 4 simulation has also provided us with some interesting discoveries. For instance, figure 4.6 shows the distribution of data for the incident neutron energy spectrum with the requirement of at least one hit in the SDD detector. We were surprised to see the peaks in this distribution. However, the simulation revealed that this distribution was correct. The requirement of an SDD hit selected events in which there was resonant neutron-silicon scattering, and figure 4.6 represents the convolution of the incident neutron spectrum with the resonant structure, as shown in figure 4.7.

4.5 Fast neutron detection with scintillator

4.5.1 Neutron detection

Neutrons are generally detected through nuclear reactions and elastic scattering. Because the cross section for neutron interactions in most materials depends strongly on neutron energy, very different techniques have been developed for neutron detection in different energy regions. The convention is that neutrons with energy ≤ 0.5 eV are called "slow neutrons", whereas KeV to MeV neutrons are called "fast neutrons".

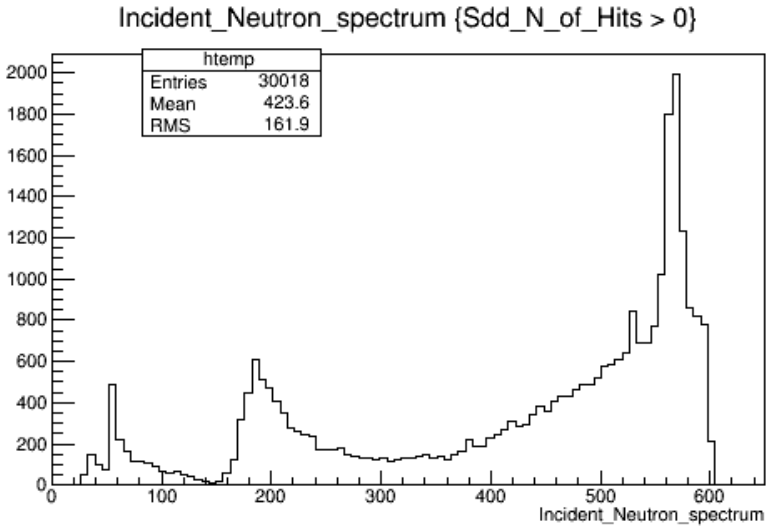

Figure 4.6: Spectrum of incident neutrons with a cut of the hit on a silicon detector

For slow neutrons, nuclear interactions are the dominant method of detection, elastic scattering is negligible because of very low kinematic energy. The most commonly used materials of detectors are : ^{10}B,^{3}He,^{6}Li, ^{155}Gd(Gadolinium) and ^{157}Gd. The cross-sections of ^{10}B,^{3}He,^{6}Li are shown in figure 4.8 [G. F. Knoll, 2000].
The element ^{157}Gd has the highest thermal neutron cross-section among any of the stable nuclides : $\sim 2.6 \times 10^5$ barns. The Daya Bay experiment for neutrino measurement has utilized Gadolinium-loaded(0.1% by mass)liquid scintillator for thermal neutron capture[W. Beriguete et al., 2015] due to its yielding properties.

Once the kinematic energy of incident neutrons reaches KeV level such that they are considered as "fast" neutrons, the recoil energy obtained by a detector from elastic scattering becomes detectable. Since the cross-section for nuclear reaction has no additional advantage, and the price of ^{10}B,^{3}He or ^{6}Li is more expensive than other detectors such as plastic scintillator detectors, elastic scattering is the primary method for fast neutron detection.

4.5.2 Fast neutron detection with a scintillator

By far, the most popular target nucleus for fast neutron detection is hydrogen. One of the reasons is that the cross-section for elastic scattering of neutrons from hydrogen is large compared to other nuclei and the energy dependence is accurately know since it is the simplest collision to model. Figure 4.9 shown the comparison of cross-section of neutrons on carbon, hydrogen, and silicon[National nuclear data center], showing that hydrogen is the largest across a broad range of energies. Another reason hydrogen is

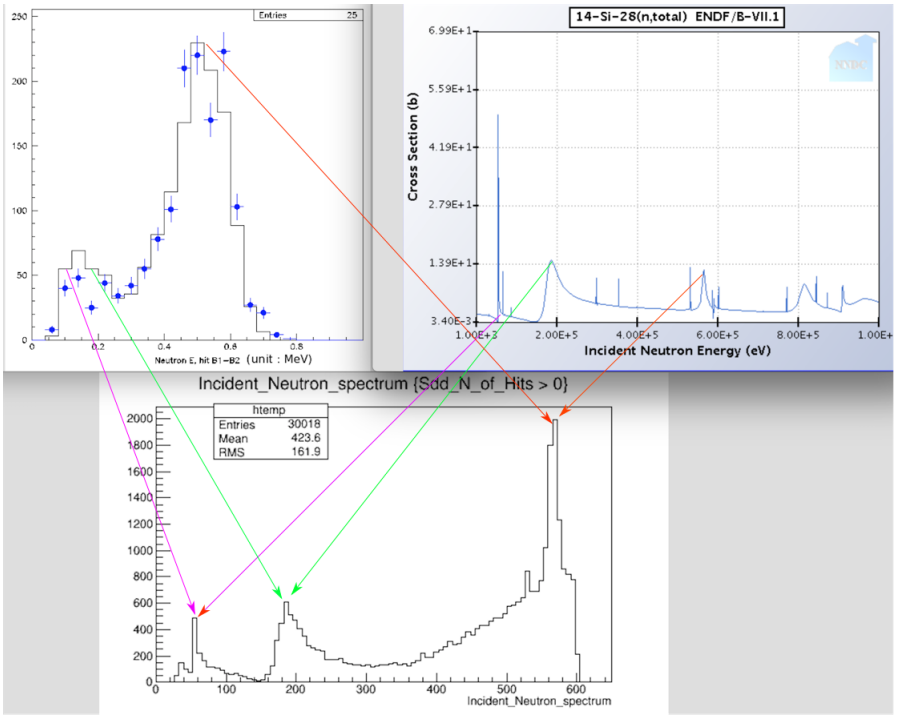

Figure 4.7: Towards undertanding the neutron energy spectrum of figure 4.6. The upper left shows the incident neutron spectrum expected at the silicon detector. The upper right plot shows the elastic cross-section resonances excited as a function of neutron energy. The lower plot shows the data measured which is a convolution of these effects.

popular is that an incident neutron can transfer up to its entire energy in a single collision with a heavy nucleus, whereas only a small fraction can be transferred in collisions with a heavy nucleus [G. F. Knoll, 2000]. Since plastic scintillator is mainly composed of hydrogen, it is an ideal material for fast neutron detection. For our experiment, time resolution is the most important property of a scintillator.
We selected EJ200 [Plastic scintillator] as the plastic scintillator for our prototype run. Figure 4.15a lists the predominant number densities of "C" and "H" of EJ200. Additional factors for using this scintillator are explained in section 4.6.1.

4.5.3 Thickness of the scintillator bar

In choosing the thickness of the plastic scintillator, several trade-offs must be made. For us, the most important one is detection efficiency versus timing. For hundreds of KeV, to reach 100% detection efficiency, a scintillator with a thickness of 10 cm should be enough. However, for such a scintillator, the chance of multi-scattering will be increased significantly, so the deposited energy and produced fluorescent light will vary widely and,

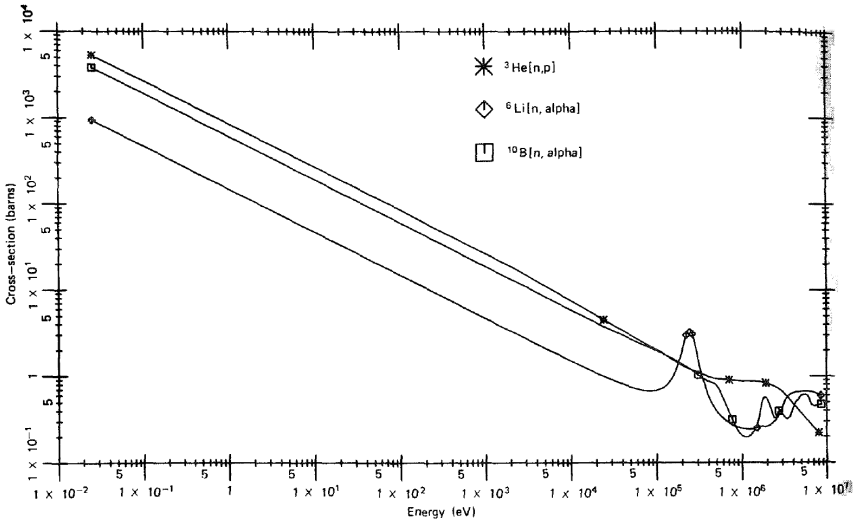

Figure 4.8: Cross-section V.S. neutron energy for ^{10}B,^{3}He,^{6}Li nuclear interaction

it is more difficult to obtain uniform light collection, making the time resolution worse. We chose the thickness of our scintillator to be 2.5 cm using a simulation optimization. Figure 4.11a shows the distribution of the number of hits recorded on the scintillator after 1M events were simulated, and figure 4.11b shows only the events in which there was at least one hit, which is 7.5×10^5. Therefore, the scintillator efficiency is determined from simulation to be 75%.

In order to determine the time resolution, we produced a simulation of the z-coordinate of the interacting position inside of the scintillator bar. The z-axis is the direction along the incident neutron beam, as shown in figure 4.4 . Figure 4.13 shows the distribution of the z-coordinates of hits, the red curve is a Gaussian fit. From this plot, one can determine that the uncertainty on the hit depth is σ_{depth} =1 cm, which is roughly equivalent to $\sigma_T \approxeq 1\ ns$ of time resolution because the speed of the incident neutron in the scintillator bar is approximately $1cm/ns$. Note that this plot is simulated with the setup of the 2015 beam test, not the 2013 one. A detailed discussion will be presented in section 4.8.2.

As will be discuss in section 4.6.2, the uncertainty on the timing of the non-mono-energy incident neutron is 5.7 ns, much greater than the one introduced by the depth of the scintillator bar. Therefore, the thickness of the scintillator contributes very little to the timing uncertainty.

In summary, a scintillator bar thickness of 2.5 cm yields a detection efficiency of 75% and a time resolution of $\sim$ 1 ns, which will be shown to be negligible compared to the contribution of time resolution coming from the indeterminacy of the neutron beam energy.

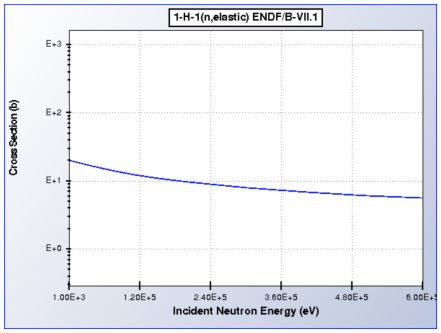

4.9a. cross section of neutrons on hydrogen.

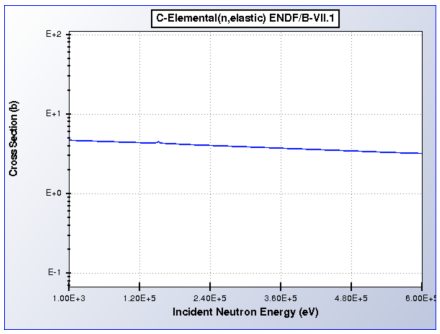

4.9b. cross section of neutrons on carbon

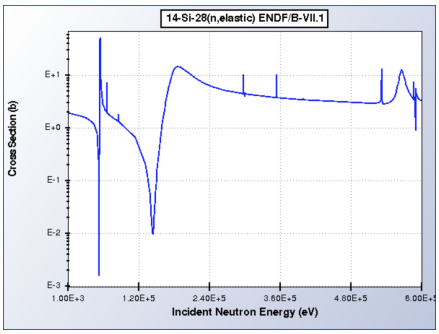

4.9c. cross section of neutrons on silicon

Figure 4.9: Comparison of neutron elastic scattering cross section of neutrons with 100s of KeV energy on various targets

Light Output, % Anthracene	64
Scintillation Efficiency, photons/1 MeV e^-	10,000
Wavelength of Max. Emission, nm	425
Rise Time, ns	0.9
Decay Time, ns	2.1
Pulse Width, FWHM, ns	~2.5
No. of H Atoms per cm^3, x 10^{22}	5.17
No. of C Atoms per cm^3, x 10^{22}	4.69
No. of Electrons per cm^3, x 10^{23}	3.33
Density, g/cc:	1.023

4.15a. Physical and scintillation constants of EJ200.

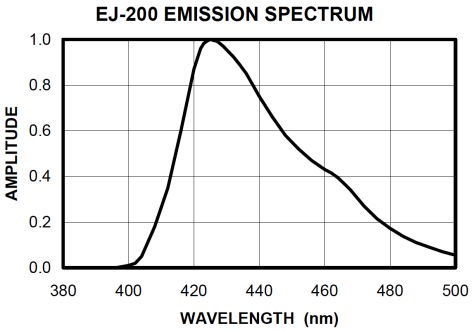

4.15b. Emission spectrum of EJ200

Figure 4.10: Physical constants and emission spectrum of plastic scintillator EJ200

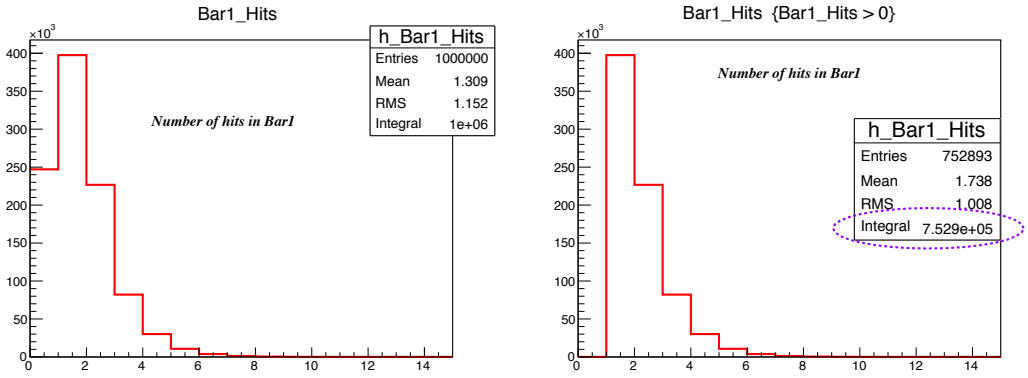

4.11a. All neutrons passing through scintillator

4.11b. Neutrons passing through scintillator and producing at least one hit

Figure 4.11: Estimation of scintillator efficiency from GEANT 4 simulation (from dividing the integrals of the two plots)

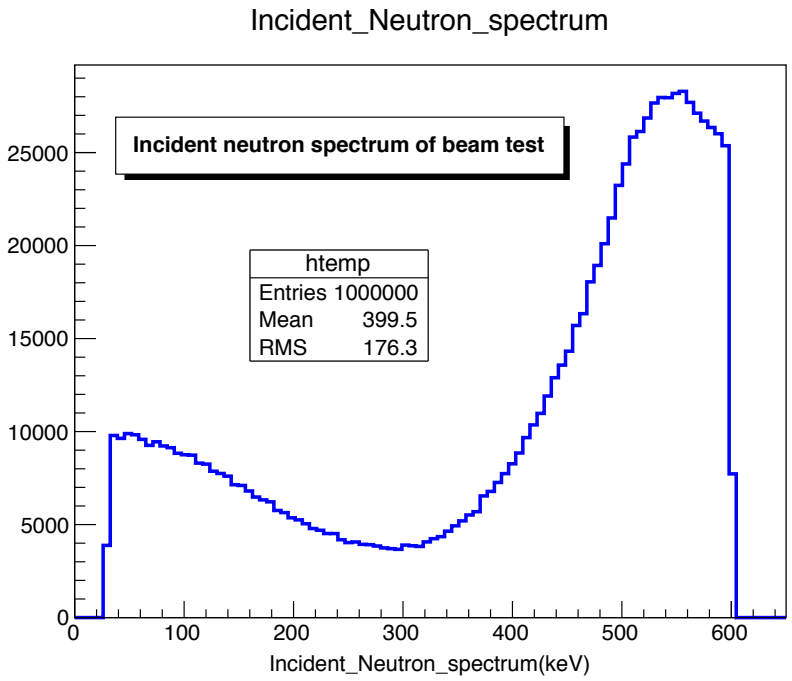

Figure 4.12: The simulated spectrum of the incident neutrons from the 2013 experimental setup.

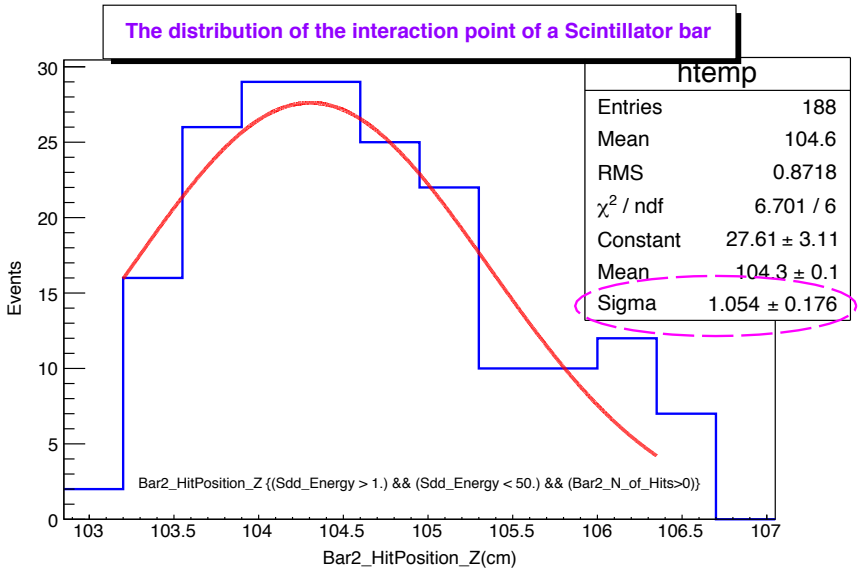

Figure 4.13: The simulated hit depth of the scintillator bar in the direction parallel to the beam (z-direction)

4.6 Characterization of the scintillator bars

4.6.1 Hardware introduction

As mentioned in section 4.3, we need plastic scintillator bars to measure the time of flight of scattered neutrons. Figure 4.14 shows such a bar. In the middle of the bar is a plastic scintillator. Every plastic bar has been wrapped by two layers of tape : the inner layer is Tyvek Housewarp which reflects all of the "leaking" photons backing into the scintillator bar; the outer layer is 3M electrical black tape to isolate against environmental photons [2].

Besides the high number density of hydrogen, there are other factors which made us choose plastic scintillator :
(1). This scintillator combines the two important properties of long optical attenuation length and fast timing and is therefore particularly useful for time-of-flight systems. Long optical attenuation length is necessary for our bars because the length of a bar is 35 cm. Fast timing is important because the smaller the rise time is, the smaller the timing jitter will be.
(2). We obtained retired ET9954B PMTs (from the Tevatron experiments at Fermilab) which are best matched to scintillator light with wavelengths of 350 - 450 nm, which is

[2] As figure 4.14 shows, there is a white tape marked with seven circles on the tape of the scintillator bar. These markers are just to indicate the positions where a ^{55}Fe source should be put when we performed tests

Figure 4.14: A scintillator bar to be calibrated in Fermilab

compatible with the average wavelength for this EJ-200 scintillator of 425 nm as shown in figure 4.15b. Also, the rise time of the PMTs is 2 ns, which is compatible with the 0.9 ns of the EJ200 scintillator. Other constants and the emission spectrum are included in figure 4.15a.

We glued two PMTs to both of the ends of the scintillator bar with EJ-500, a clear and colorless epoxy cement with refractive index of 1.57, which is ideal for optically bonding plastic scintillators[Epoxy cement]. The 9954B is a 51mm diameter end-window photomultiplier, with enhanced green sensitive bialkali photocathode, and 12 BeCu dynodes of linear focused design for good linearity and timing. The timing performance and QE(Quantum Efficiency) are shown in figure 4.16a and figure 4.16b.

Light Output, % Anthracene	64
Scintillation Efficiency, photons/1 MeV e^-	10,000
Wavelength of Max. Emission, nm	425
Rise Time, ns	0.9
Decay Time, ns	2.1
Pulse Width, FWHM, ns	~2.5
No. of H Atoms per cm^3, x 10^{22}	5.17
No. of C Atoms per cm^3, x 10^{22}	4.69
No. of Electrons per cm^3, x 10^{23}	3.33
Density, g/cc:	1.023

4.15a. Physical and scintillation constants of EJ200.

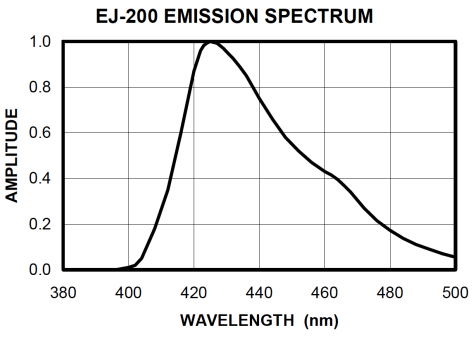

4.15b. Emission spectrum of EJ200

Figure 4.15: Physical constants and emission spectrum of plastic scintillator EJ200

timing:			
single electron rise time	ns		2
single electron fwhm	ns		3
transit time	ns		41

4.16a. Timing of PMT 9954B.

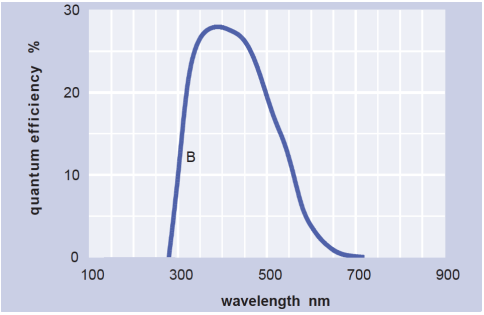

4.16b. QE of PMT 9954B

Figure 4.16: Timing and QE of PMT 9954B

The DAQ(Data Acquisition) for characterizing scintillator bars is shown in figure 4.17a. The logic diagram of DAQ is shown in figure 4.17b. The output signal of the PMT has been split into two channels, one goes to a CFD(Constant Fraction Discriminator) to get timing, another goes to an ADC to measure charge after being inverted by an inventor. The coincidence module receives the timing from the CFDs to open the gate of the ADC after 75ns delay, and set up a common stop to the TDC after a 100ns delay. The CAMAC USB is the slowest module so it connects to the inhibit of the coincidence after an or-gate. This or-gate has another input from the gate delay module. As indicated, only if both the CAMAC and the gate delay are ready will data taking start.

4.6.2 Charge and timing calibration

To calibrate the charge and timing of the scintillator+PMT, we used an ^{55}Fe source, which emits X-rays most strongly at 5.9 KeV. The attenuation length of the scintillator bar for this energy is about 1mm as shown in figure 4.18, where attenuation length is defined as the depth where the intensity of x-rays falls to $1/e$ of its value at the surface assuming a perpendicular incidence[X-Ray attenuation length]. Here, we have taken $C_{27}H_{30}$ as the chemical formula of the material of the scintillator bar, Polyvinyltoluene; the density is $1.023g/cm^3$. Both are shown in the website of [Plastic scintillator].

In order to calibrate the charge measurement, we expose the scintillator to the source, and histogram the ADC counts, making a fit. The fit function is Gaussian convoluted with Poisson. Reference [L. Bonnet et al., 2014] describes this fit function in great details. The number of photoelectrons is found from figure 4.19a to be 1.5 phe.

For the timing calibration, we used a similar but slightly different DAQ logic than shown in figure 4.17b[3]. We used the ADC of one of the PMTs to trigger another PMT, for

[3]The trigger logic of figure 4.17b is useful for the case of a quick and simple test to know if every bar and its affiliated PMTs work normally, for instance, if there is light leakage of a packaged scintillator,

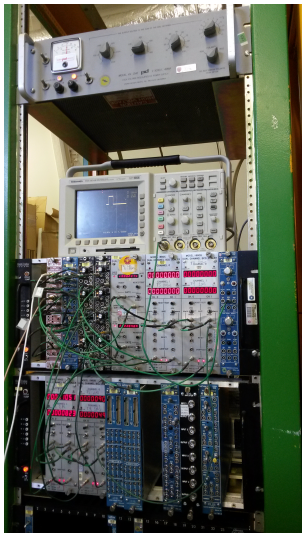

4.17a. DAQ of scintillator bars calibration.

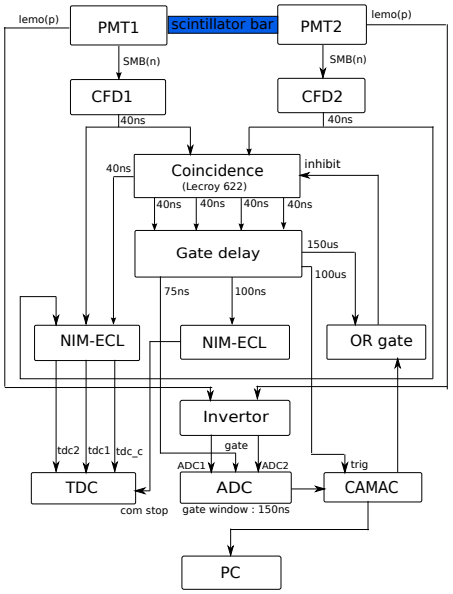

4.17b. Logic of DAQ

Figure 4.17: DAQ and logic diagram of the scintillator bar calibration system

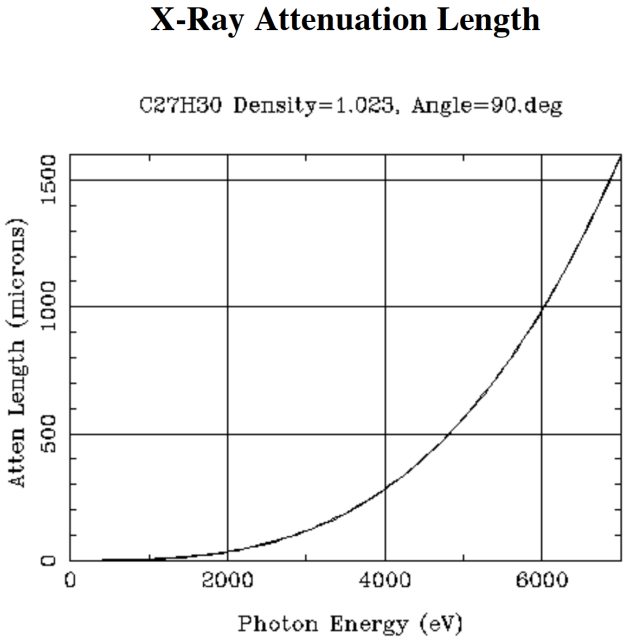

Figure 4.18: Attenuation length of a bar for a ^{55}Fe source.

instance using the "PMT1" in figure 4.17b to trigger "PMT2". This kind of trigger reduced the background events caused by cosmic rays significantly.
In this test, ^{55}Fe has been put in different places marked as circles in figure 4.14. At each place, we measured the time for each PMT, we then subtracted these two times to get a histogram and make a Gaussian fit. The σ is roughly $\sim$ 2.0 ns as shown in figure 4.19b which is expected.

The 2.0 ns sigma in figure 4.19b arises from the time jitter of two sources : the whole DAQ system and the propagation of fluorescent light in a bar. Although the attenuation length of ^{55}Fe inside of the scintillator bar is a few mm, the produced fluorescent light should be propagated isotropically.

Time distribution from the two scintillator bars with Gaussian fits for incident neutrons as shown in figure 4.20, which was also simulated.
We determine the uncertainty of timing due to the wide-spread incident neutron energy to be 5.7 ns as shown in figure 4.20a. Therefore, the time jitter due to the uncertainty in the hit depth of $\sim$ 1.0 ns[4] and the uncertainty due to the DAQ system and fluorescent light propagation in the bar of $\sim$ 2.0 ns as shown in figure 4.19b are negligible.

if both PMTs have an output signal etc. In fact, we have identified several abnormal bars in this way.

[4]The uncertainty of hit positions in Figure 4.13 is 1.0 cm which is equivalent to 1.0 ns of time jitter because the speed of $\sim$ 550 KeV neutrons propagate at the speed of 1 cm / ns in the scintillator bar.

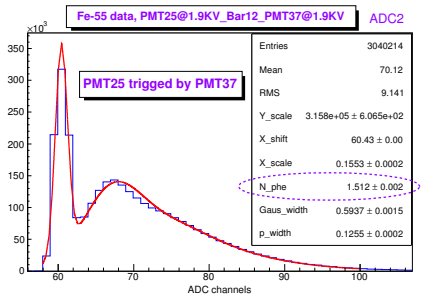

4.19a. Charge measurement .

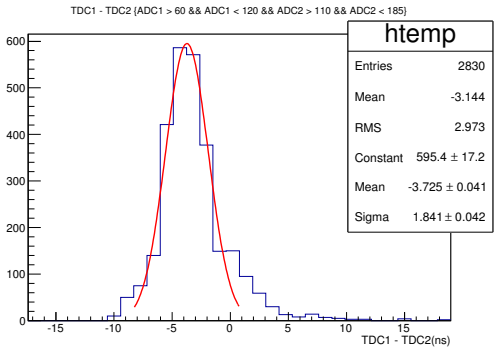

4.19b. Timing measurement.

Figure 4.19: Timing and charge measurement for a scintillator bar with ^{55}Fe source.

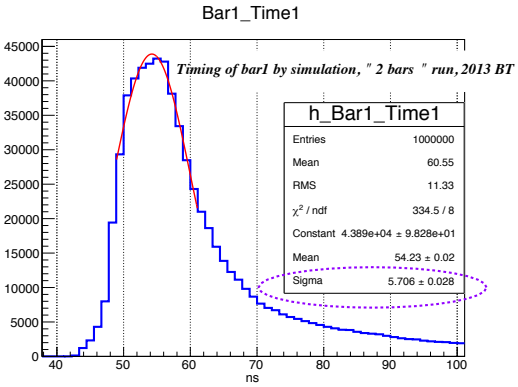

4.20a. Simulated timing of bar1 and Gaussian fit

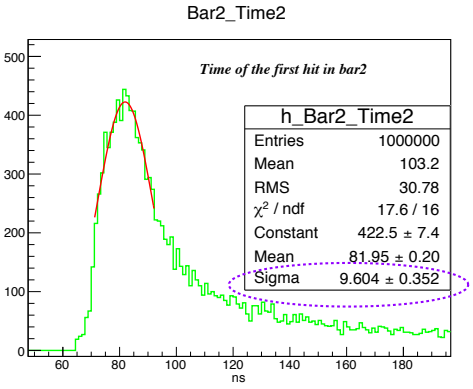

4.20b. Simulated timing of bar2 and Gaussian fit

Figure 4.20: Simulated time distribution and Gaussian fit for the events of bar 1 and bar2 , 2013 beam test, “2 bars” run

The uncertainty of the timing of the second bar was determined to be sigma = 9.6 ns, which is bigger than the first bar, as expected from simulation (as in figure 4.20b).

4.7 2013 beam test

As mentioned, for the 2013 beam test, there were two main runs : " 2 bars only " and " SDD + 2 bars ". The " 2 bars only " run used 2 scintillator bars exposed to the neutron beam, with one bar serving as the detector to be calibrated, to which neutrons hit first, and another bar located around 21 cm away to detect the scattered neutrons from the first bar. Please refer to Figure 4.21a for a schematic. This run was designed to understand the energy spectrum of the neutrons hitting the detector to be calibrated. This will be discussed further in subsection 4.7.3 below.
The " SDD + 2 bars " configuration was used to calibrate the SDD with incident neutrons using two scintillator bars located 10s of cm away to detect scattered neutrons. A Geant4 simulation drawing of this setup is shown in figure 4.30. This run produced promising results for using this setup to measure the QF. A more detailed discussion will be introduced in subsection 4.7.6.

4.7.1 Detailed description of "neutron energy spectrum" run in 2013

We measured the neutron energy spectrum using the "2 bars" setup shown in figure 4.21. In figure 4.21a, the material of the "Li target" is LiF(Lithium Fluoride), with a thickness of $18\mu m$ which maximizes the yield of neutrons.

The collimator is made of polyethylene which has been widely used as the moderator of fast neutrons. The two bars both have the dimensions of $3 \times 3 \times 25.4$ cm. For each bar, two PMTs - 9954B - have been glued on both two ends, as introduced in the subsection

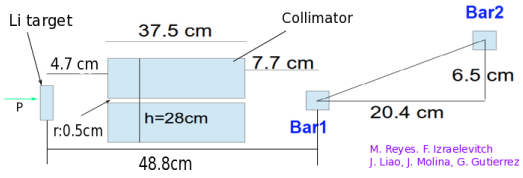

4.21a. Schematic drawing of setup.

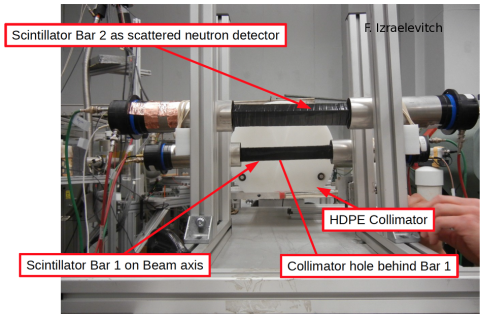

4.21b. Real setup, looking from the two bars downstream

Figure 4.21: The setup of 2013 beam test, "2 bars" run

of 4.6.1.

Before starting, all we knew about the neutron spectrum came from the reference of [C. Burke et al., 1974], as shown in figure 4.22. This paper is the most instructive reference for our tests. However, we can't take the distribution from figure 4.22a as the spectrum of our beam directly because the spectrum on figure 4.22a only considers the interaction of $Li^7(n,p)Be^7$; while for our test, we need to also consider the location of the detector and the size of the collimator in order to determine the neutron flux : the spectrum we need to know is at the place where the detector to be calibrated is located, around half meter away from the Li^7 target; also, the neutron beam has to pass through the $\phi = 1\ cm$ hole of the collimator, as figure 4.21a shows. So, we need to figure out the neutron flux in our beam test.

Our strategy for deriving the neutron energy spectrum was the following : we take the spectrum from figure 4.22a as the input flux to the GEANT4 simulation, and based on the timing of events events recorded in the two scintillator bars, we could figure out the neutron energy spectrum. We then compared the simulated neutron spectrum to the one we obtained directly from experimental data. This comparison is necessary in order to verify both the initial neutron spectrum from this reference [C. Burke et al., 1974], as well as to verify whether the detector setup and DAQ system provide reliable timing measurements. Only if both assumptions are correct would we obtain a matching neutron energy spectrum. This consistency is shown in figure 4.3b. A detailed description is included in the following sections.

The energy of the proton beam in the reference [C. Burke et al., 1974] is $E_{proton} = 2.25$ MeV, compared to our 2.3 MeV, however, this difference is small compared to other uncertainties and so we use this spectrum without corrections.

4.7.2 Geant4 simulation of "neutron energy spectrum" run in 2013

The main purpose of the "2 bars" run was to understand the neutron spectrum, however the Geant4 simulation for this run also produced a deeper understanding of the features of the experimental data.
Figure 4.23 shows the Geant4 simulation with 50 incident neutrons. The two scintillator bars have been represented as light blue and red cuboids. The red, blue and vertical green lines are the axes of coordinate system of Geant4. Other green lines represent the trajectories of neutrons and a small yellow point indicates the interaction of neutrons and the medium[5].

[5]The PMTs and auxiliary components were ignored in this simulation since their effects on the results were limited. In subsequent simulations, like "SDD + 2 bars" and "SDD + array", all of the components were considered.

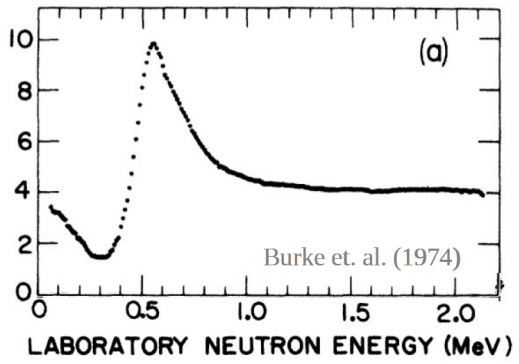

4.22a. The neutron spectrum we adapted [C. Burke et al., 1974].

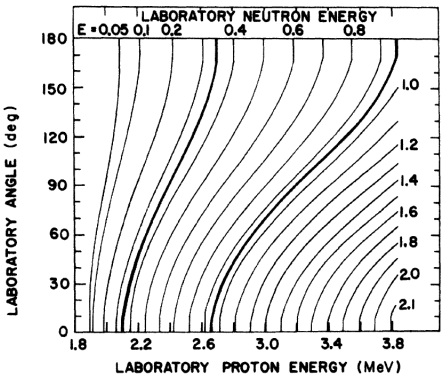

4.22b. The neutron energy depend on proton energy and interaction angle [C. Burke et al., 1974]

Figure 4.22: The neutron spectrum we assumed in beam test at University of Notre Dame, IN, U.S.

From both sub-figures of figure 4.23, we see some neutrons scattering from the first bar, and hitting the second bar, while most of the incident neutrons hit the first bar without touching the second one. To the right of Figure 4.23b shows the entrance point of the neutrons at the end of the collimator, where the LiF target is located 5 centimeters down stream. The $1cm$ diameter hole in the middle of the collimator is not visible on this figure.

Figure 4.24 shows some results of the "2 bars" run. For these results, the incident neutrons are simulated as an uniform distribution among [40, 800] KeV, as shown in figure 4.25. The uniform distribution of incident neutrons was only used for this simulation, whereas for other experimental setups the spectrum shown in figure 4.22a was used. In terms of a qualitative analysis, the simulated results with such a distribution are equivalent to those assuming the beam of figure 4.22a.

Figure 4.24 shows the number of hits, total energy deposited, energy deposited by the first hit, and timing of the first hit, for the first bar and the second bar. For single hits, the energy deposited in the first hit equals the total energy deposited; while for multi-hits, the total deposited energy is bigger than that of the first hit.

An unexpected harvest from this setup was that the simulation revealed some confusing events that did not fall in the expected distribution of arrival times on the first and second bars. The events are shown in a dashed pink horizontal box on figure 4.26, and have a bar 1 time of 0, but a bar 2 time ranging from 0 to 1000 ns. A time of 0 means that no signal was measured in this bar. Since bar 1 is in front of bar 2, and bar 2 is at an angle, it is not obvious how a scattering event could have events with hits on bar 2 without any measurable hits on bar 1. We discovered this was a real effect that was also

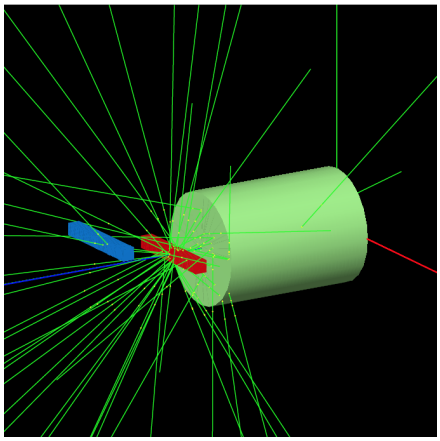

4.23a. view from beam downstream.

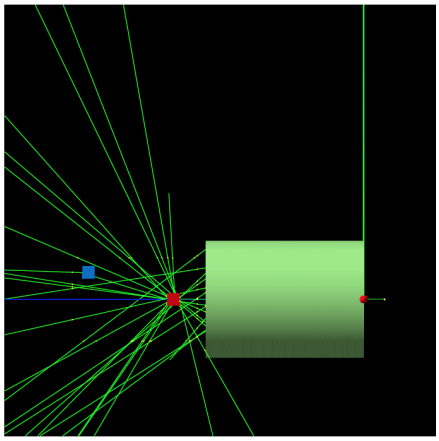

4.23b. side view

Figure 4.23: A Geant4 simulation of 50 incident neutrons on the detector setup for the "2 bars " run. The z-axis is blue, x-axis is red, and the y-axis is green

manifest in data. To understand this effect, we plotted the energy distribution of the events in the rectangle from figure 4.26. Figure 4.27a and figure 4.27b show the energy distribution of these events for bar 1 and bar 2, respectively.
All of these strange events have a low deposited energy, most below 1 KeV, imparted to the nucleus. To understand these events, it is helpful to understand the mechanism of interaction. A struck proton in the scintillator mainly interacts with electrons, with only a small chance of interacting with another nucleon. The maximum energy it transfers to the electrons in each encounter is $4 * E_0 * m_e/m_p \approxeq 1/500 E_0$, where E_0 is the energy of a proton, m_e is the mass of an electron and m_p is the mass of a proton. For a 1 KeV-proton, the maximum energy transferred to the electron would then be roughly 2eV. The threshold energy for producing fluorescence light in a plastic scintillator is 3 -4 eV [G. F. Knoll, 2000], so such a nuclear recoil would not produce measurable energy in the scintillator, thereby no hit would be recorded in the first scintillator.

The events with deposited energy above 2 KeV in figure 4.27a should have produced scintillation light if the energy was deposited in a single hydrogen nucleus. However, it is likely that in these cases either the energy was deposited to more than one proton, or the neutron interacted with a much heavier carbon atom, which has a significant number density as is shown in figure 4.15a. The simulation helped us to understand this process and the expected rate.

The events shown in the vertical box with solid red of figure 4.26 are easier to understand : neutrons hit the first bar and don't hit the second bar, so the timing of bar2 is zero while the time of bar1 ranges from 40 to 1000 ns. Most of the events above the horizontal broken line box are "good" events : neutrons hit the first bar and are scattered into the second one.

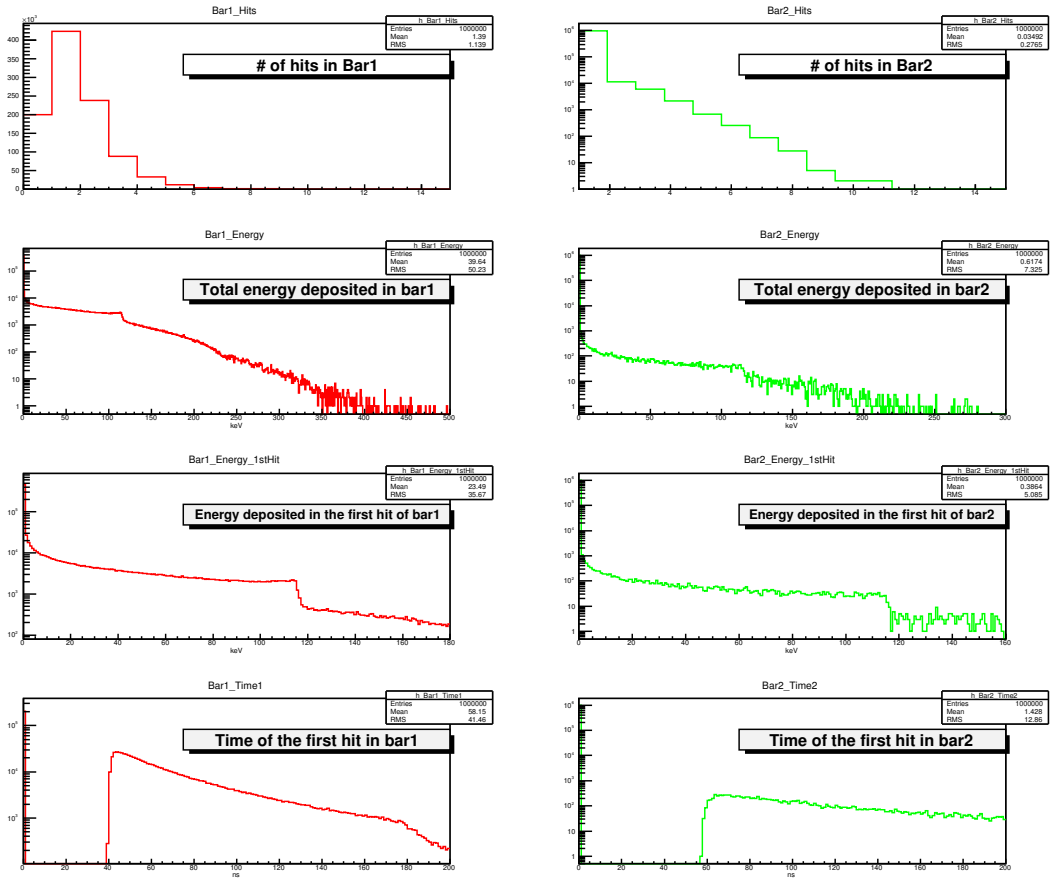

Figure 4.24: Some results of "2 bars" run

4.7.3 Data analysis of "neutron energy spectrum" run, 2013 beam test

Figure 4.28 shows the data obtained from the "2 bars" run of the 2013 neutron beam experiment. Prompt gamma-rays from the de-excitation of $^7Be^* \rightarrow ^7 Be$ of the $^7Li(p,n)^7Be$ interaction have been circled by a green ellipse. As can be determined from figure 4.21a, prompt photons take $48.8cm/(30cm/ns) \approxeq 1.6$ ns to travel from the LiF target to the first bar.

Events in the blue ellipse are random hits caused by the gammas hitting bar1 first then being scattered to bar2.

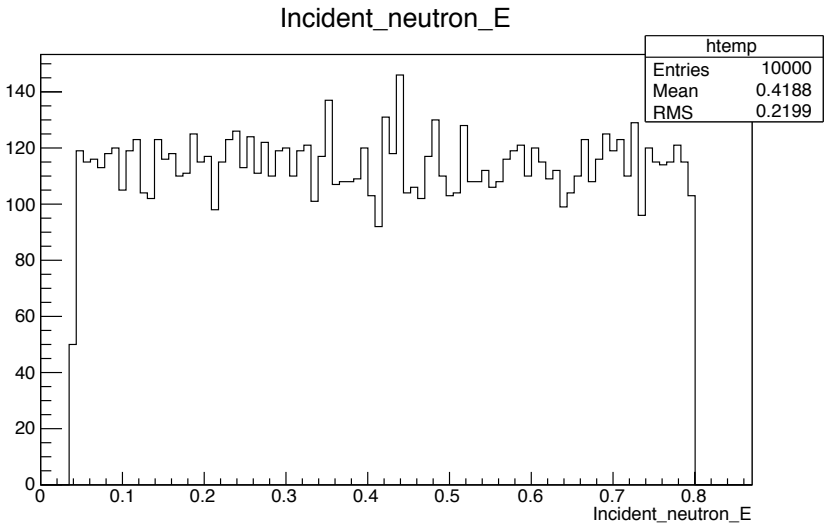

Figure 4.25: Simulated incident neutron spectrum of "2 bars" run

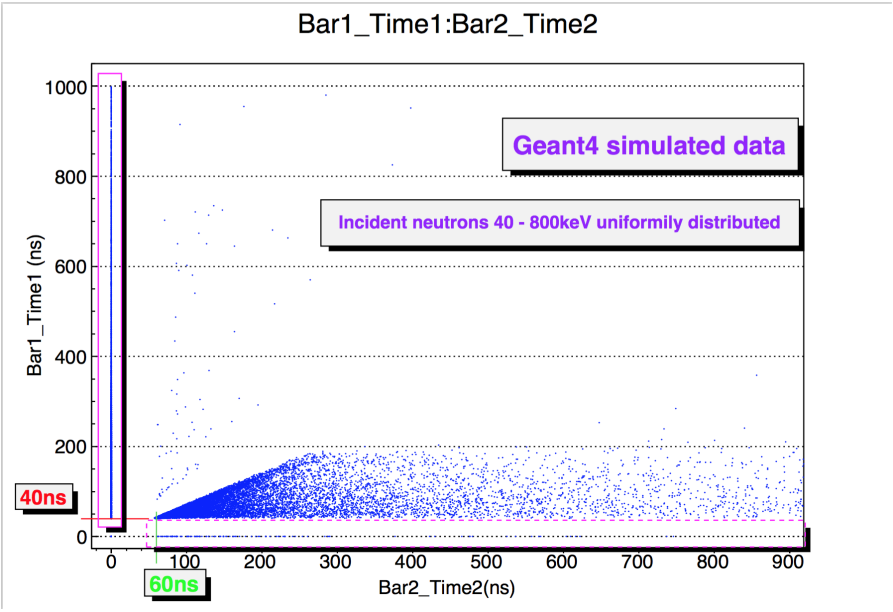

Figure 4.26: Timing of bar 1 vs bar2 using Geant4 simulation for the "2 bars" run

The events surrounded by the pink rectangle are produced by cosmic ray muons. A 3 GeV muon has a velocity close to the speed of light, so it only takes $21.4cm/(30cm/ns) \approx 0.7ns$ to travel the distance between two bars. This tiny difference is not visible on figure 4.28, so the events appear to happen in bar1 and bar 2 at the same time.
The events surrounded by the red curve labeled "Good candidate events line" are neutron events. For these events, the times are $TDC1 \gtrapprox 40ns$ and $TDC2 \gtrapprox 60ns$, which are

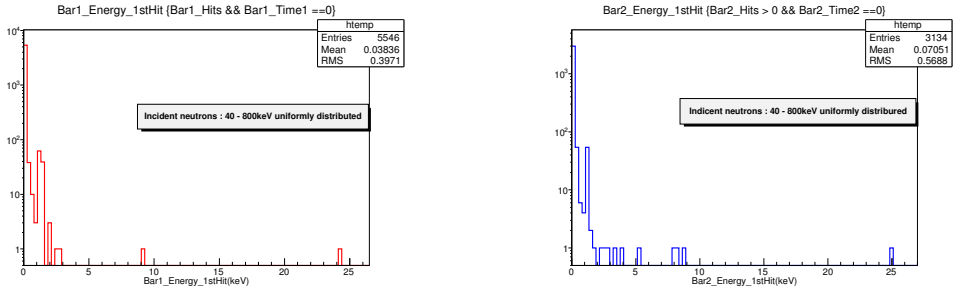

4.27a. "weird" events in bar1

4.27b. Similar events found in bar2

Figure 4.27: "weird" events in bar1 and bar2 of "2 bars" run

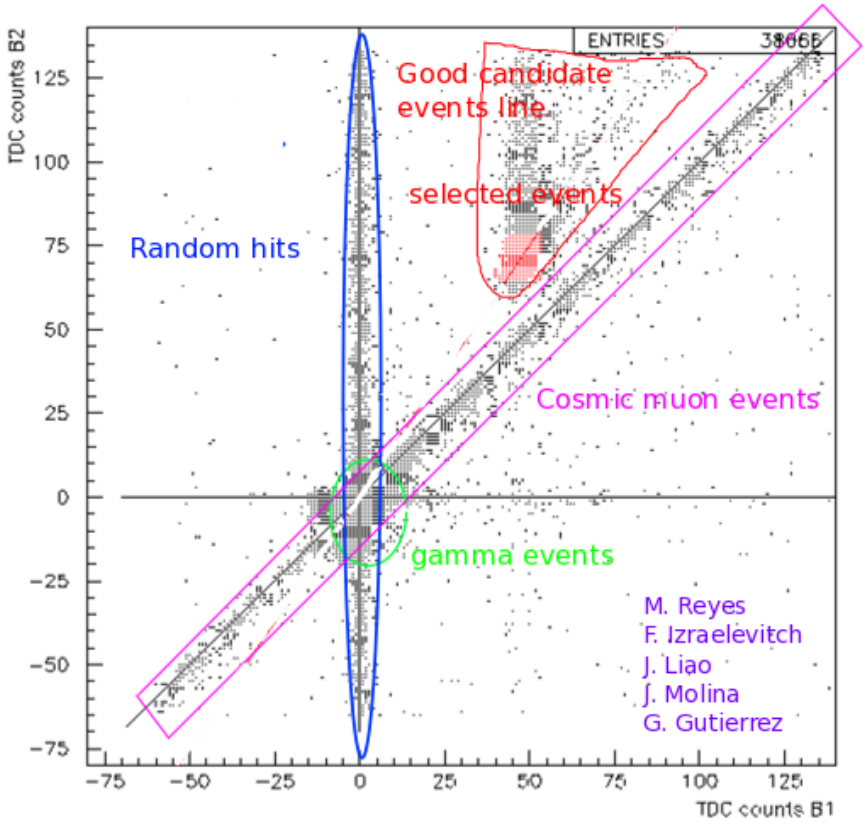

Figure 4.28: Selected data of "2 bars" run, 2013 beam test

consistent with the simulated results in figure 4.24. We further applied selection on these events and obtained the red population marked as "selected events" on figure 4.28. These selection criteria are : (1), at least one hit on both scintillator bars; (2), the time of the first hit is greater than the timing of the beam spill; (3), for the time obtained by

the two PMTs, for instance, for bar 2 it is $-16ns < T_{Left\ PMT} - T_{Right\ PMT} < 10ns$. This cut is mainly to reject coincident cosmic muon events; (4), we define an angular slice cut to select events as shown in figure 4.29. Signal events are selected using the relationship between T2 and T1, such that

$$\begin{aligned} T_2 &= T_1 + \frac{21.4}{v_{\ scattered\ neutron}} \\ &= T_1 + \frac{21.4}{\sqrt{\frac{2E_{\ scattered\ neutron}}{m_n}}} \\ &= T_1 + \frac{21.4\sqrt{m_n}}{\sqrt{2E_{\ scattered\ neutron}}} \\ &= T_1 + \frac{21.4\sqrt{m_n}}{\sqrt{2(E_0 - E_R)}} && (E_{\ scattered\ neutron} = E_0 - E_R) \\ &= T_1 + \frac{21.4\sqrt{m_n}}{\sqrt{2(E_0 - constant * E_0)}}, && (4.7) \end{aligned}$$

where T_1, T_2 are the times of neutrons recorded in bar1 and bar2, respectively. The distance between the bars is 21.4cm, $v_{\ scattered\ neutron}$ and $E_{\ scattered\ neutron}$ are the velocity and energy of the scattered neutron from bar1, m_n is the mass of neutron, E_0 and E_R are the energies of the incident neutron to bar1 and the recoil energy of the nucleus in bar1, respectively. The recoil energy can be expressed as a constant times the incident energy because the position of bar 2 and the energy of the incident neutron beam are fixed, so E_R is a constant fraction of E_0, as shown in Eq. (4.8).

$$E_R = E_n \frac{2}{(A+1)^2}(A + sin^2\theta - cos\ \theta\sqrt{A^2 - sin^2\theta}\ ) \quad (4.8)$$

In the ideal case, the data points for the signal would be parallel to cosmic muon events in the T1 vs T2 plane, as indicated in Eq (4.7), however, there are two effects which spoil this parallelism. The incident neutrons are not mono-energetic. The time of hitting bar1 and bar2 by low energy neutrons will be delayed, as shown in the top left sub-figure of fig 4.24, roughly half of the total events have 2 or more hits in bar1. The multiple hits will decrease the energy of the neutrons scattered from bar1, and accordingly the time T_2 will become bigger. Those are the population on the left side of the red events in figure 4.29.
Therefore, our selection chooses events that have a linear relation of T1 vs. T2, but not in parallel with the muon events.

After all of the cuts have been applied, we obtain the red population as shown in figure 4.28. We then converted the timing of the events to the energy of the incident neutrons which are the data points of figure 4.3b. By applying the same cuts to Geant4 simulated data, we obtained the histogram of figure 4.3b [6].

[6] For the histogram of simulated data, a $1.5ns$ resolution has been applied to compensate the time jitter caused by electronics in the experimental data.

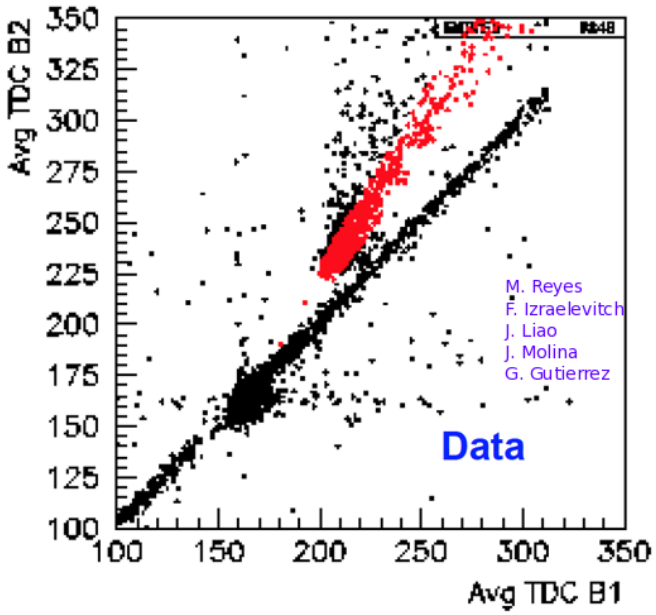

Figure 4.29: Time of bar 2 vs. bar 1 for data taken. The red popular shows the neutron events of the angular cut for "2 bars" run, 2013 beam test

4.7.4 Introduction of "QF validation" run from 2013 beam test

The setup of the "SDD + 2 bars" run of the 2013 beam test has been shown in fig 4.30. Figure 4.30a shows the setup inside of the hall of the beam test area at Notre Dame. Figure 4.30b is a diagram of the experiment implemented in the Geant4 simulation. The beam is emitted from the lower right side, travels through the 1 cm aperture at the center of the collimator, hits the SSD, and is potentially scattered into one of the two scintillating bars.

The SDD we chose was the model XR-100SDD from Amptek, Inc. Figure 4.31a shows the detector and its digital pulse processor[7]. Its main features are listed in figure 4.31b [Amptek website]. The SDD originally was designed as a photon detector. In our beam test, we used it as a neutron detector because the silicon layer of the SDD also responds to incident neutrons.

We have calibrated the energy response of the SDD in the lab with a ^{55}Fe source, as shown in figure 4.32. Although we haven't used a neutron source to calibrate the SDD due to the lack of appropriate quasi-mono-energy neutron sources in Fermilab, the consistency between the measured data in the beam test and the Geant4 simulation convinced use that the SDD and its DAQ system is reliable to respond to incident neutrons.

[7]We actually haven't used the digital pulse processor as readout, instead, we used other general preamplifier and shape electronics.

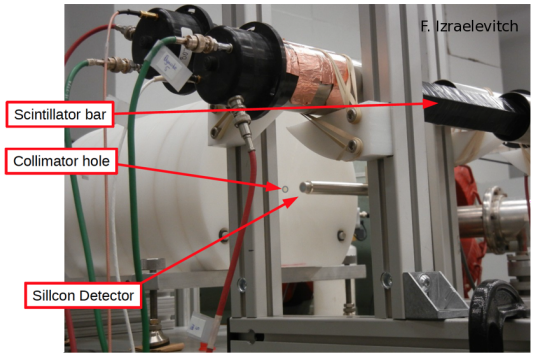

4.30a. Real setup (side view from beam downstream)

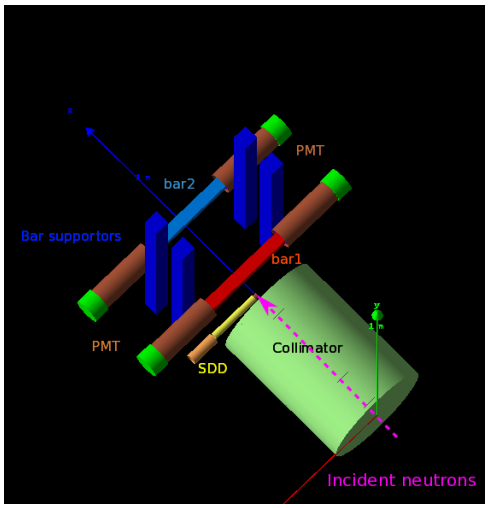

4.30b. Geant4 simulation (top view from beam upstream)

Figure 4.30: Setup of "SDD + 2 bars " run in 2013 beam test

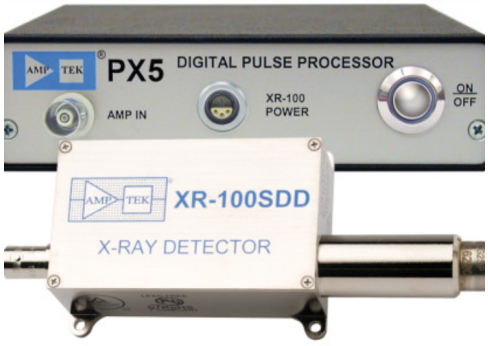

4.31a. A SDD and digital pulse processor

- 125 eV FWHM Resolution @ 5.9 keV
- High Peak-to-Background Ratio – 20,000:1
- Hight Count Rate – 500,000 CPS
- 25 mm^2 x 500 µm Silicon Drift Detector (SDD)
- 2-Stage Thermoelectric Cooler
- Temperature Monitor
- Thin Beryllium or C-Series window
- Multilayer Collimator
- Hermetic Package (TO-8)
- Wide Detection Range
- Easy to Operate

4.31b. SDD features

Figure 4.31: SDD and its features

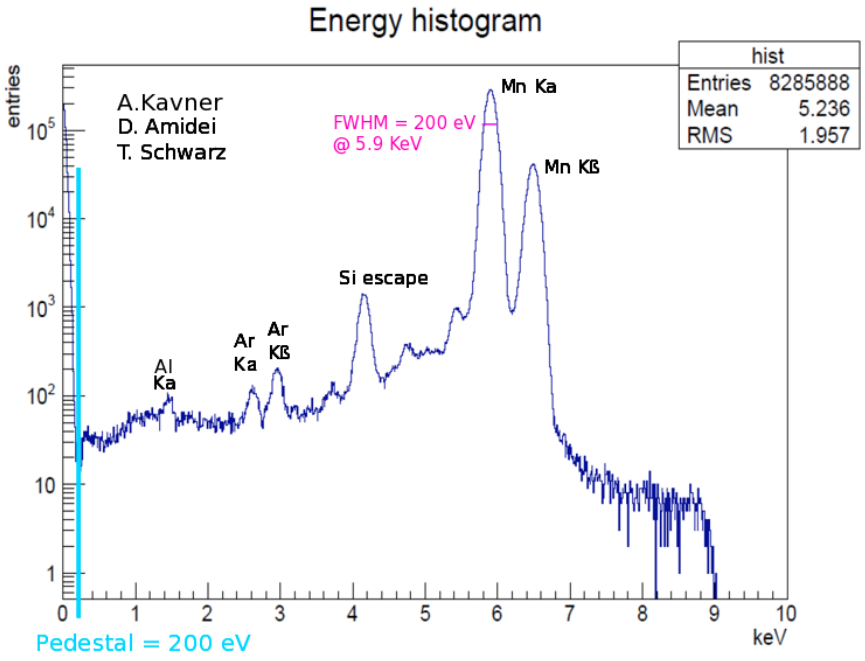

Figure 4.32: SDD calibration in Fermilab with ^{55}Fe

4.7.5 Geant4 simulation of "QF validation" run from 2013 beam test

The quality of the Geant4 simulation depends heavily on the level of the accuracy and detail of the description of the detector geometry and material.
Figure 4.33a shows the tip of the SDD in an enlarged view with both the extender and the SDD cover marked. The thick blue line is the Z-axis of Geant4 which couldn't easily be removed[8]. The size of the neutron beam is $1cm$, as the cyan broken lines indicate. A more detailed view of the SDD is shown in figure 4.33b [Amptek website] where the cover of the SDD has been removed. The very thin layer - $\phi = 2.82 \times 0.5mm$ - "detector layer" is the sensitive part of the silicon detector, which has been aligned to the center line of the $\phi = 1cm$ hole of the collimator. Other auxiliary components are also shown in the same figure.

In the simulation of this run, We have defined four sensitive detectors[9] : the collimator, the scintillator bars, the SDD detector layer and the shield of the PMTs. Because the

[8] figure 4.30b and 4.33b also show Z-axes there

[9] In Geant4, a sensitive detector means the interaction information like energy, timing etc would be recorded and traceable for users, while if a detector hasn't been defined as a sensitive detector, the interaction information will not be accessible, though the interaction will still be simulated.

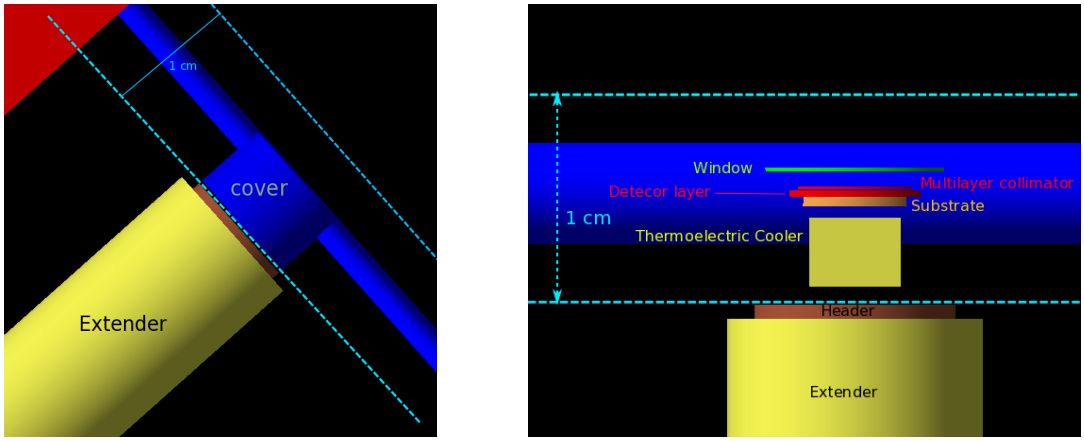

4.33a. with the cover

4.33b. the cover has been removed

Figure 4.33: Enlarged view of the SDD in beam test

material of the shields of the PMTs is Mu-metal which has a density of $8.7 g/cm^3$, we thought it might introduce non-trivial neutron scattering. It turns out the scattering caused by the shields of PMTs is not significant. The reasons are : Although the density of Mu-metal is quite high, the volume is only 20 cm^3, so the mass is only $\sim$ 170 g for each piece, and also 77% of Mu-metal is nickel, which has a cross-section of only $\sim$ 10 barns for 100-KeV neutrons[National nuclear data center].

According to the website for the SDD[Amptek website], as a photon detector, the recommended angle of incident photons for the SDD is $45 - 90°$. Although we utilize the SDD as a neutron detector, it's still meaningful to check for neutron detection whether the incident angle matters either or not. Ideally, we would put the SDD perpendicular to the incident beam direction as is shown in figure 4.33b in order to reduce the inactive material for the neutron to scatter off. However, due to the extender and the body of the SDD downstream, more backgrounds would be expected in this configuration. Also, the SDD electronics would be more exposed to the fast neutron beam during the multi-week data taking. Putting the SDD at 0 ° rather than the 45-90 ° recommended for photons would produce minimal background events and radiation damage.

The geometry of this simulation is shown in figure 4.34a and 4.34b. In figure 4.34a, the incident neutrons represented by the horizontal blue line go through the silicon layer of the SDD represented by the small ellipse at the tip of the SDD at 45°. Figure 4.34b shows the SDD perpendicular to the incident beam at three different vertical positions.

A simulation with different vertical positions is necessary to determine the effect if the silicon layer of the SDD was not aligned perfectly with the incident beam. This effect is possible since the active silicon detector layer is sealed inside the SDD and not visible to the eye. The thickness of the detector is only 0.5mm, while its placement could be off by

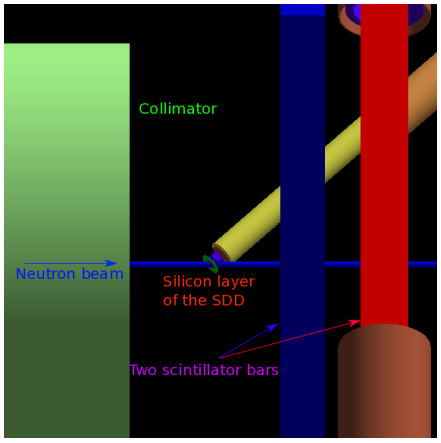

4.34a. the SDD has been put to 45° along the beam

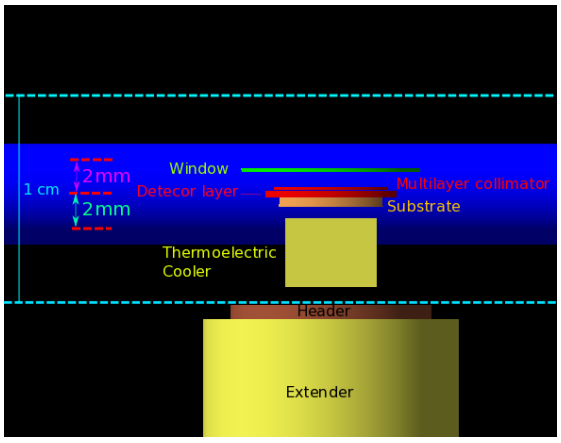

4.34b. the SDD is perpendicular to the beam but the height is different.

Figure 4.34: Simulation on the position of SDD

several mm. For the 2015 beam test, the Fermilab survey group measured the positions of the SDD to have a vertical shift of 0.4 ± 0.1 mm. To evaluate this misalignment, the simulation incorporated a shift of the detector and the SDD by ± 2 mm, as shifted from the middle of the beam. This is shown in figure 4.34b with the 3 short dashed red lines. As figure 4.34b shown, the Detector layer and the whole SDD has been set to three places : the middle of the beam, ± 2 *mm* shifted from the middle of the beam, and as the three short broken red lines show.

Figure 4.35 illustrates the effects of misalignment of the detector to the beam. The two plots show the time measured on bar 1 with and without SDD hits. The time distribution is compared for the nominal case of perfect alignment to the cases where the detector is shifted + and - 2 mm. The positive shift corresponds to the minimal exposure of the SDD, and the negative shift corresponds to the maximal exposure. For events where the SDD is hit, the timing distribution is not significantly different.

Figure 4.36 demonstrates the same simulation of alignment shifts, but for a 45° rotation of the detector, and for a selection of hits with bar 1 time greater than 10 ns in order to remove events where a signal was not recorded on bar 1. Similar conclusions can be reaches as in figure 4.35. In addition, one can see that the number of events is almost the same in these configurations as in the others. Therefore, we determined that a 45° rotation of the SDD does not improve the detection efficiency beyond the nominal orientation perpendicular to the beam. A misalignment of 2 mm does not significantly change the distribution or total number of scatters.

We also developed a simulation of the lab room, assuming 1-m thick floors, walls, and ceilings, to verify if neutron scattering reflection and random scattering would generate

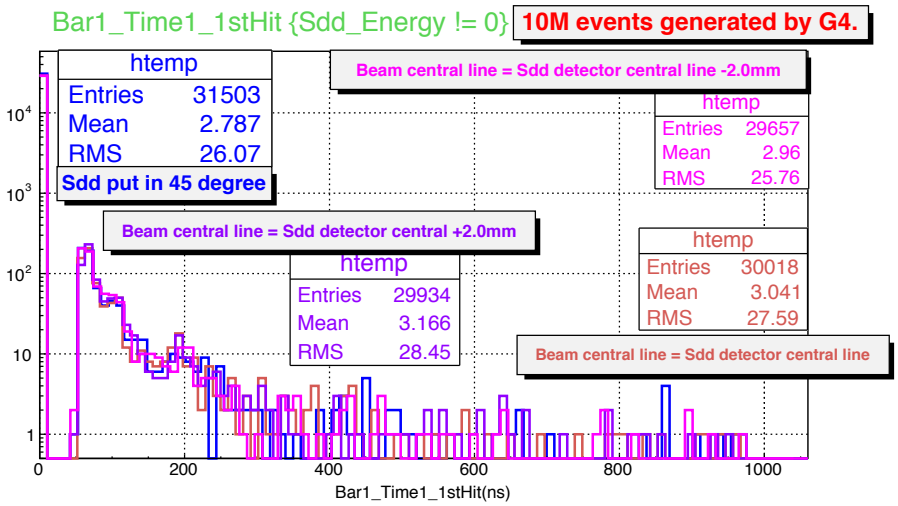

4.35a. the time with a cut of "the SDD has been hit".

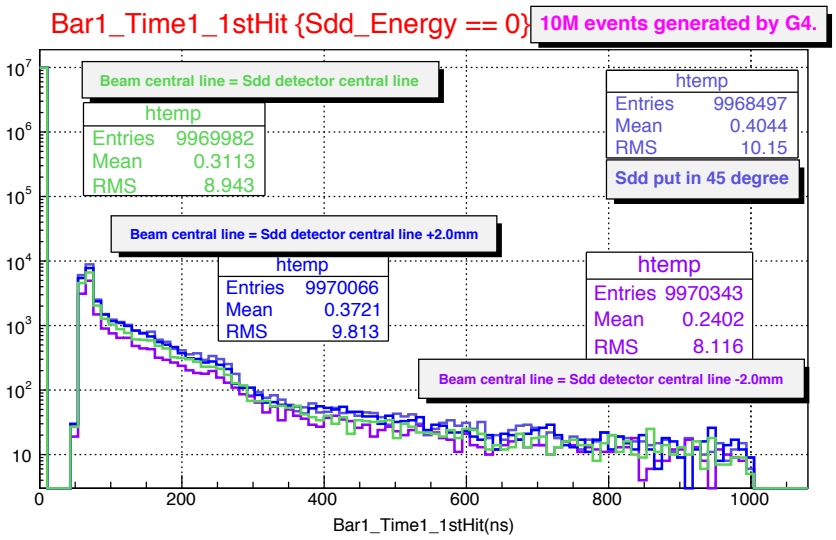

4.35b. the time with a cut of "the SDD has not been hit" .

Figure 4.35: Simulation on the time recorded in bar 1

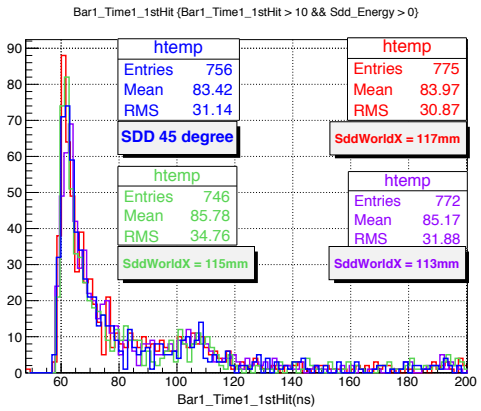

4.36a. the events with a recorded time $> 10\ ns$ time and a cut that "the SDD has been hit"

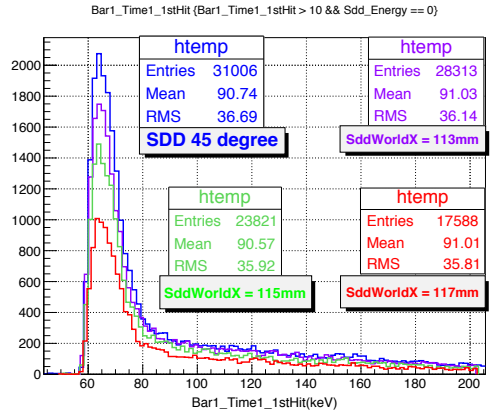

4.36b. the events with a recorded time $> 10\ ns$ time and a cut that "the SDD has not been hit"

Figure 4.36: Simulation of events with an recorded time $> 10\ ns$ in bar1

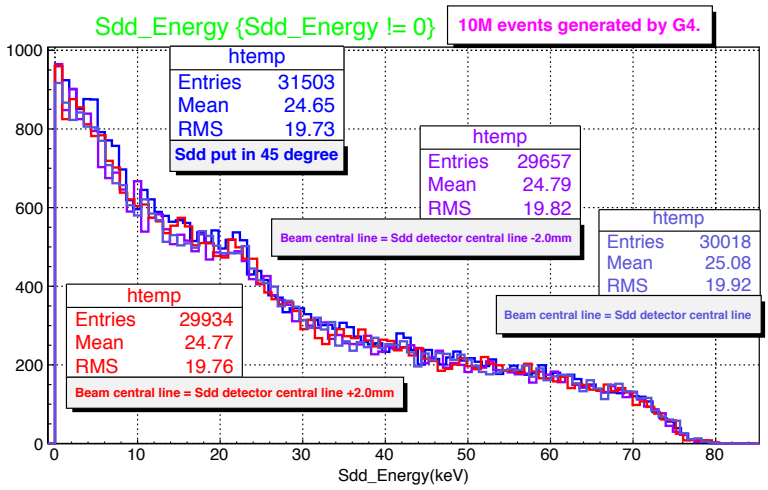

Figure 4.37: Simulation on the energy deposition under four different setups.

a significant background. Figure 4.38 shows some simulated scattering events in the lab building. Most neutrons are absorbed by the walls and it was found that the lab room provided a negligible background.

The essence of our QF test is to know the ratio of the ionized energy to the recoil energy in the SDD. In Geant4, the former can not be obtained directly because the simulated energy is the energy deposited in the SDD, which is not the same as the ionization energy. The latter could be determined from the timing of flight. Figure 4.39a shows the deposited(not ionized) energy in the SDD vs the timing measured in bar1. Figure 4.39b

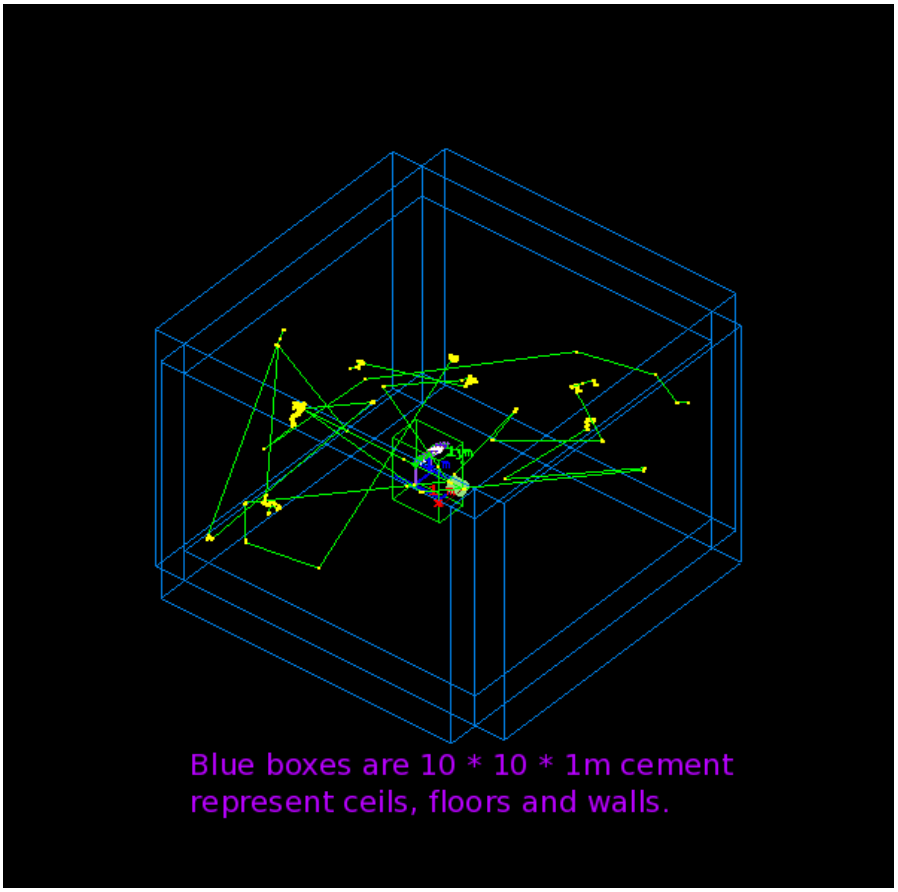

Figure 4.38: Simulation on the effect of walls, floors and celils.

shows the timing in bar2.

4.7.6 Data analysis of "QF validation" run from 2013 beam test

The energy vs. time distribution of the data sample from this run is shown in figure 4.40 as ADC vs TDC value for the two bars.
In the left sub-figure, the events in the left "column" are from prompt gammas. The time of these events has been considered as the time zero : "T_0". A typical histogram of T_0 is shown in figure 4.41. The mean value of the Gaussian fit is the value of T_0, the sigma of the fit is useful for the uncertainty analysis.

The events on the top of figure 4.40 correspond to saturated ADC values which mainly come from scattered prompt gammas. The events on the bottom come from the noise of the DAQ system. The events inside of the central box are candidate events of signal. A similar and more detailed discussion is in section 4.8.3. The right sub-figure of ADC

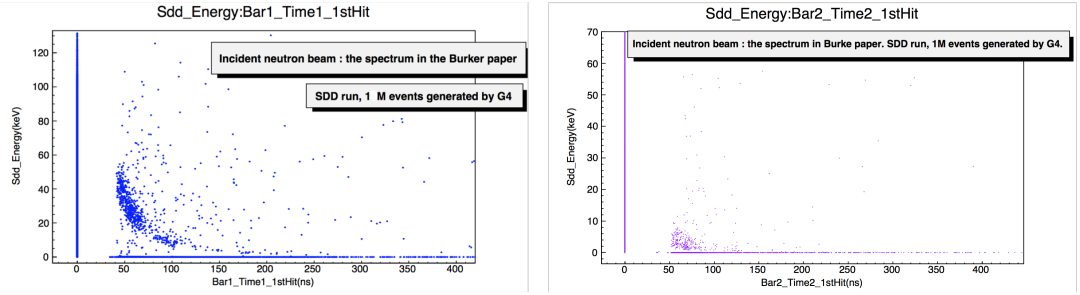

4.39a. bar1 4.39b.bar2

Figure 4.39: Energy deposited in SDD vs timing measured in two bars are determined by Geant4 simulation.

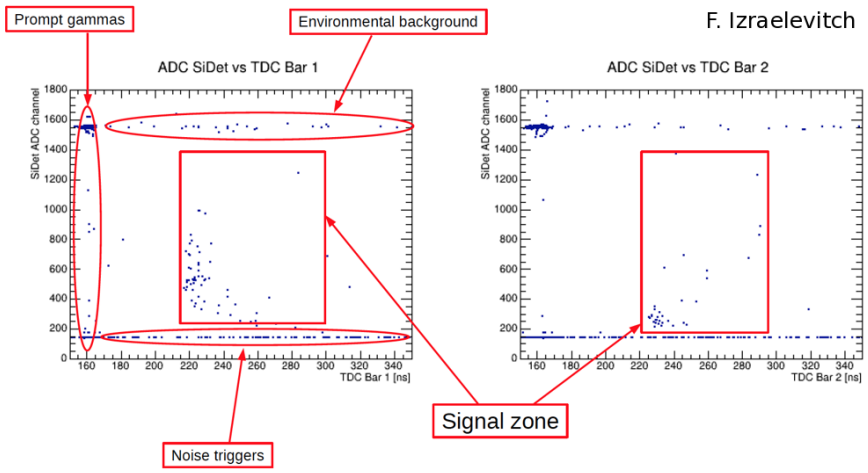

Figure 4.40: Experimental data for the run of "SDD + 2 bars" run, 2013 beam test

vs TDC for bar2 demonstrates similar features.

The comparison of experimental data and Geant4 simulation for bar 1 is shown in figure 4.42. The top two sub-figures are the ionized energy measured in the SDD vs. the time measured in the TDC. The upper left plot is for experimental data while the upper right plot is for the Geant4 simulation in which the Lindhard model has been applied to convert the recoil energy to an ionization energy to be consistent with the left upper sub-figure. The events in the signal windows are projected onto the time and energy axis in lower plots to demonstrate the agreement of simulation and data.

The results from bar 2 are shown in figure 4.43.

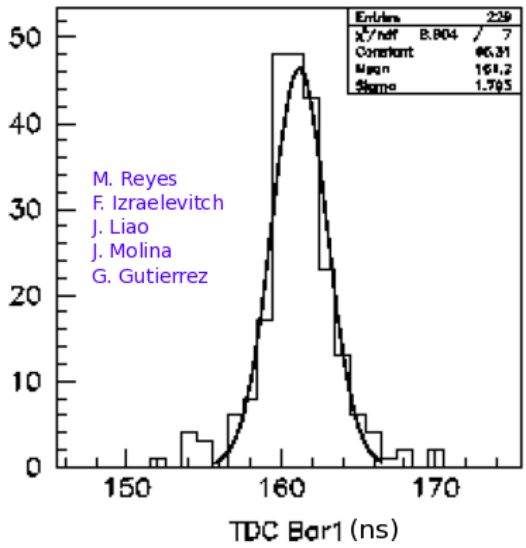

Figure 4.41: "T_0" of bar1 for the run of "SDD + 2 bars" run, 2013 beam test

The selection is based on the ToF of candidate events. The neutron ToF from the ^7Li target to the scintillator bar depends on the energy of the incident neutron and the energy transferred to the SDD. According to our simulation, most of the deposited energy in the SDD is less than 30 KeV (figure 4.53b). Since this is small compared to the peak incident neutron energy of 550 KeV (figure 4.3b), we ignore the 30 KeV deposit for the following analysis, and treat the neutron as having the same velocity along its path from the LiF target to the scintillator bar. The ToF and the incident neutron energy are then related as in Eq (4.9).

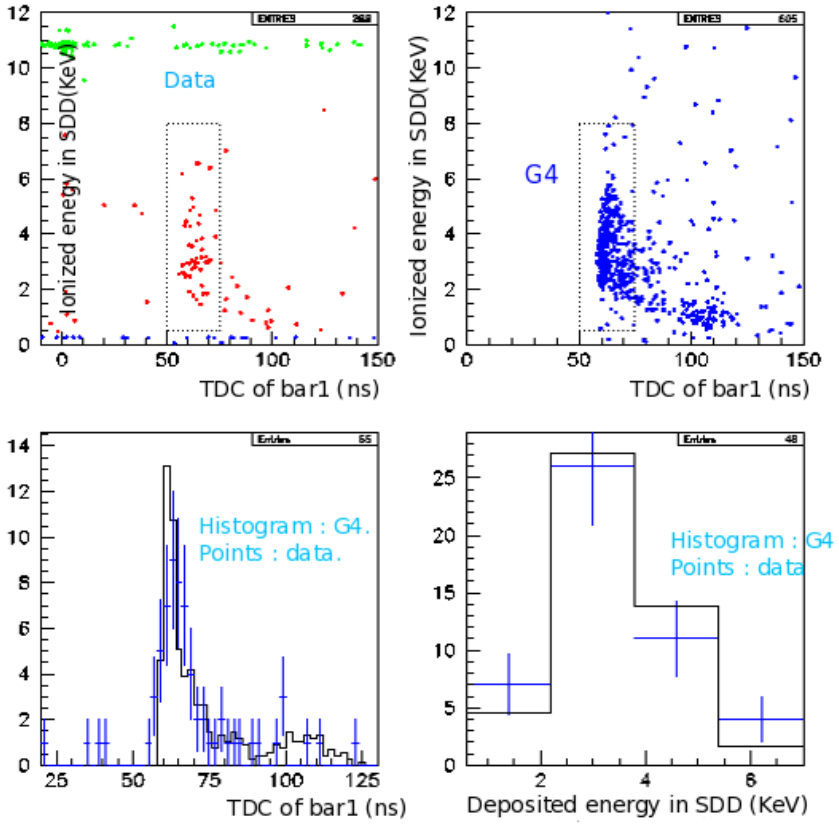

Figure 4.42: Comparison of experimental data and Geant4 simulation for bar1, "SDD + 2 bars" run, 2013 beam test.

$$
\begin{aligned}
t &= \frac{D}{V} \\
&= \frac{D}{\sqrt{\frac{2E_{in\_KeV}}{m_n}}} \\
&= \frac{D}{\sqrt{2}\cdot\sqrt{\frac{E_{in\_KeV}}{1.0GeV}}\cdot c} && (m_n \approxeq 1.0GeV) \\
&= \frac{D}{\sqrt{2}\cdot\sqrt{E_{in\_KeV}}\cdot 10^{-3}\cdot 30cm/ns} \\
& && (E_{in\_KeV} \text{ has the unit of KeV now, } c = 30cm/ns.) \\
&= \frac{1}{3\sqrt{2}\cdot 10^{-2}}\frac{D}{\sqrt{E_{in\_KeV}}} && (D \text{ has the unit of cm, t has the unit of ns}) \\
\Rightarrow \sqrt{E_{in\_KeV}} &= \frac{D}{3\sqrt{2}\cdot 10^{-2}t} \\
\Rightarrow E_{in\_KeV} &= \frac{10^4}{18}\times(\frac{D}{t})^2 && (4.9)
\end{aligned}
$$

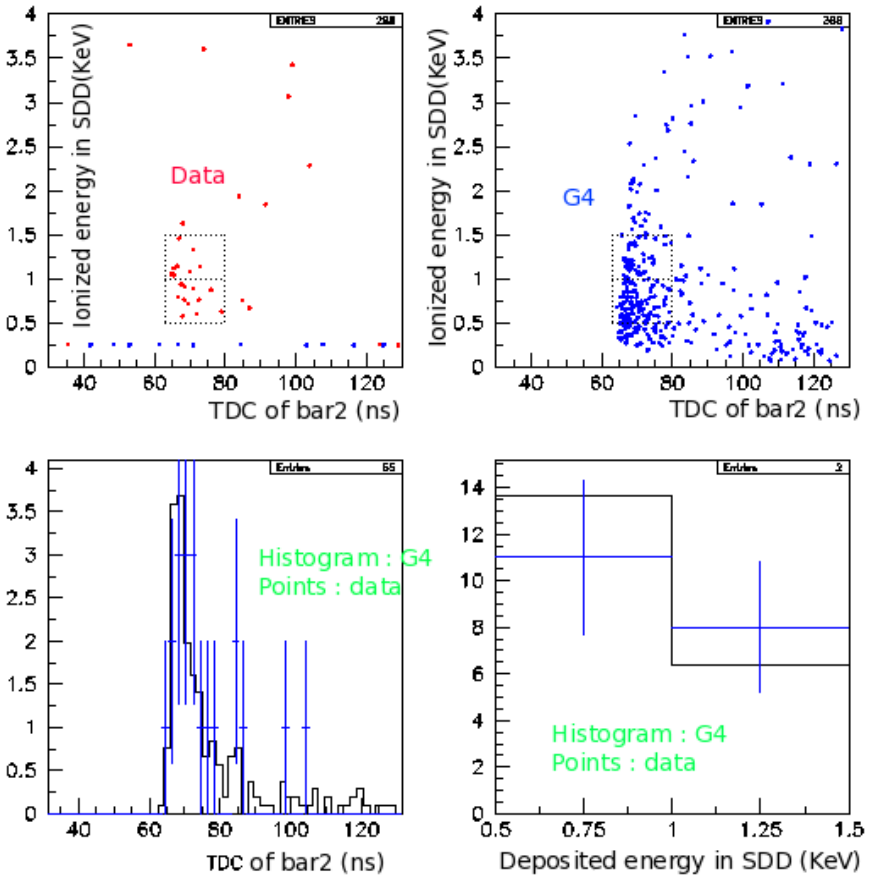

Figure 4.43: Comparison of experimental data and Geant4 simulation for bar2, "SDD + 2 bars" run, 2013 beam test.

The dimensions of the setup of "SDD + 2 bars" run of 2013 beam test are shown in figure 4.44a. From this figure, we can calculate the distance between the Li^7 target and the center of bar 1 as,

$$D_{target\_to\_bar1} = 45.3 + \sqrt{10.5^2 + 12.8^2} = 61.8\ cm.$$

Substituting $D_m = 61.8\ cm$ and the time cut from the upper right sub-figure of figure 4.42, $t_{ns} = 75\ ns$ into the equation of (4.9), we get $E_{in\_KeV} = 377.2 KeV$. Comparing this value to the energy distribution of figure 4.44b, it is clear that the time selection removes energy from the lower resonances peaked at ∼50 and ∼200 KeV.

This ToF selection cut is crucial for analyzing the 2013 data. Since there is a component of the events in the ToF window of 75 - 90 ns coming from the 200 KeV resonance (as seen in figure 4.44b), we additionally remove these events.

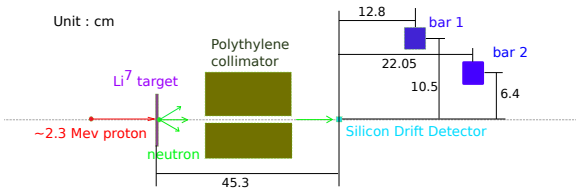

4.44a. Dimension of the setup of 2013 beam test

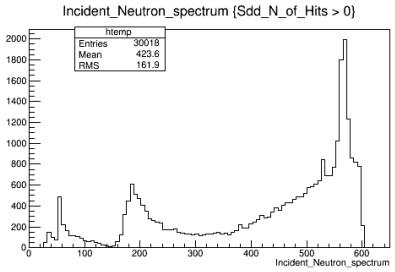

4.44b. Energy spectrum of incident neutrons in 2013 beam test[a]

[a]this plot is same as figure 4.6

Figure 4.44: 2013 detector setup and incident neutron energy spectrum.

In order to produce the upper right plot in figure 4.42, we applied the Lindhard model to convert to the simulated recoil energy, using eq. (4.10) with ϵ and $g(\epsilon)$ explained previously in equations (4.1) and (4.5).

$$QF = \frac{\kappa\ g(\epsilon)}{1 + \kappa\ g(\epsilon)} \tag{4.10}$$

For the 2013 prototype experiment, the goal of the analysis was to prove that our results are relatively consistent with the Lindhard theory for the quenching factor. Therefore, we use our data to measure κ and compare to the expected value. To do this, we hold $g(\epsilon)$ fixed according to Eq (4.1), and calculate the χ^2 distribution as a function of κ in order to determine the most likely value. Figure 4.45 (left) shows the likelihood minimization to determine κ, with the value of κ determined to be 0.152 ± 0.033. The right plot shows the functional form we derived for the QF with a red line, with $\pm 1\sigma$ constraints shown in the dashed red. It is shown to agree well with existing data from this reference [G. Gerbier et al., 1990].

Using results obtained only from bar 1, we could estimate the potential improvement in uncertainty of our upgraded 2015 experimental design, which will be explained in the next section. The 2013 data taking produced 60 good events per 8-hour data shift. In the 2015 experiment, we will use 21 bars of the same size, but at a 90-cm distance, rather than 16.3 cm. Assuming a 12-day run, we would expect a factor of increase in the dataset of :

$$Increase\ in\ data = [\ 21\ bars \cdot \frac{60\ events}{bar \cdot shift} \cdot (12\ days) \cdot \frac{3\ shifts}{day} (\frac{16.3\ cm}{90\ cm})^2\ ] \frac{1}{60\ events} \approxeq 25$$

Therefore, we would expect $\sqrt{25} = 5$ smaller uncertainties due to statistics, as well as a better energy resolution from the greater distance, and therefore, better ToF measurement, of the scintillators, as will be discussed in greater detail in the subsequent sections. Accounting for these improvements would yield an improvement in the 2015 experiment

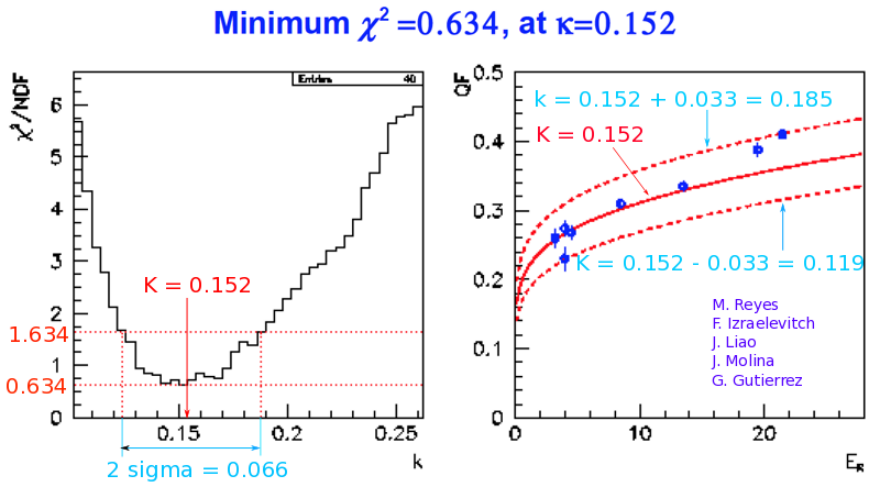

Figure 4.45: QF fit with Lindhard model.

as shown in figure 4.46 from the dashed red band to the yellow band.

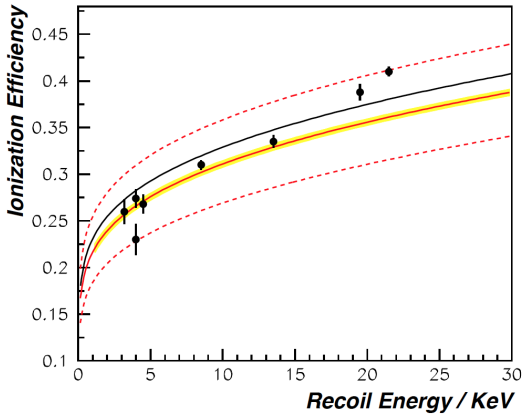

By DAMIC collaboration and G.Gutierrez

Plot of the Ionization Efficiency for silicon as a function of nuclear Recoil Energy. The black line and dots with error bars show the best measurements to date, by Gerbier et al., 1990. The solid red line shows our fit to preliminary data, from 2-20 KeV. The dashed lines display the 1 \sigma error bands. In our next run we expect these errors, for points every 1KeV, to shrink to the yellow band. The recoil energy range will cover from 1-30 KeV.

Figure 4.46: Results of 2013 beam test and the estimated results of 2015 beam test.

4.7.7 Summary of contributions from simulation to the 2013 QF experiment

The simulation used for the 2013 QF experiment was instrumental in several ways.
(1) It allowed us to interpret events below the threshold for producing scintillation light, as shown in figure 4.26 and 4.27.
(2) It improved our understanding of the neutron resonances in the silicon detector as shown in figure 4.6 shown.
(3) It helped us determine timing selection criteria for our signal window, allowing us to reject events in the 75 - 90 ns range which originate from the 200 KeV silicon-neutron resonance, and understand the efficiency for this selection in terms of events with the energy of incident neutrons below 377 KeV.
4), It allowed us to convert between ionization energy and deposited energy in the SDD as is shown in figure 4.42.
5), It allowed us to verify that the incident neutron energy spectrum and experimental setup was correctly understood.
6), It helped us to understand the effect of the collimator on the energy spectrum and beam size.

4.8 2015 QF measurement

4.8.1 Introduction to the 2015 QF beam test

Being inspired by the results from the 2013 beam test, DAMIC launched a second, improved experimental measurement of the QF in February, 2015[10].
The actual setup from the 2015 experiment is shown in figure 4.47a. Figure 4.47b depicts the Geant4 simulation used for the analysis. Neutrons are incident on the back side of the collimator, traverse the collimator and hit the SDD. Scattered neutrons are detected by the array of scintillator bars.

The detector array consists of 21 bars[11] distributed into an inner and outer layer. According to the design, the radial distance from the tip of the SDD to the center of each of the bars is 90 cm for the inner layer and 97.5 cm for the outer layer. Using the tip of the SDD as the origin, the angular distance between neighboring bars in the same layer is 5.5°, and 2.75 degrees for neighboring bars in different layers. Assuming the direction of the incident neutron beam is at 0 °, the lowest bar of the inner layer (outer layer) is at an angle of 15.0° (17.75°), while for the highest bar it is at an angle of 70° (67.25 °).

In practice, however, the location of each component of the experimental apparatus needed to be determined after installation. The Fermilab survey group measured the actual locations of the LiF target, corners and holes of the collimator, tip of the SDD, and both edges of each of the 21 scintillating bars using a 3D optical alignment system to a precision of 0.1 mm.

[10] when a heavy snowstorm invaded Notre Dame, IN and the temperature was below −20°C, driving between Chicago and Notre Dame in such weather absolutely wasn't a good experience. A salute to all of the people who joined in the 2015 beam test, ☺.

[11] The astute observed may notice that there are 22 bars, rather than 21, in figure 4.47b. This is because one of the bars did not function properly during data taking.

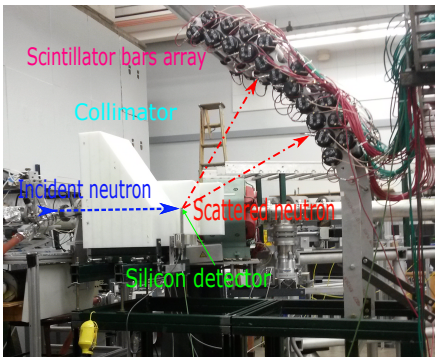

4.47a. The real setup at Notre Dame

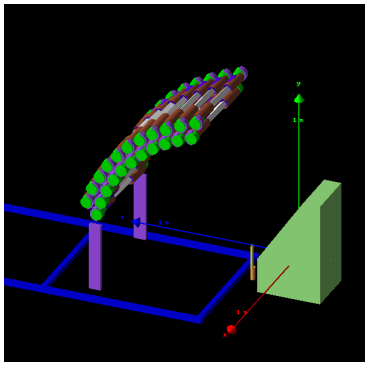

4.47b. Geant4 simulation

Figure 4.47: The QF experiment setup of 2015 QF measurement

Based on the surveyed coordinates, we then modified the corresponding ones in the experimental simulation. Figure 4.48 shows the actual locations of the scintillating bars, with a white rectangle indicating their orientation. Clearly, some of the bars had been rotated significantly as compared with their ideal positions.

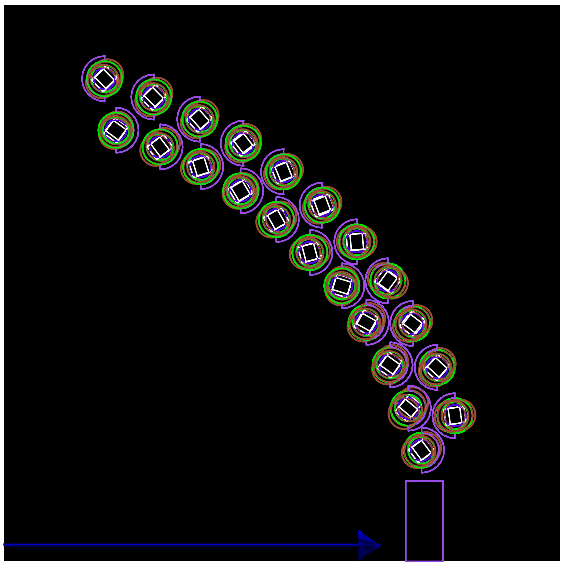

Figure 4.48: Actual geometry of the detector array determined from optical survey in a side view.

The improvements to the scintillator array in the 2015 experiment with respect to the "2 bars" prototype from the 2013 run are an expansion of the energy range of measurable recoil energy from 1.6-8.9 KeV to 1.3-25.3 KeV, and an improvement in the energy resolution of the E_R measurement.

The recoil energy can be calculated by Eq.(4.8). For a detailed derivation, please refer to Appendix A.4.

As shown in figure 4.44a, for the 2013 prototype run, the angle of θ for bar 2 is $arctan(6.4/22.05) = 16.2°$, for bar 1 is $arctan(10.5/12.8) = 39.4°$. Assuming $E_n = 550\ KeV$, substituting $\theta = 16.2°$ and $\theta = 39.4°$ into Eq.(4.8) separately, the recoil energies are 1.6 and 8.9 KeV.

For the 2015 QF experiment, substituting the angle of the lowest bar $\theta = 15.0°$ and the energy of incident neutrons of $E_n = 550KeV$ into Eq.(4.8), one gets $E_R \approxeq 1.3KeV$. Similarly, for the highest bar $\theta = 70.0°$ and $E_n = 550KeV$, $E_R = 25.2KeV$.

DAMIC is optimized for searching for low mass WIMPs, typically of order 5 GeV, as motivated by ADM models, for example. A 5 GeV WIMP has a kinematic energy of about $1/2 * 5GeV/c^2 * (10^{-3}c)^2 = 2.5KeV$. Through elastic scattering in a silicon detector, the maximum recoil energy of a silicon nuclei is roughly $0.51 * 2.5KeV = 1.25KeV$, where 0.51 is obtained by substituting A = 28 (atomic number of silicon) and theta=180 ° into Eq.(4.8). Therefore, the setup of the 2015 experiment with bars at 15° is optimal for the QF measurement of 5 GeV WIMPs.

It is clear that the smaller the angle with respect to the silicon target, the lower the recoil energy and the lower the DM mass can be probed. For instance, decreasing the angle of the first bar down to 13 and 10 deg, would theoretically allow us to measure nuclear recoils down to 1 and 0.6 KeV, respectively. However, practically, we are unable to measure such recoils since our SDD silicon detector is not capable of measuring energy well below 0.3 KeV as can be seen in figure 4.32. This 0.3 KeV ionization energy corresponds roughly to a 1.2 KeV recoil energy (according to the Lindhard model). Therefore, due to the limitations of the SDD, there is no gain for putting the scintillator detectors closer to the beam axis. Below 1 KeV, other techniques for calibration are considered, such as described in Section 4.9.

Increasing the distance of the scintillators from the silicon target decreases the solid angle of coverage of each bar, which has the the effect of improving the energy resolution. In the 2013 run, the distance between the SDD and the bars was ∼20 cm, compared to 94 cm for the 2015 run. This decreases the solid angle coverage from 8.6 ° to 1.8 °, as is depicted in figure 4.49. From Eq.(4.8), one can obtain δE_R as a function of $\delta\theta$.

$$
\begin{aligned}
E_R &= E_n \frac{2}{(A+1)^2}(A + sin^2\theta - cos\ \theta\sqrt{A^2 - sin^2\theta}\ ) \\
E_R &= E_n \frac{2}{(A+1)^2}(A - cos\ \theta A) && (sin^2\theta \lll A = 28) \\
E_R &= \frac{2E_n}{(A+1)}(1 - cos\ \theta) && (\ A + 1 \approxeq A = 28) \\
\Rightarrow \delta E_R &= \frac{2E_n}{(A+1)} sin\theta\ \delta\theta && (4.11)
\end{aligned}
$$

From Eq.(4.11), it is clear that smaller $\delta\theta$ provides smaller δE_R. For a bar in the same place (same sinθ), the energy resolution would be (8.6 ∘ / 1.8 ∘) ≈ 5 times better.
The disadvantage of moving the detector array to a larger distance is the decrease in the event rate, which goes like $1/r^2$, so that the event rate decreases to just $\sim (20/94)^2 =$

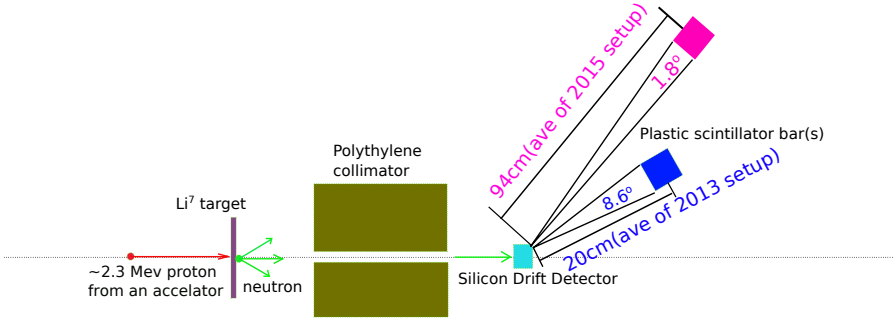

Figure 4.49: Different angles and radiuses for a bar in 2013 and 2015 beam test.

4.5^{-2}. By increasing the number of bars from 2 to 21, we gain back a factor of ∼10 in overall event rate, however. In total, the event rate is about 50% lower for the 2015 experiment than for the 2013 experiment, but this disadvantage is compensated for by the improved energy resolution.
The logic drawing of the DAQ for 2015 beam test is shown in figure 4.50. The signals of the two PMTs are connected to two "NIM edge discriminators" to obtain their timing. The two times and the "accelerator beam pulse" pulsed(logically) to be the open gate signal of the "CAMAC multihit TDC". The TDC and the "CAMAC waveform 40MHz digitizer" are both triggered by the timing of the SDD by connecting to the "NIM edge discriminator" affiliated to the SDD. The TDC and waveform are also connected to the "CAMAC controller USB board" by which data has been uploaded to a PC. The bottle neck of the DAQ was the "CAMAC controller USB board".

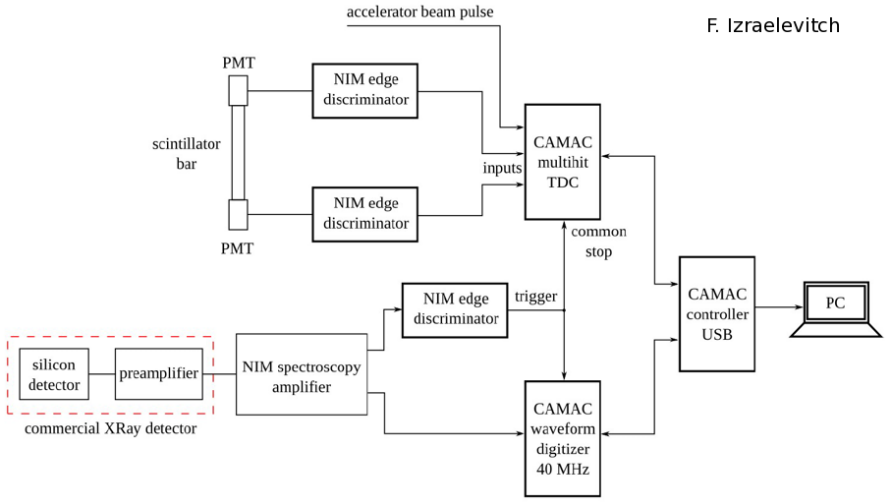

Figure 4.50: The logic drawing DAQ of 2015 beam test.

Figure 4.51 shows the timing flow of the 2015 beam test. On this plot, we consider the time-zero as the moment protons hit the LiF target. After around 4 ns which includes

trigger delay [12] , the prompt gammas hit the SDD. For a $\sim 600\ KeV$ neutron in the air, its speed is $1cm/ns$[13], so around 140 ns later, the 600 KeV neutrons will hit the SDD. The neutron beam has a spill every 1 μs.

Figures 4.50 and 4.51 are helpful for estimating the background events expected in the 2015 experiment caused by cosmic muons. In this approximation, we took the distance of the bars to be 94 cm as above; we considered the smallest angle for the array is 15°, the biggest angle was 70°, and the length of bar was 25 cm. So, looking from the top of the scintillator array, the area would be,

$$\begin{aligned} S &= 94cm \times (cos\ 15^\circ - cos\ 70^\circ) \times 25cm \\ &= 1466cm^2 \end{aligned}$$

Considering the event rate of cosmic muons on the sea level is 1 event $cm^{-2}\ min^{-1}$ [K.A.Olive et al.], the event rate of the scintillator array caused by cosmic muons is

$$\begin{aligned} Event\_rate &= 1\ cm^{-2}\ min^{-1} \times 1466cm^2 \\ &\approxeq 24s^{-1} \\ &= 2.4 \times 10^{-5}(\mu s)^{-1} \end{aligned}$$

Figure 4.50 indicates the logic for triggering an event. An event is recorded only if there is an accelerator beam pulse, two signals from the PMTs, and a signal from the silicon detector. It is possible that a cosmic muon could trigger a hit on a scintillator bar in conjunction with a beam pulse and SDD hit. Figure 4.51 indicates the time sequence of each spill of the accelerator beam pulse. The time interval between successive pulses is 1 μ s, which corresponds to a 2.4×10^-5 probability of a muon coincidence. Taking into account the 20 ns timing selection window for candidate events, the probability of a muon coincidence is 5×10^{-7}, and is negligible.

4.8.2 Geant4 simulation of 2015 beam test

Figure 4.52 depicts 100 incident neutron events input into the Geant4 simulation. Neutrons are incident on the collimator, traverse the 1 cm aperture, passing through the SDD. Several neutrons are scattered into the scintillator bars as indicated by the green lines. Yellow points indicate interactions.

[12] In the 2015 experiment, the distance between the Li^7 target and the inner scintillator bars is 510.8 mm which is equivalent to 1.7 ns for the traversal time of the gamma.

[13] $v = \sqrt{2E/m_n}$, substituting $E = 600\ KeV, m_n = 1GeV/c^2$ and c the speed of light, one gets $v \approxeq 1cm/ns$.

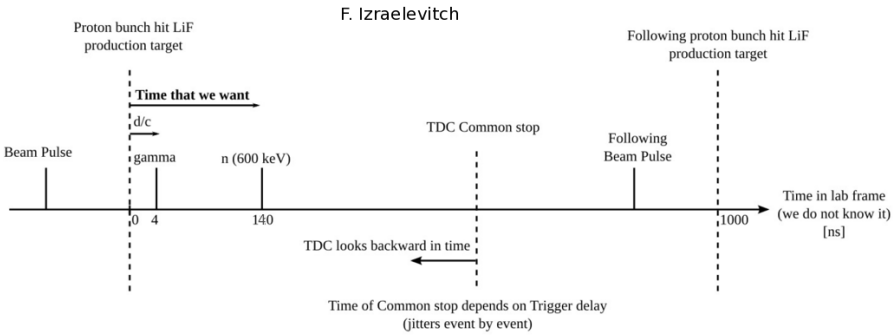

Figure 4.51: The time sequence of the 2015 beam test.

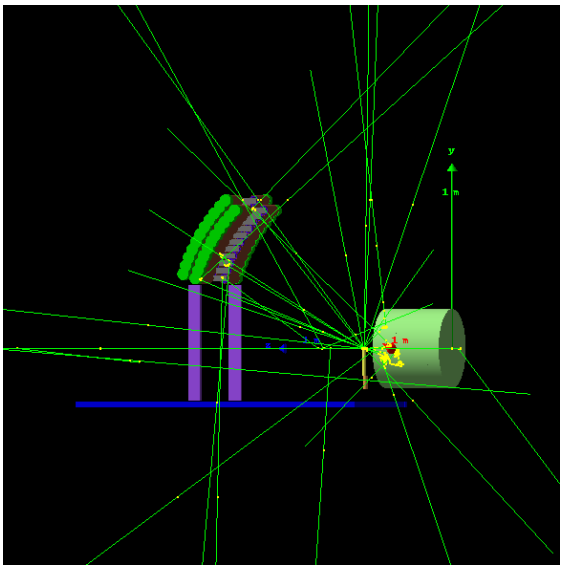

Figure 4.52: 100 incident neutron events of the 2015 beam test.

In the Geant4 simulation, the number of hits, energy, and timing of interactions are recorded in the collimator, SDD, and all 22 scintillator bars.

Figure 4.53a shows the deposited energy in the SDD vs. the timing in all of the 22 bars. Figure 4.53b is the deposited energy spectrum of the SDD from which one can estimate the simulated detection efficiency of the whole detector array which is approximiately $24355/10\ M = 0.24\%$.

For different intervals of deposited energy in the SDD, figure 4.54 show the hit positions. In these figures, the X-axis is along the length of the bar; the Y-axis is the height of bars relative to the horizontal plane of the beam. Clearly, the hit positions on the X axis are almost uniformly distributed among the whole length of the bar, 25 cm.

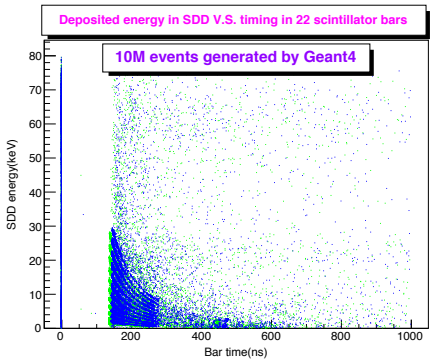

4.53a. SDD deposited energy vs. time in scintillator bar

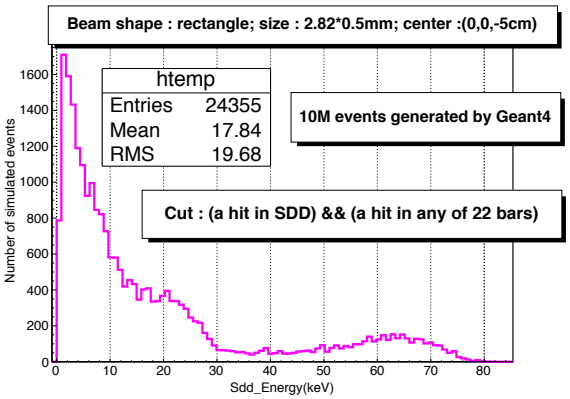

4.53b. Deposited energy in SDD

Figure 4.53: Simulation of the deposited energy and time measurement in the 2015 QF experiment

The Z-axis is the direction of the incident beam. The Z-coordinate of the hit position on a bar refers to the depth of the interaction it is. The distribution of the Z-coordinates of interactions for a random selected bar is shown in figure 4.55a. The "hit depth" is a little bit "biased" in the sense that the most likely depth is not the center of the bar, 1.5 cm, but at a depth of 1.0 cm.
Figure 4.53a shows that the uncertainty on the Z-coordinate is 1.0 cm. Figure 4.53b shows the energy deposited in the SDD which is typically less than 20 KeV. Assuming the kinematic energy of the incident neutron is 550 KeV, it would have a typical energy of at least 500 KeV after scattering from the SDD. For a neutron with $E_{kin} = 500$ KeV, v = 1 cm/ns, so that the 1 cm uncertainty translates to a timing uncertainty of 1 ns.

From the time measurement of the hit on each bar, the recoil energy can be determined as in the previous sections. Using a selection that the energy deposited on the SDD is greater than 0, the number of hits in the bar is greater than 0, and the incident energy greater than 350 KeV, we can plot the recoil energy as in Figure 4.56. The 350 KeV cut is motivated by the 2013 data run, and improves the quality of the Gaussian fit.

4.8.3 Data analysis of the 2015 QF measurement

The 2015 data run lasted 10 days in February 2015. The data analysis follows in the same way as the procedure established from the 2013 experiment. Figure 4.57 shows the raw data of the ionization energy measured in the SDD vs. the ToF of the events. Signal candidates are contained in the blue contour. Events in the vertical red box are from prompt gamma and are used to define ToF = 0. Events in the time window from 50 to 400 ns are expected to be neutrons events. The events in the red horizontal box on

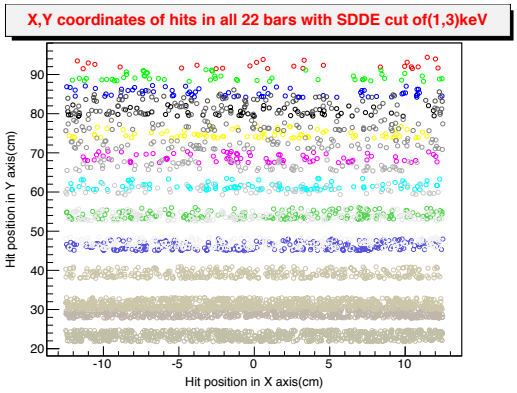

4.54a. Energy selection interval is [1,3]KeV

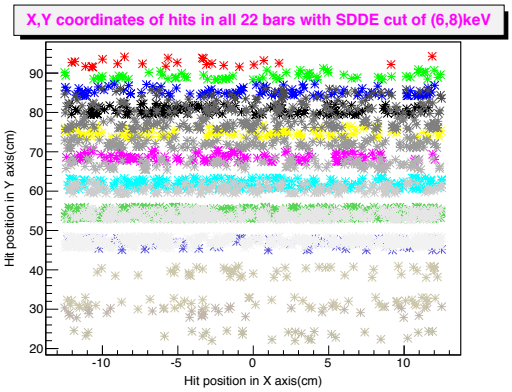

4.54b. Energy selection interval is [6,8]KeV

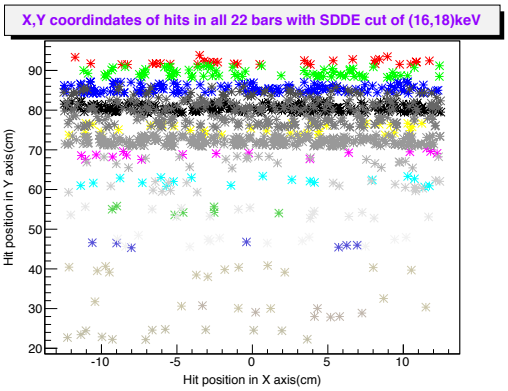

4.54c. Energy selection interval is [16, 18]KeV

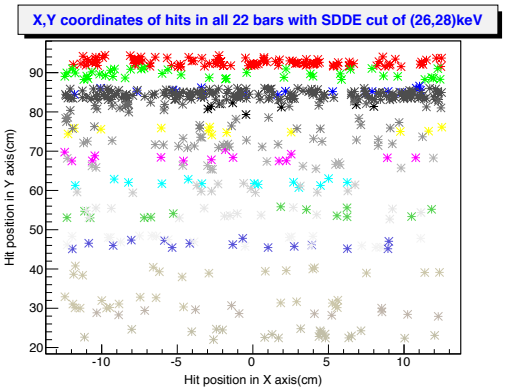

4.54d. Energy selection interval is [26, 28]KeV

Figure 4.54: Hit positions on bars under a different selection of SDD energies

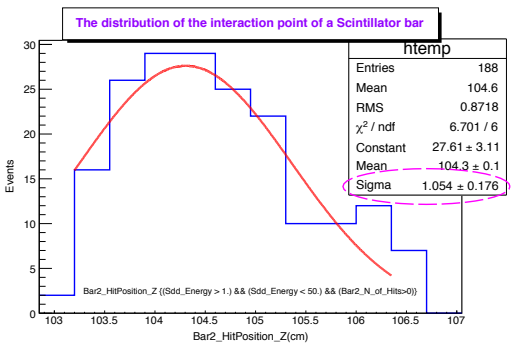

4.55a. The Z-coordinates of hit positions

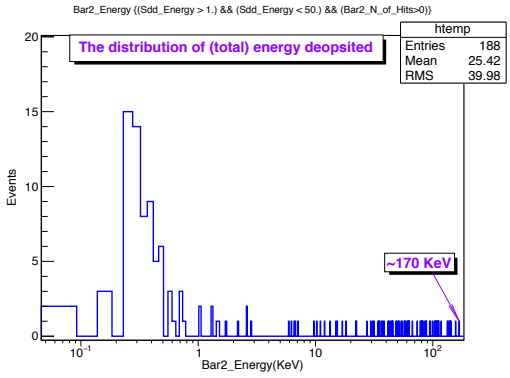

4.55b. deposited energies

Figure 4.55: Simulation of the z-coordinates of hit positions and deposited energies for a randomly selected bar in 2015 beam test

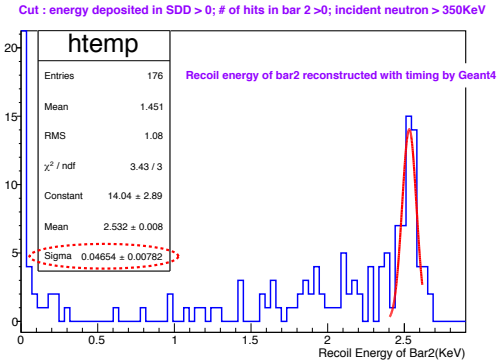

Figure 4.56: Simulation of the recoil energy determined from timing of the scintillator bar.

the top are from saturated ADC counts from environmental sources, such as scattered gammas.

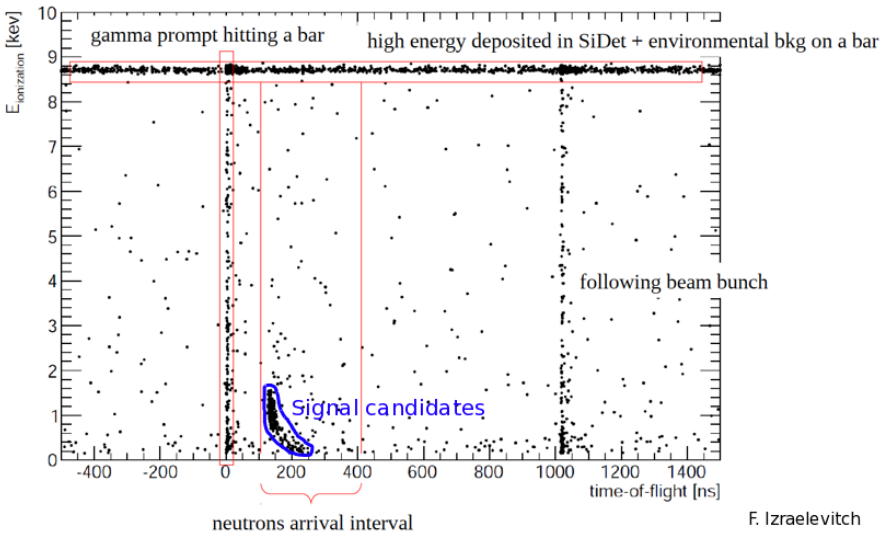

Figure 4.57: Ionization energy vs. time of flight data for the 2015 QF experiment.

After selection requirements to suppress SDD noise, requiring hits on one of the scintillator bars, and implementing the contoured selection on ToF and ionization energy shown in Figure 4.57, there are a total of 5,000 events remaining for analysis.

Using the equation from figure 4.4, the ToF can be converted to a recoil energy, as shown in figure 4.58a. The recoil energies in each of the vertical ionization energy ranges are fit, and shown in figure 4.58b as black dots. An example of a fit to one of these energy ranges is shown in figure 4.59.

From the ionization and recoil energies, the ratio determines the QF. Preliminary results of the QF are shown in figure 4.60. The dominant systematic uncertainties are the non-mono-energy incident neutron beam as explained in section 4.6.2. It can be seen that our data, while consistent with Lindhard theory and[G. Gerbier et al., 1990] at high energies, begins to deviate from the Lindhard model below 5 KeV. This would mean that the low-energy nuclear recoils expected from low-mass dark matter collisions would be even harder to measure than previously thought. These Antonella results have significant implications for the DM community, and the conclusion of these results clearly needs some independent verification.

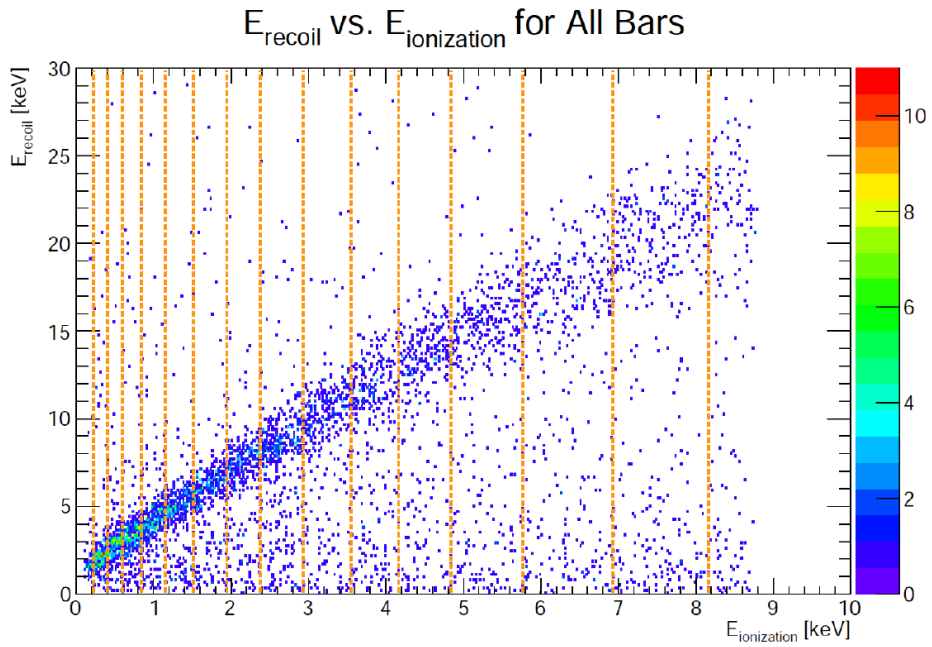

4.58a. Each interval represents a recoil energy data group

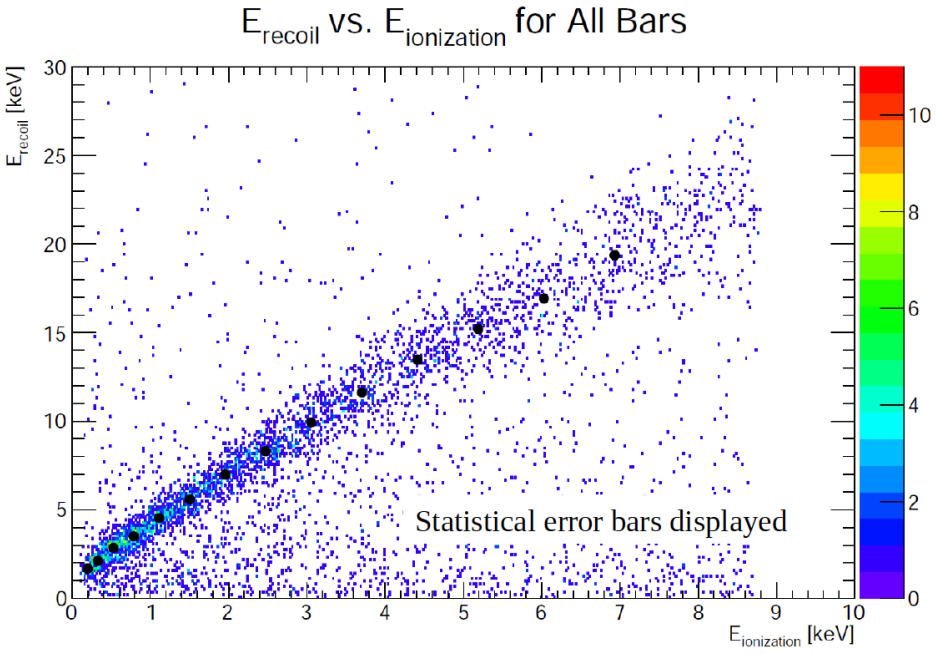

4.58b. Each recoil energy is represented by a point.

Figure 4.58: Ionization energy vs. recoil energy of all scintillator bars from data of the 2015 QF experiment

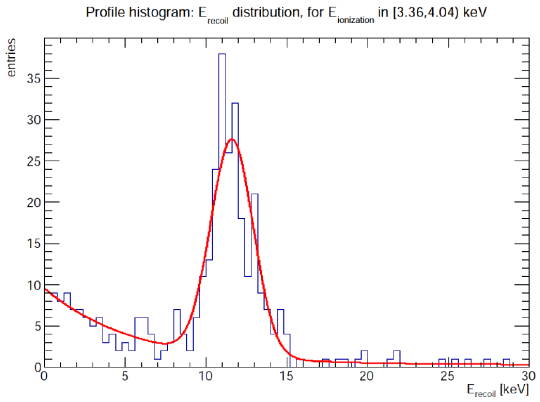

Figure 4.59: The distribution and fit of an ionization energy interval from the 2015 QF experiment.

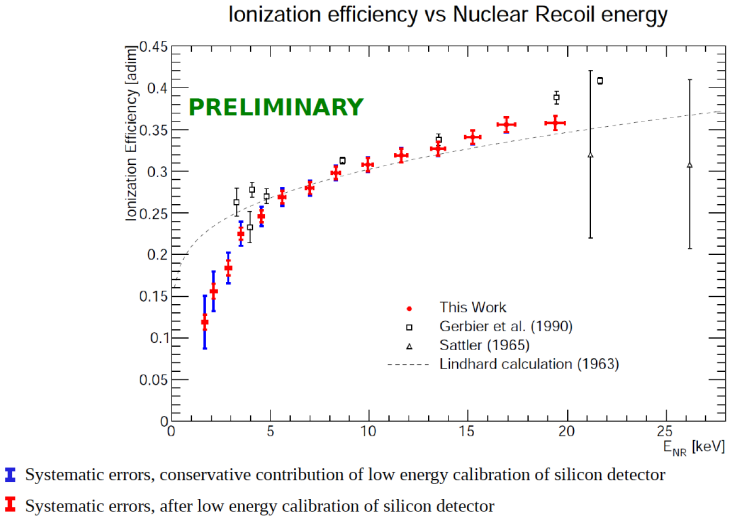

Figure 4.60: Preliminary results on the QF measured by the 2015 QF experiment at Notre Dame.

4.9 QF measurement at U Chicago

A verification of our QF measurement, as well as an extension to lower energies, was conducted by an independent group of some of our collaborators from the DAMIC experiment. I did not have a contribution to this measurement, but the result serves as a complementary cross-check of our Antonella experiment, and the results have been combined, so I present a summary here.

To produce lower energy neutrons, in order to explore the QF of lower energy dark matter particles, one can use photoneutron production as in the reaction $^{9}Be + gamma \rightarrow ^{8} Be +$

n. Using 2 MeV gammas emitted from a ^{124} Sb source results in neutrons produced with an energy of 26 KeV[R.J. Holmes]. The experimental setup is described in figure 4.61. The right upper plot is a schematic drawing of the setup, the right lower one is the real setup, the left lower one is the simulated recoil spectrum.

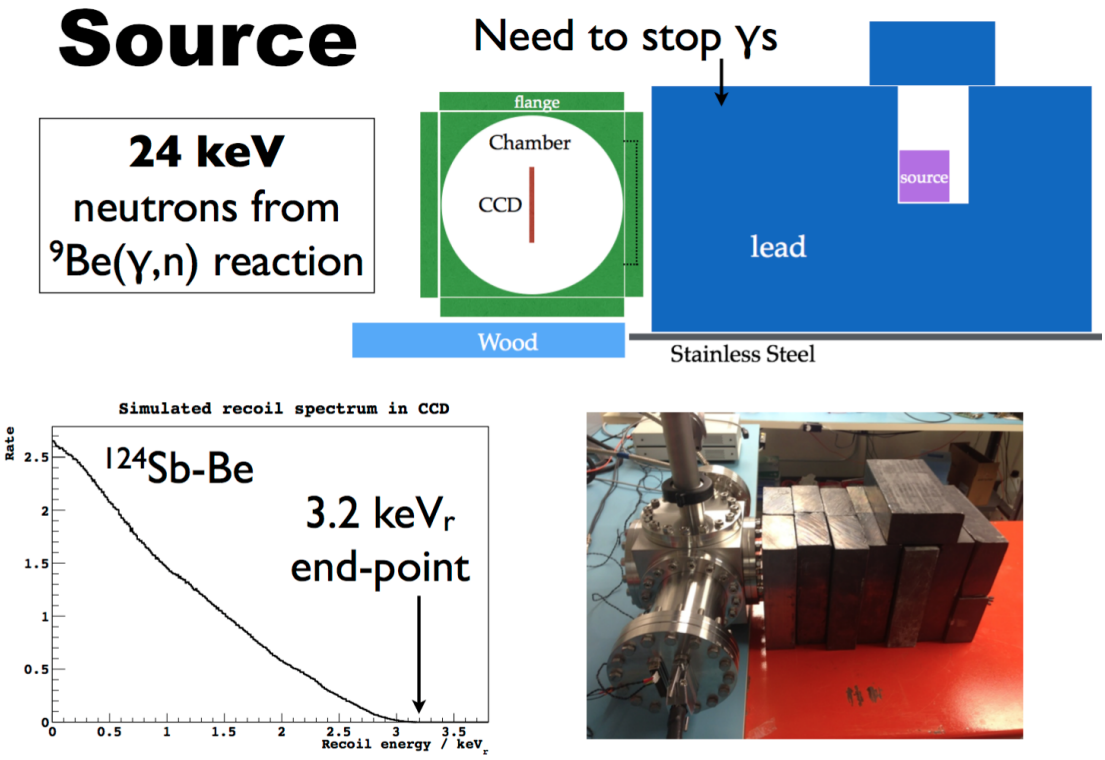

Figure 4.61: Setup of QF measurement by U Chicago group.

As was mentioned in section 4.8.1, measuring the ionization energy produced from recoils below 1.2 KeV cannot be done with a SDD with a threshold of 300 eV. Therefore, this experiment relies on using an actual CCD to measure the ionization energies. The CCD has the disadvantage that timing cannot be used to determine the energies of the neutrons, but rather an analysis of the event spectrum must be compared to simulation in order to determine the energy spectrum.

In this experiment, the ionization energy is measured in the CCD for multiple configurations of shielding. By obtaining agreement between the data and the simulation for each one of these configurations, the quenching factor could be constrained with minimal systematic uncertainty from the simulation model. Figure 4.62a shows different experimental setups for the shielding, and the energy spectra measured for each configuration in data. It also shows the simulation of each spectrum in terms of nuclear recoil energy. Using the ionization data and nuclear recoil simulations, the QF could be determined as

in figure 4.62b for the energy range 0.7 to 2.0 KeV. The results from both our Antonella measurement and this Chicago measurement are combined into Figure 4.63. The new result is consistent with that of Antonella and extends the QF measurement from 2 KeV down to 700 eV, into the full region of interest for the DAMIC experiment.

4.10 Summary of quenching factor measurements

The two neutron beam experiments known as Antonella done in 2013 and 2015 at Notre Dame allowed us to measure the quenching factor of the ratio of ionization energy to recoil energy for neutrons scattering from silicon nuclei for the energy range between 2 and 20 KeV (figure 4.60). Simulations of these experiments was instrumental in the analysis and optimization of the setup, as well as careful characterization of the detector and electronics. The detector and analysis techniques and sensitivity established in the 2013 run with two scintillator bar were utilized in the 2015 data run with an increased data set and decreased uncertainties.

Our results validate the previous results determined by[G. Gerbier et al., 1990], and extend the QF measurements from 4 KeV down to 2 KeV, improving the QF for a recoil energy range useful for low mass dark matter searches in DAMIC. While our results are consistent with the Lindhard model for energies above 5 KeV, there is a significant departure below about 5 KeV, indicating that the Lindhard approximation is not appropriate for this energy range. Our data indicate that the ionization efficiency is significantly lower than the Lindhard model below a certain value of nuclear recoil energy. It is probable that each detector material will have a departure from Lindhard model below some energy threshold. Since the Lindhard model is the standard model used by dark matter experiments, this discrepancy could lead to significantly overestimated sensitivities for the measurement of low mass dark matter candidates.
The Chicago QF measurement, using gamma-produced neutrons in the KeV range, is consistent with our Notre Dame beam experiment and extends the QF measurement down to lower energies (figure 4.63). Our DAMIC experiment will in the future plan to use a combination of these two independent and complementary sets of measurements in place of the Lindhard model. Experiments with very low energy thresholds for ionization energy like DAMIC become even more important than previously thought for identifying low mass dark matter candidates.

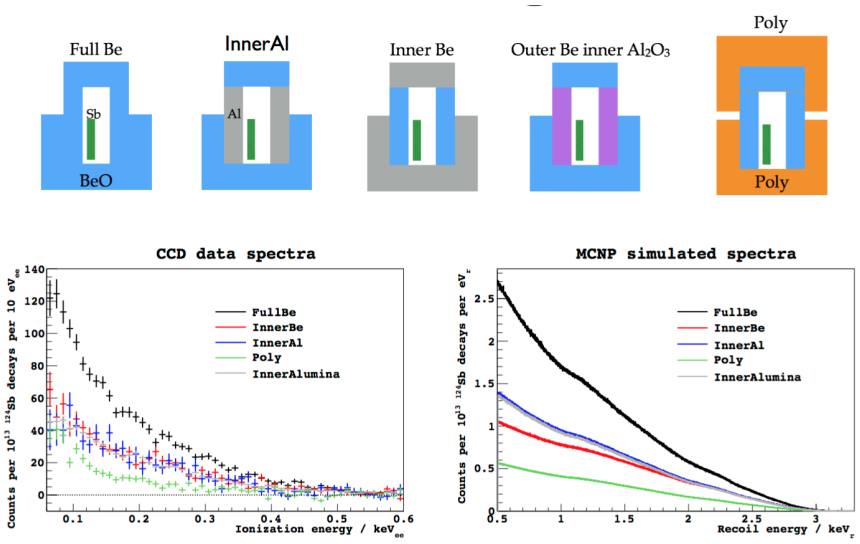

4.62a. Five different setups and corresponding measured ionization energy and simulated recoil energy

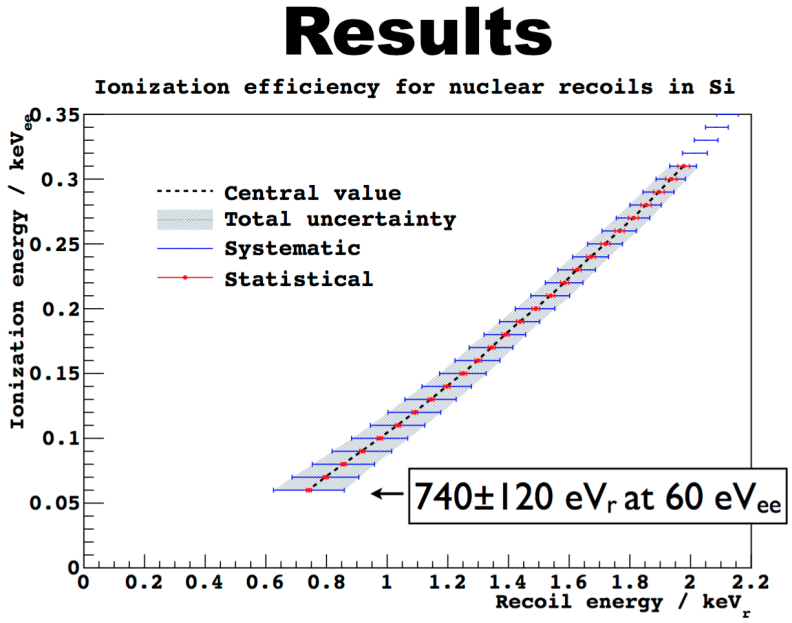

4.62b. QF results.

Figure 4.62: QF results of ionization efficiency as a function of recoil energy from the Chicago experiment

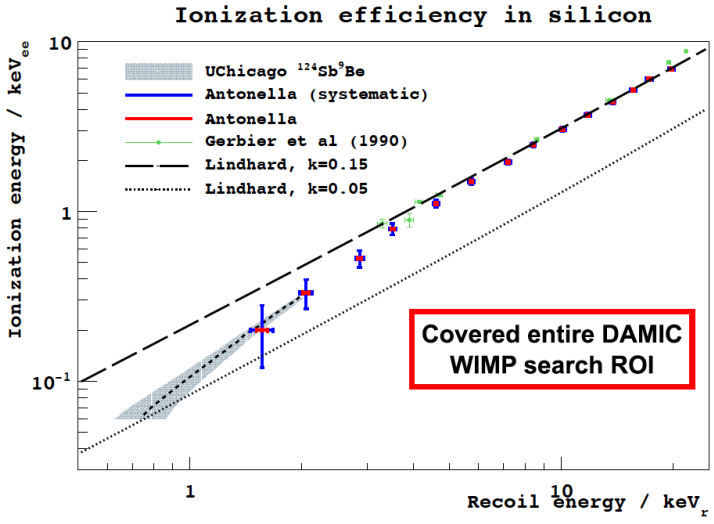

Figure 4.63: Summary of QF results from Antonella and Chicago experiments.

5

Understanding DAMIC 2015 data in the context of EFT operators

One important aspect in order to understand the dark matter signal produced in a detector, such as DAMIC, is to understand how the matter and dark matter interact at a theoretical level. In this section, we introduce the EFT approach for understanding this interaction, and compare it to the standard spin independent and spin dependent formulations typically used in dark matter searches.

5.1 An introduction to EFT

5.1.1 EFT in particle physics

EFT stands for Effective Field Theory. Usually, the EFT only takes the relevant and marginal parts and ignores the irrelevant parts of the physics of a system, as in [J. Polchinski 92, S. Carroll blog]. The differences of "relevant", "marginal" and "irrelevant" are the contribution of that part to the concerned system.
Assuming a four-dimensional space time, as in the usual $dx = d\mathbf{X}dt = d\mathbf{x}d\mathbf{y}d\mathbf{z}dt$, the energy dimension of this spacetime volume is E^{-4} because both the length$(\mathbf{x}, \mathbf{y}, \mathbf{z})$ and time(t) have the dimension of E^{-1}. If the dimension of an operator $\mathcal{O}$ is N, then when the spacetime volume integrates the operator, $\int \mathcal{O}dx$, the dimension of the action of the concerned system is E^{N-4}. For different values of N, $N < 4, N = 4$ or $N > 4$, the energy dimension corresponds to E^{-n}, 1 or E^n where n is a positive integer or, negative, zero and positive, respectively. So, the parts (terms) of the expression of an interaction could be separated into three sections : lower-energy sensitive, intermediate-energy sensitive and high-energy sensitive.
For instance, assuming $n = 1$, then the energy dimension of the three categories are : E^{-1}, 1, and E^1. Furthermore, suppose $E = 1\ GeV$ is low energy, $E = 1000\ GeV$ for high energy. The E^{-1} term gives $\frac{1}{1} = 1\ GeV^{-1}$ for low energy, while $\frac{1}{1000}\ GeV^{-1}$ for the high-energy one. Evidently, E^{-1} is more sensitive for low energy than for the high-energy one because $1\ GeV^{-1} \ggg \frac{1}{1000}\ GeV^{-1}$. A similar conclusion could be drawn if we are more interested in high energy physics, E^1 is more sensitive than E^{-1} because

$E^1 \mid_{1000\ GeV} = 1000\ GeV \ggg E^1 \mid_{1\ GeV} = 1\ GeV$.

So, for an experiment, if low energy is the only interesting energy interval of the system, we can ignore the terms of high energy(and vice versa if high energy physics is concerned). The terms of low-energy that are most important for the experiment therefore are notated as "relevant". The high energy ones can be ignored so are "irrelevant". The "marginal" terms which correspond to intermediate energy should remain.

In some sense, physics itself is an EFT. For instance, if the speed of a particle is equivalent to the speed of light, c, we use relativistic theory to characterize it; if the speed is much slower than c, we use non-relativistic theory or Newtonian mechanics to describe it. That is to say, different speeds decide different mechanics, or, different energy decides different physics.

In particle physics, there are many EFT applications, as is listed in figure 5.1, [J. Polchinski 92].

High Energy Theory	E_0	Low Energy Theory
1. Weinberg-Salam	$M_W \sim 80$ GeV	Fermi weak interaction theory
2. grand unified theory	$M_{\text{GUT}} \sim 10^{16}$ GeV	$SU(3) \times SU(2) \times U(1)$
3. QCD	$M_\rho \sim .8$ GeV	current algebra
4. lattice field theory	–	continuum field theory
5. string theory	$M_{\text{string}} \sim 10^{18}$ GeV	field theory of gravity and matter

Figure 5.1: Some EFT examples in particle physics, [J. Polchinski 92].

A well-known example of EFT is the Fermi theory of beta decay. This theory was developed during the early study of weak decays of nuclei when only the hadrons and leptons undergoing weak decay were known. The typical reactions studied were :

$$n \to p + e^- + \bar{\nu}_e$$
$$\mu^- \to e^- + \bar{\nu}_e + \nu_\mu$$

Enrico Fermi posited a point like interaction between the four fermions involved in these actions as shown in figure 5.2.

The corresponding Lagrangian is

$$\mathcal{L}_{Fermi} = -2\sqrt{2}\ G_F\ [\bar{\Psi}_d\ \gamma_u\ \frac{1-\gamma^5}{2}\ \Psi_\mu][\bar{\Psi}_{\nu_e}\ \gamma^\mu\ \frac{1-\gamma^5}{2}\ \Psi_e] + h.c.$$

where $G_F = 1.16371 \times 10^{-5}\ GeV^{-2}$ is Fermi coupling constant.

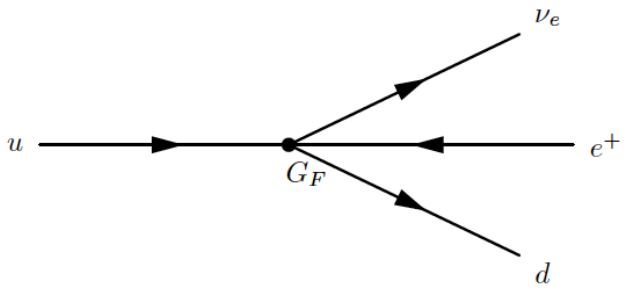

Figure 5.2: The Fermi's assumed (EFT) interaction for a muon decay in the 1930s.

The theory had great phenomenological success and was eventually understood in the 1970s along with the rise of the gauge theory of electroweak interactions, which forms a part of the standard model of particle physics. Figure 5.3 shows the difference between the original point-like (EFT) interaction, and the interaction mediated by the W boson.

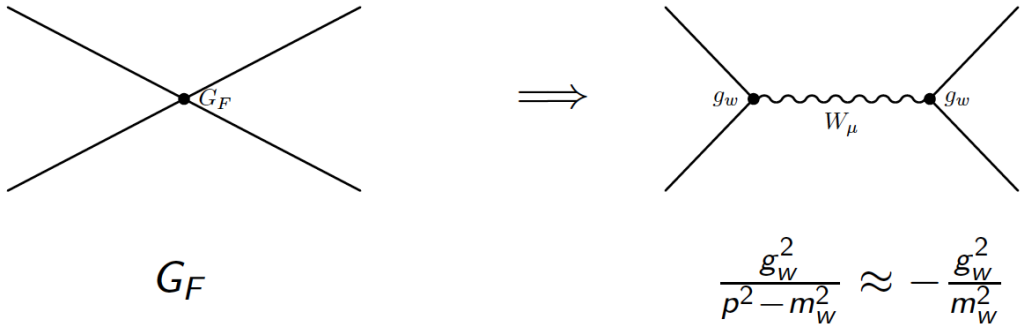

Figure 5.3: The Fermi interpretation of nuclei decay turns out to be the EFT version of the electroweak interaction of the SM.

The Fermi theory was successful because the energy scale of the interactions in the 1930s was 10 MeV which was much less than the mass scale of the W boson of 80 GeV, and therefore the Fermi theory was able to approximate the true theory.

5.2 Applying EFT to the interaction of a WIMP and nucleus

5.2.1 WIMP-nucleon elastic scattering

The standard S.I. and S.D. models assume the possible WIMP-nucleons signal is generated by a WIMP being scattered elastically off of a target, a contact interaction independent of momentum exchange. The simple assumption ignores the possible sensitivity to direct detection of other DM scenarios. Other interactions actually could also generate sizable signals in DM experiments [J. Fan et al., 10].
When the momentum transfer, q, is such that the wavelength h/q is no longer large compared to the nuclear radius, the effective cross-section begins to fall with increasing q, and a form factor can be included to represent this decreasing. However, the introduction of a form factor is not sufficient since new operators could also arise if one considers more detailed dynamics between the incident WIMPs and the nucleons in the target detector. These new operators turn out to be parametrically enhanced for large classes of EFT interactions.
Typically, the event rates of EFT $\mathcal{O}$s are a few orders smaller than standard S.I. / S.D. models because these $\mathcal{O}$s are essentially leading order(LO), next-to-leading order(NLO) or next-to-next-leading order(N^2LO) terms.

In WIMP "direct-detection" experiments, the possible signals might appear as event rates according to certain (complete) models. Most models of WIMPs invoke new physics associated with electroweak symmetry, where new phenomena can appear at scales of 100 GeV. However, the typical momentum transfer in direct detections experiments is less than 100s of MeV. Consequently, EFT provides a general and very efficient way to characterize experiments : regardless of the complexity or variety of candidate ultraviolet theories of dark matter, their low-energy consequences can be encoded in a small set of parameters describing the strength of the contact coupling of the WIMP to the nucleon or nucleus [EFT PRC 14].

All of the EFT operators can be built with combinations of the following four basic terms : $i\frac{\overrightarrow{q}}{m_N}$, $\overrightarrow{v}^{\perp}$, $\overrightarrow{S}_{\chi}$ and $\overrightarrow{S}_{N}$, [EFT JCAP 13, EFT PRC 14], where $\overrightarrow{q}$ is the momentum transfer, m_N is the nuclear mass of the target detector and $\overrightarrow{S}_{\chi}$ and $\overrightarrow{S}_{N}$ represent the spin of a WIMP and a nucleon(a proton or neutron) of a detector, respectively.

The two spins must be considered if one considers a S.D. interaction. The two other ingredients, $i\overrightarrow{q}$ and $\overrightarrow{v}^{\perp}$ arise naturally after some constraints have been applied to DM-nucleon elastic scattering. For $i\overrightarrow{q}$, the constraints are momentum conservation, Galilean invariance, and the hermiticity of the interaction (or crossing symmetry). For $\overrightarrow{v}^{\perp}$, the constraints of energy conservation, Galilean invariance, and the Hermiticity of an interaction have been applied.

For a DM-nucleon interaction, with momentum conservation, the momentum transfer q is,

$$\overrightarrow{q} = \overrightarrow{p}' - \overrightarrow{p} = \overrightarrow{k} - \overrightarrow{k}' \tag{5.1}$$

where $p(p')$ and $k(k')$ are the incoming(outgoing) momentum of the χ and N.

Galilean invariance allows a constant shift in all velocities. It is easy to see that the momentum transfer is Galilean-invariant as is the relative incoming velocity, $\overrightarrow{v}$ which is defined as following,

$$\overrightarrow{v} \equiv \overrightarrow{v}_{\chi,in} - \overrightarrow{v}_{N,in} \tag{5.2}$$

where $\overrightarrow{v}_{\chi,in}$ and $\overrightarrow{v}_{N,in}$ are the incident velocity of the WIMP and nucleon respectively. The $\overrightarrow{q}$ in Eq. 5.1 follows Galilean invariance because $\overrightarrow{q} = m(\overrightarrow{v}_{\chi,in} - \overrightarrow{v}_{N,in})$.

Another constraint that should be applied to the momentum $i\overrightarrow{q}$ is Hermiticity. This is essentially equivalent to a crossing symmetry, since the Hermitian conjugation exchanges incoming for outgoing particles, i.e. $(\phi^-)^\dagger = \phi^+$. Consequently, the $\overrightarrow{q}$ is effectively anti-Hermitian, and it will be more convenient to work with the Hermitian operator $i\overrightarrow{q}$ [EFT JCAP 13].
Instead of $i\overrightarrow{q}$, the reference [EFT PRC 14] has introduced m_N as a scale to get $i\overrightarrow{q}/m_N$ which is more natural after considering all of the nucleons as a composite system in Jacobi coordinates.

After three fundamental constraints, momentum-conservation, Galilean invariance and hermiticity have been applied, $i\overrightarrow{q}$ or $i\overrightarrow{q}/m_N$ becomes one of the basic ingredients of EFT.

The $\overrightarrow{v}^\perp$ has been defined as the following,

$$\begin{aligned}
\overrightarrow{v}^\perp &\equiv \overrightarrow{v} + \frac{\overrightarrow{q}}{2\mu_N} \\
&= \frac{1}{2}\overrightarrow{v} + \frac{1}{2}(\overrightarrow{v} + \frac{\overrightarrow{q}}{\mu_N}) \\
&= \frac{1}{2}(\overrightarrow{v}_{\chi,in} - \overrightarrow{v}_{N,in} + \overrightarrow{v}_{\chi,out} - \overrightarrow{v}_{N,out}) \\
&= \frac{1}{2}(\frac{\overrightarrow{p}}{m_\chi} - \frac{\overrightarrow{k}}{m_N} + \frac{\overrightarrow{p}'}{m_\chi} - \frac{\overrightarrow{k}'}{m_N})
\end{aligned} \tag{5.3}$$

where $\overrightarrow{v}$ is the relative WIMP-nucleon incoming velocity, as defined in Eq. (5.2).
The $\overrightarrow{v}^\perp$ in Eq.(5.3) has been constructed to follow the constraint of energy conservation and hermiticity of the interaction. In a WIMP-nucleon scattering, considering the center-of-mass system, the initial energy is the incident energy of $E_{in} = \frac{1}{2}\mu_N \overrightarrow{v}^2$; the final state energy is $E_{out} = \frac{1}{2}\mu_N(\overrightarrow{v} + \frac{\overrightarrow{q}}{\mu_N})^2$ because $\overrightarrow{v}_{final} = \overrightarrow{v}_{\chi,out} - \overrightarrow{v}_{N,out} = \overrightarrow{v} + \frac{\overrightarrow{q}}{\mu_N}$.

Imposing energy conservation of $E_{in} = E_{out}$ produces,

$$\begin{aligned} E_{in} &= E_{out} \\ \Rightarrow \frac{1}{2}\mu_N \vec{v}^2 &= \frac{1}{2}\mu_N(\vec{v} + \frac{\vec{q}}{\mu_N})^2 \\ \Rightarrow \vec{v}\cdot\vec{q} &= -\frac{\vec{q}^2}{2\mu_N} \end{aligned} \tag{5.4}$$

So, the definition of $\vec{v}^{\perp} \equiv \vec{v} + \frac{\vec{q}}{2\mu_N}$, as shown in Eq.(5.3), would arise naturally from Eq. (5.4) with the application of energy conservation.

Besides, $\vec{v} + \frac{\vec{q}}{2\mu_N}$ is Hermitian also, so

$$\begin{aligned} (\vec{v}^{\perp})^{\dagger} &= (\vec{v} + \frac{\vec{q}}{2\mu_N})^{\dagger} \\ &= \vec{v}^{\dagger} + \frac{\vec{q}}{2\mu_N}^{\dagger} \\ &= \vec{v} + \frac{\vec{q}}{\mu_N} - \frac{\vec{q}}{2\mu_N} \qquad (\vec{v}^{\dagger} \to \vec{v}_{\chi,out} - \vec{v}_{N,out} = \vec{v} + \tfrac{\vec{q}}{\mu_N},\ \vec{q}^{\dagger} = -\vec{q}) \\ &= \vec{v} + \frac{\vec{q}}{2\mu_N} \end{aligned} \tag{5.5}$$

Therefore, it's clear that $\vec{v}^{\perp}$ follows energy-conservation, Galilean invariance and hermiticity. Other choices like $\vec{v}$ do not because they do not have definite parity because $\vec{v}^{\dagger} = \vec{v} + \frac{\vec{q}}{\mu_N}$ which equals neither $\vec{v}$ nor $-\vec{v}$.

In summary, the four basic "building blocks" of EFT, $i\frac{\vec{q}}{m_N}$, $\vec{v}^{\perp}$, $\vec{S}_{\chi}$ and $\vec{S}_{N}$, have been chosen with fundamental physical constraints, momentum-conservation, energy-conservation, Galilean invariance and hermiticity, which are expected to be the physical laws of our universe.

The 14 EFT operators have been developed based on those ingrediants plus an additional constraint of T-symmetry, as Eq. (5.6) shows, [EFT JCAP 13, EFT PRC 14]. $\mathcal{O}_2$ has been ignored because it is a relativistic one. The first 10 operators, $\mathcal{O}_1 - \mathcal{O}_{11}$ can be associated with interactions involving only spin-0 and spin-1 mediators, and their momentum exchanges are at most second-order. That is to say, $\mathcal{O}_1 - \mathcal{O}_{11}$ at most quadratic in either spin $\vec{S}$ or speed $\vec{v}$. While $\mathcal{O}_{12} - \mathcal{O}_{15}$ don't have such limitations.

$$
\begin{aligned}
\mathcal{O}_1 &= 1_\chi 1_N \\
\mathcal{O}_3 &= i\vec{S}_N \cdot \left(\frac{\vec{q}}{m_N} \times \vec{v}^\perp \right) \\
\mathcal{O}_4 &= \vec{S}_\chi \cdot \vec{S}_N \\
\mathcal{O}_5 &= i\vec{S}_\chi \cdot \left(\frac{\vec{q}}{m_N} \times \vec{v}^\perp \right) \\
\mathcal{O}_6 &= \left(\vec{S}_\chi \cdot \frac{\vec{q}}{m_N} \right) \left(\vec{S}_N \cdot \frac{\vec{q}}{m_N} \right) \\
\mathcal{O}_7 &= \vec{S}_N \cdot \vec{v}^\perp \\
\mathcal{O}_8 &= \vec{S}_\chi \cdot \vec{v}^\perp \\
\mathcal{O}_9 &= i\vec{S}_\chi \cdot \left(\vec{S}_N \times \frac{\vec{q}}{m_N} \right) \\
\mathcal{O}_{10} &= i\vec{S}_N \cdot \frac{\vec{q}}{m_N} \\
\mathcal{O}_{11} &= i\vec{S}_\chi \cdot \frac{\vec{q}}{m_N} \\
\mathcal{O}_{12} &= \vec{S}_\chi \cdot \left(\vec{S}_N \times \vec{v}^\perp \right) \\
\mathcal{O}_{13} &= i \left(\vec{S}_\chi \cdot \vec{v}^\perp \right) \left(\vec{S}_N \cdot \frac{\vec{q}}{m_N} \right) \\
\mathcal{O}_{14} &= i \left(\vec{S}_\chi \cdot \frac{\vec{q}}{m_N} \right) \left(\vec{S}_N \cdot \vec{v}^\perp \right) \\
\mathcal{O}_{15} &= - \left(\vec{S}_\chi \cdot \frac{\vec{q}}{m_N} \right) \left[\left(\vec{S}_N \times \vec{v}^\perp \right) \cdot \frac{\vec{q}}{m_N} \right]
\end{aligned}
\tag{5.6}
$$

In a general sense, the EFT interaction can be expressed in the following form,

$$
\sum_{\alpha=n,p} \sum_{i=1}^{15} c_i^\alpha \mathcal{O}_i^\alpha, c_2^\alpha \equiv 0 \tag{5.7}
$$

where, n, p are neutron and proton separately. The c_i^α are the coefficients of each operator $\mathcal{O}_i^\alpha$.

From Eq. (5.6) and (5.7) , one can see that by introducing momentum transfer, $i\frac{\vec{q}}{m_N}$ and velocity $\vec{v}^\perp$, the EFT provides much more possible dynamics of a WIMP-nucleon interaction compared to standard S.I. and S.D. models. Except $\mathcal{O}_1$ and $\mathcal{O}_4$, which are equivalent to the standard S.I. and S.D., other operators could not be obtained by the standard S.I. or S.D. plus a form factor, essentially because those models assume a point-like nucleus which unavoidably misses the possible full internal dynamics of the nucleus.

An alternative interpretation is assuming that a point-like nucleus is equivalent to assuming $\overrightarrow{q} \cdot \overrightarrow{x}(i) \approxeq 0$. Accordingly, $e^{-i\overrightarrow{q}\cdot\overrightarrow{x}(i)}\mathcal{O}_i = e^0\mathcal{O}_i = \mathcal{O}_i$, where $\overrightarrow{q}$ is the momentum transfer and $\overrightarrow{x}(i)$ is the position of a WIMP-nucleon interaction in Jacobi coordinates of a nucleus for $\mathcal{O}_i$. The dynamical part $e^{-i\overrightarrow{q}\cdot\overrightarrow{x}(i)}$ of an operator has been ignored by assuming $\overrightarrow{q} \cdot \overrightarrow{x}(i) \approxeq 0$, However, once $\overrightarrow{q} \cdot \overrightarrow{x}(i) \approxeq 1$ instead of $\approxeq 0$, $e^{-i\overrightarrow{q}\cdot\overrightarrow{x}(i)}\mathcal{O}_i$ can not be simplified to $\mathcal{O}_i$.
Consequently, the EFT operators arise naturally with the condition of $\overrightarrow{q} \cdot \overrightarrow{x}(i) \approxeq 1$. These operators are an enhancement to the standard S.I. and S.D. when considering the detailed dynamics of a WIMP-nucleus scattering.

As mentioned above, the EFT operators are all non-relativistic ones. Reference [EFT PRC 14] provides a relativistic matching for those operators, as is shown in table 5.1.
The interactions of table 5.1 describe the interactions of spin-$\frac{1}{2}$ WIMPs with nucleons. There are two new defined momenta as Eq. 5.8 shows,

$$\begin{aligned} P^\mu &= p^\mu + p^{'\mu} \\ K^\mu &= k^\mu + k^{'\mu} \end{aligned} \tag{5.8}$$

where, p^μ and $p^{'\mu}$ are the incoming(outgoing) four-momentum of the dark matter particle χ; k^μ and $k^{'\mu}$ are the incoming(outgoing) four-momentum of the nucleon N.
Accordingly, the relative velocity of Eq. (5.3) can be written in terms of $P^\mu and K^\mu$.

$$\begin{aligned} \overrightarrow{v}^\perp &\equiv \frac{1}{2}\left(\frac{\overrightarrow{p}}{m_\chi} - \frac{\overrightarrow{k}}{m_N} + \frac{\overrightarrow{{}'p}}{m_\chi} - \frac{\overrightarrow{{}'k}}{m_N}\right) \\ &= \frac{1}{2}\left(\frac{\overrightarrow{P}}{m_\chi} - \frac{\overrightarrow{K}}{m_N}\right) \end{aligned} \tag{5.9}$$

The relativistic WIMP-nucleon interactions are constructed as bilinear WIMP-nucleon products of the available two scalar($\bar{\chi}\chi$, $\bar{\chi}\gamma^5\chi$) and four vector($\bar{\chi}P^\mu\chi$, $\bar{\chi}P^\mu\gamma^5\chi$, $\bar{\chi}i\sigma^{\mu\nu}q_\nu\chi$, $\bar{\chi}\gamma^\mu\gamma^5\chi$) amplitudes. There are $2^2 + 4^2 = 20$ combinations, as shown in table 5.1.

5.2.2 WIMP nucleus interaction

By embedding the EFT WIMP-nucleon interaction into a nucleus, one could figure out the general form of the WIMP-nucleus interaction. The basic assumption is that the nuclear interaction is the coherent sum of the interactions of the WIMP with the individual nucleons in the nucleus.

For EFT, a WIMP-nucleus interaction naturally introduces the intrinsic part of the nuclear operators : a nuclear axial charge operator, a convection current and a spin-velocity

j	$\mathcal{L}^j_{\rm int}$	Nonrelativistic Reduction	$\sum_i c_i\mathcal{O}_i$	P/T
1	$\bar{\chi}\chi\bar{N}N$	$1_\chi 1_N$	$\mathcal{O}_1$	E/E
2	$i\bar{\chi}\chi\bar{N}\gamma^5 N$	$i\frac{\vec{q}}{m_N}\cdot\vec{S}_N$	$\mathcal{O}_{10}$	O/O
3	$i\bar{\chi}\gamma^5\chi\bar{N}N$	$-i\frac{\vec{q}}{m_\chi}\cdot\vec{S}_\chi$	$-\frac{m_N}{m_\chi}\mathcal{O}_{11}$	O/O
4	$\bar{\chi}\gamma^5\chi\bar{N}\gamma^5 N$	$-\frac{\vec{q}}{m_\chi}\cdot\vec{S}_\chi\frac{\vec{q}}{m_N}\cdot\vec{S}_N$	$-\frac{m_N}{m_\chi}\mathcal{O}_6$	E/E
5	$\frac{P^\mu}{m_{\rm M}}\bar{\chi}\chi\frac{K_\mu}{m_{\rm M}}\bar{N}N$	$4\frac{m_\chi m_N}{m_{\rm M}^2}1_\chi 1_N$	$4\frac{m_\chi m_N}{m_{\rm M}^2}\mathcal{O}_1$	E/E
6	$\frac{P^\mu}{m_{\rm M}}\bar{\chi}\chi\bar{N}i\sigma_{\mu\alpha}\frac{q^\alpha}{m_{\rm M}}N$	$-\frac{m_\chi}{m_N}\frac{\vec{q}^2}{m_{\rm M}^2}1_\chi 1_N - 4i\frac{m_\chi}{m_{\rm M}}\vec{v}^\perp\cdot\left(\frac{\vec{q}}{m_{\rm M}}\times\vec{S}_N\right)$	$-\frac{m_\chi}{m_N}\frac{\vec{q}^2}{m_{\rm M}^2}\mathcal{O}_1 + 4\frac{m_\chi m_N}{m_{\rm M}^2}\mathcal{O}_3$	E/E
7	$\frac{P^\mu}{m_{\rm M}}\bar{\chi}\chi\bar{N}\gamma_\mu\gamma^5 N$	$-4\frac{m_\chi}{m_{\rm M}}\vec{v}^\perp\cdot\vec{S}_N$	$-4\frac{m_\chi}{m_{\rm M}}\mathcal{O}_7$	O/E
8	$i\frac{P^\mu}{m_{\rm M}}\bar{\chi}\chi\frac{K_\mu}{m_{\rm M}}\bar{N}\gamma^5 N$	$4i\frac{m_\chi}{m_{\rm M}}\frac{\vec{q}}{m_{\rm M}}\cdot\vec{S}_N$	$4\frac{m_\chi m_N}{m_{\rm M}^2}\mathcal{O}_{10}$	O/O
9	$\bar{\chi}i\sigma^{\mu\nu}\frac{q_\nu}{m_{\rm M}}\chi\frac{K_\mu}{m_{\rm M}}\bar{N}N$	$\frac{m_N}{m_\chi}\frac{\vec{q}^2}{m_{\rm M}^2}1_\chi 1_N + 4i\frac{m_N}{m_{\rm M}}\vec{v}^\perp\cdot\left(\frac{\vec{q}}{m_{\rm M}}\times\vec{S}_\chi\right)$	$\frac{m_N}{m_\chi}\frac{\vec{q}^2}{m_{\rm M}^2}\mathcal{O}_1 - 4\frac{m_N^2}{m_{\rm M}^2}\mathcal{O}_5$	E/E
10	$\bar{\chi}i\sigma^{\mu\nu}\frac{q_\nu}{m_{\rm M}}\chi\bar{N}i\sigma_{\mu\alpha}\frac{q^\alpha}{m_{\rm M}}N$	$4\left(\frac{\vec{q}}{m_{\rm M}}\times\vec{S}_\chi\right)\cdot\left(\frac{\vec{q}}{m_{\rm M}}\times\vec{S}_N\right)$	$4\left(\frac{\vec{q}^2}{m_{\rm M}^2}\mathcal{O}_4 - \frac{m_N^2}{m_{\rm M}^2}\mathcal{O}_6\right)$	E/E
11	$\bar{\chi}i\sigma^{\mu\nu}\frac{q_\nu}{m_{\rm M}}\chi\bar{N}\gamma^\mu\gamma^5 N$	$-4i\left(\frac{\vec{q}}{m_{\rm M}}\times\vec{S}_\chi\right)\cdot\vec{S}_N$	$-4\frac{m_N}{m_{\rm M}}\mathcal{O}_9$	O/E
12	$i\bar{\chi}i\sigma^{\mu\nu}\frac{q_\nu}{m_{\rm M}}\chi\frac{K_\mu}{m_{\rm M}}\bar{N}\gamma^5 N$	$\left[i\frac{\vec{q}^2}{m_\chi m_{\rm M}} - 4\vec{v}^\perp\cdot\left(\frac{\vec{q}}{m_{\rm M}}\times\vec{S}_\chi\right)\right]\frac{\vec{q}}{m_{\rm M}}\cdot\vec{S}_N$	$\frac{m_N}{m_\chi}\frac{\vec{q}^2}{m_{\rm M}^2}\mathcal{O}_{10} + 4\frac{\vec{q}^2}{m_{\rm M}^2}\mathcal{O}_{12} + 4\frac{m_N^2}{m_{\rm M}^2}\mathcal{O}_{15}$	O/O
13	$\bar{\chi}\gamma^\mu\gamma^5\chi\frac{K_\mu}{m_{\rm M}}\bar{N}N$	$4\frac{m_N}{m_{\rm M}}\vec{v}^\perp\cdot\vec{S}_\chi$	$4\frac{m_N}{m_{\rm M}}\mathcal{O}_8$	O/E
14	$\bar{\chi}\gamma^\mu\gamma^5\chi\bar{N}i\sigma_{\mu\alpha}\frac{q^\alpha}{m_{\rm M}}N$	$-4i\vec{S}_\chi\cdot\left(\frac{\vec{q}}{m_{\rm M}}\times\vec{S}_N\right)$	$4\frac{m_N}{m_{\rm M}}\mathcal{O}_9$	O/E
15	$\bar{\chi}\gamma^\mu\gamma^5\chi\bar{N}\gamma^\mu\gamma^5 N$	$-4\vec{S}_\chi\cdot\vec{S}_N$	$-4\mathcal{O}_4$	E/E
16	$i\bar{\chi}\gamma^\mu\gamma^5\chi\frac{K^\mu}{m_{\rm M}}\bar{N}\gamma^5 N$	$4i\vec{v}^\perp\cdot\vec{S}_\chi\frac{\vec{q}}{m_{\rm M}}\cdot\vec{S}_N$	$4\frac{m_N}{m_{\rm M}}\mathcal{O}_{13}$	E/O
17	$i\frac{P^\mu}{m_{\rm M}}\bar{\chi}\gamma^5\chi\frac{K_\mu}{m_{\rm M}}\bar{N}N$	$-4i\frac{m_N}{m_{\rm M}}\frac{\vec{q}}{m_{\rm M}}\cdot\vec{S}_\chi$	$-4\frac{m_N^2}{m_{\rm M}^2}\mathcal{O}_{11}$	O/O
18	$i\frac{P^\mu}{m_{\rm M}}\bar{\chi}\gamma^5\chi\bar{N}i\sigma_{\mu\alpha}\frac{q^\alpha}{m_{\rm M}}N$	$\frac{\vec{q}}{m_{\rm M}}\cdot\vec{S}_\chi\left[i\frac{\vec{q}^2}{m_N m_{\rm M}} - 4\vec{v}^\perp\cdot\left(\frac{\vec{q}}{m_{\rm M}}\times\vec{S}_N\right)\right]$	$\frac{\vec{q}^2}{m_{\rm M}^2}\mathcal{O}_{11} + 4\frac{m_N^2}{m_{\rm M}^2}\mathcal{O}_{15}$	O/O
19	$i\frac{P^\mu}{m_{\rm M}}\bar{\chi}\gamma^5\chi\bar{N}\gamma_\mu\gamma^5 N$	$4i\frac{\vec{q}}{m_{\rm M}}\cdot\vec{S}_\chi\vec{v}_\perp\cdot\vec{S}_N$	$4\frac{m_N}{m_{\rm M}}\mathcal{O}_{14}$	E/O
20	$\frac{P^\mu}{m_{\rm M}}\bar{\chi}\gamma^5\chi\frac{K_\mu}{m_{\rm M}}\bar{N}\gamma^5 N$	$-4\frac{\vec{q}}{m_{\rm M}}\cdot\vec{S}_\chi\frac{\vec{q}}{m_{\rm M}}\cdot\vec{S}_N$	$-4\frac{m_N^2}{m_{\rm M}^2}\mathcal{O}_6$	E/E

Table 5.1: Relativistic interacting Lagrangians, their non-relativistic analogs for evaluation between Paul spinors, the corresponding results as linear combinations of the $\mathcal{O}_i$, and the transformation properties of the interactions[event(E) or odd(O)] under parity and time reversal. Bjorken and Drell spinor and γ matrix conventions are used [EFT PRC 14].

current. After some mathematical manipulation, the interaction could then be expressed as an addition of the following transforms : vector charge, vector transverse magnetic, axial transverse electric, axial longitudinal, vector transverse electric, and vector longitudinal operators. These six operators are allowed under the assumption that the nuclear ground state is an approximate eigenstate of P and CP. Thus, the EFT has derived the most general form of the cross section [EFT PRC 14].

The expression of the cross section is usually very complex because it is expressed in terms of the single-reduced matrix elements of one-body operators of definite angular momentum, which can actually be simplified as a product of the one-body density matrix, and the single-particle matrix elements of the one-body operator. The latter can be evaluated algebraically [EFT PRC 14].

Reference [EFT PRC 14] provides a detailed explanation on the application of EFT to DM direct detection. The model has been derived in an elegant and natural way. For instance, the coefficient of each operator, c_i, has been normalized to have the dimension of $(energy)^{-2}$, to compensate for this, the dimensionless input value(by a user) is multiplied by m_V^{-2}, with $m_V \equiv 246.2\ GeV$. Since $(\sqrt{2}G_F)^{-1/2} \approxeq 246.2\ GeV \Rightarrow (246.2\ GeV)^{-2} = 2\ G_F$ which means c_i has the unit of $2\ G_F$. An additional convention is to set the coupling such that $c_p = c_n = \frac{1}{2}c_i = G_F$, where c_p and c_n are the coupling of a WIMP to a proton and neutron, respectively. As a result, once the constants of c_p and c_n have been obtained(by a fit to the data for a signal, for instance), one immediately knows their relative coupling strength with respect to the Fermi coupling.

An open source mathematical script, "dmformfactor-V6.m" is appended in [EFT PRC 14]. Users can calculate interesting physics quantities like : differential and/or total cross-sections, event rate, etc. According to [W. Haxton PC], an improved version of the script should be released soon with a number of improvements : an upgraded version of the form factor will be included, as explained in [New form factor], and the event rates of standard S.I. and S.D. models will be supplied, also.

5.2.3 Current analysis with EFT models

There exist two types of analysis with the application of EFT operators. One is a global fit where all of the operators have been summed up with coefficients to set a limit, as is explained in reference [EFT global fit 14], such that a likelihood has been used to fit for a potential signal. Another technique is to constrain each operator individually, as the SuperCDMS paper shows [EFT SuperCDMS 15]. Reference [EFT SuperCDMS 15] also have projected the limits on future detectors for LZ and SuperCDMS.

We have launched an EFT analysis of the DAMIC analysis in order to search for signals represented by each of the individual operators based on a 2015 dataset of 0.38 kg days of data. Since we have not observed any signal, and have instead set limits, we have not

done a global fit to determine which operators are more favored by the data.

5.3 The selection of DAMIC 2015 data

The experimental setup for DAMIC at the Snolab underground detector hall is described in chapter 2. Since the first installation in Dec. 2012, the main effort has been to improve the noise performance of the CCDs and to reduce backgrounds.
The $\sim 0.4 Kg \times day$ data we analyzed here was taken in 2015 with DAMIC-100 CCDs and a background level of $\sim$ 15 *dru*. A *dru* represents "differential rate unit". It is used for event and background rates such that 1dru = 1 event $keV^{-1}kg^{-1}\ day^{-1}$, [Lewin and Smith, 1996] .

The typical procedure for obtaining a data-quality exposure is :
Step 1, zero CCDs by flushing out all of the electrons registered in the pixels of the CCDs. After this step, CCDs are ready for data taking.
Step 2, take physical data with a CCD exposure of 30,000 seconds ($\sim$ 8.3 hours). This long exposure decreases the noise by minimizing the number of readouts which incur noise, and prevents the build up of dark current. Step 3, after readout of data exposure, take an additional blank image of a CCD with zero readout time, so that it reflects only the noise from the readout electronics.
In the offline analysis, to remove the noise of the readout electronics from physical images, the blank image is subtracted from the physical image. A similar(but not identical) procedure is outlined in figure 3.5 of chapter 3.

In order to improve the quality of the data, several standard technologies for CCD image analysis are applied, such as blank image subtraction and saturated pixel removal, as are explained in chapter 3. After these corrections, the image ideally contains only physics data, with low levels of noise and dark current. We then extract the charge and position of all hits from the set of images, and proceed to reconstruct the hit clusters.

As shown in figure 2.5c, the energy cluster hit patterns from different particles on a CCD image have different shapes, while we are only interested in the diffusion-limited energy clusters.
To select such energy clusters, we have applied three selection criteria. The first is based on a 2D Gaussian fit to the energy distribution in the horizontal and vertical direction. A 2D Gaussian fit function is compared to each 7×7 pixel square on the CCD. For this square of pixels, we build a likelihood function comparing the Delta LL of two possibilities : "2D Gaussian hit cluster + noise", and "noise only". Using cut on $\Delta\mathcal{LL}$ we remove event candidates that are consistent with "noise only. The second criteria for event selection is a consistency requirement that the center of the energy cluster from the Gaussian fit is close to the energy-weighted mean position of the cluster. Finally, we require the events to be above an energy threshold of 60 eV, which is above our 5σ

threshold for noise(40 eV) and has a value of energy for which we can evaluate the event detection efficiency and ionization efficiency.
After collecting a dataset of 0.4 kg * days using 6 CCDs, we selected a set of events using a $\Delta\mathcal{LL}$ of less than -25, a cut between the distance to the center of the cluster of less than 1.75 pixels. The selected DAMIC 2015 dataset is shown in figure 5.4. We do not consider events above 10 KeV since these events do not contribute to our low-mass dark matter reach, and DAMIC is not competitive with 100-kg scale dark matter experiments optimized for 100-GeV scale dark matter.

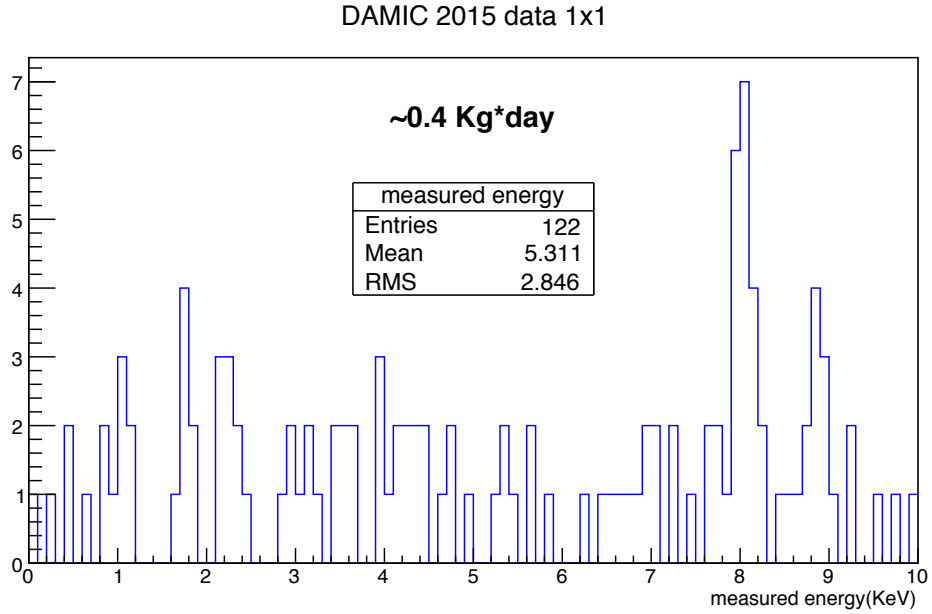

Figure 5.4: The selected 2015 DAMIC data, with the exposure of $\sim 0.4 Kg * day$. The title 1x1 signifies that every pixel was read out independently (rather than summing the charge on multiple pixels before reading out.

In order to interpret this ionization energy data in terms of a potential dark matter signal, we first need to understand what the expected energy recoil distribution would be for various dark matter candidates, second, we need to correct this recoil distribution according to an energy-dependent detection efficiency, and third, we need to use the QF to determine the ionization energy that would be produced in our detector. Once we have such a distribution, we can put constraints on the cross-section of dark matter interactions as a function of dark matter mass.
The detection efficiency is shown in figure 5.5. In the EFT analysis, the efficiency has been applied to the data: all of the measured data has been divided with the efficiency curve[1].

[1] An equivalent and alternative method is multiplying the expression of a model with the detection efficiency curve.

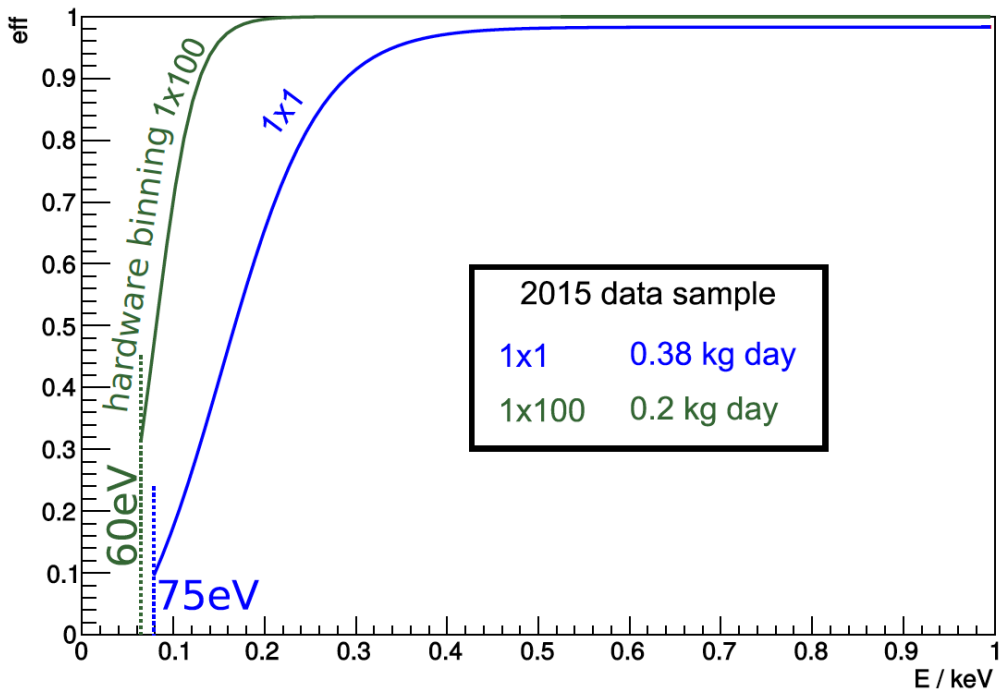

Figure 5.5: The detection efficiency of CCDs for 2015 datasets. The title 1x1 is the same as figure 5.4. The title 1x100 means that the charge from 100 pixels is accumulated on the readout gate before the charge is read out.

5.4 Spin-independent EFT formulation of dark matter interactions

In section 5.2.1, the EFT formulation provides a more complete set of operators to describe possible WIMP-nucleon interactions. However, the $\mathcal{O}_1$ and $\mathcal{O}_4$ EFT operators provide an equivalent representation of the well-known spin independent (S.I.) and spin dependent (S.D.) interactions, respectively [EFT JCAP 13, EFT PRC 14] .
In this section we will mainly discuss $\mathcal{O}1$ and its comparison to the S.I. operator, since DAMIC is more sensitive to S.I. interactions since Si_{14}^{28} has an even number of nucleons and therefore no spin-dependent enhancement. However, comparisons of $\mathcal{O}4$ and the S.D. operator, which both consider spin, would also provide similar agreement.
The compared results of EFT $\mathcal{O}_1$ V.S. the standard S.I. can be easily transplanted to the comparison of $\mathcal{O}_4$ vs. the standard S.D. .

5.4.1 The event rate of standard S.I. interactions

The differential cross-section of S.I. is [G. Jungman et al, 96]

$$\frac{d\sigma}{d \mid \mathbf{q} \mid^2} = G_F^2 \frac{C}{v^2} F^2(\mid \mathbf{q} \mid) = \frac{\sigma_0}{4m_{red}^2(m_{nuc})v^2} F^2(\mid \mathbf{q} \mid) \tag{5.10}$$

where $\mathbf{q}$ is the momentum transfer, G_F is the Fermi Coupling constant, v is the WIMP speed, C is a dimensionless number, $F(\mid \mathbf{q} \mid)$ is the form factor($F(0) = 1$), $m_{red}(m_{nuc})$ is the reduced mass of a WIMP and a nucleus, σ_0 is the total momentum-transfer cross section as defined below in Eq.5.11.

$$\sigma_0 \equiv \int_0^{4m_{red}^2(m_{nuc})v^2} \frac{d\sigma(q=0)}{d \mid \mathbf{q} \mid^2} d \mid \mathbf{q} \mid^2 = 4G_F^2 m_{red}^2(m_{nuc}) C \tag{5.11}$$

Qualitatively, an event rate could be expressed as

$$R \approxeq n\sigma < v > \frac{M_{det}}{m_N} N_A \tag{5.12}$$

where n is the WIMP number density $n = \rho_0/m_\chi$, σ is the elastic-scattering cross-section, $< v >$ is the average speed of the WIMP relative to the target, we divide the detector mass M_{det} by the target mass m_N(= atomic number A) to get the number of target nuclei, N_A is Avogadro constant.

Quantitatively, the event rate[2] per unit detector mass [3] of the standard S.I. has been defined as [G. Jungman et al, 96]

$$dR = \frac{\rho}{m_\chi} \frac{1}{m_N} \frac{d\sigma}{d \mid \mathbf{q} \mid^2} v f_1(v) d \mid \mathbf{q} \mid^2 dv \tag{5.13}$$

where ρ is the local mass density of WIMPs, m_χ is mass of the WIMP, and $f_1(v)$ is speed of the WIMP as defined in (5.14) [G. Jungman et al, 96]. Other variables have defined above.

$$f_1(v)dv = \frac{vdv}{v_E v_0 \sqrt{\pi}} \{exp[-\frac{(v - v_E)^2}{v_0^2}] - exp[-\frac{(v + v_E)^2}{v_0^2}]\} \tag{5.14}$$

In Eq. 5.14, v_E is the Earth's velocity in the galactic rest frame and v_0 is the speed of the Sun around the galactic center.

[2]The RHS of Eq.(5.13) could be simplified as $\frac{\rho}{m_\chi} \frac{1}{m_N} d\sigma v f_1(v) dv$. The unit of this term is $\frac{1}{(length)^3} \frac{1}{mass} (length)^2 \frac{length}{time} = 1/(mass \cdot time)$. The $f_1(v)dv$ part is the probability of speed distribution, therefore it's dimensionless.

[3]Here, the unit detector mass is the mass of one nucleon, proton or neutron. To get the number per kg, one needs to multiply by a factor of $10^3 * N_A$ where N_A is Avogadro constant. Since for a 1 kg detector, there exists $1Kg/(A * g/mol) = 10^3 mol/A = 10^3 * N_A/A$ nucleus where A is the atomic number of the detector.

The total event rate is

$$\begin{aligned}
\frac{dR}{dE_R} &= \frac{dR}{d \mid \mathbf{q} \mid^2 /2m_N} \qquad (\ E_R = \mid \mathbf{q} \mid^2 /(2m_N),\ \text{[G. Jungman et al, 96]}) \\
&= 2m_N \frac{dR}{d \mid \mathbf{q} \mid^2} \\
&= \frac{2\rho}{m_\chi} \frac{d\sigma}{d \mid \mathbf{q} \mid^2} \int v f_1(v) dv \\
&\text{(substitute (5.13), or integrate } dR \text{ over all possible incoming velocities.)} \\
&= \frac{2\rho}{m_\chi} \frac{\sigma_0}{4m_{red}^2(m_{nuc})v^2} F^2(\mid \mathbf{q} \mid) \int v f_1(v) dv \\
&\qquad\qquad \text{(substitute (5.10), or integrate over momentum transfer.)} \\
&= \frac{\sigma_0 \rho}{2m_\chi m_{red}^2(m_{nuc})} F^2(\mid \mathbf{q} \mid) \int \frac{f_1(v)}{v} dv \qquad (5.15)
\end{aligned}$$

If we change the notation as is done in [A. Kurylov & M. KamionKowski 03], the event rate(per unit time per unit detector mass(nucleus) per unit recoil energy) [4] of dR/dE, eq. (5.15) could be expressed as,

$$\frac{dR}{dE} = \frac{\rho_\chi}{2m_\chi m_{red}^2(m_{nuc})} \times [\sigma_{0\chi N}^{SI} F_{SI}^2(E)] \int_{v_{min}}^{\infty} \frac{f_1(v)}{v} dv \qquad (5.16)$$

where ρ_χ is the WIMP mass density, m_χ is the mass of the WIMP, $m_{red}^2(m_{nuc})$ is the reduced mass of the dark matter and the target nucleus, $\sigma_{0\chi N}^{SI}$ is the S.I. cross-section of the WIMP and target nucleus, $F_{SI}^2(E)$ is the form factor, v_{min} is the minimum velocity of the WIMP in order to deposit detectable energy, and $f_1(v)$ is the WIMP speed distribution, defined above.
The following derivation follows from reference [A. Kurylov & M. KamionKowski 03].

$$\begin{aligned}
(5.16) &= \frac{\rho_\chi}{2m_\chi m_{red}^2(m_{nuc})} \times \frac{m_{red}^2(m_{nuc})}{m_{red}^2(m_p)} [Z + (A-Z)\frac{f_n}{f_p}]^2 \sigma_{\chi p}^{SI} \times F_{SI}^2(E) \times \int_{v_{min}}^{\infty} \frac{f_1(v)}{v} dv \\
&= \frac{\rho_\chi}{2m_\chi} \times \frac{1}{m_{red}^2(m_p)} [Z + (A-Z)\frac{f_n}{f_p}]^2 \sigma_{\chi p}^{SI} \times F_{SI}^2(E) \times \int_{v_{min}}^{\infty} \frac{f_1(v)}{v} dv \\
&= \frac{\rho_\chi}{2m_\chi} \times \frac{1}{m_{red}^2(m_p)} A^2 \times \sigma_{\chi p}^{SI} \times F_{SI}^2(E) \times \int_{v_{min}}^{\infty} \frac{f_1(v)}{v} dv \qquad (\text{ assuming } f_n = f_p) \\
&= \underline{\frac{A^2 \rho_\chi}{4v_E} \frac{\sigma_{\chi p}^{SI}}{m_\chi} \times \frac{1}{m_{red}^2(m_p)}} \times \underline{\underline{F_{SI}^2(E)}} \underbrace{[erf(\frac{v_{min}+v_E}{v_0}) - erf(\frac{v_{min}-v_E}{v_0})]}
\end{aligned} \qquad (5.17)$$

[4] The units can be obtained by dividing dR with dE_R, since the former has the units of "per unit time per unit detector mass" as shown in the footnote 2, the latter has the units of "unit recoil energy". Alternatively, the related units are, $\sigma \to length$, $\rho/m_\chi \to 1/(length)^3$, and the form factor and $f_1(v)dv$ have no dimension. Substituting the units into the RHS of Eq.(5.15), one gets $\frac{(length)^2}{mass^2} \frac{1}{(length)^3} \frac{length}{time} = \frac{1}{(mass)^2 \cdot time} = \frac{1}{mass \cdot energy \cdot time}$.

In Eq. 5.17, $m^2_{red}(m_p)$ is the reduced mass of the WIMP and the proton, A and Z are the atomic and proton number of target nucleus, f_n and f_p represent the WIMP coupling to the neutron and proton and are considered to be the same, and $\sigma^{SI}_{\chi p}$ is the cross-section of the WIMP interaction with the proton. In contrast to Eq. (5.15), note that the units of rate of Eq. (5.17) are "per unit time per *nucleon* (instead of per nucleus) per unit recoil energy." The underlined terms have a correspondence in EFT $\mathcal{O}_1$, which will be introduced below.

5.4.2 The event rate of stand EFT $\mathcal{O}_1$

For EFT $\mathcal{O}_1$, the differential cross-section is defined as following [EFT PRC 14]

$$\frac{d\sigma}{dE_R} = \frac{m_T}{2\pi v^2} P_{tot} \tag{5.18}$$

where m_T is the mass of target, v is the WIMP velocity, P_{tot} is transition probability which represents the coupling of WIMP-nucleon.

The event rate, dR/dE, of $\mathcal{O}_1$ cannot be figured out analytically because it involves a complex nuclear matrix with an integration over the WIMP speed distribution. A user of the Mathematica script appended in reference [EFT PRC 14] can however print out the event rate numerically by calling the function of "$EventRate()$" of the Mathematica script. Assuming the WIMP mass is m_χ, a "quasi-derivative" version of the event rate of $\mathcal{O}_1$ can be expressed as

$$\frac{dR}{dE} = n \cdot \frac{d\sigma}{dE_R} \cdot v$$

(n is the number density of WIMPs, v is the speed of WIMPs with respect to earth.)

$$= N_T \frac{\rho_\chi m_T}{2\pi m_\chi} < \frac{1}{v} P_{tot}(v^2, q^2) >$$

($< P_{tot}(v^2, q^2) >$ is the dimensionless transition probability.)

$$= N_T \frac{\rho_\chi m_T}{2\pi m_\chi} \int_{v>v_{min}} \frac{f(\overrightarrow{v} + \overrightarrow{v}_e(t))}{v} P_{tot}(v^2, q^2) d^3v$$

$$= N_T \frac{\rho_\chi m_T}{2\pi m_\chi} \int_{v>v_{min}} \frac{f(\overrightarrow{v} + \overrightarrow{v}_e(t))}{v} \frac{1}{2j_\chi + 1} \frac{1}{2j_N + 1} \sum_{spins} \mid \mathcal{M}_{\mathcal{NR}} \mid^2 d^3v$$

$$= N_T \frac{\rho_\chi m_T}{2\pi m_\chi} \int_{v>v_{min}} \frac{f(\overrightarrow{v} + \overrightarrow{v}_e(t))}{v} \frac{4\pi}{2j_N + 1} (\sum_{j=0,2..}^{\infty} \mid \langle j_N \mid\mid \sum_{i=1}^{A} M_J(q\chi_i)[c_1^0 + c_1^1 \tau_3(i)] \mid\mid j_N \rangle \mid^2) d^3v$$

(A form factor is hidden in this formula)

$$= \frac{1}{m_\chi^3} 9.2 \times 10^{-49} cof^2 m_\chi^2 e^{-0.0023 E_R} (7.4 - 0.0073 E_R + 1.3 \times 10^{-6} E_R^2)^2$$

$$\times (\ erf[1.05 - 1362.7(0.00014\sqrt{E_R}(26.3 + m_\chi)/m_\chi)]$$

$$+ erf[1.05 + 1362.7(0.00014\sqrt{E_R}(26.3 + m_\chi)/m_\chi)] \ )$$

(Being calculated by the "dmformfactor-V6.m" of [EFT PRC 14].)

$$= \underline{9.2 \times 10^{-49} \frac{cof^2}{m_\chi}} \underline{\underline{e^{-0.0023 E_R} (7.4 - 0.0073 E_R + 1.3 \times 10^{-6} E_R^2)^2}}$$

$$\times \underbrace{(erf[1.05 - 0.19\sqrt{E_R}(26.3 + m_\chi)/m_\chi] + erf[1.05 + 0.19\sqrt{E_R}(26.3 + m_\chi)/m_\chi])}$$

(5.19)

where N_T is the number of target nuclei per detector mass, ρ_χ is the dark matter density, "cof" is the coefficient of isospin(same to proton and neutron)[5], m_χ is the mass of the WIMP, m_T is the nucleon mass, E_R is recoil energy, v_{min} is the minimum velocity for a WIMP to deposit detectable energy, v_e is the Earth's velocity in the galactic rest frame, $P_{tot}(v^2, q^2)$ is proportional to the total transition probability(and cross-section), j_χ and j_N are the spins of WIMP and nucleus, respectively, $\mid \mathcal{M}_{NR} \mid^2$ denotes the square modulus of the non-relativistic scattering amplitude $\mathcal{M}_{NR}$, $M_J(q\chi_i)$ is the charge multipole operator, and c_1^0 and c_1^1 are the coefficients of O1 and τ_3 is the isospin operator.

A term in Eq. (5.19) with a same underscore corresponds to the one with same underscore in Eq. (5.17). This will be discussed further in the following section.

[5] by multiplying a Fermi coupling constant, $cof \times 2G_F = cof/246.2GeV$ indicates the interaction in the units of the standard weak interaction strength

5.4.3 Comparison of the event rate of EFT $\mathcal{O}_1$ and the standard S.I.

Comparing the event rates only from the two equations of Eq. (5.17) and (5.19), it is not obvious whether our EFT $\mathcal{O}_1$ formulation and the S.I. formulation agree. We first simplify the equations by collecting all of the terms into constants and those that depend on the mass of the particles.

$$\begin{aligned}(5.17) &= \underline{\frac{A^2\rho_\chi}{4v_E}\frac{\frac{\sigma_{\chi p}^{SI}}{m_{red}^2(m_p)}}{m_\chi}} \times \underline{\underline{F_{SI}^2(E)}}\ \underbrace{[erf(\frac{v_{min}+v_E}{v_0}) - erf(\frac{v_{min}-v_E}{v_0})]}\\ &= (constant1) \times \frac{1}{m_\chi}\frac{1}{m_{red}^2(m_p)} \times \sigma_{\chi p}^{SI} \end{aligned} \tag{5.20}$$

$$\begin{aligned}(5.19) &= \underline{9.2\times10^{-49}\frac{cof^2}{m_\chi}}\underline{\underline{e^{-0.0023E_R}(7.4-0.0073E_R+1.3\times10^{-6}E_R^2)^2}}\\ &\times \underbrace{(erf[1.05-0.19\sqrt{E_R}(26.3+m_\chi)/m_\chi] + erf[1.05+0.19\sqrt{E_R}(26.3+m_\chi)/m_\chi])}\end{aligned} \tag{5.21}$$

Dividing Eq.(5.17) by Eq.(5.19) will produce,

$$\begin{aligned}&\frac{dR/dE\mid_{SI}}{dR/dE\mid_{O1}} = \frac{(5.17)}{(5.19)} = \frac{(5.20)}{(5.21)} = (constant3)\frac{\sigma_{\chi p}^{SI}}{m_{red}^2(m_p)cof^2}\\ &\Rightarrow \frac{dR/dE\mid_{SI}}{dR/dE\mid_{O1}} \times m_{red}^2(m_p)cof^2 = (constant3)\sigma_{\chi p}^{SI}\end{aligned} \tag{5.22}$$

Eq. (5.22) could be further simplified to :

$$\begin{aligned}\frac{dR/dE\mid_{SI}}{dR/dE\mid_{O1}} \times m_{red}^2(m_p)cof^2 &= (constant3)\sigma_{\chi p}^{SI}\\ &= (constant3)\frac{4f_p^2}{\pi}M_{red}^2(M_p)\\ &\qquad ([\text{A. Kurylov \& M. KamionKowski 03}])\\ &= (constant4)M_{red}^2(M_p)f_p^2\\ \Rightarrow \frac{dR/dE\mid_{SI}}{dR/dE\mid_{O1}} &= \frac{(constant4)M_{red}^2(M_p)f_p^2}{m_{red}^2(m_p)cof^2}\\ &= constant5\\ &\qquad (M_{red}(M_p) = m_{red}(m_p),\ f_p = cof)\end{aligned} \tag{5.23}$$

where f_p is coupling constant, $M_{red}(M_p)$ is the reduced mass of a WIMP and a nucleon, M_p is the mass of a proton.

In summary, Eq (5.23) clearly shows the event rate of the standard S.I. and EFT $\mathcal{O}_1$ should be the same or different by a constant due to different parameter conventions

(for instance, some cosmology constants.) [6] After making some practical corrections to obtain the same results for S.I. and EFT $\mathcal{O}_1$, we obtained good agreement for the event rates predicted by both formulations as shown, for one particular dark matter mass of 5 GeV, in figure5.6.

5.4.4 Some comments on EFT $\mathcal{O}_s$ and the standard S.I.

In fact, starting from an EFT $\mathcal{O}_1$ differential cross-section, one could also derive an event rate with a standard "S.I.-formulation", though it is not recommended [W. Haxton PC].

The essence of this formulation is to use the idea of "momentum-transfer cross section" to get the total cross section by integrating a differential cross section over the whole range of momentum transfer (from the minimum to the maximum). Although the typical differential cross section with this method would be slightly different since it uses a small angle slice $\frac{d\sigma}{d\Omega}(\theta)$ where θ is a scattering angle, the total "momentum-transfer cross section" then can be obtained by integrating the whole cubic angle like $\int \frac{d\sigma}{d\Omega}(\theta)(1 - cos\theta)d\Omega$, [momentum transfer XS]. This kind of cross section can be useful for describing the average momentum transferred cross section for a particle collision with a target.

At first, we define the cross-section of a WIMP and a nucleus by integrating $d\sigma/dE_R = m_T/2\pi v^2$ over E_R for a fixed speed(equivalent to a momentum transfer of zero, same as the assumption of Eq.(5.11)).

[6] In practice, I found that the EFT script provided by the authors of [EFT PRC 14] was missing a factor of "$m_{red}^2(m_p) * cof^2$", which caused me many days of work tracking through Mathematica code.

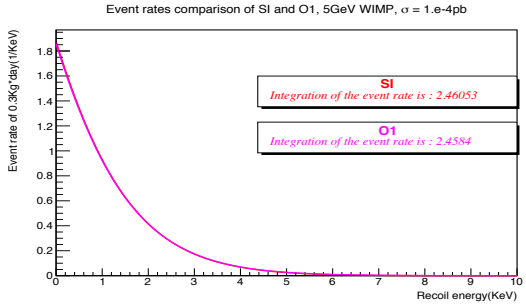

Figure 5.6: 5.6. Comparison of SI and O1 operators for a 5 GeV WIMP candidate.

$$
\begin{aligned}
\sigma &= \int_0^{E_{R_{max}}} \frac{d\sigma(q=0)}{dE_R} dE_R && \text{(q is momentum transfer)} \\
&= \frac{m_T}{2\pi v^2} E_{R_{max}} && (d\sigma/dE_R = m_T/2\pi v^2, \text{ [EFT PRC 14]}) \\
&= \frac{m_T}{2\pi v^2} \frac{2m_{red}^2(m_{nuc})v^2}{m_T} && (E_{R_{max}} = 2m_{red}^2(m_{nuc})v^2/m_T, \text{ [EFT PRC 14]}) \\
&= \frac{m_{red}^2(m_{nuc})}{\pi} \\
\Rightarrow \pi &= \frac{m_{red}^2(m_{nuc})}{\sigma} && (5.24)
\end{aligned}
$$

Where $m_{red}^2(m_{nuc})$ is the reduced mass of a WIMP and a nucleus(as above).

Accordingly,

$$
\begin{aligned}
\frac{d\sigma}{dE_R} &= \frac{m_T}{2\pi v^2} \\
&= \frac{m_T}{2v^2} \frac{\sigma}{m_{red}^2(m_{nuc})} && \text{(substitute Eq.(5.24))} \\
&= \frac{m_T \sigma}{2m_{red}^2(m_{nuc})v^2} && (5.25)
\end{aligned}
$$

Furthermore, we can get the event rate of an unit detector mass(like one nucleon) with this EFT version of differential cross-section as in the following.

$$
\begin{aligned}
\frac{dR}{dE_R} &= \int d^3v f(v) \cdot (\eta \cdot v) \frac{1}{m_T} \frac{d\sigma}{dE_R} \\
&\text{(A } \tfrac{1}{m_T} \text{ has been added because the unit mass here is a nucleon. } \eta \text{ is DM number density.)} \\
&= \int 4\pi v^2 dv f(v) \cdot (\eta \cdot v) \frac{1}{m_T} \frac{d\sigma}{dE_R} \\
&\quad (\textstyle\int f(v) d^3v = \int_0^{2\pi} d\phi \int_{-1}^{+1} d(cos\theta) \int f(v) v^2 dv = \int 4\pi v^2 f(v) dv) \\
&= \int 4\pi v^2 dv f(v) \cdot (\frac{\rho}{m_\chi} \cdot v) \frac{1}{m_T} \frac{m_T \sigma}{2m_{red}^2(m_{nuc})v^2} \\
&\text{(substitute } \eta = \tfrac{\rho}{m_\chi} \text{ which changes DM number density to mass density, and Eq.(5.25))} \\
&= \frac{\rho \cdot \sigma}{2m_\chi m_{red}^2(m_{nuc})v^2} \int 4\pi v^2 \frac{f(v)}{v} dv \\
&= \frac{\rho \cdot \sigma}{2m_\chi m_{red}^2(m_{nuc})} \int 4\pi \frac{f(v)}{v} dv && (5.26)
\end{aligned}
$$

where the $f(v)$ is the velocity distribution following Maxwell-Boltzman,

$$
f(v) = \frac{1}{\pi^{3/2} v_0^3} e^{-v^2/v_0^2} \qquad (5.27)
$$

The RHS of Eq.(5.26) is almost identical to the one of Eq.(5.15) except the form factor is absent and the the velocity integration is different since we are using a slightly different speed distribution. The form factor difference is exactly the difference expected between the EFT $\mathcal{O}_1$ and the standard S.I.. The actual differences in the event rate between the EFT $\mathcal{O}_1$ and the standard S.I. are tiny, as shown in figure 5.6 because for those two models, the contribution to the event rate from the form factor is very limited [Lewin and Smith, 1996].

For the standard S.I., as mentioned in reference [G. Jungman et al, 96] explicitly, the total cross section σ_0 in Eq. (5.15) actually is *not* really a total cross section. The real one could be obtained by integrating $dR/d \mid \mathbf{q} \mid^2$ over $d \mid \mathbf{q} \mid^2$ including the form factor. The form factor must be integrated into the velocity distribution because the form factor is a function of the recoil energy and the recoil energy is affected by the WIMP velocity, [G. Jungman et al, 96, Lewin and Smith, 1996, EFT PRC 14]. Taking the form factor out of the integration makes the expression much more simpler but unavoidably leaves room of improvement. The script appended in reference EFT14 improved on this. In this script, all of the EFT $\mathcal{O}$s have been integrated with the velocity distribution.

5.5 Testing data with EFT $\mathcal{O}s$

5.5.1 Introduction to analysis of data with EFT $\mathcal{O}s$

In order to test our data for signal, we compare the likelihood of two different hypotheses, "b only" (only backgrounds) and "s + b" (sum of backgrounds and signal).
In our analysis, we calculate the log likelihood for "b only" and "s + b" for each bin, then take the sum to get the log likelihood for the background-only model and signal-plus-background model. Subtracting these gives us a $\Delta\mathcal{LL}$, which can be compared to a standard χ^2 distribution in order to determine the signal contribution.

If there is no signal like excess, we can proceed to set limits. The χ^2 distribution indicates fluctuations due to Poisson statistics in each bin, and is also dependent on the number of degrees of freedom of the model. We determine the $\Delta\mathcal{LL}$ distribution as a function of the signal rate. Calculating the signal rate is done by comparing the data to the Poisson fluctuations of the background model, and scanning across the $\Delta\mathcal{LL}$ in order to find the most likely expected signal, as well as the range of values of signal that are allowed or excluded at a certain Confidence Level (CL).

5.5.2 The results of limit setting with EFT $\mathcal{O}$s

There are 14 EFT $\mathcal{O}$s, as shown in Eq (5.6). Four of them are spin independent, $\mathcal{O}_1$, $\mathcal{O}_5$, $\mathcal{O}_8$ and $\mathcal{O}_{11}$, whereas the other operators are spin dependent.

S.I. models are independent of spin and have the same cross-section to neutrons and protons. The cross-section is proportional to the atomic number of the element of the target, A^2. For S.D. interactions the scattering amplitude changes sign with spin direction. So although the interaction with a nucleus is still coherent, in the sense that the scattering amplitudes are summed, paired nucleons contribute zero scattering amplitude and only the residual unpaired nucleons contribute. Thus only nuclei with an odd number of protons and/or an odd number of neutrons can detect spin-dependent interactions [Lewin and Smith, 1996].

The bulk of our CCDs is natural silicon. The natural abundance of ^{28}Si is $\sim 92.2\%$, ^{29}Si is $\sim 4.7\%$ and ^{30}Si is $\sim 3.1\%$ [Silicon wikipedia]. In our analysis, for S.I. analysis, we assumed all of the data is exposed by ^{28}Si; for S.D., we assumed the material is ^{29}Si, the exposure has been scaled down according to its natural abundance. For instance, the exposure of DAMIC 2015 data is $\sim 0.4\ Kg*day$, for S.I., we take this exposure to set a limit; for S.D. analysis, we scale it according to the natural abundance of ^{29}Si, $0.4\ Kg*day \times 4.7\% = 0.018\ Kg*day$.

Although $\mathcal{O}_1$, $\mathcal{O}_5$, $\mathcal{O}_8$ and $\mathcal{O}_{11}$ are all S.I. $\mathcal{O}$s, the shapes of the event rates are not the same. Figure 5.7 shows the event rates of all of these $\mathcal{O}$s assuming 5 GeV WIMP and the exposure of 0.3 $Kg*day$. A vertical cyan line has been added on each sub-figure to indicate the recoil energy(240 eV) corresponding to 5 σ noise(40 $eVee$).
These figures show clearly that (1), DAMIC CCDs are capable of detecting 5 GeV WIMPs for all of the EFT S.I. $\mathcal{O}$s because for all S.I. operators, most of the event rate spectrum is higher than the 5 σ noise of CCDs . (2), These event rates are calculated under the same coupling constant, $5.75e-6$, but the event rates of $\mathcal{O}_5$, $\mathcal{O}_8$ and $\mathcal{O}_{11}$ are much smaller than $\mathcal{O}_1$. This verifies that $\mathcal{O}_1$ is a tree level operator, $\mathcal{O}_5$ is next-to-leading order(NLO) one, while $\mathcal{O}_8$ and $\mathcal{O}_{11}$ are leading order(LO) ones.

Since the data was not consistent with a signal in addition to the expected background, we proceed to set limits on the signal cross section as a function of dark matter mass. Figure 5.8 shows the limit comparison of EFT $\mathcal{O}_1$ and the standard S.I. analyzed with DAMIC 2015 data, 0.4 $Kg*day$. The limits are all set with 90% C.L.. Two models of the quenching factor have been applied, the standard Lindhard model, and the QF measured by our Antonella experiment and our Chicago collaborators. Please refer to chapter 4 for a detailed explanation of these calibrations. For each quenching factor, the limits from the EFT $\mathcal{O}_1$ and the standard S.I. operator are the same as expected.

The limits with our new QF measurements are not as strong as the limits that would be obtained from the Lindhard model since our new QF measurement implies that the ionization energy produced from nuclear recoils below 4 KeV is less than that expected by the Lindhard model as is shown in figure 4.63.

Figure 5.9 shows the 90% C.L. limits of all of the EFT S.I. $\mathcal{O}$s and the standard S.I. with 0.4 kg*d of DAMIC 2015 data. Figure 5.9a applies the Lindhard model as a quenching

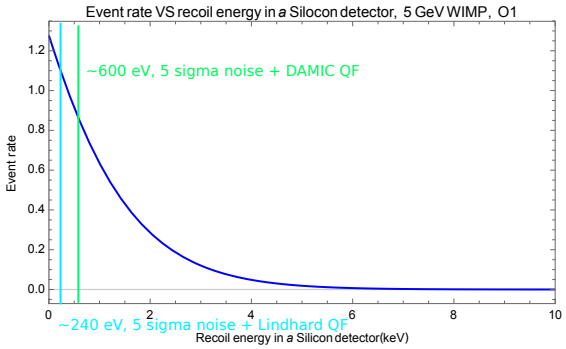

5.7a. Event rate of $\mathcal{O}_1$, 5 GeV WIMP

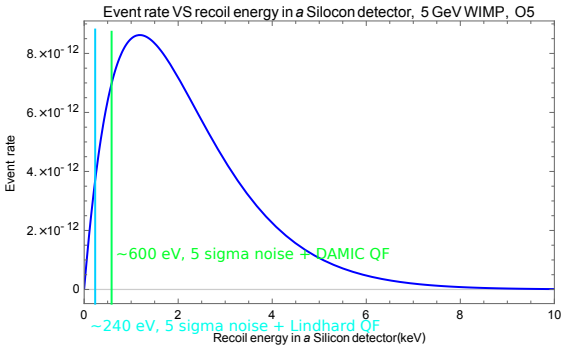

5.7b. Event rate of $\mathcal{O}_5$, 5 GeV WIMP.

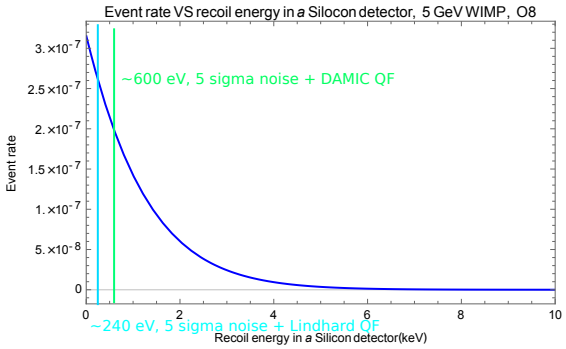

5.7c. Event rate of $\mathcal{O}_8$, 5 GeV WIMP.

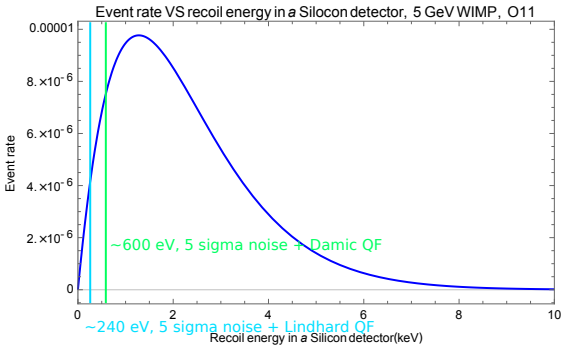

5.7d. Event rate of $\mathcal{O}_{11}$, 5 GeV WIMP.

Figure 5.7: Event rate of all EFT spin independent $\mathcal{O}$s assuming 5 GeV WIMP and the exposure of 0.3 $Kg*day$: $\mathcal{O}_1$, $\mathcal{O}_5$, $\mathcal{O}_8$ and $\mathcal{O}_{11}$. A vertical cyan line has been added in each sub-figure to indicate the recoil energy(240 eV) corresponding to 5 σ noise(40 $eVee$)

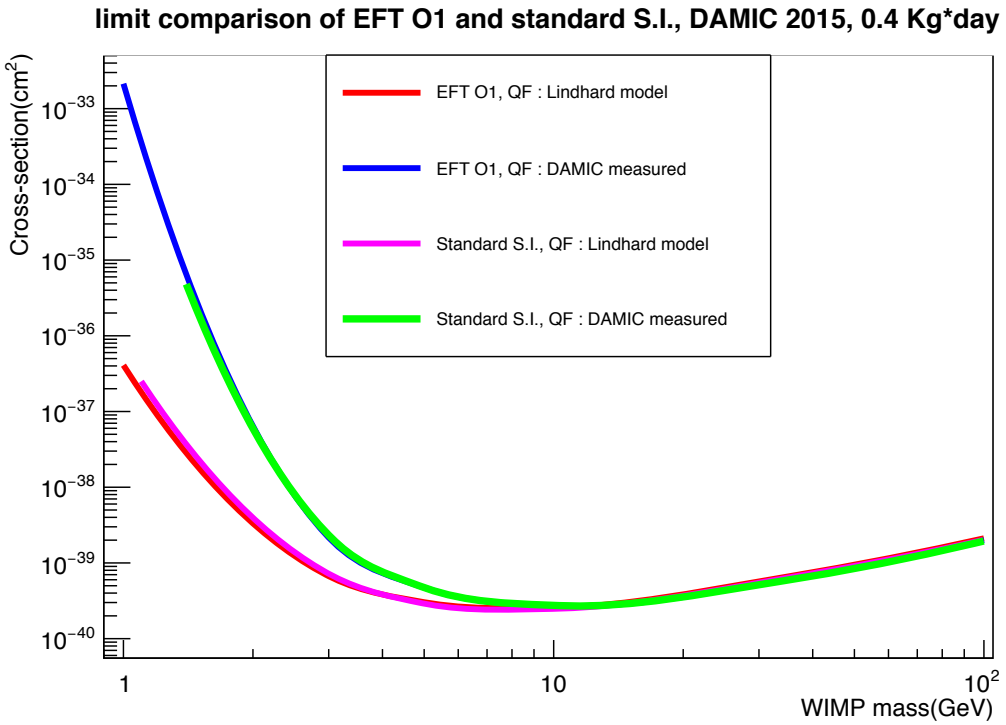

Figure 5.8: The 90% CL upper on the cross-section for dark matter based on 0.4 kg*d of DAMIC 2015 data. Limits are shown comparing EFT $\mathcal{O}_1$ and S.I. operators, and for two energy-dependent quenching factors from the Lindhard model and as measured in this work.

factor; Figure 5.9b applies the DAMIC measured results for a quenching factor.

Figure 5.10 shows the 90% C.L. limits of all of the EFT S.D. $\mathcal{O}$s with DAMIC 2015 data, $\sim 0.018\ Kg*day$. Figure 5.10a applies the Lindhard model as a quenching factor; Figure 5.10b used the DAMIC measured results as a quenching factor.

5.6 Conclusions on EFT analysis

This work explains the direct search for dark matter in CCDs using the DAMIC experiment. DAMIC is ideally suited for searching for low-mass dark matter that produces very low energy nuclear recoil signals when interacting elastically with detector nuclei. Of major importance in interpreting DAMIC data in terms of a potential dark matter signal is the application of an appropriate quenching factor in order to relate the nuclear recoil energy of a dark matter collision with the ionization energy expected. We conducted two experiments in 2013 and 2015 in order to provide such an energy calibration down

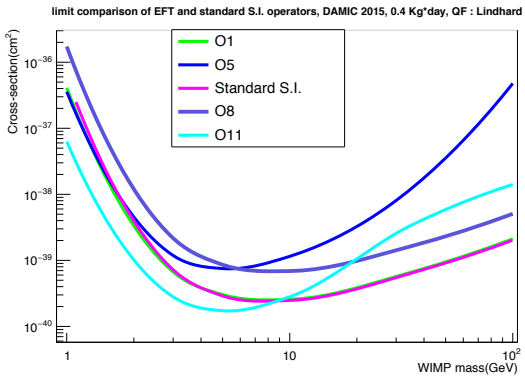

5.9a. The Lindhard quenching factor has been applied.

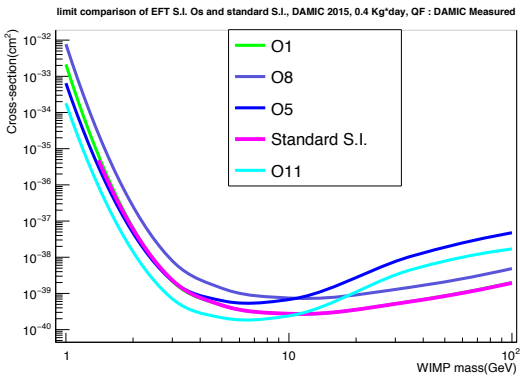

5.9b. Our measured quenching factor has been applied.

Figure 5.9: The 90% C.L. limits of all of the spin-independent EFT $\mathcal{O}$s and the standard S.I. with DAMIC 2015 data, 0.4 $Kg * day$.

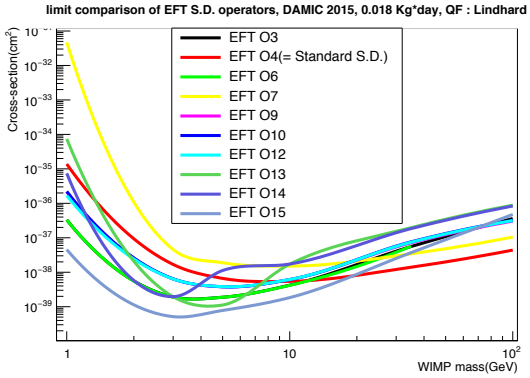

5.10a. The Lindhard quenching factor has been applied.

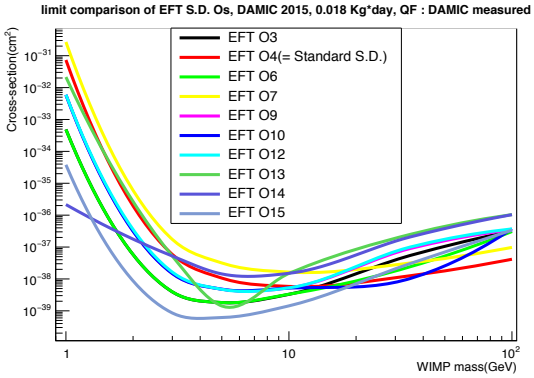

5.10b. Our measured quenching factor has been applied.

Figure 5.10: The 90% C.L. limits of all of the spin-dependent EFT $\mathcal{O}$s with DAMIC 2015 data, ~ 0.018 $Kg * day$.

to the lowest ionization energies that DAMIC can reach. Such calibrations indicated a departure at low energies from the standard quenching factor model used for dark matter searches. Using a dataset of 0.4 kg * d of DAMIC 2015 data, we next proceeded to search for dark matter using the full set of relevant Effective Field Theory operators. After verifying that our EFT formulation agrees with standard spin-independent an spin-dependent interaction formulations, we tested for a number of different S.I. and S.D. type EFT operators. We find that DAMIC provides the best constraints on the S.I. $\mathcal{O}_{11}$ EFT operator, the $\mathcal{O}_{15}$ S.D. EFT operator for M_{DM} between 1.5 GeV and 10 GeV, and for the S.D. EFT $\mathcal{O}_{14}$ for M_{DM} below 1.5 GeV.

DAMIC 100, which will contain 100 grams of active silicon detectors, has now achieved its expected background rate, has installed many of its CCDs, and is expected to begin data taking before the end of 2016, for first results in 2017.

References

[Dark Matter Annenberg] https://www.learner.org/courses/physics/unit/text.html?unit=10&secNum=0.

[Planck 2015, XIII] P. Ade et al.. Planck 2015 results. XIII. Cosmological parameters https://arxiv.org/pdf/1502.01589v3.pdf.

[WMAP, 2013] G.F., et al. Nine-year Wilkinson Microwave Anisotropy Probe(WMAP) observations: Cosmological parameter results 2013, ApJS., 208, 19H

[Zwicky] F. Zwicky, Republication of : The redshift of extragalactic nebulae. Gen Relativ Gravit(2009)41:207-224

[Zwicky German] F. Zwicky, Die Rotverschiebung von extragalaktischen Nebeln Helvetica Physica Acta 6 (1933) 110.

[Rubin 1970] Rubin VC, Ford WK Jr. Rotation of the Andromeda nebula from a spectroscopic survey of emission regions 1970 Ap.J. 159 : 379-403.

[Rubin 1980] Rubin VC, Thonnard N, Ford WK Jr. Rotational properties of 21 Sc galaxies with a large range of luminosities and randii, from NGC 4605(R = 4 kpc) to UGC 2885(R = 122 kpc) 1980. Ap. J. 238:471.

[Milgrom 1983] Milgrom, M. A modification of the Newtonian dynamics as a possible alternative to the hidden mass hypothesis 1983 Ap.J. 270 : 365.

[S. Schlamminger et al., 2008] S. Schlamminger et al.. Test of the equivalence principle using a rotating torsion balance PRL, 100, 041101(2008)

[E.L. Turner, 1988] E. Turner et al.. Gravitational Lenses Scientific American July, 54(1988)

[D. Clowe et al., 2006] D. Clowe et al.. A direct empirical proof of the existence of dark matter The astrophysical journal, 648:L109-L113

[A. Robertson et al., 16] A. Robertson et al.. What does the Bullet Cluster tell us about self-interacting dark matter arxiv: 1605.04307

[Berkeley Cosmology] http://cosmology.berkeley.edu/Education/CosmologyEssays/The_Cosmic_Microwave_Background.html.

[CMB of Hu & White] http://w.astro.berkeley.edu/ mwhite/sciam03_short.pdf.

[Planck 2015 results. IX.] A. Adam et al.. Planck 2015 results. IX. Diffuse component separation : CMB maps arxiv: 1502.05956

[V. Springel et al., 2005] V. Springel et al.. Simulations of the formation, evolution and clustering of galaxies and quasars Vol 435, 2 June 2005, dos:10.1038nature03597

[Local DM density] J.Read. The local dark matter density arxiv: 1404.1938.

[M. Vogelsberger et al., 2009] M. Vogelsberger et al.. Phase-space structure in the local dark matter distribution and its signature in the direct detection experiments Mon. Not. R. Astron. Soc. 395, 787-811(2009)

[V. Springel, 2005] V. Springel The cosmological simulation code GADGET-2 Mon. Not. R. Astron. Soc. 364, 1105-1134(2005)

[Gaia] http://sci.esa.int/gaia/.

[Aquarius project] V. Springel et al.. The Aquarius project : the subhaloes of galactic haloes Mon. Not. R. Astron. Soc. 391, 1685-1711(2008)

[Scherrer & Turner 86] R. Scherrer & M. Turner On the relic, cosmic abundance of stable, weakly interacting massive particles PRD Volume 33, number 6, (1986)

[B. Paczynski] B. Paczynski Gravitational microlensing by the the galactic halo Astrophys.J.304 1(1986)

[C. Alcock] C. Alcock et al.. The MACHO project: Microlensing results from 5.7 years of large Magellanic could observations Astrophys.J.542 257(2000)

[DarkSide-20k experiment] DarkSide collaboration The DarkSide-20k Yellow Book Unpublished

[Peccei & Quinn 77] R. Peccei & H. Quinn CP conservation in the presence of pseudoparticles PRL 38, 1440 (1977)

[Nussinov 85] S. Nussinov Technocosmology - could a technibaryon excess provide a natural missing mass candidate ? PLB 165, 55 (1985)

[Feng & Kumar 08] J. Feng & J. Kumar. Dark-Matter Particles without Weak-Scale masses or Weak Interactions PRL 101, 231301(2008)

[Hierarchy problem] H. Hatanaka et al.. http://cds.cern.ch/record/354663/files/9805067.pdf

[Peskin & Schroeder 95] M.E. Pesky, D.V.Schroeder. (1995). An introduction to quantum field theory. 0-201-50397-2, Westview Press.

[Feng review 10] J. Feng. Dark matter candidates from particle physics and methods of detection Annu. Rev. Astron. Astrohphs. 2010. : 48:495-545

[D. Baumann lecture] http://www.damtp.cam.ac.uk/user/db275/Cosmology/Chapter3.pdf.

[Cresst 15] Cresst collaboration http://arxiv.org/pdf/1509.01515v1.pdf.

[DarkSide 14] DarkSide collaboration http://arXiv:1410.0653.

[LUX 15] LUX collaboration. http://arXiv: 1512.03506.

[Xenon low mass, 16] XENON collaboration. http://arXiv: 1605.06262.

[Billard 13] Billard et al. http://arxiv.org/pdf/1307.5458v2.pdf.

[SuperCDMS 14] SuperCDMS collaboration. http://arXiv:1402.7137.

[SuperCDMS 15] SuperCDMS collaboration. http://arXiv:1509.02448.

[XENON100 13] XENON collaboration. http://arXiv:1301.6620.

[G. Jungman et al, 96] G. Jungman et al.. Supersymmetric dark matter Physics Reports 267 (1996) 195-373

[CMS-8TeV DM 14] The CMS collaboration http://arXiv:1408.3583.

[ATLAS-8TeV DM 15] The ATLAS collaboration http://arXiv:1502.01518.

[Darwin collaboration] http://darwin.physik.uzh.ch.

[Hochberg et al, 15] Hochberg et al .. Superconducting detectors for super light dark matter http://arXiv:1504.07237.

[Schutz & Zurek, 16] K. Schutz & K. Zurek. On the detection of light dark matter with superfluid Helium http://arXiv:1604.08206.

[Feng et al, 08] J. Feng et al.. Thermal relics in hidden sectors J. Cosmol. Astropart. Phys. 0810:43

[J. Pendlebury et al, 15] J. Pendlebury et al. Revised experimental upper limit on the electric dipole moment of the neutron Physical review D 92, 092003(2015)

[ADMX 14] ADMX collaboration https://arxiv.org/pdf/1403.5332v2.pdf.

[K. Zurek, 13] K. Zurek. Asymmetric dark matter : theories, signatures, and constraints Physics Report 537(2014)91-121

[A.G. Cohen et al, 93] J. Pendlebury et al. Progress in electroweak baryogenesis Annu. Rev. Null. Part. Sci. 1993. 43:27-70

[A. Kurylov & M. KamionKowski 03] A. Kurylov & M. KamionKowski http://arxiv.org/pdf/hep-ph/0307185.pdf.

[Pico 15] C. Amole et al.. arXiv : 1503.00008v2 [astro-ph.CO].

[SIMPLE 11] TA. Girard et al.. arXiv : 1101.1885v1.

[Snowmass CF1 13] Daniel. Bauer et al. arXiv : 1310.8327v2 [hep-ph].

[DAMA 13] R. Bernabei et al. arXiv : 1308.5109v2 [astro-ph.GA].

[DMIce 16] E. Barbosa de Souza et al. arXiv : 1602.05939v [physics.ins-det].

[Mayet 16] F. Mayet et al.. arXiv : 1602.03781.

[Drift 11] J. Battat et al.. Physics of the Dark Universe 9-10(2015)1-7.

[Newage 10] Kentaro. Miuchi et al.. Physics Letters 686(2010)11-17.

[Mimac 16] MIMIC collaboration arxiv : 1607.08765.

[Dmtpc 13] DMTPC collaboration arxiv : 1301.5685.

[Drift 11] E. Daw et al.. arXiv : 1110.0222.

[Hooper review 08] D. Hooper & E. A. Baltz Annu. Rev. Nucl. Part. Sci. 2008. 58:293-314..

[SuperK 15] K. Choi et al.. PRL 114, 141301(2015)..

[IceCube 16] M. Aartsen al.. http://arxiv.org/pdf/1606.00209v1.pdf.

[FermiLAT 15] O. Adriani et al.. Phys. Rev. Lett 116, 241105(2015).

[FermiLAT 15] M. Ackermann et al.. arXiv : 1503.02641v1 [astro-ph.HE].

[Hooper 15] D. Hooper arXiv : 1504.02087v1 [astro-ph.HE].

[AMS 02] M. Aguilar et al.. Physics Reports 366, (2002) 331-405 .

[AMS 14] L. Accardo et al.. PRL 113, 121101(2014)..

[ATLAS & CMS DM searches 15] ATLAS and CMS collaboration arXiv : 1507.00966v1 [hep-ex].

[EFT PRC 14] N. Anand et al.. PRC 89, 065501(2014).. arXiv : 1308.6288 [hep-ph]

[Janesick, 2001] Janesick, J. R. (2001). *Scientific Charge-Coupled Devices*. 0-8194-3698-4. SPIE EXPRESS.

[PDG 15] K.A. Olive et al. (Particle Data Group), Chinese Physics C38, 090001(2014) and 2015 update.

[Cowan, 1998] Glen Cowan. Statistical Data Analysis. 0-19-850155-2. Oxford University Press

[Behnke et al., 2013] Behnke Olaf et al., Data Analysis in High Energy Physics. 978-3-527-41058-3. WILEY-VCH

[Baker and Cousins, 1984] Steve Baker and Robert D. Cousins Nuclear Instruments and Methods in Physics Research 221 (1984) 437-442.

[Hoel, 1971] Hoel,Paul G. Introduction to mathematical statistics. 0-471-40365. John Wiley & Sons, Inc

[Joel Heinrich, 2003] Joel Heinrich PHYSTAT2003, SLAC, Standford, California, September 8-11, 2003.

[DES, 2005] DES collaboration. The Dark Energy Survey. arxiv: 0510346.

[Holland et al., 2003] S.E. Holland et al.. Fully depleted, Back-illuminated charge-Coupled Devices Fabricated on High-Resistivity Silicon. IEEE Trans.Electron Dev., 50 225(2003).

[Barreto et al., 2012] J.Barreto et al.. Direct Search for Low Mass Dark Matter Particles with CCDs Phys. Lett. B 711, 264 (2012), arxiv: 1105.5191.

[CDMS Si 13] R.Agness et al.. Silicon Detector Dark matter Results from the Final Exposure of CDMS II arxiv: 1304.4279.

[Tiffenberg talk @UCLA2016] J.Tiffenberg. WIMP search status

[J. Tiffenberg et al., 2013] J.Tiffenberg et al.. DAMIC : a novel dark matter experiment arxiv: 1310.6688.

[Chavarria et al., 2014] A.Chavarria et al.. DAMIC at SNOLAB arxiv: 1407.0347.

[J. Estrada et al., 2011] J. Estrada et al.. Plasma effect in Silicon Charge Coupled Devices(CCDs) arxiv: 1105.3229v3.

[T. Abbott et al., 2014] T.Abbott et al.. Comparison of DECam engineering CCDs with the DES technical requirements(internal note)

[A. Aguilar-Arevalo et al., 2015] A. Aguilar-Arevalo et al.. Measurement of radioactive contamination in the high-resistivity silicon CCDs of the DAMIC experiment arxiv: 1506.02562v2.

[J. Lindhard et al., 1963] J. Lindhard et al.. Integral equations governing radiation effects(notes on atomic collisions, III) Mat. Fys. Medd. Dan. Vid. Selsk. 33, no.10(1963).

[H. Chagani et al., 2008] H. Chagani et al.. Measurement of the quenching factor of Na recoils in NaI(Tl) arxiv: 0806.1916v1.

[Lewin and Smith, 1996] J.D. Lewin and P.F. Smith Review of mathematics, numerical factors, and corrections for dark matter experiments based on elastic nuclear recoil. Astroparticle Physics 6(1996) 87-112.

[G. Gerbier et al., 1990] G. Gerbier et al.. Measurement of the ionization of slow silicon nuclei in silicon for the calibration of a silicon dark-matter detector Physical review D, volume 42, number 9, 1 November 1990.

[E. Simon et al., 2003] E. Simon et al.. SICANE : a detector array for the measurement of nuclear recoil quenching factors using a mono energetic neutron beam NIM(A), 507(2003) 643-656.

[Th. Jagemann et al., 2005] Th. Jagemann et al.. Neutron scattering facility for the measurement of nuclear recoil quenching factors NIM(A), 551(2005) 245-260.

[Geant4] http://geant4.cern.ch.

[C. Burke et al., 1974] C. Burke et al.. Li-7(p,n0)Be-7 angular distributions to Ep = 3.8MeV Physical review C, volume 10, number 4, October 1974.

[Plastic scintillator] http://www.eljentechnology.com/index.php/products/plastic-scintillators/48-ej-200.

[X-Ray attenuation length] http://henke.lbl.gov/optical_constants/atten2.html

[Polyvinyltoluene] National Center for Biotechnology Information. PubChem Compound Database; CID=16213094, https://pubchem.ncbi.nlm.nih.gov/compound/16213094.

[Epoxy cement] http://www.eljentechnology.com/index.php/products/accessories/93-ej-500

[Tevatron experiments] http://www.fnal.gov/pub/tevatron/experiments/index.html.

[L. Bonnet et al., 2014] L. Bonnet et al.. Study on GASTOF - A 10 ps resolution timing detector NIM(A), 762(2014) 77-84.

[G. F. Knoll, 2000] G. F. Knoll (2000). *Radiation detection and measurement, edition 3.* ISBN-13 : 9780471073383. John Wiley and Sons, Inc.

[K.A.Olive et al.] (Particle Data Group), Chinese Physics C38, 090001(2014) .

[R.J. Holmes] http://www.iaea.org/inis/collection/NCLCollectionStore/_Public/14/792/14792880.

[Amptek website] http://www.amptek.com/products/xr-100sdd-silicon-drift-detector/.

[D. Griffiths, 2008] David. Griffiths (2008). *Radiation detection and measurement, edition 3.* ISBN-13 : 978-3-527-40601-2. Wiley-VCH Verlag GmbH & Co. KGaA, Weinheim.

[Elastic Scattering website] http://www.virginia.edu/ep/Interactions/1__introduction_&_collision_kinematics.htm.

[National nuclear data center] http://www.nndc.bnl.gov/sigma/index.jsp.

[ENDF webpage] https://t2.lanl.gov/nis/data/endf/.

[Y. Hochbert et al., 2015] Y. Hochbert et al.. Superconducting detector for super light dark matter arXiv:1504.07237v1.

[W. Beriguete et al., 2015] W. Beriguete et al.. Production of Gadolinium-loaded liquid scintillator for the Daya Bay reactor neutrino experiment http://arxiv.org/pdf/1402.6694v1.

[J. Polchinski 92] J. Polchinski. Effective field theory and the Fermi surface arXiv:hep-th/9210046v2.

[S. Carroll blog] S. Carroll. http://www.preposterousuniverse.com/blog/2013/06/20/how-quantum-field-theory-becomes-effective/

[J. Fan et al., 10] J. Fan et al.. Non-relativistic effective theory of dark matter direct detection JCAP(2010), 042. ArXiv : 1008.1591.

[W. Haxton PC] W. Haxton. Private communications.

[EFT JCAP 13] A. Fitzpatrick et al.. JCAP 02, (2013)004.. arXiv : 1203.3542[hep-ph]

[EFT global fit 14] R. Catena et al.. JCAP 09, (2014)045.. arXiv : 1405.2637

[EFT SuperCDMS 15] K. Schneck et al.. SuperCDMS collaboration. arXiv : 1503.03379

[New form factor] L. Vietze et al.. arXiv : 1412.6091

[Snolab website] https://www.snolab.ca

[J. Wall, 96] J. Wall. Q.J.R. astr. Soc.(1996),37,519-563..

[Silicon wikipedia] https://en.wikipedia.org/wiki/Silicon

[momentum transfer XS] https://www.phys.ksu.edu/personal/thumm/RESEARCH/PUBLICATIONS/1993_PRA47_AngDiffX_el+Cs.pdf

[XENON Likelihood 11] XENON collaboration. http://arXiv:1103.0303.

A

Appendix

A.1 The CTI analysis for a CCD image requires a Gaussian fit

For an image in our CTI analysis, typically, the ^{55}Fe peak contained ∼1000 events[1] and followed a Gaussian distribution. There are at least two options to do a Gaussian fit : χ^2 and likelihood. To know the quality of fit, or the "Goodness-of-Fit(GoF)", people usually use Pearson χ^2 to evaluate the GoF ([K.A.Olive et al.], [Cowan, 1998],). However, when utilizing Pearson χ^2 option there is a limitation : the bin content of a histogram to be fit should big enough, usually ≥5 for all of the bins, see for instance, [Behnke et al., 2013] and [Baker and Cousins, 1984].

To get a satisfactory fit quality, there are two solutions : either using another fit option of "likelihood",or decreasing the number of bins such that there are≥ 5 events per bin. The first solution doesn't suffer from the low statistics[Behnke et al., 2013], however, the drawback is one can't use the returned "χ^2/ndf " from ROOT(in the statistics box) directly because it's a still a Pearson "χ^2" therefore it is not good to evaluate GoF. To get a meaningful "χ^2/ndf ", one needs to convert it to "χ^2_λ"[Baker and Cousins, 1984]. Under ROOT, one can get this χ^2_λ by a couple of commands, see below appendix A.2 and A.3 for details.

A.2 Comparison of two fit options for a Gaussian fit : χ^2 and likelihood

In the case of a Gaussian fit, mathematically, these two options, χ^2 and likelihood, are exactly same,[K.A.Olive et al.].

$$\chi^2(\boldsymbol{\theta}) = -2lnL(\boldsymbol{\theta}) + constant = \sum_{i=1}^{N} \frac{(y_i - F(x_i;\boldsymbol{\theta}))^2}{\sigma_i^2} \tag{A.1}$$

[1] For a $5.9KeV$ X-ray, the number of generated electron-hole pairs is, $5.9KeV/3.65eV \cong 1620$. And the produced electron clouds are contained within a diameter of only $0.4\mu m$(FWHM), [Janesick, 2001]

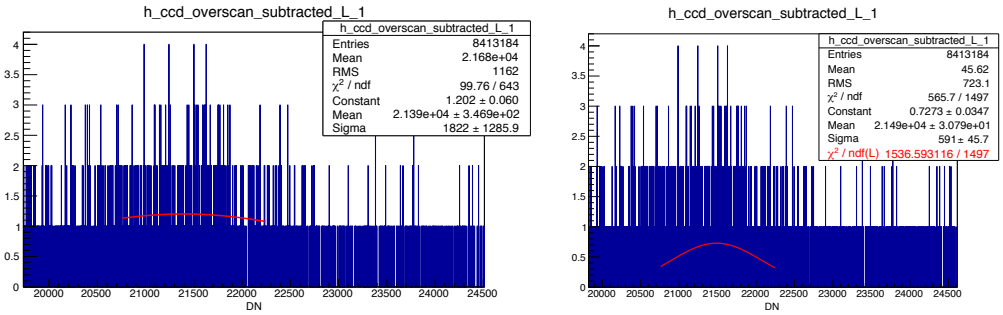

A.1a. fit option : χ^2 A.1b. fit option : likelihood

Figure A.1: Comparison of two Gaussian fit options using same fits file: χ^2 and likelihood

where N is the number of (independent)measurements, y_i is measured data, x_i are the known points to be measured, $F(x_i;\ \boldsymbol{\theta})$ and σ_i^2 are the mean and variance of a Gaussian distribution.
However, in the case of small statistics(typically, bin contents<5), a Gaussian fit with these two options might produce totally different results : as shown in figure A.1. Figure A.1 shows the Fe-55 peak of a CCD image after its overscan has been subtracted. The fit in Figure A.1a is a Gaussian using a "χ^2 / ndf" distribution to determine the fit parameters. The fit in Figure A.1b uses a likelihood distribution to determine the Gaussian Fit parameters. The "χ^2 / ndf" in the statistical boxes of both figures are the values calculated according to the default fit option of χ^2. While in figure A.1b, there is an extra item, the "χ^2 / ndf(L)", in the statistical box, which is the χ^2_λ that could be used to evaluate the "Goodness-of-Fit"(GoF).
It turns out that, when doing a Gaussian fit to a histogram, the χ^2_λ for a small statistics histogram could be considered as an equivalent one as the general χ^2(Pearson χ^2) for a large statistics one. A detailed discussion will be followed below.

Figure A.2 compares two Gaussian fit options to small and large statistics with simulated (randomly generated) data.
The upper two histograms are identical Gaussians with 200K events, fitting with "Chi2" and "likelihood" respectively. The fit results have a very small difference(including "χ^2 / ndf", "Mean" and "Sigma" etc).
In the lower two plots of figure A.2, 20 events are randomly selected from the Gaussian distributions above, and fit with the "Chi2" and "likelihood" methods. Note that the "ndf" number for the lower two histograms is not the same: for the lower left plot, it is 13 = 16 - 3.
Note that empty bins are not taken into account in this fit.
Apparently, in figure A.2, the fit curve(with option of χ^2) in the lower left plot has a big bias; while the bias in the lower right plot is much smaller.

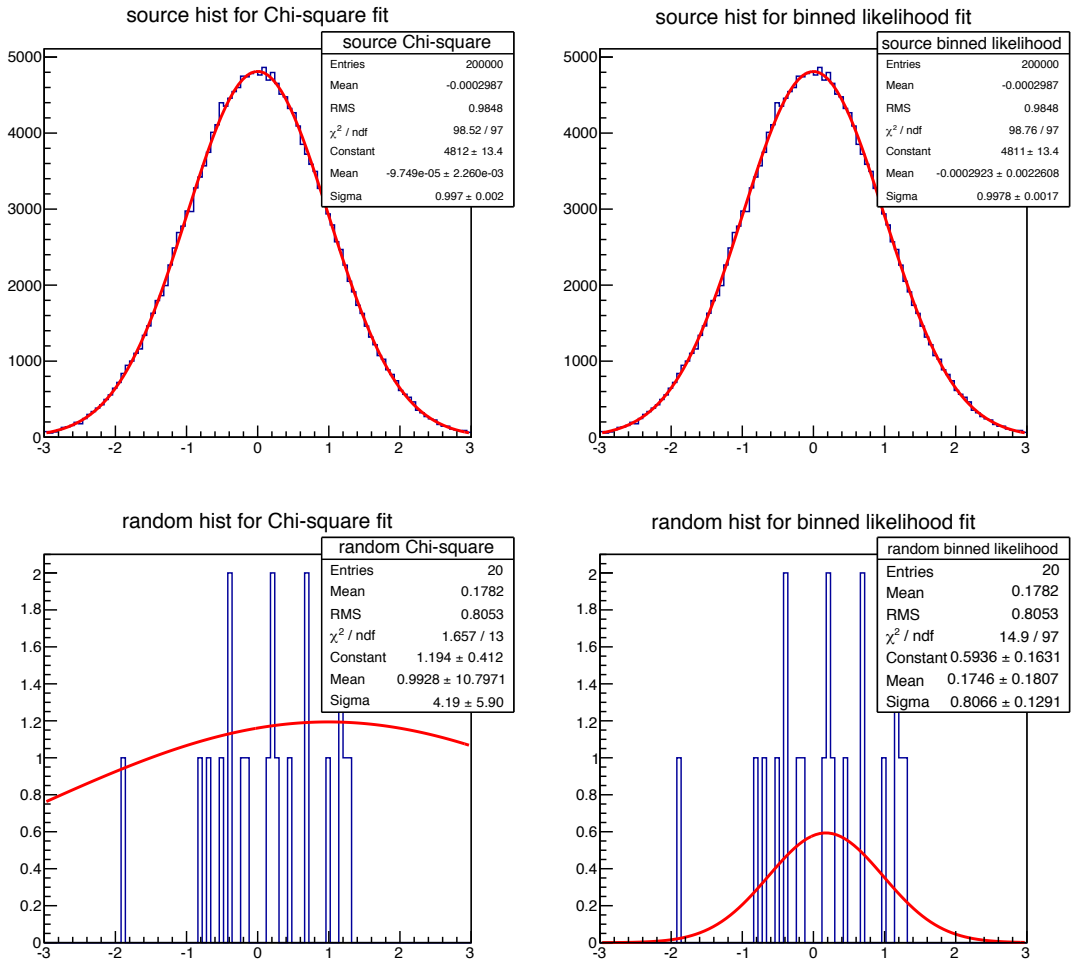

Figure A.2: An example to compare fit options of χ^2 and likelihood

It turns out the existence of this bias is an intrinsic problem of applying a least-square fit to a low-statistics histogram, no matter which type of χ^2 it is : Pearson χ^2 or Neyman χ^2.
The Pearson χ^2 is defined as [Behnke et al., 2013],

$$\chi^2_{Pearson}(\boldsymbol{\theta}) = \sum_{i=1}^{B} \frac{[n_i - \nu_i(\boldsymbol{\theta})]^2}{\nu_i(\boldsymbol{\theta})} \tag{A.2}$$

where θ are the parameters to be estimated, B is the number of bins, n_i and ν_i are the observed and expected number of entries respectively for bin i.
The Neyman χ^2 is defined as [Behnke et al., 2013], where parameters have the same meanings as Pearson χ^2.

$$\chi^2_{Neyman}(\boldsymbol{\theta}) = \sum_{i=1}^{B} \frac{[n_i - \nu_i(\boldsymbol{\theta})]^2}{n_i} \tag{A.3}$$

Take the Neyman χ^2 as an example first. If the bins have few entries(typically < 5), there are two main sources of bias : (1). variances of the number of bin entries is poorly estimated, (2) bins with zero entries lead to an estimated variances of zero therefore can't be used in equation (A.2)(the denominator can't be zero). The fit option of Pearson χ^2 suffers also from the same problems.
More specifically, for Pearson χ^2, by solving $\partial\chi^2/\partial\nu = 0$, the best estimate is

$$\hat{\nu}^{Pearson} = N + \frac{\chi^2_{min}}{2} \ . \tag{A.4}$$

Similarly, for Neyman χ^2,

$$\hat{\nu}^{Neyman} = N - \chi^2_{min} \ . \tag{A.5}$$

From equation (A.4) and (A.5), obviously, both estimates are biased.
Because the χ^2 function approximately follows a $\chi^2(B-m)$ distribution with $E(\chi^2) = B - m$, where "B" is the number of bins and "m" is the number of parameters, the bias is negligible only if the observed number of events $N \gg B - m$.
As a comparison, thanks to the lack of any χ^2 function, the maximum-likelihood method(equation (A.6) doesn't suffer from a bias and the low statistics of bins(there is no χ^2 function that has been involved).

$$lnL(n;\ \nu, \boldsymbol{\theta}) = \sum_{i=1}^{B} n_i ln\nu_i(\nu, \boldsymbol{\theta}) - \nu + constant \tag{A.6}$$

A.3 Goodness of fit tests of Gaussian fits

As is explained in A.2, it is better to use a likelihood method for fitting low-statistics histograms. Often, one wants to know the quality of the fit, or the so called Goodness-of-Fit (GoF). To do this, one should use a λ^2_χ likelihood ratio[Baker and Cousins, 1984], explained in more detail in [Hoel, 1971], which is defined in Eq.(A.7).

$$\chi^2_\lambda = -2ln\ \lambda = -2ln\ L(\boldsymbol{y};\ \boldsymbol{n}) + 2ln\ L(\boldsymbol{m};\ \boldsymbol{n}) \tag{A.7}$$

where the λ is defined as following,

$$\lambda = L(\boldsymbol{y};\ \boldsymbol{n})/L(\boldsymbol{m};\ \boldsymbol{n}) \tag{A.8}$$

where $L(\boldsymbol{y};\ \boldsymbol{n})$ and $L(\boldsymbol{m};\ \boldsymbol{n})$ both represent likelihood functions, $\boldsymbol{y} = (y_1, y_2, ...y_k)$ represents the number of events predicted by the model to be in each bin, $\boldsymbol{n} = (n_1, n_2, ...n_k)$ is the number of events in each bin, $\boldsymbol{m} = (m_1, m_2, ...m_k)$ is the true(unknown) value of $\boldsymbol{n}$ bins that one would get if there were no uncertainties.
One should be aware also that if a histogram is un-binned, one is strongly recommended not to use the λ^2_χ to do a GoF test, as pointed out by this reference, [Joel Heinrich, 2003], instead, one should consider using Kolmogorov-Smirnov or the Anderson-Darling tests, [Behnke et al., 2013].
The following figure A.3a is the same as A.3b but binned with different bin sizes. Figure A.3a has a big number of bins therefore in each bin the bin contents is relatively smaller. Figure A.3b has a small number of bins, and accordingly the bin contents are bigger.
A Gaussian fit has been applied to both of the two sub-figures using likelihood (figure A.3a) and chi-square (figure A.3b) methods. The fit results have almost no difference for the two fit options in terms of the χ^2/ndf.
This comparison demonstrates that for a low statistic histogram, using a likelihood method for fitting provides a good result of χ^2/ndf.

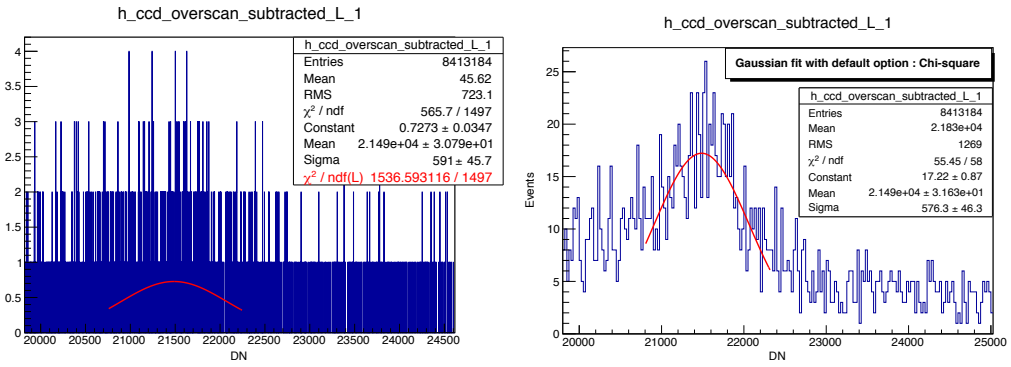

A.3a. fit option : χ^2 A.3b. fit option : likelihood

Figure A.3: Gaussian fit using two methods for low-statistics and high-statistics data samples.

A.4 The derivation of the formula for recoil energy E_R in elastic scattering

The formula for the recoil energy from elastic scattering has been shown in Eq.(3.1) in chapter 3. However, I have found no reference to the full calculation, so I derive it here, starting with a formula for recoil energy from [Elastic Scattering website]. Figure A.4 shows an elastic scattering in the lab and center-of-mass frames.

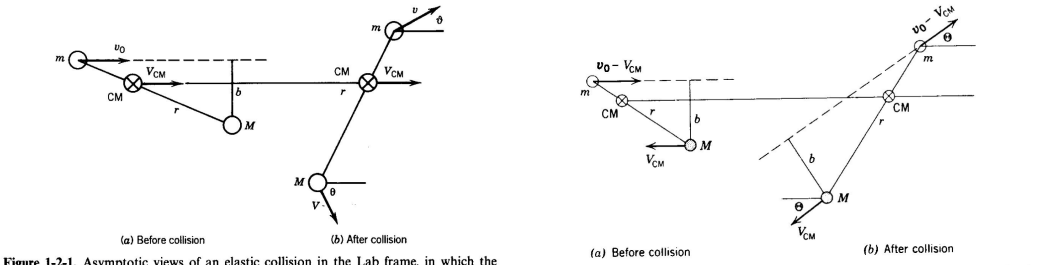

Figure 1-2-1. Asymptotic views of an elastic collision in the Lab frame, in which the target M is initially at rest. In each view the distance between the particles r is much greater than the range of the interaction between the particles. The initial velocity of the projectile is v_0; it is scattered through the angle ϑ in the Lab system. The target M recoils through the Lab angle θ.

Figure 1-2-2. Asymptotic views of the elastic collision of Fig. 1-2-1, now shown in the center-of-mass frame. Here both particles are scattered through the common CM angle Θ, so that the distinction between projectile and target vanishes.

A.4a. Lab system χ^2 A.4b. CMS system

Figure A.4: Comparison of elastic scattering in lab and CMS system.

According to this website [Elastic Scattering website], the recoil energy is,

$$\begin{aligned} E_R &= \gamma E_0 sin\ ^2\frac{\Theta}{2} \\ &= E_0\frac{4mM}{(m+M)^2}sin\ ^2\frac{\Theta}{2} \\ &= E_0\frac{4mM}{(m+M)^2}\frac{1-\cos\Theta}{2} \\ &= E_0\frac{2mM}{(m+M)^2}(1-\cos\Theta) \end{aligned} \tag{A.9}$$

where E_R is the recoil energy, E_0 is the incident energy of the neutron, Θ is the angle of the recoiled nucleus in the CMS frame as is shown in figure A.4b, and m and M are the mass of incident neutron and the nucleus, respectively.

Also, the angle of the scattered neutron in the lab frame ϑ and the Θ in CMS frame have the relationship [Elastic Scattering website],

$$\tan\vartheta = \frac{sin\ \Theta}{\frac{n}{M} + cos\ \Theta}. \tag{A.10}$$

So, the next step is quite straight forward, figuring out how to express Θ with ϑ.

$$\tan\vartheta = \frac{sin\ \Theta}{\frac{n}{M} + cos\ \Theta}$$
$$\frac{\sin\vartheta}{\cos\vartheta} = \frac{sin\ \Theta}{\frac{n}{M} + cos\ \Theta}$$
$$\frac{\sin^2\vartheta}{\cos^2\vartheta} = \frac{\sin^2\Theta}{(\frac{n}{M})^2 + 2\frac{n}{M}\cos\Theta + \cos^2\Theta} \qquad \text{(squaring both sides)}$$
$$\frac{\sin^2\vartheta + \cos^2\vartheta}{\cos^2\vartheta} = \frac{\sin^2\Theta + (\frac{n}{M})^2 + 2\frac{n}{M}\cos\Theta + \cos^2\Theta}{(\frac{n}{M})^2 + 2\frac{n}{M}\cos\Theta + \cos^2\Theta}$$
$$\frac{1}{\cos^2\vartheta} = \frac{1 + (\frac{n}{M})^2 + 2\frac{n}{M}\cos\Theta}{(\frac{n}{M})^2 + 2\frac{n}{M}\cos\Theta + \cos^2\Theta}$$
$$(\frac{n}{M})^2 + 2\frac{n}{M}\cos\Theta + \cos^2\Theta = \cos^2\vartheta + (\frac{n}{M})^2\cos^2\vartheta + 2\frac{n}{M}\cos\Theta\cos^2\vartheta$$
$$\cos^2\Theta + 2\frac{n}{M}\cos\Theta(1-\cos^2\vartheta) + (\frac{n}{M})^2(1-\cos^2\vartheta) - \cos^2\vartheta = 0$$
$$\cos^2\Theta + 2\frac{n}{M}\sin^2\vartheta\cos\Theta + (\frac{n}{M})^2\sin^2\vartheta - \cos^2\vartheta = 0$$
$$\cos\Theta = \frac{-2\frac{m}{M}\sin^2\vartheta \pm \sqrt{(2\frac{m}{M}\sin^2\vartheta)^2 - 4[(\frac{n}{M})^2\sin^2\vartheta - \cos^2\vartheta]}}{2}$$
$$\cos\Theta = -\frac{m}{M}\sin^2\vartheta + \sqrt{(\frac{m}{M})^2\sin^2\vartheta(\sin^2\vartheta - 1) + \cos^2\vartheta}$$
(discard the root with "-" because $\cos\Theta$ is not always negative.)
$$\cos\Theta = -\frac{m}{M}\sin^2\vartheta + \cos\vartheta\sqrt{1 - (\frac{m}{M})^2\sin^2\vartheta}$$
$$\cos\Theta = -\frac{1}{M}(m\sin^2\vartheta - \cos\vartheta\sqrt{M^2 - m^2\sin^2\vartheta}) \qquad \text{(A.11)}$$

Substituting Eq.(A.11) into Eq.(A.9), one gets,

$$\begin{aligned} E_R &= E_0\frac{2mM}{(m+M)^2}(1-\cos\Theta) \\ &= E_0\frac{2mM}{(m+M)^2}(1 + \frac{1}{M}(m\sin^2\vartheta - \cos\vartheta\sqrt{M^2 - m^2\sin^2\vartheta})) \\ &= E_0\frac{2m}{(m+M)^2}(M + m\sin^2\vartheta - \cos\vartheta\sqrt{M^2 - m^2\sin^2\vartheta}) \end{aligned}$$

Substituting $m = 1, M = A$ which separately represent the mass of the neutron and the atomic number of target detector, one gets,

$$E_R = E_0\frac{2}{(1+A)^2}(A + \sin^2\vartheta - \cos\vartheta\sqrt{A^2 - \sin^2\vartheta}) \qquad \text{(A.12)}$$

Eq.(A.12) is exactly the same as Eq.(4.8) in chapter 4.

Next, we should figure out another expression of E_n in figure 4.4.
The total time of flight could be expressed as two parts,

$$\begin{aligned} \Delta t &= \Delta t_l + \Delta t_r \\ &= \frac{l}{v_0} + \frac{r}{v} \\ \Rightarrow (\Delta t)^2 &= (\frac{l}{v_0} + \frac{r}{v})^2 \end{aligned} \tag{A.13}$$

where, Δt is defined as the whole time of flight, Δt_l is the time of flight over the distance of l with speed v_0, Δt_r is the time of flight over the distance of r with speed v.

From the website of [Elastic Scattering website], the velocity of scattered neutrons can be expressed as

$$v^2 = v_0^2[1 - \frac{4mM}{(m+M)^2}\cos^2\theta] \tag{A.14}$$

where the θ in Eq.(A.14) is the same symbol but isn't the same angle of figure 4.4, since the angle in figure 4.4 corresponds to ϑ in figure A.4a. So, one needs to convert the θ in figure A.4a to ϑ in figure A.4a.

From the website of [Elastic Scattering website],

$$\theta = \frac{1}{2}(\pi - \Theta)$$
$$\Rightarrow \cos\Theta = -\cos 2\theta$$
$$\Rightarrow \cos^2\theta = \frac{1-\cos\Theta}{2}$$
$$\cos^2\theta = \frac{1+\frac{1}{M}(m\sin^2\vartheta - \cos\vartheta\sqrt{M^2 - m^2\sin^2\vartheta})}{2} \quad \text{(From Eq.(A.11))}$$
$$= \frac{1}{2M}(M + m\sin^2\vartheta - \cos\vartheta\sqrt{M^2 - m^2\sin^2\vartheta})$$
$$\Rightarrow 1 - \frac{4mM}{(m+M)^2}\cos^2\theta = 1 - \frac{4mM}{(m+M)^2}\frac{1}{2M}(M + m\sin^2\vartheta - \cos\vartheta\sqrt{M^2 - m^2\sin^2\vartheta}) \quad \text{(from Eq.(A.14))}$$
$$= \frac{1}{(m+M)^2}[(m+M)^2 - 2mM - 2m^2\sin^2\vartheta + 2m\cos\vartheta\sqrt{M^2 - m^2\sin^2\vartheta}]$$
$$= \frac{1}{(m+M)^2}[m^2 + M^2 - 2m^2\sin^2\vartheta + 2m\cos\vartheta\sqrt{M^2 - m^2\sin^2\vartheta}]$$
$$= \frac{1}{(m+M)^2}[M^2 - m^2\sin^2\vartheta + 2m\cos\vartheta\sqrt{M^2 - m^2\sin^2\vartheta} + m^2 - m^2\sin^2\vartheta]$$
$$= \frac{1}{(m+M)^2}[\sqrt{M^2 - m^2\sin^2\vartheta} + m\cos\vartheta]^2 \quad \text{(A.15)}$$

So, from Eq.(A.14),

$$v = v_0\sqrt{1 - \frac{4mM}{(m+M)^2}\cos^2\theta}$$
$$= \frac{v_0}{m+M}(\sqrt{M^2 - m^2\sin^2\vartheta} + m\cos\vartheta) \quad \text{(A.16)}$$

Substituting Eq.(A.16) into Eq.(A.13), one gets,

$$(\Delta t)^2 = (\frac{l}{v_0} + \frac{r}{v})^2$$
$$= (\frac{l}{v_0} + \frac{r}{\frac{v_0}{m+M}(\sqrt{M^2 - m^2\sin^2\vartheta} + m\cos\vartheta)})^2$$
$$= \frac{1}{v_0^2}(l + r\frac{m+M}{\sqrt{M^2 - m^2\sin^2\vartheta} + m\cos\vartheta})^2$$
$$= \frac{m_n}{2E_n}(l + r\frac{m+M}{\sqrt{M^2 - m^2\sin^2\vartheta} + m\cos\vartheta})^2$$
$$\Rightarrow E_n = \frac{m_n}{2(\Delta t)^2}(l + r\frac{m+M}{\sqrt{M^2 - m^2\sin^2\vartheta} + m\cos\vartheta})^2 \quad \text{(A.17)}$$

Substituting $m = 1, M = A$ which separately represent the mass of the neutron and the atomic number of target detector, one gets,

$$E_n = \frac{m_n}{2(\Delta t)^2}(l + r\frac{A+1}{\sqrt{A^2 - \sin^2\vartheta} + \cos\vartheta})^2 \tag{A.18}$$

This is exactly the expression of E_n in figure 4.4.

A.5 CCD data analysis

A.5.1 Pedestal subtraction

In DAMIC, to increase the speed of readout, a CCD has been connected to two amplifiers. The amplifier connected to the left side of the CCD typically only reads the image of the left half of the CCD, and the right amplifier reads out the right side of the image. In DAMIC, we read out the entire CCD image from the left amplifier, while simultaneously reading out the right amplifier with no image data. This allows us to understand the noise of the readout.

Pedestal subtraction is one of the key steps of CCD image analysis. There are two options of noise subtraction in DAMIC CCD data analysis. One is to subtract the pedestal noise from the other side of CCD. This is supposed to subtract the correlated noise on the right side from the left side of CCDs. However, it turns out this kind of subtraction will introduce some additional noise as is shown in figure A.5, where the RMS value has increased from 20.01 to 34.12 following this procedure.

Alternatively, there is another subtraction which is to subtract the pedestal from the same side. Figure A.6 shows it does not introduce additional noises : the RMS value in figure A.5a 19.98, is consistent with the one in figure A.5b, 18.37.

A.5.2 Correlation study of the left and right CCD

In this section, the analysis of correlation between the left and right CCD is achieved using this procedure :
(a) Randomly picking up a segment of pixels from the right CCD, putting it in an array, array_R;
(b) Looping over the left CCD, taking segments with the same length as the segment chose from the right CCD in step (a), putting them in arrays, array_{L1}, array_{L2} ... array_{Ln}.
(c) Calculating the correlation factor for (array_{L1}, array_R), (array_{L2}, array_R) ... (array_{Ln}, array_R).
(d) Changing the length of segments and repeating steps (a) to (c).

As can be seen in figure A.7, no matter how long the segment is, the correlation factor is not big enough to demonstrate the existence of a correlation. For reference, a strong correlation should yield a correlation factor close to 1 as is shown in figure A.8 or A.9 for some arbitrary functions with correlated data. Figure A.10 shows a function based on random values that has a weak correlation factor.

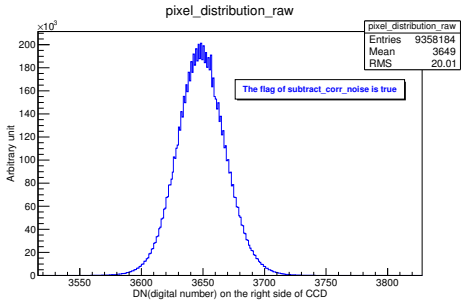

A.5a. before subtraction

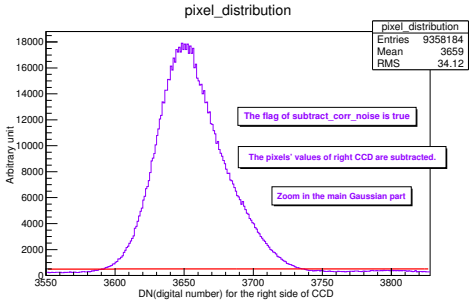

A.5b. after subtraction

Figure A.5: The comparison of before and after subtraction, the flag of "subtract_corr_noise" is on, meaning pedestal subtraction on other half side of CCD.

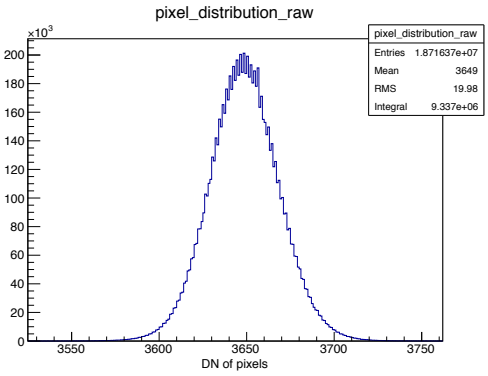

A.6a. before subtraction

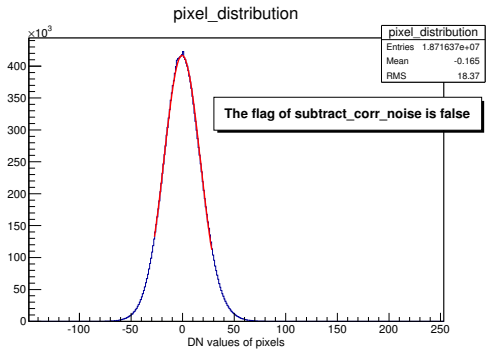

A.6b. after subtraction

Figure A.6: The comparison of before and after subtraction, the flag of "subtract_corr_noise" is off, meaning pedestal subtraction on the same half side of CCD

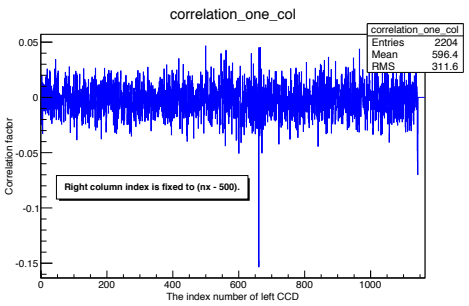

A.7a. ∼4k pixels

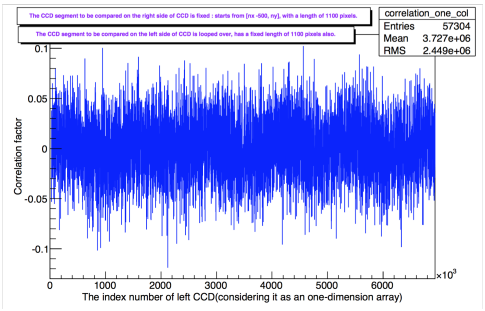

A.7b. 1100 pixels

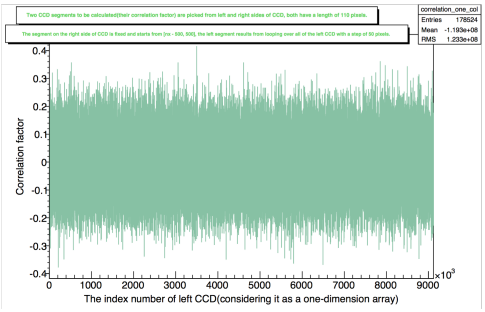

A.7c. 110 pixels

Figure A.7: The comparison of correlation factors with different length of segments.

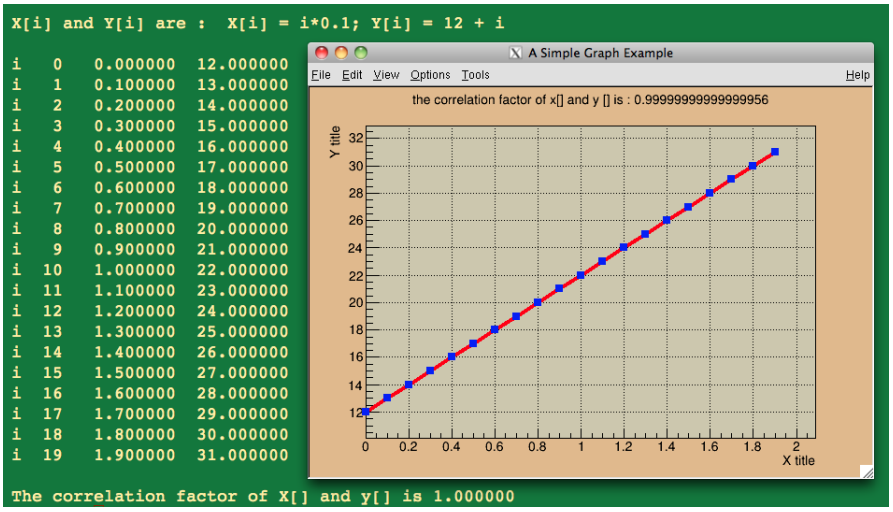

Figure A.8: $y = 10 \times x + 12$, array x[ ] and y[ ] have a strong correlation, correlation factor = 1.0.

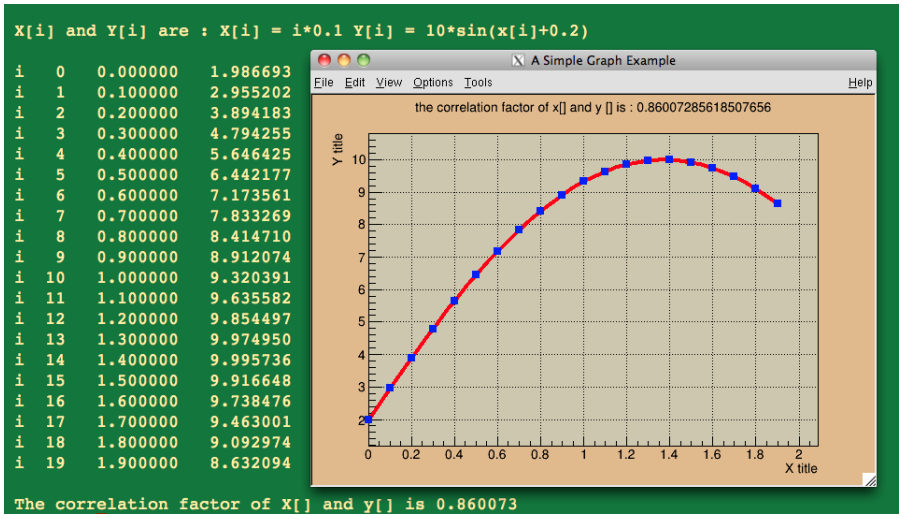

Figure A.9: $y = 10 \times sin(x+0.2)$, array x[ ] and y[ ] have a kind of correlation, correlation factor = 0.86.

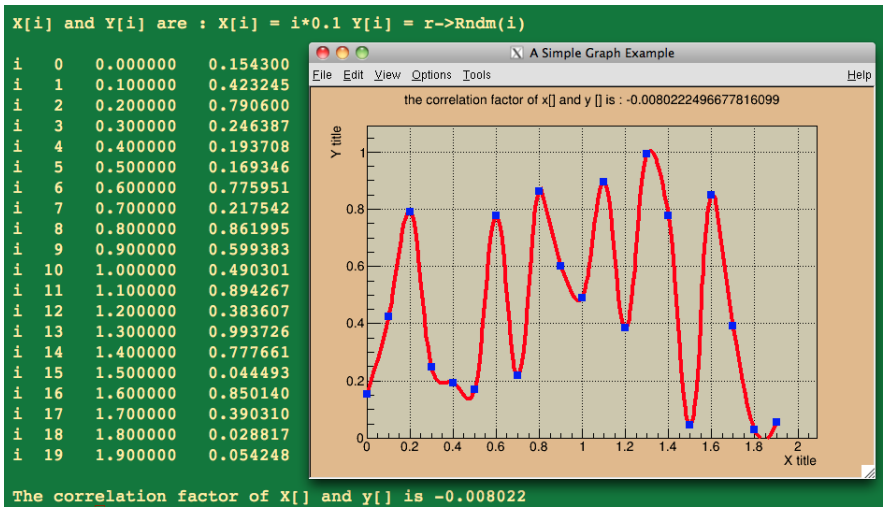

Figure A.10: $x = 0.1 \times i, y$ are random values. array x[ ] and y[ ] have a weak correlation, correlation factor = -0.008.

List of Figures

List of Tables